

**REMOVAL OF DYES AND ANTIBIOTICS BY
ADSORPTION AND PHOTOCATALYTIC
DEGRADATION USING ZN-BASED COMPOSITES**

**A Thesis Submitted to
the Graduate School of Engineering and Sciences of
İzmir Institute of Technology
in Partial Fulfillment of the Requirements for the Degree of**

DOCTOR OF PHILOSOPHY

in Chemical Engineering

**by
Gizem SAYGI**

**June 2023
İZMİR**

We approve the thesis of **Gizem SAYGI**

Examining Committee Members:

Prof. Dr. Fehime AKICIOĐLU ZKAN

Chemical Engineering, Izmir Institute of Technology

Prof. Dr. Canan VARLIKLI

Photonics, Izmir Institute of Technology

Doc. Dr. Aslı YÜKSEL ZŐEN

Chemical Engineering, Izmir Institute of Technology

Prof. Dr. Günseli ZDEMİR

Chemical Engineering, Ege University

Prof. Dr. Saadet YAPAR

Chemical Engineering, Ege University

20 June 2023

Prof. Dr. Fehime AKICIOĐLU ZKAN

Supervisor, Chemical Engineering,
Izmir Institute of Technology

Prof. Dr. Erol ŐEKER

Head of Chemical Engineering

Prof. Dr. Mustafa M. DEMİR

Dean of Engineering Faculty

ACKNOWLEDGMENT

I would like to express my appreciation to my supervisor Prof. Dr. Fehime ÇAKICIOĞLU ÖZKAN for her continuous support, knowledge, supervision and motivation. Her guidance helped me during research and writing of the thesis. I would like to thank sincerely to my PhD Thesis Committee Members, Prof. Dr. Canan VARLIKLI and Assos. Prof. Dr. Aslı YÜKSEL ÖZŞEN for their knowledge, motivation and supportive criticism. I would also like to thank other Jury Members, Prof. Dr. Günseli ÖZDEMİR and Prof. Dr. Saadet YAPAR for their insightful comments.

I thank to Integrated Research Center in İzmir Institute of Technology for technical support.

I would like to thank my family for their love, patience, caring and support.

ABSTRACT

REMOVAL OF DYES AND ANTIBIOTICS BY ADSORPTION AND PHOTOCATALYTIC DEGRADATION USING ZN-BASED COMPOSITES

In this study, the ZIF-8 was synthesized and immobilized on the clinoptilolite surface (ZIF8@CLN) and doped with Ag nanoparticles, forming the Ag-ZIF8 and Ag-ZIF8@CLN composite materials. The characterization results indicated that the ZIF-8 was well-deposited on the clinoptilolite surface and doped successfully with Ag nanoparticles. The adsorption and photocatalytic activity of these adsorbents/catalysts were evaluated by the removal of the organic pollutants such as dyes and antibiotics. The target dyes were cationic Methylene blue (MB), anionic Methyl orange (MO) and Congo red (CR), and zwitterionic Rhodamine B (RhB). The target antibiotic was tetracycline (TC).

The influence of various parameters on removal was investigated using different initial pH, photocatalyst amount, pollutant concentrations and ionic strength. The results showed that ZIF-8 and ZIF-8@CLN are excellent adsorbents. However, the photocatalytic activity of Ag-ZIF8 and especially Ag-ZIF8@CLN composites were much better than ZIF-8 and ZIF-8@CLN for degradation of all dyes. The Ag-ZIF8 and Ag-ZIF8@CLN composite catalysts exhibited more than 90% removal capacity under UV irradiation for 120 min with the dye concentration of 25 mg L⁻¹ at the optimum pHs of each dye. The enhanced adsorption and photocatalytic performance of the composite photocatalysts was attributed to the synergistic effect between the ZIF-8, CLN and Ag. The adsorption data were evaluated by considering adsorption isotherms, kinetics and thermodynamics using target dyes and antibiotics. Proposed photodegradation mechanism of the dyes over Ag-ZIF8@CLN was explained detailed. This work introduced the ZIF-8-based composite photocatalysts with high efficiency, and may provide to prefer these catalysts in photocatalytic field.

ÖZET

BOYALARIN VE ANTİBİYOTİKLERİN ZN TEMELLİ KOMPOZİTLER KULLANILARAK ADSORPSİYON VE FOTOKATALİTİK PARÇALAMA İLE UZAKLAŞTIRILMASI

Bu çalışmada, ZIF-8 sentezlenerek klinoptilolit yüzeyi üzerine tutturulmuştur (ZIF8@CLN) ve Ag nanoparçacıkları ile katkılanarak Ag-ZIF8 ve Ag-ZIF8@CLN kompozit malzemeleri üretilmiştir. Karakterizasyon sonuçları, ZIF-8'in klinoptilolit yüzeyine iyi tutturulduğunu ve Ag nanoparçacıkları ile başarılı bir şekilde katkılandığını göstermiştir. Bu adsorbanların/katalizörlerin adsorpsiyon ve fotokatalitik aktivitesi, boya ve antibiyotik gibi organik kirleticilerin uzaklaştırılmasıyla değerlendirilmiştir. Katyonik Metilen mavisi (MB), anyonik Metil turuncusu (MO) ve Kongo kırmızısı (CR) ve zwitter iyonik Rodamin B (RhB) kullanılan hedef kirletici boyalardır. Tetrasiklin (TC) ise antibiyotik sınıfından seçilen kirleticidir.

Çeşitli parametrelerin giderim üzerindeki etkisi, farklı başlangıç pH'ı, fotokatalizör miktarı, kirletici konsantrasyonu ve iyonik kuvvet kullanılarak incelenmiştir. Sonuçlar, ZIF-8 ve ZIF-8@CLN'nin mükemmel adsorbanlar olduğunu göstermiştir. Bununla birlikte, Ag-ZIF8 ve özellikle Ag-ZIF8@CLN kompozitlerinin fotokatalitik aktivitesi ZIF-8 ve ZIF-8@CLN'ye kıyasla tüm boyaların bozunmasında daha iyi sonuç göstermiştir. Ag-ZIF8 ve Ag-ZIF8@CLN kompozit katalizörleri, her bir boyanın optimum pH'ında 25 mg L⁻¹ boya konsantrasyonu ile 120 dakikalık UV ışınması altında % 90'dan fazla giderim kapasitesi sergilemiştir. Kompozit fotokatalizörlerin gelişmiş adsorpsiyon ve fotokatalitik performansı, ZIF-8, CLN ve Ag arasındaki sinerjistik etkiyle açıklanabilir. Boya ve antibiyotik gideriminde elde edilen adsorpsiyon verileri adsorpsiyon izotermeleri, kinetiği ve termodinamiği dikkate alınarak değerlendirilmiştir. Boyaların Ag-ZIF8@CLN üzerinde fotokatalitik parçalanma mekanizması ayrıntılı olarak açıklanmıştır. Bu çalışma ZIF-8 temelli yüksek verimli kompozit fotokatalizörleri tanıtmış ve bu katalizörlerin fotokatalitik alanda tercih edilebileceğini göstermiştir.

TABLE OF CONTENTS

LIST OF FIGURES	ix
LIST OF TABLES	xii
CHAPTER 1. INTRODUCTION	1
CHAPTER 2. BACKGROUND INFORMATION	5
2.1. Organic Pollutants	5
2.1.1. Organic Dyes	5
2.1.2. Pharmaceuticals and Personal Care Products	8
2.1.3. Pesticides	9
2.1.4. Aromatic Compounds	10
2.2. Removal of Organic Pollutants	11
2.2.1. Adsorption	13
2.2.1.1. Adsorption Process	13
2.2.1.2. Adsorption Parameters	15
2.2.1.3. Adsorption Equilibrium	16
2.2.1.4. Adsorption Kinetics	22
2.2.1.5. Adsorption Thermodynamics	26
2.2.2. Photocatalytic Degradation	27
2.2.2.1. Photocatalytic Degradation Process	28
2.2.2.2. Photocatalytic Degradation Parameters	29
2.2.2.3. Photocatalytic Degradation Kinetics	33
2.3. Adsorbents and Photocatalysts	34
2.3.1. Metal Organic Frameworks (MOFs)	35
2.3.2. Zeolitic Imidazolate Frameworks-8 (ZIF-8)	37
2.3.3. Immobilization on the Support Surface	38

2.3.4. Doping of Metal	41
2.3.5. ZIF-8-Clinoptilolite-Silver Composites as Adsorbent and Photocatalyst	42
2.3.6. Contributions to the Literature	46
 CHAPTER 3. MATERIAL AND METHODS	 47
3.1. Materials	47
3.2. Synthesis of Adsorbents/Photocatalysts	47
3.2.1. Synthesis of ZIF-8 and ZIF8@CLN	47
3.2.2. Synthesis Ag-ZIF8 and Ag-ZIF8@CLN.....	48
3.3. Characterization Methods	49
3.4. Adsorption of Organic Pollutants	50
3.5. Photocatalytic Degradation of Organic Pollutants	51
 CHAPTER 4. RESULTS AND DISCUSSION	 53
4.1. Characterization	53
4.1.1. Crystal Structure Analysis	53
4.1.2. Surface Analysis	55
4.1.3. Structural Properties	56
4.1.4. Morphology Analysis	57
4.1.5. Thermal Analysis	59
4.1.6. Optical Properties	60
4.1.7. XPS Analysis	61
4.2. Adsorption	66
4.2.1. Adsorption of Dyes	66
4.2.1.1. Dye Adsorption Parameter	66
4.2.1.2. Dye Adsorption Isotherms	72
4.2.1.3. Dye Adsorption Kinetics	75

4.2.1.4. Dye Adsorption Thermodynamics	77
4.2.1.5. Reusability	81
4.2.1.6. Dye Adsorption Mechanism	82
4.2.2. Adsorption of Tetracycline	86
4.2.2.1. TC Adsorption Parameter	86
4.2.2.2. TC Adsorption Isotherms	90
4.2.2.3. TC Adsorption Kinetics	92
4.2.2.4. Reusability	94
4.2.2.5. TC Adsorption Mechanism	95
4.3. Photocatalytic Degradation	97
4.3.1. Photodegradation Parameter	97
4.3.1.1. Effect of pH	97
4.3.1.2. Effect of Photocatalyst Amount	100
4.3.1.3. Effect of Initial Dye Concentration	101
4.3.2. Photodegradation Kinetics.....	103
4.3.3. Reusability.....	107
4.3.4. Photodegradation Mechanism	108
 CHAPTER 5. CONCLUSION	 116
REFERENCES	118
APPENDICES.....	151
APPENDIX A. SUPPLEMENTARY INFORMATION FOR CHAPTER 4	151
APPENDIX B. PERMISSIONS FOR REPRODUCING PUBLISHED ARTICLE.....	158

LIST OF FIGURES

<u>Figure</u>		<u>Page</u>
Figure 2.1.	Transport process for the adsorption by using the porous adsorbent	14
Figure 2.2.	The mechanism of photocatalytic degradation of organic pollutants.....	29
Figure 2.3.	Operating parameters affected to photocatalytic activity.....	30
Figure 2.4.	The crystal structure of ZIF-8	38
Figure 2.5.	Three dimensional structure of clinoptilolite.....	41
Figure 3.1.	The synthesis procedures of (a) ZIF-8 and (b) ZIF8@CLN.....	48
Figure 3.2.	The synthesis procedures of Ag-ZIF-8 and Ag-ZIF8@CLN.....	49
Figure 4.1.	XRD spectra of synthesized catalysts	54
Figure 4.2.	BET adsorption-desorption isotherms of synthesized photocatalysts	56
Figure 4.3.	ATR-IR spectra of synthesized photocatalysts.....	57
Figure 4.4.	SEM images of (a) ZIF8, (b) ZIF8@CLN, (c) Ag-ZIF8 and (d) Ag-ZIF8@CLN. The mapping analysis of (e) Ag-ZIF8 and (f) Ag-ZIF8@CLN	58
Figure 4.5.	TGA spectra of (a) ZIF-8, raw CLN, ZIF8@CLN and (b) Ag-ZIF8, Ag- ZIF8@CLN.....	59
Figure 4.6.	Optical properties, (a) and (b) the UV-DRS spectra of photocatalysts, (c) and (d) Bandgap of photocatalysts, (e) PL spectra.....	61
Figure 4.7.	XPS survey of the synthesized photocatalysts.....	62
Figure 4.8.	XPS spectra of the synthesized photocatalysts. (a) Zn2p, (b) C1s, (c) N1s, (d) O1s, (e) Ag3d and (f) Cl2p.....	65
Figure 4.9.	Effect of ph (a) ZIF-8@CLN, (b) ZIF-8.....	68
Figure 4.10.	Effect of adsorbent amount (a) MB, (b) MO, (c) CR and (d) RhB.....	69
Figure 4.11.	Effect of dye concentration (a) MB, (b) MO, (c) CR and (d) RhB.....	70
Figure 4.12.	Effect of ionic strength (a) MB, (b) MO, (c) CR and (d) RhB.....	71
Figure 4.13.	Adsorption isotherms of dyes.....	74

<u>Figure</u>	<u>Page</u>
Figure 4.14. Pseudo-second-order kinetics for (a) ZIF-8@CLN, (b)ZIF-8. Intraparticle diffusion model for (c) ZIF-8@CLN, (d) ZIF-8. Boyd model for (e) ZIF-8@CLN, (f) ZIF-8.....	76
Figure 4.15. Van't Hoff plots for ΔH° and ΔS° calculations (a) MB, (b) MO, (c) CR and (d) RhB.....	78
Figure 4.16. Adsorption isotherms of dyes at various temperatures (a) MB, (b) MO, (c) CR and (d) RhB.....	79
Figure 4.17. The removal efficiencies of MB, MO, CR and RhB for four consecutive cycles.....	81
Figure 4.18. ATR-IR spectras of ZIF-8 and ZIF-8@CLN (a) before and after adsorption.....	84
Figure 4.19. Possible mechanism for MB adsorption on ZIF8@CLN and ATR-IR spectra of ZIF-8 and ZIF-8@CLN after MB adsorption	84
Figure 4.20. Possible mechanism for MO adsorption on ZIF8@CLN and ATR-IR spectra of ZIF-8 and ZIF-8@CLN after MO adsorption	85
Figure 4.21. Possible mechanism for CR adsorption on ZIF8@CLN and ATR-IR spectra of ZIF-8 and ZIF-8@CLN after CR adsorption	85
Figure 4.22. Possible mechanism for RhB adsorption on ZIF8@CLN and ATR-IR spectra of ZIF-8 and ZIF-8@CLN after RhB adsorption	86
Figure 4.23. Effect of pH on TC adsorption.....	88
Figure 4.24. Effect of adsorbent amount on TC adsorption.....	88
Figure 4.25. Effect of TC concentration.....	89
Figure 4.26. Effect of ionic strength on TC adsorption.....	90
Figure 4.27. Suitable adsorption isotherm models of TC on ZIF-8 and ZIF-8@CLN.....	92
Figure 4.28. Kinetics models, (a) Pseudo-second-order, (b) Intraparticle diffusion model, (c) Boyd model.....	93
Figure 4.29. The adsorption efficiencies of TC for four consecutive cycles.....	94
Figure 4.30. Possible mechanism for TC adsorption on ZIF8@CLN and ATR-IR spectra of ZIF-8 and ZIF-8@CLN after TC adsorption	96

<u>Figure</u>	<u>Page</u>
Figure 4.31. The effect of pH for photodegradation of MB, MO, CR and RhB by using Ag-ZIF8 and Ag-ZIF8@CLN.....	99
Figure 4.32. The effect of catalyst amount for photodegradation of MB, MO, CR and RhB by using Ag-ZIF8 and Ag-ZIF8@CLN.....	101
Figure 4.33. The effect of initial dye concentration for photodegradation of MB, MO, CR and RhB by using Ag-ZIF8 and Ag-ZIF8@CLN.....	103
Figure 4.34. The initial rate of a reaction method for the photodegradation of MB, MO, CR and RhB over Ag-ZIF8@CLN.....	105
Figure 4.35. The Langmuir-Hinshelwood plot for the photodegradation of MB, MO, CR and RhB over Ag-ZIF8@CLN.....	106
Figure 4.36. Reusability of Ag-ZIF8 and Ag-ZIF8@CLN.....	107
Figure 4.37. The active species trapping experiment.....	111
Figure 4.38. Proposed photodegradation mechanism of the dyes over Ag-ZIF8@CLN.....	112

LIST OF TABLES

<u>Table</u>	<u>Page</u>
Table 2.1. The chemical structures of common organic pollutants.....	6
Table 2.2. Physicochemical properties of MB, MO, CR and RhB.....	7
Table 2.3. Organic pollutants in wastewater.....	11
Table 2.4. The physical and chemical features of Clinoptilolite.....	41
Table 4.1. Textural properties of the synthesized photocatalysts.....	55
Table 4.2. SEM-EDX Results.....	58
Table 4.3. Isotherm parameters and error functions calculated for MB, MO, CR and RhB adsorption onto ZIF-8 and ZIF-8@CLN.....	73
Table 4.4. Kinetic parameters and error functions calculated for MB, MO, CR and RhB adsorption onto ZIF-8 and ZIF-8@CLN.....	77
Table 4.5. Thermodynamic parameters calculated for MB, MO, CR and RhB adsorption onto ZIF-8 and ZIF-8@CLN at various temperatures.....	80
Table 4.6. Isotherm parameters and error functions for TC adsorption on ZIF-8 and ZIF-8@CLN.....	91
Table 4.7. Kinetic parameters and error functions for TC adsorption on ZIF-8 and ZIF-8@CLN.....	94
Table 4.8. Effect of pH.....	99
Table 4.9. Effect of photocatalyst amount (m).....	100
Table 4.10. Effect of initial dye concentration (C_0).....	102
Table 4.11. Initial rates (r_0) at different concentrations (C_0).....	105
Table 4.12. The rate constants (k_i) and the reaction orders (n).....	106
Table 4.13. Parameters of Langmuir-Hinshelwood model.....	107
Table 4.14. The comparison of ZIF8-based photocatalysts' removal performances for the target organic pollutants	115

CHAPTER 1

INTRODUCTION

Water is one of the defining characteristics of the world and indispensable to many aspects of life. Unfortunately, the rapid development of industries causes to increasing anthropogenic pollutants, which makes the water pollution main problem (Shen, Liao, and Li 2021). Dyes and pharmaceutical and personal care products are considered as common contaminants due to their potential damage to environment and human health, bioaccumulation abilities, and aquatic contamination (da Silva Bruckmann et al. 2022).

Dyes are common toxic contaminants in the environment, and have been used in textile, print, architecture, paper, leather, cosmetic, food, pharmaceutical, etc. It is asserted that 7×10^5 tons of dyes are produced and about 9 billion tons of them are discharging per year (Gao et al. 2021). The color of wastewater affects the public perceptions significantly. Even low concentration of dyes is visible and undesirable in wastewater and decreases the water quality (Gupta et al. 2013). In addition to aesthetic perceptions, many organic dyes are nonbiodegradable, toxic, mutagenic and carcinogenic due to their aromatic structures (Shen, Liao, and Li 2021).

Antibiotics are commonly used to heal the human, livestock, and aquatic life which infected by microorganisms such as bacterias and viruses. Globally, 200,000 tons of antibiotics are utilizing annually (Hu et al. 2017). The high amount of antibiotics are releasing from the body as feces and urine through the aquatic life, which causes to continual contamination and leads to develop resistant genes in environment (Kashmery and El-Hout 2022). Tetracyclines, quinolones, sulfonamides and macrolides are the most widely used antibiotics (Kashmery and El-Hout 2022; Baynes et al. 2016). Therefore, there has been growing interest to improve effective and cheap technology for organic pollutant removal from aquatic environment.

The methods for the removal of organic pollutants have been investigated for few decades, consisting of electrochemical methods, biological methods, photocatalytic

degradation and adsorption (Naikwade et al. 2020; Kitazono et al. 2012; Belkheiri et al. 2015; Thinley et al. 2022). Among these methods, the adsorption and photocatalytic degradation have various advantages such as easy management, high efficiencies, very low energy consumption, efficient environmental protection and small investment. Therefore, adsorption and photocatalytic degradation methods have been used for the treatment of water pollution extensively (Ali et al. 2020; Qingchun Zhang et al. 2020; Jing et al. 2014). Clay, activated carbon, zeolite, agricultural wastes and metal organic frameworks are generally used as an adsorbent (Blachnio et al. 2020; B. Chen et al. 2021; Streit et al. 2019; Kadhom et al. 2020); and TiO_2 , ZnO and Fe_2O_3 are used as an photocatalyst for wastewater treatment (Priyadharshini et al. 2021; Rasheed et al. 2019). The exploring of the novel adsorbents/photocatalysts which are environmentally friendly and cost-effective is the main consideration of the removal process (Y. Meng et al. 2022).

Metal-organic frameworks (MOFs) are the novel three-dimensional porous materials. MOFs are designed to use for wastewater treatment due to their distinctive properties such as large specific surface area, plenty of interaction sites, regular channels, adjustable pore size and high porosity process (K. Fan et al. 2018). They have regular pores and nano-sized cavities that avoid the aggregation of nanoparticles. During the MOFs synthesis, pore structure can be controlled. Zeolite imidazole frameworks (ZIFs) are a subclass of MOFs. ZIFs especially ZIF-8 have gain much attention owing to environmentally friendly synthesis method at room temperature and high chemical stability in aqueous media. These properties make it attractive candidate for the removal of organic pollutants in water process (Miao et al. 2022).

Although MOFs are effective adsorbents/photocatalysts in the removal of organic pollutants, some of them have some disadvantages such as high cost, low reusability, poor moisture and chemical stability and the difficulties on handling process (Abbasnia et al. 2022). Meanwhile, MOFs crystals are generally present in small-sized powders, which adversely affect the process effectiveness and practicability process (Miao et al. 2022). To overcome these disadvantages, MOFs have been constructed with other practical support materials, such as zeolite (O. Singh et al. 2022), clay (Shahriyari Far et al. 2022), graphene and graphene oxides (Szczęśniak, Choma, and Jaroniec 2019) and etc. Therefore, the synthesized MOF composites contain the advantages of both pristine MOF and support material. The natural zeolite, Clinoptilolite, could be used as the support substances for the immobilization of ZIF-8.

Clinoptilolite (CLN) is a natural zeolite in heulandite group, which includes 39% porosity and Si/Al ratio from 4.0 to 5.3 (Estrada-Cabrera et al. 2021). CLN contains two dimensional frameworks, tetrahedral SiO₄ and AlO₄ units and includes three sets of intersecting channels. The molecular formula of CLN is (Na,K)₆Al₆Si₃₀O₇₂.20H₂O (Ullah et al. 2020). It has high thermal and chemical stability, low price and high availability around the world (Akgül 2014). It is resistant to corrosion and radiation. The cation organization of CLN is different due to their multiple network cation sites, which provides enhanced cation exchange capacity (Estrada-Cabrera et al. 2021; Kennedy and Tezel 2018). Based on remarkable properties of ZIF-8 and CLN, they have been used in wastewater treatment applications (Yu and Wu 2020; Abdi 2020; Molla Mahmoudi et al. 2019). However, the composite material of ZIF-8 and CLN has not been studied as an adsorbent or photocatalyst yet.

In this study, we have synthesized ZIF-8 and immobilized on the CLN surface (ZIF-8@CLN) to study adsorption of the organic dyes such as methylene blue (MB), methyl orange (MO), congo red (CR) and rhodamine B (RhB). The adsorption behavior of tetracycline (TC) has been also examined on both ZIF-8 and ZIF8@CLN composite. TC was selected as the representative of ionizable antibiotics. The effects of process parameters such as pH, adsorbent amount, initial dye concentration, ionic strength on the dye removal capacity were investigated in details. Isotherm studies were carried out by using Langmuir, Freundlich, Dubinin-Radushkevich, Radke Prausnitz, Redlich Peterson and Langmuir-Freundlich isotherm models. In addition, kinetics, thermodynamics, and reusability studies were also performed to elaborate the adsorption process. Overall, the ZIF-8 and the designed ZIF-8@CLN are effective and reusable adsorbents for wastewater treatment application.

It is also aimed to synthesize the ZIF8@CLN, Ag-ZIF8 and Ag-ZIF8@CLN composites to use as a photocatalyst by combining attractive properties of ZIF-8, CLN support and Ag nanoparticles. The Ag-ZIF8@CLN nanocomposite has both the ZIF-8 porous structure with CLN support and doped Ag nanoparticles. Therefore, our strategy consists of two aspects: one is the utilization of porous and superior surface area of ZIF-8, the other is the combination of ZIF-8 with CLN and/or Ag to enhance photocatalytic performance. Inspired by the previous studies, it is recorded that ZIF-8 and Ag-ZIF8 have impressive potential as a novel photocatalyst (G. Fan, Zheng, et al. 2018; Thi Thanh et al. 2017; Abdollahi et al. 2021). As far as we know, no study focusing on ZIF8@CLN and Ag-ZIF8@CLN photocatalyst has been reported. In this study,

photocatalytic degradation ability of these photocatalysts for the cationic MB, the anionic MO and CR, and the zwitterionic RhB dyes under UV irradiation was investigated. The experiments were conducted varying different parameters such as pH, photocatalyst amount and initial dye concentration. Such parameter study is carried out to determine the optimum conditions for photocatalytic degradation of dyes. The reaction kinetics study was performed considering both the initial rate of a reaction and Langmuir-Hinshelwood model.

CHAPTER 2

BACKGROUND INFORMATION

2.1. Organic Pollutants

Water pollution is a common problem facing people around the world due to the industry, human activities and agriculture. The industrial and domestic wastewater are generally environmentally persistent to the conventional treatment systems (Ye et al. 2021). The large amounts of these pollutants are produced and released to the water bodies. Therefore, these organic contaminants have been threatened the human and animal health (Ye et al. 2021; Brausch and Rand 2011). The water bodies are seriously polluted by four main classes of organic pollutants including dyes, pharmaceuticals and personal care products, pesticides and aromatic compounds. The chemical structures of commonly used organic pollutants are given in Table 2.1.

2.1.1. Organic Dyes

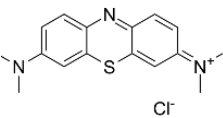
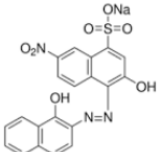
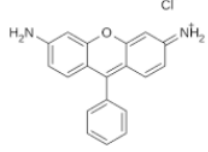
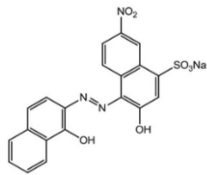
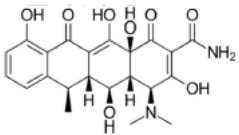
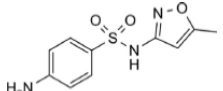
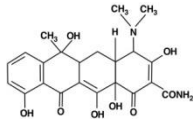
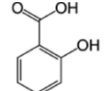
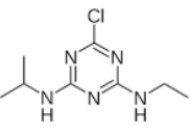
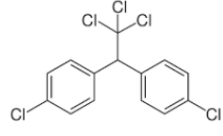
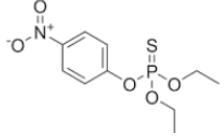
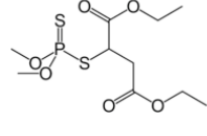
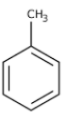
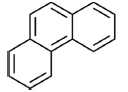
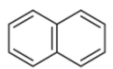
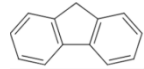
Organic dyes are used to give color to fabrics and other materials. The worldwide usage of organic dyes causes a serious environmental contamination. The textile industry is the main source for this pollution (Konstantinou and Albanis 2004). According to World Bank, about 17 - 20 % of water contamination is caused by textile

Some parts in this chapter have been published in the following paper. Reproduced with permission from Springer Nature.

Saygı, G., Kap, Ö., Çakıcıoğlu-Özkan, F., Varlıklı, C., 2023. Photocatalytic Reactors Design and Operating Parameters on the Wastewater Organic Pollutants Removal. Springer, Published Book Chapter, in book: Photocatalysis for Environmental Remediation and Energy Production.

and dyeing industries (Rafiq et al. 2021). Current studies demonstrated that 10 - 12 % of total consumption of dyes such as Methylene Blue, Indigo Red, Rhodamine B, Eriochrome, Black-T, Congo red, Thymol blue, Methyl orange and Caramine, Red 120 are used in textile industries and approximately 20 % of the used dye are lost during process and create wastewater (Rafiq et al. 2021; A. Kumar 2017). The release of these reactive, direct, disperse, acidic or basic dyes may have carcinogenic effects and may cause rhinitis, asthma, allergic reactions and dermatitis (Osagie et al. 2021). Therefore, the removal of organic dyes from aquatic environments is essential.

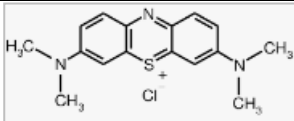
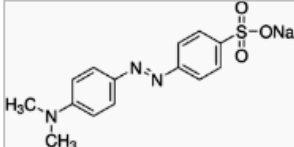
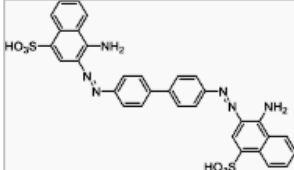
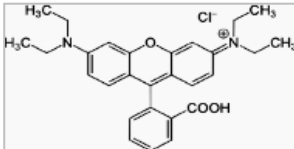
Table 2.1. The chemical structures of common organic pollutants.

Organic Dyes			
Methylene Blue: 	Eriochrome: 	Rhodamine B: 	Indigo Carmine: 
Pharmaceuticals and Personal Care Products			
Doxycycline: 	Sulfamethoxazole: 	Tetracycline: 	Salicylic acid: 
Pesticides			
Atrazine: 	Dichlorodiphenyl trichloroethane (DDT): 	Parathion: 	Malathion: 
Aromatic Compounds			
Toluene: 	Phenanthrene: 	Naphthalene: 	Fluorene: 

Methylene blue (MB), methyl orange (MO), congo red (CR) and rhodamine B (RhB) are among the dyes commonly used. The cationic MB, the anionic MO and CR, and the zwitterionic RhB dyes whose removal from wastewater have been usually investigated due to their harmful effects on the ecosystem (G. Fan, Luo, et al. 2018; Baziar et al. 2021; Ba Mohammed et al. 2021; X. Chen et al. 2021). The physicochemical properties of these dyes were given in Table 2.2.

MB is a heterocyclic aromatic cationic dye, which is the most commonly encountered dyes in the aquatic life. Annually, tens of MB tons are releasing to the water systems (Baziar et al. 2021). MB exposure could cause to human ailments, such as hemolysis, nausea, neurological disorders and vomiting (G. Fan, Luo, et al. 2018). MO dye is in azo dye group, which is commonly used in various industries such as printing, food, leather, paper, and textile (Ba Mohammed et al. 2021). Azo dyes are high chroma and very toxic dyes and it is hard to degrade in nature. Azo bonds can be easily broken into benzidine in wastewater. This compound is carcinogen to human and it can insert into human body with the food chain (Cao et al. 2021). Acute exposure to MO can cause to the shock, increasing heart rate, tissue necrosis, jaundice, vomiting, quadriplegia and cyanosis (Ba Mohammed et al. 2021).

Table 2.2. Physicochemical properties of MB, MO, CR and RhB.

Organic Dye	Chemical Formula	Chemical Structure	Molecular Weight (g mol ⁻¹)	Solubility in water (g L ⁻¹)	λ_{\max} (nm)
Methylene Blue	C ₁₆ H ₁₈ ClN ₃ S		319,85	43.6	664
Methyl Orange	C ₁₄ H ₁₄ N ₃ NaO ₃ S		327,33	5.0	463
Congo Red	C ₃₂ H ₂₂ N ₆ Na ₂ O ₆ S ₂		696.67	10.0	497
Rhodamine B	C ₂₈ H ₃₁ ClN ₂ O ₃		479,02	15.0	554

CR is an ionic azo dye containing benzidine group, which is widely used in paper, printing, plastics and textile industries, although it is carcinogenic (X. Chen et al. 2021). RhB is a synthetic dye that has the characteristics of high toxicity and carcinogenicity, causing harmful effects on human health such as kidney damage, cognitive impairment, anemia, and detriment to the reproductive systems (Jing Wang et al. 2021). These dyes are highly stable and xenobiotic in nature (Nazir et al. 2021). Therefore, they must be removed from industrial wastewater, before releasing it to aquatic environment.

2.1.2. Pharmaceuticals and Personal Care Products

Pharmaceuticals and personal care products (PPCPs) are common organic pollutants produced over one million tons worldwide (Xue Zhao et al. 2021). The municipal wastewater could enter water, soil and air by different stages, which is the major pathway of PPCPs contaminant (H. Yang, Zhang, and Wu 2018). PPCPs are encountered in groundwater, rivers, reservoirs and even in oceans. Urban areas are the main zones where PPCPs releases through large amounts of industrial and domestic effluents (Y. Zhang et al. 2018). Pharmaceuticals such as antibiotics, analgesics, anti-inflammatory, hypertensive blockers, antipyretics, hypertensive blockers, adrenergic agonists, endocrine disrupting compounds and psycholeptics are nonbiodegradable and persistent products with significant risks on ecology and human health (Antoniadou, Falara, and Likodimos 2021). The long term exposure of PPCPs causes genotoxicity, endocrine disruption, fetal development and carcinogenicity (Xue Zhao et al. 2021; X. Jin et al. 2014).

Antibiotics is a class of medicines widely used to heal the diseases. However, the large fractions of these drugs are excreted from the body with unchanged form because they are slightly absorbed and metabolized (da Silva Bruckmann et al. 2022). Antibiotics is largely utilized in the medical industry, aquaculture and animal husbandry. Although the antibiotics have the beneficial roles in our lives, their overuse causes to problem (W. Zhang et al. 2023). It is expected that the global consumption of antibiotics for veterinary would rise up 67 % from 2010 to 2030. Moreover, the global

consumption of them for the edible animals was determined as 63,000 tons in 2015, and it is estimated that it will increase up 70 % in 2030 (Abbasnia et al. 2022).

The large amount of antibiotics have released to the natural environments, and mostly concentrated in water. Because the antibiotics have continuous mass injection, they are potential threat to environment and human life (W. Zhang et al. 2023). Even their low concentrations could have potential risk on human health and the ecosystem via bioaccumulation and growing of resistant genes and bacteria (da Silva Bruckmann et al. 2022).

Tetracyclines (TCs) are the second most used antibiotics globally. TCs have remarkable advantages such as low cost, high quality and broad-spectrum activity through bacteria (gram positive and negative), rickettsia and fungus (chlamydia). They are preferred for human treatment, agricultural and veterinary purposes (Abbasnia et al. 2022; Daghrir and Drogui 2013). TC can maintain in the ecological life for a long time, which can cause adverse effects on humans and environment even at low concentrations (Sheng et al. 2022). TCs are often observed in wastewater, groundwater, sludge, surface water, drinking water and sediment, which cause to destruction of the ecosystem balance. The existence of TCs in aquatic environment hinders the growth of aquatic species and causes various problems on human health such as endocrine disruption, mutagenicity, nephropathy, probable change in photosensitivity and central nervous system defect (Abbasnia et al. 2022). They can also accumulate in the food chain and impress the human health via this way. TCs structure consists of both electron rich and deficient moiety. They contain three different pKa values that are 3.3, 7.7 and 9.7 (J. Yang et al. 2022).

2.1.3. Pesticides

Pesticides are considered as one of the deadly contaminants. Among the twelve most hazardous chemicals around the world, nine of them are determined as pesticides and the intermediate compounds of pesticides (Khan and Pathak 2020). Pesticides are the synthetic chemicals used for destroying pests and providing food security to meet the global population demand (Ahmed et al. 2011). Pesticides contamination caused by

different sources such as industrial effluents, agricultural runoff and chemical spills grows via bio-magnification (Duirk and Collette, n.d.). They can have direct or indirect routes of entering the environment. The classification of pesticides is created considering the target organisms such as herbicides (kill weeds), algaecide (kill algae), bactericide (kill bacteria), insecticide (kill insects), fungicide (kill fungi), rodenticide (kill rodents), etc. (Khan and Pathak 2020). Another classification is carried out by considering the chemical groups such as organochlorine, triazines, substituted urea, organohalogen, organophosphorus, synthetic pyrethroid, carbamates and phenol derivatives (Khan and Pathak 2020).

The structure of pesticides comprises complex groups and their intermediate products could be more lethal than precure compound. Many studies reported that approximately 98 % of insecticides can not achieve quick degradation and enter the environment (Muhamad 2010). The potential health and environmental risks of pesticides is a great concern all over the world.

2.1.4. Aromatic Compounds

Aromatic compounds are one of the most persistent and recalcitrant among environmental organic contaminants. Aromatic compounds are classified as polycyclic aromatic hydrocarbons (PAHs), heterocyclic compounds including one or more S, O or N atoms in the aromatic ring, alkylated PAHs, etc. (Hyun Chung, Meshref, and Ranjan Dhar 2021; Ahad et al. 2020). Some of them is considered as highly-toxic and carcinogenic. It is critical to detect these compounds to protect human health and ecology (Hyun Chung, Meshref, and Ranjan Dhar 2021; Wallace et al. 2020). PAHs are the significant aromatic compounds caused by incomplete combustion of fossil fuels and/or fuel spills. PAHs interfere the water bodies directly or indirectly and cause increasing concerns due to the largely unknown synergic/agonistic and individual effects on the environment (Vecchiato et al. 2021).

The organic pollutants in wastewater and their toxic concentrations for living species are summarized in Table 2.3. Due to the toxic and persistent nature of these organic polutants, they can not be completely removed by using conventional

biological, physical and chemical water treatment processes such as flocculation, adsorption, filtration, chlorination, precipitation, bioremediation and coagulation (Antoniadou, Falara, and Likodimos 2021). The innovative methods for removing organic compounds from wastewater have attracted much attention currently. Photocatalytic degradation process has been most promising solution due to low cost and high efficiency (Antoniadou, Falara, and Likodimos 2021).

Table 2.3. Organic pollutants in wastewater. (Data was collected from Ref. (N. Ahmad et al. 2021)).

Pollutant	Toxic concentrations to human health and aquatic species	Removal challenges
Organic dyes (anionic and cationic dyes)	>1 ppm	Nonbiodegradability and stability
Pesticides	>0.3 ppm	Phosphorus and nitrogen containing pesticides released from industry cause a significantly high chemical oxygen demand (COD) value. Many different types of pesticides with different structures and various pH values of the waste water (range 0.5-14)
PPCPs	It is reported in ng/l - µg/l in wastewater	Hydrophilicity and persistence
Aromatic compounds	Benzene >0.01 ppm	Difficulty for oxidizing and stability
	Xylene >0.5 ppm Toluene >0.7 ppm	Nonbiodegradability, low recovery while treating through adsorption and membrane filtration
	PAHs >0.0007 ppm	

2.2. Removal of Organic Pollutants

The removal of organic pollutants from water bodies is the significant task to prevent detrimental effects to human and environment. In general, biological, physical,

and chemical methods are the main three types of water treatment technologies. Each technology involves their own advantages and disadvantages (Sarkodie et al. 2023).

Biological methods: Biological technique is potentially ecofriendly way for treatment of organic pollutants. For this aim, various microorganisms such as bacteria, yeasts and fungi have been used to remove organic pollutants. Some enzymes such as oxidases and peroxidases could degrade the azo dyes (R. L. Singh, Singh, and Singh 2015).

Despite some advantages, developing of degradation-effective microorganisms may take time at the present-day biotechnology. It is the long-term solution. Contrarily to adsorption and oxidation techniques, biological degradation is sluggish in organic pollutant removal. To obtain complete decomposition of organics, researchers mainly focus on the physical or chemical technologies (Sarkodie et al. 2023; Qingchun Zhang et al. 2020).

Physical methods: Physical methods consist of physical adsorption, electrostatic attraction/repulsion, precipitation, membrane, interfacial chelation and ion-exchange (Ullah et al. 2020; Sarkodie et al. 2023). Multiple physical techniques can also used to obtain high removal efficiency. Coagulation, followed by flotation, sedimentation and filtration could remove higher weight dyes. To obtain higher efficiency without byproducts and with well recovery potential, the adsorption process is the most popular strategy (Sarkodie et al. 2023).

Chemical methods: The advanced oxidation processes are the commonly used chemical methods to remove the organic pollutants, which include photocatalytic degradation, plasma process and ozonation. These chemical strategies consist of producing radicals, reactive ions or electrons, or neutral species (Sarkodie et al. 2023; Pálfi, Wojnárovits, and Takács 2011). These reactive species can attack organic molecules to decompose it into CO₂ and H₂O.

Among these methods, there are many advantages of adsorption and photocatalytic degradation processes. Adsorption has the advantages like simplicity, reuses of adsorbents, effectiveness, less residual and low cost (N. Kumar and Kumar 2022). The photocatalytic degradation has been also considered the most trustworthy and efficient method owing to its high efficiency and low cost. This method offers unique advantages such as mild operating conditions (pressure and temperature) and the capability to convert the organic pollutants in the aqueous media into harmless materials (Karami et al. 2022).

2.2.1. Adsorption

The adsorption method is used for the treatment of water pollution extensively. The performance of the adsorption process is generally defined by maximum absorption capacity (Lou, Osemwegie, and Ramkumar 2020). The adsorption of organic pollutants can be affected by various factors such as particle size, contact time, surface area of adsorbent, the interaction between adsorbate and adsorbent, pH and temperature. The other properties such as the pore size of adsorbent and the diameter of adsorbate molecule could be also considered for developing adsorption process. Low-cost adsorbent with high adsorption capacity is required to obtain effective process (Osagie et al. 2021).

In the adsorption studies, there can be the experimental or theoretical adsorption capacity values. The theoretical adsorption capacity value could be calculated by using the model equations of isotherms/kinetics through drawing the graph and determining the slope and intercept. The adsorption capacity values calculated by the theoretical basis may be greater than the experimental values. If the theoretical model and experimental values match with each other, it will be the fitting of the selected model (Osagie et al. 2021).

2.2.1.1. Adsorption Process

Figure 2.1 indicates a porous adsorbent with the hydrodynamic boundary layer or film. The adsorbent has the macropores which are large enough. Therefore, the diffusion is not hindered by the pore walls. The adsorbent could have also the micropores which have the similar radii to the diffusing species. In this case, the diffusion could be obstructed by the pore walls. This concept consists of resistance rate series illustrated in Figure 2.1. The overall rate of adsorption depends on the steps causing the highest resistance to mass transport (Weber and Smith 1987).

The transport process can be expressed with four main steps during adsorption by using porous adsorbents. These steps were expressed in Figure 2.1 (Tran et al. 2017).

The first step is bulk transport. It is transport in the solution phase and it happens quickly. When the adsorbent is added to the adsorbate solution, bulk transport takes place instantaneously. The second step is film diffusion. It takes place slowly. At this step, the adsorbate molecules are moving from the bulk liquid phase to the external surfaces of adsorbent via the film or hydrodynamic boundary layer. The third step is intraparticle diffusion. This slow step comprises the diffusion of adsorbate from the exterior to the pores of the adsorbent via pore-wall surfaces. The last step is adsorptive attachment, it happens quickly (Tran et al. 2017).

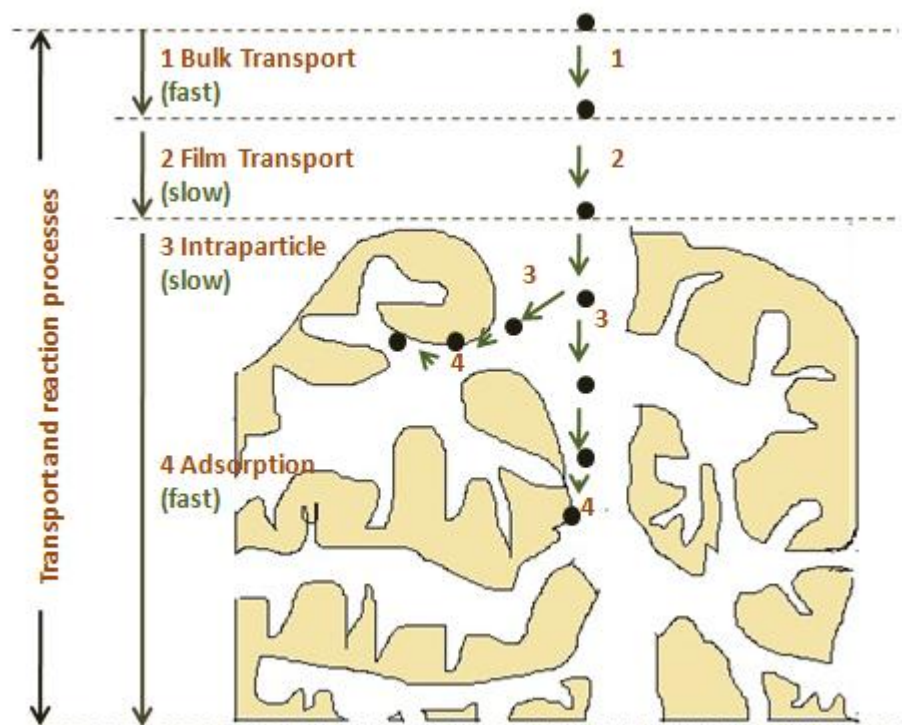


Figure 2.1. Transport process for the adsorption by using the porous adsorbent (Reprinted (adapted) with permission from (Weber and Smith 1987). Copyright (2023) American Chemical Society)

2.2.1.2. Adsorption Parameters

There are many parameters that affect the adsorption of organic pollutants such as pH, adsorbent dosage, initial concentration, ionic strength and temperature.

pH: The pH of the solution is generally most significant parameter that affects the adsorption efficiency directly. The difference in solution pH can affect the surface chemistry of both adsorbent and adsorbate molecule. It also influences the degree of ionization and size of the electrostatic charges (Mudunkotuwa and Grassian 2010). Frequently, the adsorption of the cationic pollutants are higher at high pH, meanwhile, the adsorption of the anionic pollutants are higher at low pH (Al-Shaalan et al. 2019). At low pH, anionic molecules and the positively charged adsorbent surface interact with each other (Lan et al. 2022). When the pH gets higher value, anionic molecules repel the negatively charged adsorbents surface.

The point of zero charge (PZC) is a major factor which defines the electrokinetic properties of a surface. Many adsorption studies have focused on the PZC of the adsorbents to understand adsorption mechanism. The cationic organics can be more preferably adsorbed when pH is higher than PZC due to the presence of OH^- and COO^- groups. Conversely, the positively charged adsorbent prefers anionic dye removal when pH is lower than PZC (Lan et al. 2022; Tmsek and Avci 2013).

Adsorbent dosage: The minimum adsorbent amount with maximum adsorption efficiency is the main economic consideration. The adsorption capacity is directly affected by adsorbent dosage. The amount of adsorption sites on the adsorbents surfaces enhances with increasing adsorbent amount (Sonawane and Shrivastava 2009). When the dosage is in optimum level, the removal process can be fast and efficient owing to the available active sites (Lan et al. 2022). Conversely, when the dosage is in very high level, the organic molecules could not interact with all adsorption sites.

Initial concentration: The adsorption efficiency is also considerably influenced by the initial organic pollutant concentration. The adsorption performance depends on the interaction between the surface available sites of adsorbents and the pollutant concentration. Generally, the removal efficiency reduces with increasing pollutant concentration due to the saturated active sites on adsorbent surfaces (Eren and Acar 2006). When the adsorption active sites are unsaturated, the rising of initial

concentration causes to the higher adsorption capacity (Lan et al. 2022). The higher initial concentration of pollutant increases the driving force for mass transfer in removal process.

Ionic strength: Ionic strength is one of the significant parameters, because, industrial wastewaters generally include many inorganic salts. The existence of the salts in water causes to strong ionic strength, which influences the entire adsorption process. It is known that the NaCl, and CaCl₂ salts affect the adsorption of organic compounds prominently (Anirudhan and Ramachandran 2007). The increase of the ionic strength could compress the diffuse double layer of adsorbents and impress the electrostatic attractions and the adsorption process. Frequently, the adsorption efficiency reduced with increasing salt concentration. The excessive salt ions can screen the adsorbent surface and reduce the electrostatic attraction between the organic compound and adsorbent surface (Lan et al. 2022).

Temperature: Temperature influences the reaction rate. Therefore, the temperature of the solution is notable factor for effective process. In endothermic process, the removal is enhanced with increasing temperature due to the higher mobility of organics and active sites of adsorbents (Argun et al. 2008). Conversely, in exothermic process, the removal is reduced with increasing temperature due to the decreasing interaction between organics and active sites of adsorbents.

2.2.1.3. Adsorption Equilibrium

In literature, a plenty of adsorption isotherm models have been applied until now. The classification of the models can be expressed as follows:

- one parameter and irreversible isotherms (i.e. Henry isotherm),
- two parameter isotherms (i.e. Langmuir, Freundlich, Dubinin-Radushkevich, Temkin),
- three parameter isotherms (i.e., Radke Prausnitz, Redlich Peterson, Langmuir-Freundlich, Sips),
- more than three parameter isotherms (i.e., Fritz Schlunder, and Baudu, Weber-van Vliet)

Among them, the most commonly used models have been Langmuir and Freundlich models. The Dubinin Radushkevich, Radke Prausnitz, Redlich Peterson and Langmuir-Freundlich models are followed these models. Because they are simple; their parameters are beneficial; they can be interpreted easily (Tran et al. 2017; Hamdaoui and Naffrechoux 2007).

Langmuir isotherm

Langmuir theory depends on a continuous sorption of molecules on an adsorbent surface and desorption or evaporation processes of molecules from the surface. Therefore, there is no accumulation rate on the surface. The rates of adsorption and desorption processes are the same. The Langmuir isotherm relation is expressed for the aqueous phase adsorption as follow (Langmuir 1918):

$$q_e = \frac{q_{m,1}K_L C_e}{1+K_L C_e} \quad (2.1)$$

where $q_{m,1}$ (mg g^{-1}) represents the maximum adsorption capacity for Langmuir model. K_L (L mg^{-1}) is the constant of the model. The q_e (mg g^{-1}) and C_e (mg L^{-1}) are the adsorption capacity and the concentration at equilibrium, respectively.

The assumption of Langmuir model is monolayer adsorption. In other words, the thickness of the adsorption layer is only single molecule. The adsorption is performed at the identical localized sites. There is no lateral interactions and steric barrier between the hold molecules (Vijayaraghavan et al. 2006). The other assumption of Langmuir model is homogenous adsorption. Every molecule have constant enthalpies and homogenous activation energies. Therefore, the active sites show the same affinity to the adsorbate (Kundu and Gupta 2006). The rise of distance causes to reduce of the intermolecular attractive forces (Al-Ghouti and Da'ana 2020).

There are six different adsorption mechanisms of Langmuir process. The variety of the surface chemistry and the geometry of the adsorbent cause these different Langmuir classifications as follows (Al-Ghouti and Da'ana 2020; Swenson and Stadie 2019):

(1) Single-site Langmuir adsorption: There are elementary identical adsorption sites on the surface that capture the single molecule.

(2) Multi-site Langmuir adsorption: There are different elementary adsorption sites on the surface that fit to only single adsorbed molecule. There is independent binding sites and no interaction between adsorbent and adsorbate.

(3) Generalized Langmuir adsorption: There are many different adsorption sites with different adsorbate affinities. The interactions between adsorbent and adsorbate can be neglected. The adsorption isotherm is interested in the binding energies distribution of the active sites.

(4) Cooperative adsorption: The active sites of the surface are identical and can capture multiple molecules. The adsorption energy depends on the different adsorbates at the same adsorption site.

(5) Dissociative adsorption: There are two stages during adsorption process. The first stage is the chemical bonding on the active site and molecular dissociation. Afterthat, the second stage is desorption and leaving the surface, due to the re-association of two neighboring atoms into the diatomic molecule.

(6) Multi-layer adsorption: There are identical and independent active sites. There is no limitation for the amount of adsorbed molecules. They could be hold above each other.

In addition, Weber and Chakravorti (1974) suggested the dimensionless constant, which is entitled as separation factor (R_L):

$$R_L = \frac{1}{1+K_L C_0} \quad (2.2)$$

where C_0 (mg L^{-1}) is the initial adsorbate concentration. The $0 < R_L < 1$ indicates favorable adsorption, $R_L > 1$ means unfavorable adsorption, $R_L = 0$ shows irreversible adsorption, and also $R_L = 1$ indicates linear adsorption (Xiong et al. 2021).

Freundlich isotherm

Freundlich theory depends on non-ideal adsorption system. In contrast to Langmuir model, the multilayer adsorption is feasible instead of monolayer formation. It is not necessary to the uniform distribution of heat and affinities. There is the heterogeneous surface (Al-Ghouti and Da'ana 2020). This model is recognized as the surface heterogeneity and the exponential distribution of sorption sites and the sites energies.

The non-linearized form of Freundlich model is defined in Eq. 2.3. The graph of $\log q_e$ versus $\log C_e$ yields a straight line. The $1/n$ and $\log (K_F)$ can be calculated from the slope and the intercept of the graph, respectively.

$$q_e = K_F C_e^{\frac{1}{n}} \quad (2.3)$$

where K_F ($L g^{-1}$) shows the model constant and n is the Freundlich exponent.

According to this model, the ratio of the adsorbate to the solute is not constant at the various concentrations of the solution. The adsorbed amount is corresponded to the sum of the adsorbed molecules on each site. At the beginning, the adsorbates attack to the stronger binding sites. Afterthat, the adsorption energy is reducing exponentially until completion of adsorption process. Recently, Freundlich isotherm model is widely applied to the adsorption systems such as adsorption of organic pollutants on various adsorbents. This model is suitable for sorption systems which include heterogeneous surfaces in liquid or gas phase. In gas phase systems, the application is restricted in a narrow range of pressure. At low pressure, there is an unavailable behavior of Freundlich model towards Henry's law. At the sufficiently high pressure, there is no finite limit (Al-Ghouti and Da'ana 2020). Therefore, this adsorption model is valid narrow range of adsorption data.

The Freundlich isotherm parameters of K_F and n depend on temperature. The intensity of the adsorption and surface heterogeneity can be defined by the value of $1/n$. When $1/n$ value is closer to zero, the adsorption is more heterogeneous. If $1/n$ value is below unity, there is a chemisorption process. $1/n$ above one indicates a cooperative adsorption process.

The irreversible behaviour of this isotherm can be corresponded to the considerably decreasing of pressure or concentration before the desorption of adsorbate from the surface (Ayawei, Ebelegi, and Wankasi 2017; Chen 2015). The Freundlich model is defined with empirical equation (Eq. 2.3). The equation was created by the assumption of surface heterogeneity and patch wise topography of adsorbent surface. The patch wise topography means that one of the patch consists of all sites with equal adsorption energy. The adsorption energy is formed due the interaction between adsorbent and adsorbate. Every patch is independent from the others, due to the fact that there are no interactions between the patches (Al-Ghouti and Da'ana 2020).

Dubinin-Radushkevich model

Dubinin-Radushkevich isotherm model is constructed for the sorption of subcritical vapors on the micropore solid by using pore filling mechanism. This model with Gaussian energy distribution for heterogeneous surfaces is commonly defined the adsorption mechanism (Da 2001). Dubinin-Radushkevich model is generally fitted well to the high solute activities. The data of intermediate range of concentrations are also well fitted to the model. However, the model is not suitable to Henry's law at low pressure and presents undesirable asymptotic properties (Altın, Önder Önder Zbelge, and Dog 1998; Foo and Hameed 2010).

The nonlinear form of Dubinin-Radushkevich isotherm model was given in Eq. 2.4.

$$q_e = q_{m,2} * \exp[-K_{DR} * \left[RT * \ln\left(1 + \frac{1}{c_e}\right)\right]^2] \quad (2.4)$$

where $q_{m,2}$ demonstrates the maximum adsorption capacity value. K_{DR} ($\text{mol}^2 \text{kJ}^{-2}$) is the model constant. T (K) indicates absolute temperature. R ($8.314 \text{ J mol}^{-1} \text{ K}^{-1}$) is molar gas constant (Dubinin 1960).

One of the most prominent properties of Dubinin-Radushkevich isotherm is the temperature-dependency (Razmi et al. 2019). The characteristic curve of the model includes the adsorption data at different temperatures. All available data are plotted in logarithm of the adsorbed amount versus the square of potential energy (Foo and Hameed 2010).

By contrast with Langmuir and Freundlich models, this isotherm has the semiempirical equation and there is a mechanism of pore filling. A multilayer character is an assumption of the model. This character includes Van der Waal's forces and the model can be utilized for the physical adsorption processes (Israel and Eduok, n.d.). The prediction of chemical and physical adsorption is possible by using this model (Al-Ghouti and Da'ana 2020).

Dubinin-Radushkevich model suggests the description of solute adsorption on the solid, however, it was not same for gas adsorption. Because, there are some ignoring issues such as the solvent influence (especially pH of the solution), the functional groups of surface and charges of it. Thus, the mean free energy can not be determined accurately. It prevents to suggest whether the adsorption system is physical or chemical (Al-Ghouti and Da'ana 2020).

Radke Prausnitz model

The Radke-Prausnitz isotherm is commonly used model which has some specific features at lower adsorbate concentrations. The Eq. 2.5 indicates the Radke-Prausnitz model.

$$q_e = \frac{q_{m,3} K_{RP} C_e}{(1 + K_{RP} C_e)^{m_{RP}}} \quad (2.5)$$

where $q_{m,3}$ (mg g^{-1}) shows the maximum adsorption capacity value. The K_{RP} (L mg^{-1}) and m_{RP} represent the model constant and the exponent of Radke-Prausnitz, respectively (Radke, Prausnitz, and Radke 1972).

At lower adsorbate concentrations, the isotherm is linear. At higher adsorbate concentrations, the isotherm converts to Freundlich model. When the m_{RP} is zero, it converts to Langmuir model. Radke-Prausnitz isotherm can be applied in a wide range of concentration (Mozaffari Majd et al. 2022). The model parameters can be determined by using nonlinear fit of experimental data.

Redlich-Peterson model

Redlich-Peterson model is a hybrid model which have the properties of both Langmuir and Freundlich models. It is an empirical equation with three parameters. The isotherm equation (Eq. 2.6) comprises the linear concentration term in the numerator and the exponential concentration term in the denominator (Ng, Cheung, and McKay 2002). The model equation demonstrates adsorption equilibrium through the wide concentration range and it can be utilized in homogeneous or heterogeneous systems (Foo and Hameed 2010).

$$q_e = \frac{K_R C_e}{1 + \alpha_R C_e^\beta} \quad (2.6)$$

where K_R (L g^{-1}) and α_R (L mg^{-1}) are the model constants. The β represents the exponent of the model (Redlich and Peterson 1959).

At high concentration (the exponent approaches zero), the model converts to Freundlich, whereas, at low concentration (all values approach one), it converts to Langmuir (Nimbalkar and Bhat 2021). There is a minimized procedure for solving the isotherm equations. The correlation coefficient can be maximized with the predictions of the theoretical value and the experimental data (Al-Ghouti and Da'ana 2020).

Langmuir-Freundlich model

Langmuir-Freundlich isotherm model is the combination of Langmuir and Freundlich models, which predicts heterogeneous adsorption systems. The Langmuir-Freundlich model equation is represented in Eq. 2.7.

$$q_e = \frac{q_{m,4}(K_{LF}C_e)^{m_{LF}}}{1+(K_{LF}C_e)^{m_{LF}}} \quad (2.7)$$

where $q_{m,4}$ (mg g^{-1}) indicates the maximum adsorption capacity. The K_{LF} (L mg^{-1}) is the model constant. The m_{LF} shows the exponent of the model (Uzunkavak et al. 2019; Tran et al. 2021).

The Langmuir-Freundlich constant K_{L-F} shows the adsorption energy. When the m_{L-F} value approaches to zero, there could be heterogeneous sorbent. When the m_{L-F} value approaches to unity, there is homogeneous distribution of adsorption sites (Uzunkavak et al. 2019).

The operating parameters such as pH, temperature and organic pollutant concentration govern the calculated parameters of Langmuir-Freundlich model.

2.2.1.4. Adsorption Kinetics

In aqueous-phase adsorption studies, three kinetic reaction models (i.e., Pseudo-first-order, Pseudo-second-order and Weber-Morris intraparticle diffusion model), and the Boyd model have been commonly used to describe the adsorption mechanism and determine the kinetic adsorption constant.

Pseudo-first-order model

The Pseudo-first-order model was suggested by Lagergren (1898) at first. The nonlinear form of this model is given in Eq. (2.8)

$$q = q_e(1 - e^{-k_1 t}) \quad (2.8)$$

where q (mg g^{-1}) shows the adsorption capacity at time t . The t (min) is time. k_1 (min^{-1}) represents the rate of adsorption constants for the model (An et al. 2020).

There are three conditions to satisfy this model hypothesis (Wang and Guo 2020):

The first condition is the high value of C_0 .

The second condition is that adsorption is at the early stages. It is reported that when the operation time close to zero, the Pseudo-second-order model replace to the Pseudo-first-order model (Wang and Guo 2020). Frequently, the Pseudo-first-order model is only suitable for the contact time of initial 20-30 minutes. It can not be appropriate for the whole adsorption range (Ho and McKay 1998). Therefore, model plots are only linear during the first 30 min. After 30 min passed, theoretical and experimental data could not fit sufficiently (Tran et al. 2017).

The third condition is the few adsorption sites of the adsorbent. The rate controlling step of the process is internal or external diffusion. Generally, the adsorptive removal of hydrophilic compounds and metals ions by using microplastics fits to the Pseudo-first-order model (Wang and Guo 2020; Guo and Wang 2019). Because, the hydrophobic nature of microplastics prevents the diffusion of hydrophilic adsorbate to the microplastics surface. In this case, the rate limiting step is internal or external diffusion. Conversely, the adsorption of hydrophobic adsorbates (lubrication oil, etc.) on the microplastics fits to the Pseudo-second-order model (Hu et al. 2017). The hydrophobic adsorbates can easily diffuse to the microplastics surface compared to hydrophilic adsorbates. In this case, the rate controlling step could be the adsorption on the binding sites. Thus, Pseudo-first-order model needs to the condition of a few active sites of the adsorbent or few interaction of adsorbate with the active sites (Wang and Guo 2020).

Pseudo-second-order model

Until now, physical meaning of the Pseudo-second-order kinetics model has been considered. It is suggested that the Pseudo-second-order model is available at the lower C_0 value. It is also predicted that the Pseudo-second-order model is attributed to the vacant active sites (Wang and Guo 2020). The equation of Pseudo-second-order isotherm is given in Eq. 2.9.

$$q = \frac{q_e^2 k_2 t}{1 + q_e k_2 t} \quad (2.9)$$

where k_2 ($\text{g mg}^{-1} \text{ min}^{-1}$) indicates the rate of adsorption constants for the model (An et al. 2020).

There are three conditions to represent this model hypothesis (Wang and Guo 2020):

The first condition is the low value of C_0 .

The second condition is that adsorption is at the final stage. Compared to Pseudo-first-order model, the Pseudo-second-order is better fitted to the adsorption applications at the contact time of more than 20 minutes. This situation extends the applications of this model, all the adsorption kinetics data from the initial to the final stage can be represented by Pseudo-second-order model.

The third condition is the abundant adsorption sites of the adsorbent. The modified materials such as modified MOFs, modified biochars and modified silica comprise the plenty of active sites. Therefore, these adsorption processes generally follows Pseudo-second-order model. The dominated stage of the kinetics is the adsorption on active sites (Wang and Guo 2020).

Mostly, the kinetics data of organic pollutant adsorption by porous materials are well fitted to the Pseudo-second-order model (Ba Mohammed et al. 2021; Cao et al. 2021; Santoso et al. 2021). The well fitting of this kinetic model generally shows that the adsorption process consists of chemisorption. There are valence forces and sharing electrons between the adsorbent and organic pollutant.

However, some researchers have suggested that fitting kinetic models (i.e. Pseudo-second-order model) and simple kinetic studies may not explain the adsorption mechanisms directly (Tran et al. 2017). The kinetic data, thermodynamic data and the analysis results (i.e. FTIR, SEM, BET, XRD and XPS) are necessary together to approve whether the adsorption of organic pollutants is a physical or chemical (Tran et al. 2017).

Weber-Morris intraparticle diffusion model

The intraparticle diffusion model is suggested by Weber and Morris, the isotherm equation is indicated in Eq. 2.10. This model is based on Fick's law. The adsorption of pollutants is directly proportional to the root square of time (Vareda 2023).

$$q = k_i\sqrt{t} + B_i \quad (2.10)$$

where k_i ($\text{mg g}^{-1} \text{min}^{-1/2}$) represents the rate of adsorption model constant. B_i indicates the thickness of the boundary layer (Weber Jr. and Morris 1963).

By using porous adsorbents, one of the important phenomena (pore diffusion or intra-particle diffusion) must be considered. It has a significant role during adsorption processes. Many researchers have investigated the role of intra-particle diffusion on adsorption to explicate the adsorption kinetics and mechanism (Sen Gupta and Bhattacharyya 2011).

Pseudo-second-order model can sufficiently define the kinetic experimental data. However, the reaction pathways and reaction mechanisms can not be explained by this model. Conversely, Weber-Morris intraparticle diffusion model is useful to determine the reaction pathways, mechanisms and the rate-controlling step. During solid-liquid adsorption process, the transfer of adsorbate happens through external diffusion, surface diffusion, pore diffusion or both of pore and surface diffusion. When the q_t vs $t^{0.5}$ graph is linear and passing through the origin, the whole adsorption process is managed by intraparticle diffusion (Tran et al. 2017). Conversely, when the q_t vs $t^{0.5}$ graph has multiple linear sections, the adsorption process is governed by the multistep mechanism.

Boyd model

In many of the adsorption systems, the controlling stage is diffusion (intraparticle or/and film). Because, the reaction step is faster than the diffusion. When the resistance of intraparticle and film diffusion is equivalent, the governing mass transfer equations are solved numerically. The coefficients of film and intraparticle diffusion are determined by matching the empirical and numerical solution data. On the contrary, when one of the film and intraparticle diffusion resistance is very higher than the other, mass transfer equations are solved analytically. In this case, the diffusion coefficients are determined analytically (Yao and Chen 2017).

The quantity of film and intraparticle resistances is influenced by operating conditions such as adsorbent amount/size and stirring rate. The higher stirring rate can diminish or even disappear the mass transfer resistance (Yao and Chen 2017). The less particle size causes to diminish the intra-particle diffusion resistance.

Eq. 2.11 and 2.12 are recognized as Boyd or Reichenberg kinetics model.

$$Bt = \pi \left(1 - \sqrt{1 - \frac{\pi q_t}{3 q_e}} \right)^2 \quad \text{for } q_t/q_e < 0.85 \quad (2.11)$$

$$Bt = -\ln \frac{\pi^2}{6} - \ln \left(1 - \frac{q_t}{q_e} \right) \quad \text{for } q_t/q_e > 0.85 \quad (2.12)$$

where B represents the Boyd model parameter.

In this model, the Boyd plot (Bt vs t) is drawn. The straight line pass through the origin of this plot indicates that the adsorption process is managed by intraparticle diffusion. Otherwise, the process is governed by film diffusion or intraparticle and film diffusions together. The slope of the plot gives the Boyd model parameter (effective intraparticle diffusion coefficient) (Yao and Chen 2017).

2.2.1.5. Adsorption Thermodynamics

Adsorption thermodynamics is beneficial to predict adsorption mechanisms such as physical or chemical. The thermodynamic parameters, Gibb's free energy (ΔG°), enthalpy (ΔH°) and entropy (ΔS°), were determined by using the Eq. 2.13 - 2.15. The ΔG° is directly determined from Eq. 2.13. However, the plot of $\ln K_D$ versus $1/T$ (Eq. 2.15) is drawn to obtain the ΔH° and ΔS° from the slope and intercept, respectively.

$$\Delta G = -RT \ln K_D \quad (2.13)$$

$$\Delta G = \Delta H - T\Delta S \quad (2.14)$$

$$\ln K_D = -\frac{\Delta H}{RT} + \frac{\Delta S}{R} \quad (2.15)$$

where the units of ΔG° , ΔH° and ΔS° are J/mol, J/mol, J/mol.K, respectively. T is absolute temperature (K), R is gas constant (8.3144 J mol⁻¹K⁻¹).

K_D is dimensionless distribution coefficient calculated using the K_F value from the Freundlich isotherm as suggested by Tran et al. (2017) (H. N. Tran et al. 2017; Uzunkavak et al. 2019):

$$K_D = 1,000 K_F \quad (2.16)$$

Generally, the adsorption capacity is decreased with an increasing temperature, which demonstrates the exothermic adsorption process. During exothermic adsorption process ($\Delta H^\circ < 0$), the energy is releasing as heat to the surrounding. There can be

either chemisorption or physisorption or both of them. At the exothermic process, the adsorbed energy during breaking of bonds is less than the released energy during making of bonds. It provides the releasing of the extra energy as heat.

On the contrary, during endothermic process ($\Delta H^\circ > 0$), the energy is adsorbed as heat from the surrounding. It is associated to the chemisorption. The adsorbate molecules could replace more than one water molecule, which is about endothermic adsorption process (Tran, You, and Chao 2016). When $\Delta H^\circ < 84 \text{ kJ mol}^{-1}$, there are physical adsorption type bonds. When $84 \text{ kJ mol}^{-1} < \Delta H^\circ < 420 \text{ kJ mol}^{-1}$, there are chemisorption bond strengths (Al-Degs et al. 2008). To explain adsorption process more detailed, it is necessary to determine the other thermodynamic parameters.

The Gibb's free energy change generally indicates the degree of spontaneousness of the adsorption system. The more negative ΔG° shows the more favorable adsorption. The adsorption process at a certain temperature is spontaneous and favourable when the ΔG° has negative sign. Otherwise, the process could carry out non-spontaneously and non-favourably. Additionally, the magnitude of ΔG° can also display whether the adsorption process is chemical or physical.

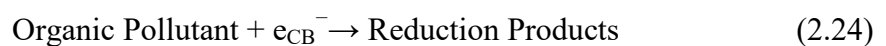
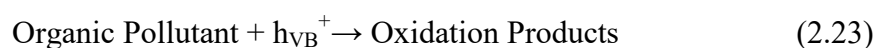
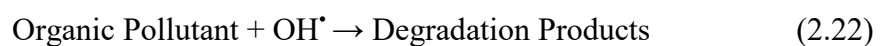
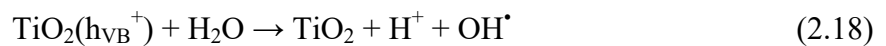
The other important thermodynamic parameter is ΔS° . It indicates the organization of the organic pollutant at the solid interface during the adsorption. If the $\Delta S^\circ < 0$, the adsorption is less random. Otherwise (if $\Delta S^\circ > 0$), the adsorption is more random. The $-\Delta S^\circ$ demonstrates the associative mechanism and the $+\Delta S^\circ$ shows the dissociative mechanism. In addition, $+\Delta S^\circ$ indicates the higher degree of freedom of ions in the solution (Tran, You, and Chao 2016).

2.2.2. Photocatalytic Degradation

The photocatalytic degradation process is an eco-friendly method used for degradation of various organic pollutants such as dyes, PPCPs, pesticides, and aromatic compounds into non-toxic products like CO_2 , H_2O and other harmless compounds (Khan and Pathak 2020).

2.2.2.1. Photocatalytic Degradation Process

The reactions of the photocatalytic degradation process initiates with the absorption of a photon that has the energy ($h\nu$) equal or higher than the band gap energy of the photocatalyst (Carp, Huisman, and Reller 2004), shown in Figure 2.2. The absorption of photon causes the charge separation; the electron (e^-) at the valence band (VB) of the semiconductor is promoted to the conduction band (CB) and leaves a hole (h^+) behind (Figure 2.2). The recombination of the hole and the electron has to be prevented for achieving high degradation efficiency. The reactions for the photocatalytic degradation of organic pollutant on the semiconductor (TiO_2) surface are defined in Eq. 2.17- 2.24 (Konstantinou and Albanis 2004; Akpan and Hameed 2009). The activated electrons react with the oxidant to form the oxidized product. The O_2 which is adsorbed on the surface of semiconductor or dissolves in water can react with generated electrons and produce superoxide radical anion ($O_2^{\cdot-}$). The generated electrons can reduce the organic pollutant, and generated holes could oxidize the pollutant or react with H_2O or OH^- to form OH^{\cdot} radicals. The OH^{\cdot} radicals have the redox potential of +2.8 V and they are strong oxidizing agents. These radicals and the other oxidant species such as peroxide radicals provides the photocatalytic degradation of organic pollutants (Akpan and Hameed 2009).



The photocatalytic degradation processes on the semiconductor carry out in the following main steps (Khan and Pathak 2020): (i) Transfer of reactants to the semiconductor surface; (ii) adsorption of the reactants; (iii) photocatalytic reactions in the adsorbed phase; (iv) desorption of the generated products; (v) diffusion of the products from the semiconductor surface.

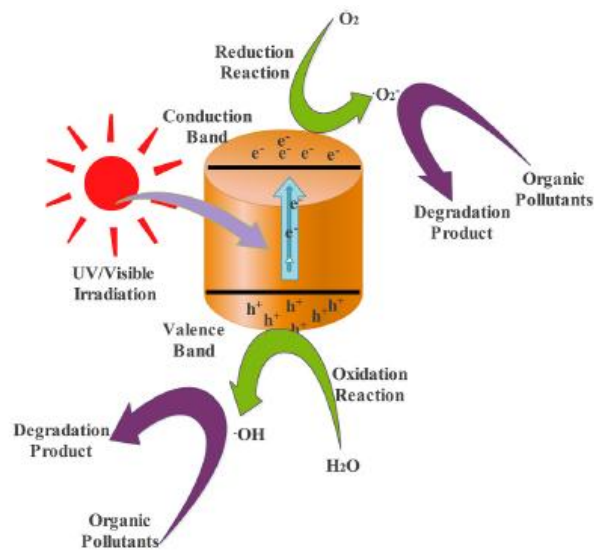


Figure 2.2. The mechanism of photocatalytic degradation of organic pollutants (Reprinted Ref. from (N. Ahmad et al. 2021) with permission).

2.2.2.2. Photocatalytic Degradation Parameters

The photocatalytic degradation of organic pollutants is affected by various significant parameters including pH, pollutant concentration, catalyst dosage, oxidants, temperature and coexisting inorganic anions (Figure 2.3) (Saygi et al. 2023). The efficiency of a photocatalytic reaction can be enhanced by using the optimum reaction parameters (Zare et al. 2021).

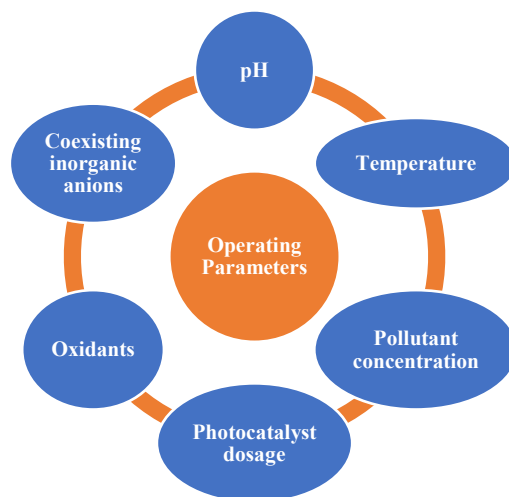


Figure 2.3. Operating parameters affected to photocatalytic activity.

pH: For the photocatalytic degradation of organic pollutants, pH is one of the most significant parameter that affects the effectiveness in numerous ways (Rafiq et al. 2021). The optimum pH for a photocatalytic reaction is associated with organic pollutant, nature and type of the catalyst, and electrostatic forces between them (Vaya and Surolia 2020). The effect of pH on the photocatalytic process is generally complicated and depends on: (i) the agglomeration of semiconductor; (ii) the ionization state of semiconductor surface; (iii) the location of CB and VB of the catalyst; (iv) hydroxyl radicals in solution (Riaz and Park 2020). The adjustment of the solution pH can change the surface charge or the isoelectric point. The pH effect on the photocatalytic degradation could be determined by using the PZC of the semiconductor. The positively charged organic pollutants are adsorbed at $\text{pH} > \text{PZC}$ and the negatively charged contaminants are adsorbed at $\text{pH} < \text{PZC}$ (Riaz and Park 2020). Photocatalytic degradation process starts with the adsorption of organic pollutants on the photocatalyst surface (Vaya and Surolia 2020). The adsorption of the neutral molecules is also affected by the pH due to the dissociation of them to the charged species.

Photocatalyst dosage: Photocatalyst dosage is a significant parameter affecting the photocatalytic performance. Regarding economic feasibility of a process, using a minimum catalyst amount is preferable to obtain maximum efficiency. There is a positive correlation between the photocatalyst dosage and reaction rate until adding an

optimum dosage (R. Malik et al. 2016). Using photocatalyst above the optimum dosage causes the negative effects. The excessive photocatalyst dosage leads to the blocking effect, reducing luminous transmission, decreasing light penetration depth and increasing turbidity (Zare et al. 2021). Light hindering causes the dead zones that not be activated by light (Serrà et al. 2021). Due to excessive catalyst amount, the catalyst may tend to agglomerate with high surface energy. The diffusion path length rises and the effective surface area reduces due to the agglomeration of catalyst (Zare et al. 2021). Furthermore, the photocatalyst amount is directly relevant to the capital expenses, the lower cost of catalyst materials are preferable for water purification (Serrà et al. 2021).

Pollutant concentration: The initial organic pollutant concentration is a crucial factor that must be considered. The photocatalytic degradation process depends on the adsorption of organic pollutant on the photocatalyst surface. Only the adsorbed amount of pollutant can undergo the photocatalytic reaction, not the amount in bulk of the pollutant solution (Rafiq et al. 2021). By using the fixed photocatalyst dosage, the degradation percentage reduces with increasing initial concentration of pollutant (Reza, Kurny, and Gulshan 2017). As the amount of pollutant concentration increases, more pollutant is adsorbed on the catalyst surface, and less photon could reach the catalyst surface. The excessive pollutants cause to the blocking effect, therefore, there would be less OH^{*} ions generation and photocatalytic activity reduces (Rafiq et al. 2021). The excessive pollutant also hinders the direct contact between photogenerated radicals or holes and the organic pollutant in bulk (Zare et al. 2021).

Temperature: The temperature of photocatalytic reaction affects the catalyst performance and overall efficiency of the system (Zare et al. 2021). Photocatalytic degradation of organic pollutants is generally carried out at room temperature. The photocatalytic reactions could be performed between 20-80 °C. Between the temperature of 20-60 °C, the photo decomposition rate is increased (Riaz and Park 2020). The formation of bubbles and generation of free radicals are observed with the increase of temperature. The temperature increase would also reduce the electron-hole recombination (Rafiq et al. 2021). Molecular collisions are increased with the higher kinetic energy at higher temperatures. When the temperature is below 20 °C, the photocatalyst activity reduces and the desorption of the final products could be the rate limiting step. At the temperature around 0 °C, the activation energy is high (Xuesong Zhao, Zhang, and Zhang 2020). Conversely, at temperature above 80 °C, the exothermic adsorption of the organic pollutant becomes difficult, which would be the rate limiting

step (Riaz and Park 2020; Mozia 2010). Above 80 °C, the temperature of the system is close to the the boiling point of water and this inhibites the surface interactions (Zare et al. 2021).

Oxidants: The electron-hole recombination of the photocatalytic process is the main limitation. Using the appropriate donor or electron acceptor reduces the recombination rate and rises the quantum yield. The addition of external electron acceptors/oxidants to the solution could enhance the photocatalytic efficiency significantly (Vaya and Surolia 2020). Molecular oxygen is the commonly used electron acceptor. Recently, many studies focused to increase the photocatalytic degradation of organic pollutants by the addition of oxidants such as H₂O₂, (NH₄)₂S₂O₈ and KBrO₃ (Huang et al. 2008; Khavar et al. 2018; Gong et al. 2021). The addition of oxidants prevents the e⁻/h⁺ pair recombination and increases the generation of hydroxyl radicals (Vaya and Surolia 2020).

H₂O₂ is the most commonly used oxidant that produces strong hydroxyl radicals by peroxide bond cleavage and generated electron trapping (Dong et al. 2020). The degradation rate was increased with increasing H₂O₂ concentration until reaching the optimum concentration. Exceeding the optimum amount caused to decrease in the degradation efficiency. The sufficient concentration of H₂O₂ provides to the generation of hydroxyl radicals (Huang et al. 2008).

Coexisting inorganic anions: The coexisting inorganic anions such as Cl⁻, SO₄²⁻, CO₃²⁻, HCO₃⁻, HPO₄²⁻ and NO₃⁻ significantly affect the photocatalytic activity. The impact of coexisting species has been studied so far (Mahvi et al. 2009; C. Zhang et al. 2021; Tong et al. 2021). The influence of the inorganic anions is generally complicated (Xuesong Zhao, Zhang, and Zhang 2020). These species compete with the organic pollutant and cover the active sites, therefore, decrease the surface activity. They also lead to the scavenging of generated charge carriers (Zare et al. 2021). The photocatalyst surface was positively charged when the pH was lower than the PZC value of the catalyst, and anions could be adsorbed on the active sites of the photocatalyst surface, which hinder the degradation reaction. Sulfate anions inhibited the photocatalytic activity more than chloride ions due to the carrying of higher charges compared to chloride ion (Chang et al. 2021).

2.2.2.3. Photocatalytic Degradation Kinetics

The initial rate method

The initial rate method is commonly used to explain the reaction kinetics of photodegradation of organic pollutants. The initial rate of a reaction (r_0) is the instantaneous rate at the beginning of the reaction ($t = 0$). The initial rate is determined by the curve of dye concentration (C_t) versus time (t) graph. The negative slope of the curve at $t = 0$ gives the initial rate. The r_0 values are determined for each initial concentration (C_0). At this method, kinetic data at the initial short period can be used with the considering of constant light intensity.

The initial rate of a reaction can be given as (Thanh et al. 2018):

$$r_0 = k_i * C_0^n \quad (2.25)$$

where k_i is the overall reaction rate constant observed, n is the reaction order. By taking natural logarithm, Eq. 2.25 is linearized and the Eq. 2.26 yields.

$$\ln r_0 = \ln k_i + n \ln C_0 \quad (2.26)$$

The graph of the $\ln r_0$ vs $\ln C_0$ is a straight line, where the slope gave n value and the intercept on the ordinate showed $\ln k_i$.

Langmuir-Hinshelwood model

Langmuir-Hinshelwood model is the kinetic expression which is widely used to understand kinetics of heterogeneous catalytic process and represented with the Eq. 2.27 (Saïen and Khezrianjoo 2008):

$$\frac{1}{r_0} = \frac{1}{k_r} + \frac{1}{k_r K C_0} \quad (2.27)$$

where k_r is reaction rate constant ($\text{mg L}^{-1} \text{s}^{-1}$), K is dye adsorption constant (L mg^{-1}), r_0 and C_0 were defined as above. The plot of $1/r_0$ vs $1/C_0$ gives the Langmuir-Hinshelwood model parameters (k_r and K) (Tang and Huren An 1995).

2.3. Adsorbents and Photocatalysts

The adsorbent/photocatalyst selection is one of the most significant stage in order to reach the higher removal performance. Therefore, there has been many studies carried out by using the different adsorbent/photocatalyst in the last couple of decades (B. Chen et al. 2021; Blachnio et al. 2020; Priyadharshini et al. 2021; Rasheed et al. 2019; Streit et al. 2019; Kadhom et al. 2020).

So far, many adsorbents have been used such as silica gel, activated carbon, polymeric porous materials frameworks, and activated alumina to remove organic pollutants (Tzvetkova, Vassileva, and Nickolov 2010; Romero-Anaya, Lillo-Ródenas, and Linares-Solano 2010; Costanzo et al. 2010; Camacho et al. 2010). Lowcost, high performance, easy regeneration and high porosity are desired properties for selection of adsorbent (F. Li et al. 2015). The elementary composition, the morphology and chemical properties of adsorbents are also significant, which can be determined by various characterizations techniques. Some researchers have modified the adsorbents to enhance the adsorption efficiency without influencing of their original feature (Osagie et al. 2021; Mesbah et al. 2020).

Photocatalytic degradation of organic pollutants is performed with the aid of a catalyst, generally metal oxides semiconductors such as TiO_2 , ZnO , SnO_2 , WO_3 , CuO , LaCoO_3 , Fe_2O_3 , MoO_3 , V_2O_5 , SrTiO_3 , CdS , and SnO_2 (Ambigadevi et al. 2021; Variar et al. 2021). The photocatalyst should be non-toxic, inexpensive, chemically/biologically inert, stable and be active for the light in visible or/and UV region (Variar et al. 2021). In order to achieve an efficient photocatalytic degradation of organic pollutants, there are some properties to be considered such as morphology, surface area and band gap energy of photocatalysts (Ambigadevi et al. 2021; Enesca 2021). The semiconductors can be used as pristine, dopped or as a composite by immobilization on support material for the photocatalytic degradation of organic pollutants (Velempini, Prabakaran, and Pillay 2021).

Although metal oxide semiconductors are great photocatalysts, they are affected from corrosion especially at the highly acidic or basic conditions, and the other challenges are the post-separation step and the agglomeration of nanoparticles. Therefore, it is necessary to explore the highly active and stable photocatalysts (A.

Malik and Nath 2019). Recently, metal-organic frameworks (MOFs), a novel porous structure, has been discovered to have the adsorption and photocatalytic activity and it is promising as photocatalyst due to its large surface area, tuneable pore size, innate doping with heteroatoms, easily tailored structures, low density, large crystalline porous networks and high pore volume (A. Malik and Nath 2019; G. Fan, Luo, et al. 2018).

2.3.1. Metal Organic Frameworks (MOFs)

Metal organic frameworks (MOFs) are novel materials consisted of inorganic blocks and organic linkers with a textured structure and permanent porosity. The inorganic blocks are small clusters or isolated polyhedral. Meanwhile, the organic linkers part generally consists of di, tri, or tetra-dentate ligands. The inorganic part is in charge of the final topology of MOFs. Inorganic clusters could be in different arrangements such as square planner, tetrahedron, trigonal and di-metal paddle wheel (Saeed et al. 2020).

MOF-5, MOF-74, MOF-801, ZIF-7, ZIF-8, ZIF-67, MIL-53(Fe), MIL-88B, MIL-100(Fe), MIL-101, UIO-66 and UIO-67 are widely produced MOFs for utilizing in many applications.

Generally, the used starting materials (inorganic part and organic linker) influence all the properties of MOFs. It is also extremely important how these starting materials are connected each other. The length of organic ligands without any change in metal specie could effect the porosity and isorecticular coordination polymers. The different metallic components without any change in ligand also affect the porosity of the MOFs (Saeed et al. 2020; Alfonso Herrera et al. 2020). The longer carbon chain of linkers can change pore size, however, the symmetry of the MOF and its structure could be the same. The linker type and the substitution ways can cause to the different unit cell parameters with respect to the chain elongation, as seen in UIO-66, UIO-67, etc. The symmetry can be changed by the mutual arrangement of functional groups, as seen in MOF-1 and MOF-101 (Saeed et al. 2020).

Various effective synthesis methods to produce MOFs were summarized in the following:

Solvothermal or hydrothermal synthesis method: Solvothermal or hydrothermal is the most commonly used method to synthesize MOFs with the reaction between metal clusters and organic ligands (S. Li, Tan, and Meng 2020). The temperature is significant for the crystal growth rate regardless of pressure. Generally, the energy source is supplied from an electric oven during synthesis of MOFs. The synthesis temperature usually enforces crystal growth rate of MOFs. A polar solvent could have low boiling point. The higher pressure and low boiling point of solvent lead to increase partial pressure due to increased solvent evaporation, which cause to rapid crystal growth (Haider et al. 2022). Single-phase MOF crystals can be produced by using solvothermal method, applying slow crystal growth under low temperature with long reaction time (Rönfeldt et al. 2020).

Microwave-assisted technique: Microwave irradiation could enhance crystal growth rate of MOFs with the help of energy via waves. In this method, heat is generated by electromagnetic waves, ions/molecules are moving in polar solvent, and a high temperature is provided for the reaction. The crystals growth could be examined by altering the operating parameters such as energy power, reaction time, solvent nature and concentration of reactants (Haider et al. 2022). The morphological properties of MOFs can be changed by altering these parameters. The advantages of microwave techniques are particle size reduction, morphology control, high efficiency and phase selectivity (Couvreur et al. 2006).

Electrochemical approach: The electrochemical method includes an anode and cathode in a reaction medium that involves a metal salt and organic ligand. In electrochemical medium, the dissolved metal ions (anodic) lead to the reaction between the organic linker and the salt. In order to inhibit deposition of metal on cathode, various protic solvents are utilized, and H₂ is released with the reaction. This method requires higher solid contents compare to batch synthesis methods (Haider et al. 2022).

Ultrasonic-assisted technique: The ultrasonic-assisted method consists of acoustic cavitation approach, which rises the temperature and pressure (~5000 K and ~1000 atm). Bubbles generation and collapse take place during sonication. The irradiation conditions of ultrasonic system are significant for the reaction. The ultrasonic waves can also clean the MOFs surface and activate the unsaturated reactive sites of metal. The resonant cavitation bubbles can break down to clusters and provide to form nanoscale MOFs at less reaction time compared to solvothermal method (Haider et al. 2022).

Mechanochemical approach: Mechanochemical method is a solvent-free-MOFs-synthesis approach by using large organic linkers at room temperature. With the aid of mechanical force, bonds in metal salts are broken and new bonds form between metal and organic linkers. In this approach, metal oxides can be used as reactants instead of metal salts, thereby, water is formed as a by-product. Only a few MOFs types could be synthesized by mechanochemical method (Jiaqiang Liu et al. 2019).

Reverse microemulsion method: The reverse microemulsion method is generally used for the synthesis of nano MOFs appropriate for medical applications. In this method, the synthesis of nano MOFs is performed in the emulsified liquid phase. There are organic-solvent-droplets in water or water-drops in organic solvent. The stabilization of emulsified phase is achieved by using surfactant. It inhibits the agglomeration and improves the stability of MOFs crystal (Haider et al. 2022; Cui, Chen, and Qian 2014).

2.3.2. Zeolitic Imidazolate Frameworks-8 (ZIF-8)

Zeolitic imidazolate frameworks (ZIFs) are in MOFs class, which have similar structures with molecular sieves like zeolites. ZIFs are excellent crystalline microporous materials because they have distinctive properties from both MOFs and zeolites, such as high surface area, well crystallinity, control of the pore size, large micropore volume, high thermal and chemical stability and uniform micropores (Park et al. 2006).

ZIF-7, ZIF-8, ZIF-67, ZIF-69, ZIF-78, ZIF-80, ZIF-82, ZIF-91, ZIF-95, ZIF-100 and ZIF-L are different materials in ZIFs class (K. Ahmad et al. 2022).

ZIF-8 is of the most commonly investigated materials among the ZIFs. ZIF-8 has a faujasite zeolite topology with a cubic lattice. It is highly stable up to 500 °C and has excellent sorption properties due to high internal surface area (Chirra et al. 2021). ZIF-8 has distinctive morphological properties that include sodalite topology and rhombic octahedral crystals, as illustrated in Figure 2.4. ZIF-8 was discovered by Chen and coworkers (Kukkar et al. 2021). ZIF-8 is composed of imidazole ring based ligand (2-methylimidazole) and coordinative bridging of metal ion (Zn^{2+}), which is defined as imidazolate frameworks.

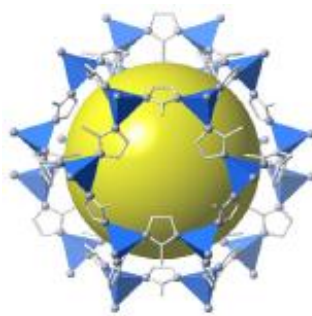


Figure 2.4. The crystal structure of ZIF-8.

ZIF-8 has the nanoscale processibility and resistance to alkali solutions, water and hydrophobic solvents. These unique features distinguish ZIF-8 from other MOFs, which make them more appropriate for various applications. ZIF-8 is more resistant to hydrolysis in water and methanol than the other zinc-based MOFs (Kukkar et al. 2021).

ZIF-8 has been studied in many applications such as membrane, electrochemical sensor, hydrogen production, photocatalysis and adsorption processes (Y. Pan et al. 2012; Jing et al. 2014; Y. F. Jin et al. 2018; Thi Thanh et al. 2017; Feng et al. 2016). ZIF-8 has been used as the adsorbent and photocatalyst for the removal of the norfloxacin, methylene blue and trichloroethylene (Heydari Moghaddam et al. 2019; Feng et al. 2016; Zhou et al. 2019). The synthesis of ZIF-8 is generally performed at the time durations from < 1 h to several days (Çalik et al. 2022). Different synthesis recipes can not change the ZIF-8 crystals. High structural similarity can be obtained due to the substantial reproducibility of ZIF-8 (Kukkar et al. 2021).

Two approaches to develop the adsorption and photocatalytic activity of ZIF-8 are immobilization on the zeolite surface and metal doping.

2.3.3. Immobilization on the Support Surface

In addition to desirable properties of MOFs, there is a significant issue that inhibits the practical application. The reported studies about MOFs generally use powder MOF particles with micron scales, that hinder the application of MOFs in

industry. The adsorption process is commonly performed using large scale adsorption columns (J. Wu et al. 2021). To increase the adsorption effect of the MOFs and ease of use in the practical application, immobilization of them on the natural or synthetic zeolite and grafen oxide, has been applied (Al-Naddaf, Thakkar, and Rezaei 2018; B. Chen et al. 2021).

Most of the photocatalysts are utilized in powder form and have some shortcomings during photocatalytic degradation process (Deng et al. 2021): (i) Powder catalysts can be easily agglomerated at the preparation step (Luna et al. 2019); (ii) Powder catalysts is separated from water phase difficultly, therefore treatment costs could be increased (G. Zhang et al. 2007); (iii) Powder catalysts can behave as shortcircuit microelectrode in water, which increase the recombination of electrons and holes (Jie Wang et al. 2020). The immobilization of photocatalysts on the support surfaces is a remarkable solution to overcome these shortcomings (Deng et al. 2021). The assembly of photocatalyst into the photocatalytic reactors can be easily accomplished by the selection of suitable support material.

The widely used support materials are glasses, zeolites, clays, silicon-rich ceramics, adsorbents and graphene (R. Zhang et al. 2018; Ma et al. 2013; W. Wang et al. 2018). The support materials could be organic or inorganic and each one has some advantages and disadvantages. Therefore, while the choosing of support material, some significant points must be considered such as specific surface area, types of reactor design, price, reusability, characteristics of the pollutants, catalytic activity, degradation resistance, adhesion for photocatalyst, light transmittance and operating conditions (Deng et al. 2021). The preferable support material should have high surface area, easy separation from liquid, well light transmittance and strong adhesion to the photocatalyst (Deng et al. 2021; You et al. 2019).

The immobilization of photocatalyst on the selected support material can be performed by using various methods such as chemical vapor deposition, coupling method, seeding method, sol-gel method, liquid phase deposition and impregnation method (Yiren Wang and Yang 2019; Akpan and Hameed 2010; Tian et al. 2015). The suitable immobilization method can be selected by considering the types, properties and structure of support, the type of photocatalyst and the application conditions (Deng et al. 2021).

Zeolites are also known as a catalyst support due to their excellent thermal and chemical stabilities (Du et al. 2017).

Zeolites are three-dimensional structures of AlO_4 and SiO_4 tetrahedra linkage with sharing of oxygen atoms. Simple geometric structures of zeolites are produced from the combining of single tetrahedra (rings of 3 to 6 tetrahedra). There can be also more complex polyhedral structures with more tetrahedra, cages, chains and layers (Noviello et al. 2021). The zeolites are divided into two main groups such as synthetic and natural.

Synthetic zeolites are produced by chemical processes. They have more uniform pore size, crystal structure and chemical composition than the natural zeolites. The properties of synthetic zeolites could be modified according to the certain commercial usages. However, their cost is significantly higher than natural ones (Król 2020).

Natural zeolites are of volcanic origin and some of them are abundant such as erionite, clinoptilolite, phillipsite, chabazite and mordenite. They have a honeycomb like structure with the pores/channels (Ahmadi and Shekarchi 2010). Zeolite-rich rocks consist of >50 % of pure zeolite, which are used in many applications. The worldwide production of natural zeolites was 1,1 million tons in 2020 (Noviello et al. 2021).

Natural zeolites can include some impurities respective of extracted area, which could limit their application. Some treatment methods are used to eliminate impurities and enhance the physicochemical properties. Pore size, specific surface area, acidity and pore volume are the significant parameters of natural zeolites for the applications in adsorption and photocatalytic degradation (de Souza et al. 2018).

The clinoptilolite (CLN) is the most abundant and most commonly used natural zeolite. It is in heulandite group, whose members are of same structure. This group member is differentiated only with the amount of aluminum existence in network. Therefore, some properties like thermal stability can be different in each member. The clinoptilolite has the highest thermal stability (de Souza et al. 2018). The main chemical and physical features of the most commonly used natural zeolite/c clinoptilolite are given in Table 2.4. The corresponding clinoptilolite structure is given in Figure 2.5.

The CLN includes a monoclinic symmetric structure with microporous aluminosilicate crystals (Ackley, Giese, and Yang 1992). Aluminosilicate tetrahedrons consist of aluminum and silicon atoms which are bonded covalently to oxygen atoms, shown in Figure 2.5. It has a three-dimensional framework with cation enriched channels and interconnected cages (Yanzhi Wang et al. 2021).

Table 2.4. The physical and chemical features of Clinoptilolite. (Noviello et al. 2021)

Zeolite name	Chemical formula	Accessible volume (%)	Idealized cell data (Å)	Si/Al ratio	Cation exchange capacity (cmol ₍₊₎ kg ⁻¹)
Clinoptilolite	Ca ₄ (H ₂ O) ₂₄ [Al ₈ Si ₂₈ O ₇₂]	9.42	Monoclinic; a = 17.5 b = 17.6 c = 7.4 β = 116.1	4.3-5.3	220

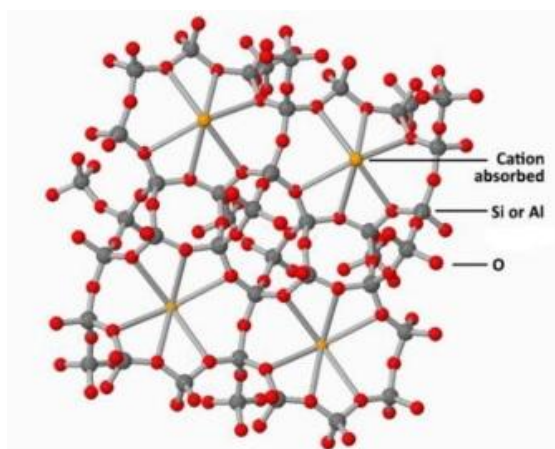


Figure 2.5. Three dimensional structure of clinoptilolite (Reprinted Ref. from (Raja et al. 2021) with permission).

There are different methods were applied for the combination of the other MOFs and zeolite. The seeding method has been discovered as effective and feasible for the synthesis of MOFs-zeolite composite (Thi Thanh et al. 2017; Keser Demir et al. 2014; Tate et al. 2017).

2.3.4. Doping of Metal

Heterogeneous photocatalysts have become the most promising technology to improve the photocatalytic degradation of organic pollutants (Vaya and Surolia 2020).

Metal ion doping, non-metal doping or co-doping of metals are applied to decrease charge carrier recombination. Metals dopants like Pt, Ag, Pd, V, Au, Th, Mo, etc. and non-metal dopants like C, F, N, S, etc. are used to increase photocatalytic performance of photocatalysts (Vaya and Surolia 2020; Akpan and Hameed 2009).

Dopants enhance the photocatalytic activity of photocatalyst in a number of ways such as band gap narrowing, specific surface area for adsorption, oxygen vacancies, electron trapping and impurity energy level formation (Rafiq et al. 2021).

Due to the narrow band gap of photocatalyst, more electron hole pairs are formed and photocatalytic activity is increased (Yousefi, Allahverdi, and Hejazi 2013). Impurity energy levels, band gap narrowing, and oxygen vacancies enhance the photocatalytic performance even at visible light (Rafiq et al. 2021; Rodríguez-González et al. 2008). Doping of the photocatalyst prohibits the recombination of the holes and electrons, which improves the photocatalytic activity (Quan Zhang et al. 2013). Under the visible light region, electronic properties of semiconductor could be modified by doping of metal to the crystal lattice of photocatalyst (Rafiq et al. 2021). Nevertheless, the increment of photocatalytic activity could decrease beyond the optimum amount of dopant.

2.3.5. ZIF-8-Clinoptilolite-Silver Composites as Adsorbent and Photocatalyst

ZIF-8 is a prominent functional material for the removal of organic pollutants such as dyes and antibiotics (Wang et al. 2019). The surface functionality, pore sizes and surface area are the major properties that improve the removal capacity (Santoso et al. 2021). However, nano ZIF-8 still have shortcomings such as aggregation and being lost during recycle (Wang et al. 2019). In this study, the novel composite adsorbent/photocatalyst (ZIF-8@CLN) was synthesized for the adsorption of organic pollutants. Additionally, the Ag is doped on the ZIF-8 and ZIF-8@CLN structure to enhance the photodegradation capacity of these materials.

Due to its inexpensiveness, thermal and chemical stabilities and nontoxicity, the clinoptilolite is promising support material to use in organic pollutant treatment. The

combination of ZIF-8, clinoptilolite and silver has some advantages over the pure counterparts, discussed in the following. These novel adsorbents/photocatalysts are the potential interests for future applications.

- The existence of CLN support prevents the aggregation of ZIF-8 particles. Thus, well distributed ZIF-8 particles on CLN supplies more adsorption and photodegradation sites for organic pollutants.
- There are many functional groups in ZIF-8 (C=C, O-H, N-H, C-N, C=N, Zn-O) and CLN (O-Si(Al)-O, O-H, Si-OH, Si-O) structure, which provides the excellent adsorption of organic pollutants such as MB, MO, CR, RhB and TC. These structures provide the electrostatic interactions, π - π stacking interactions, hydrogen bonding, surface complexation and coordination, and ion exchange between the organic pollutants and ZIF8@CLN.
- The CLN is cheap and abundant material. The pretreatment of raw CLN is effortless. The presence of CLN in composite decreases the price of the photocatalyst considerably.
- The ZIF-8@CLN is produced by seeding method easily. In addition, the recycle of ZIF-8@CLN composite after usage is much easier than pure ZIF-8. It is separated from water phase easily. Thus, the hybrid material reduces the production and treatment costs (G. Zhang et al. 2007).
- The assembly of the adsorbents with suitable support material is easier than ones without support.
- With the help of the adsorption process, the concentrated organic compounds can be efficiently degraded by the ZIF-8 based photocatalysts.
- ZIF-8 has 3D open cavities which allow light penetration and access to the active sites (Yao et al. 2018). The homogeneously immobilized ZIF-8 onto the CLN maximizes the light irradiance, which enhances the quantum efficiency. The supported ZIF-8 also have higher dispersion of the organic pollutants.
- CLN support has high electron storage capacity, which can place the excited electrons for the separation of electron hole pairs. It increases the photocatalytic degradation capacity of ZIF-8.
- The immobilization of ZIF-8 on CLN support lead to high durability to the heat and chemicals.

- This hybrid catalyst improves the adsorption capacity and provides more exposed ZIF-8 active sites for the using of generated carriers. It increases the photocatalytic activity compared to pure ZIF-8.
- The enrichment of organic pollutants around ZIF-8 cavities develops local concentration effect, which ensures to prolong refention time of pollutants on the active sites (Yao et al. 2018).
- The doping of Ag into the ZIF-8 and ZIF-8@CLN is a beneficial technique to increase the photocatalytic performance. The pores of ZIF-8 ensure the dispersion of Ag nanoparticles and form the different microenvironment around the active sites. The semiconductor behaviour of ZIF-8 can be enhanced with the encapsulation of tiny Ag particles for the degradation of persistent organic pollutants.
- The tiny Ag particles are isolated by ZIF-8@CLN structure and the exposed surfaces of Ag sites in Ag-ZIF8@CLN could be considerably higher than pristine Ag.
- The design of Ag-ZIF8@CLN photocatalyst can not only increase the exposure of active sites to the organic pollutants, but can also instantly degrade the arrested pollutants within the highly porous ZIF-8 structure. The composite structure of Ag-ZIF8@CLN guarantees accessibility of the organic pollutant and formed intermediates to the generated holes. Because, the light-harvesting centers, the enriched organic pollutants and active sites are placed at the same confined space.
- The doping of Ag on ZIF-8 improves the electron excitation and migration from ZIF-8 to organic pollutants due to their relatively low Fermi energy level and surface plasmon resonance. Therefore, ZIF-8 with CLN provides high specific surface areas and high porosity for the dispersion of Ag, facilitating the photocatalytic performance of ZIF8@CLN hybrid catalyst (X. Meng et al. 2020).
- The CLN structure could supply the electron migration from AgCl to Ag, and then Ag to ZIF-8 via multiple transfers on CLN support area. The generated pairs can be transferred further to the surfaces of AgCl and ZIF-8 and they would be used in the reaction continuously.

- The Ag generally behaves as a reservoir for photoinduced electrons. The Ag into the ZIF-8@CLN can reduce the recombination rate of photogenerated charge carriers and improve the light-harvesting ability, which increases the photocatalytic activity (V. A. Tran et al., 2020).
- The Ag-ZIF8@CLN has the narrow band gap and forming more electron hole pairs compared to other synthesized photocatalysts. Therefore, photocatalytic performance is increased.
- Ag is increased the photocatalytic activity with the impurity energy levels, oxygen vacancies and electron trapping (Rafiq et al. 2021; Rodríguez-González et al. 2008).
- The functional groups of the organic linker in ZIF-8 can act as an antenna to increase the absorption of light and stimulates active sites. The excited electrons can easily transfer owing to the intimate interfacial relation between Ag and ZIF-8@CLN (Yao et al. 2018).
- There can be a Schottky barrier between the Ag and ZIF-8@CLN interface, which assists interfacial electron transfer and increases the separation of charge carriers (Mamaghani, Haghghat, and Lee 2017).
- Many of the accumulated holes can degrade conquered organic pollutants instantly without remaining leaving carbonaceous species on the surface of catalyst. It prevents the catalyst deactivation.
- The diffusion of reactive species into the bulk solution was hard. Only the adsorbed organic pollutants on the photocatalyst could be oxidized (Liu et al. 2017). The high adsorption capacities of Ag-ZIF8 and Ag-ZIF8@CLN encourage the utilization of reactive species for the degradation reactions. There was an adsorption-desorption process between the dyes and catalysts. The adsorption equilibrium was broken with the degradation of adsorbed molecules. Then new organic pollutants transport from the solution to the photocatalyst surface quickly. This adsorption-desorption process increased the photodegradation performance (Fan et al. 2018).

2.3.6. Contributions to the Literature

The contributions of this thesis to the literature are summarized in the following:

- Until now, CLN and ZIF-8 are generally used for separation processes individually, however, the combination of ZIF-8 and CLN has not been studied yet. Therefore, there is no reported study focusing on the synthesis of ZIF-8@CLN and Ag-ZIF8@CLN.
- The adsorption and photocatalytic degradation ability of these novel materials were not investigated for our selected persistent organic pollutants (MB, MO, CR, RhB and TC).
- Additionally, the adsorption and photocatalytic degradation mechanisms of these ZIF-8-based materials have not been explained detailed in literature.

CHAPTER 3

MATERIAL AND METHODS

3.1. Materials

Zinc nitrate hexahydrate (>98.0 %) was obtained from Acros Organics. 2-methyl imidazole was purchased from Alfa Aesar. Methanol, ethanol, AgNO₃, NaCl, HCl, and NaOH, tetracycline and the dyes (MB, MO, CR and RhB) were acquired from Merck in analytical reagent grade. The natural zeolite tuff (from Gördes, TURKEY) was kindly supplied by INCAL Mineral Co.

3.2. Synthesis of Adsorbents/Photocatalysts

3.2.1. Synthesis of ZIF-8 and ZIF8@CLN

ZIF-8 was prepared using the synthesis procedure of Demir et al. (2014), illustrated in Figure 3.1.a. Each of the 2.4 g of Zn(NO₃)₂.6H₂O and 5.3 g of 2-methyl imidazole were dissolved in 90.4 g of methanol, separately. Afterthat, the solutions were mixed and stirred for 1 h at room temperature. The solid ZIF-8 was centrifuged, washed with methanol twice and dried at 80 °C overnight (Keser Demir et al. 2014).

For ZIF8@CLN synthesis, The CLN was washed with deionized water and sonicated 20 min. The seeding method suggested by Tate et al. (2017) was used to prepare CLN surface (Figure 3.1.b). The 5 g of heated CLN (150 °C for 5 min) was

added to the ZIF-8-deionized water (2 wt %) suspension and sonicated for 5 min. The obtained seeded zeolite was dried at 100 °C overnight (Tate et al. 2017). After that, at the immobilization step, the seeded CLN was added to the ZIF-8 solution at the beginning of the ZIF-8 synthesis procedure. Then, the synthesis procedure of ZIF-8 was followed and ZIF-8 immobilization on the CLN surface was achieved and denominated as ZIF8@CLN.

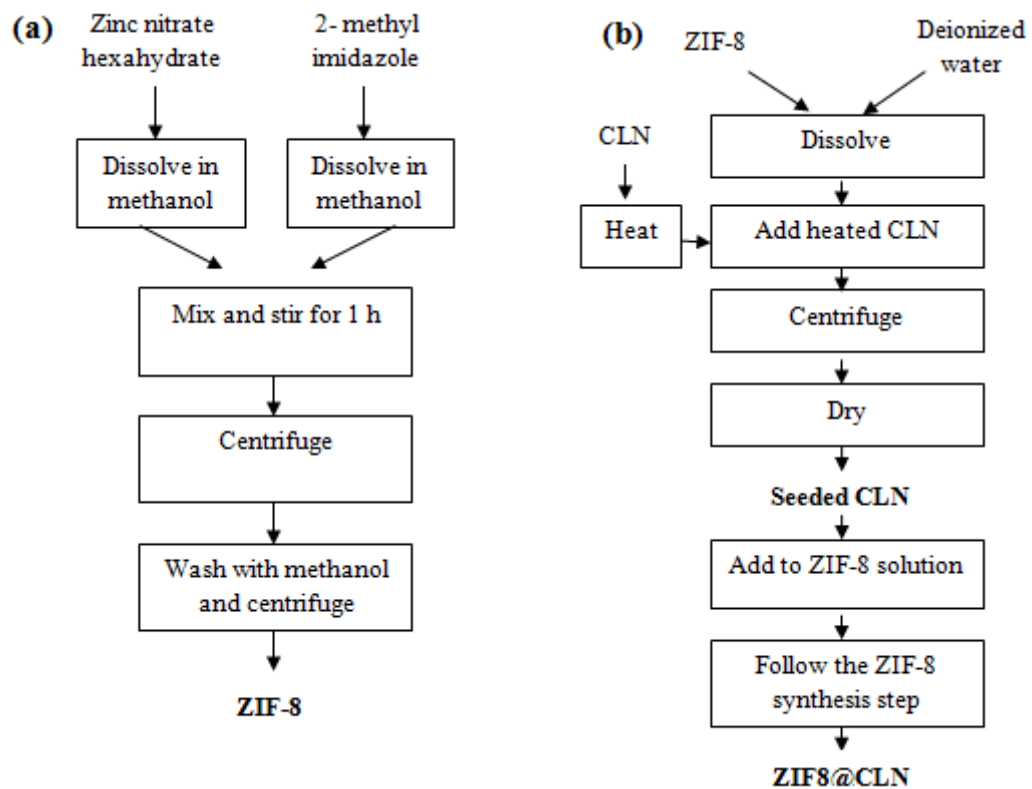


Figure 3.1. The synthesis procedures of (a) ZIF-8 and (b) ZIF8@CLN.

3.2.2. Synthesis of Ag-ZIF8 and Ag-ZIF8@CLN

The synthesis procedure of Ag-ZIF8 and Ag-ZIF8@CLN was illustrated in Figure 3.2. 0.2 g of ZIF-8 (or ZIF8@CLN) was dispersed in 53.7 mM AgNO₃ water (2 ml)-ethanol (12 ml) mixture with stirring for 3 h. After that, the solution was added to

the 10.48 mM NaCl water (14 ml)-ethanol (84 ml) mixture dropwise within 20 min, and stirred for 10 h at room temperature. The product was centrifuged, solid part was washed with deionized water three times, and then dried at 70 °C for 12 h (G. Fan, Zheng, et al. 2018). The Ag-doped catalysts were denominated as Ag-ZIF8 and Ag-ZIF8@CLN.

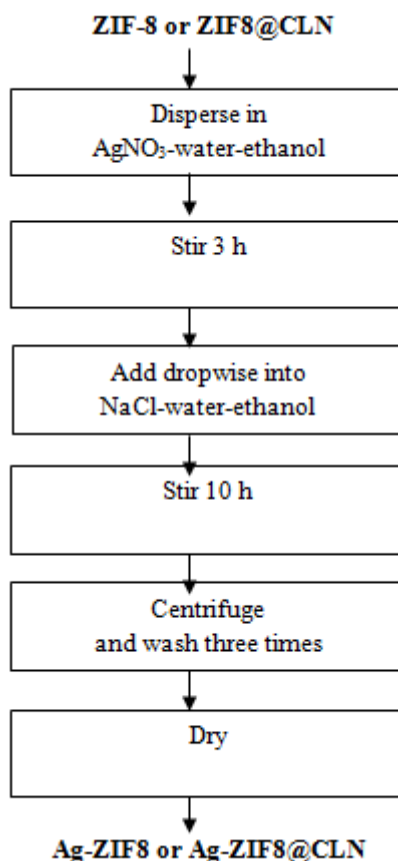


Figure 3.2. The synthesis procedures of Ag-ZIF-8 and Ag-ZIF8@CLN.

3.3. Characterization Methods

X-ray diffraction patterns (XRD) were taken with a Philips X'Pert Pro diffractometer. Attenuated Total Reflectance (ATR-IR) spectra were provided by a Perkin Elmer Spectroscopy in transmission mode. The morphology of the catalysts was

analyzed by a FEI Quanta 250 FEG model scanning electron microscope (SEM) with the Energy Dispersive X-Ray Analysis (EDX). N₂ adsorption-desorption isotherms were performed on Mikromeritics Gemini V. after degas at 250 °C for 24 hours by using N₂. The pH of the solutions was measured with a pH meter with Sartorius Docu-ph⁺ meter model. The dye concentrations were determined by using Perkin Elmer Lambda 45 UV-Vis spectrophotometer. Band gap energies of the photocatalysts were determined by UV-Visible Diffuse Reflectance Spectroscopy (UV-DRS). This analysis was carried out using Shimadzu UV-ISR 2600. The thermogravimetric analysis (TGA) was performed on Shimadzu TGA-51. The samples were heated in the range of 30-1000°C with the 10° C/min heating rate under the nitrogen atmosphere. The PL spectrum of the photocatalysts were taken with the Perkin Elmer LS 55 Fluorescence spectrometer. The elemental composition was explored by X-ray photoelectron spectroscopy (XPS) using Thermo Scientific K-Alpha model.

3.4. Adsorption of Organic Pollutants

The dye and tetracycline adsorption experiments were performed at room temperature under dark conditions. The effect of pH (2.0-12.0), adsorbent amount (0.25 - 2 g L⁻¹) and ionic strength (0.05 M and 2 M NaCl) on the adsorption were studied. The effect of initial dye concentration (1.25-17.5 mg L⁻¹) and initial TC concentration (10-80 mg L⁻¹) were also considered. The adsorbents were mixed with the magnetic stirrer during 2 h for dyes and 5 h for TC in 40 mL of solution. The adsorbents were taken with 0.45 µm syringe filters and the MB, MO, CR, RhB and TC concentrations were determined by measuring the absorbance at 664, 463, 497, 554 and 357 nm, respectively. Each experiments and measurements was performed in duplicate.

The adsorption capacity (q (mg g⁻¹)) and the percentage dye removal efficiency, (R (%)) were determined according to the following equations.

$$q_e = \frac{(C_i - C_e)V}{m} \quad (3.1)$$

$$R(\%) = \frac{(C_i - C_e)}{C_i} \times 100 \quad (3.2)$$

where C_i and C_e (mg L^{-1}) are initial and final concentration of dye solutions, m (g) is the adsorbent weight and V (L) is the volume of dye solution.

Equilibrium isotherm, kinetic and thermodynamic studies were carried out using the conditions determined in parameter experiments. During the adsorption equilibrium study, Langmuir, Freundlich, Dubinin-Radushkevich, Radke-Prausnitz, Redlich-Peterson and Langmuir-Freundlich models were used to evaluate the experimental data, given in Eq. 2.1 - 2.7 (Langmuir 1918; Dubinin 1960; Redlich and Peterson 1959; Radke, Prausnitz, and Radke 1972; Uzunkavak et al. 2019).

The best suitable isotherm model was defined by R^2 close to 1, lower Δq value and lower RMSE error function value, given in Eq. 3.3 and 3.4.

$$\Delta q = \frac{1}{N} \sum \left| \frac{q_{model} - q_{exp}}{q_{exp}} \right| \quad (3.3)$$

$$RMSE = \left[\frac{(\sum_{i=1}^N (q_{exp} - q_{model})^2)}{N-2} \right]^{\frac{1}{2}} \quad (3.4)$$

The pseudo-first order, pseudo-second order, Weber Morris intraparticle diffusion and Boyd kinetic models were used to analyze the kinetic data, shown in Eq. 2.8-2.12 (An et al. 2020; Weber Jr. and Morris 1963; Yao and Chen 2017).

During the thermodynamics study, the temperatures of 20°, 30°, 40° and 50 °C and the dye concentration of 1.25-17.5 mg L^{-1} were the parameters. Gibbs free energy (ΔG°), enthalpy (ΔH°) and entropy (ΔS°) of the process were determined from the adsorption isotherms (Eq. 2.13-2.16).

For the reusability of the adsorbents, the dye-loaded on ZIF-8 and ZIF-8@CLN were desorbed using ethanol. They were soaked in ethanol for 1 h. The TC-loaded ZIF-8 and ZIF-8@CLN were also desorbed using the deionized water, and then, washed with deionized water three times (Ba Mohammed et al. 2021). After that, they were filtered and dried overnight, used in four consecutive cycles.

3.5. Photocatalytic Degradation of Organic Pollutants

In order to investigate the photocatalytic degradation of MB, MO, CR and RhB dyes, one of the ZIF-8, ZIF8@CLN, Ag-ZIF8 and Ag-ZIF8@CLN photocatalysts was added to the 40 mL of dye solution. Next, the solution was stirred under magnetic stirrer

for 60 min (MB and MO) and 120 min (CR and RhB) in a dark cabin to achieve adsorption equilibrium. Then, the solution was exposed to the 15W ultraviolet lamp (UV) for 120 min under continuous stirring. There was 12 cm distance between the reactor and the light source. At each 20 min, the samples were taken from the solution using a 0.45 μm syringe filter. Afterthat, the concentration of the samples were determined by using a UV-Vis spectrophotometer at their maximum adsorption wavelengths. All experiments were carried out duplicate.

The photodegradation (%) were calculated by the Eq. 3.5:

$$\text{Photodegradation (\%)} = \frac{C_0 - C_t}{C_0} \times 100 \quad (3.5)$$

where C_0 is the initial dye concentration and C_t is the dye concentration at time t .

The effect of the various parameters on photocatalytic activity of the synthesized photocatalysts was investigated through the following experimental conditions:

- The effect of pH (pH 4, 8, 11): The photocatalyst amount was 0.04 g. The initial concentration of MB, MO, CR and RhB solutions were 25 mg L^{-1} . The pH of solution was arranged by using 0.1 M HCl or 0.1 M NaOH.
- The effect of photocatalyst amount (0.01 g, 0.04 g, 0.08 g): The initial concentration of MB, MO, CR and RhB solutions were 25 mg L^{-1} . The pH of the MB, MO, CR and RhB dye solutions were 11, 4, 4 and 8, respectively.
- The effects of initial dye concentration (5-35 mg L^{-1}): The photocatalyst amount was 0.04 g. The pH of MB, MO, CR and RhB dye solutions were 11, 4, 4 and 8, respectively.

Furthermore, the photodegradation kinetics study was carried out by using the models defined in Eq. 2.25-2.27. Afterthat, the used photocatalysts (Ag-ZIF8 and Ag-ZIF8@CLN) were collected by filter paper and washed with 50 % (v/v) ethanol-water solution for the three-cycle test to check the reusability of the photocatalysts.

CHAPTER 4

RESULTS AND DISCUSSION

4.1. Characterization

Various characterization techniques such as XRD, BET, ATR-IR, SEM-EDX, TGA, UV-DRS, PL and XPS were utilized to examine the properties of synthesized ZIF8, ZIF8@CLN, Ag-ZIF8 and Ag-ZIF8@CLN.

4.1.1. Crystal Structure Analysis

The XRD spectra of samples were investigated to identify the formation of ZIF-8, ZIF8@CLN, Ag-ZIF8 and Ag-ZIF8@CLN in Figure 4.1. The characteristic peaks of cubic ZIF-8 were placed at around $2\theta = 7.36^\circ$, 9.91° , 12.59° and 18.13° , which can be indexed to the (0 1 1), (0 0 2), (1 1 2) and (2 2 2) plane reflections, respectively (G. Fan, Zheng, et al. 2018). The additional peaks of CLN pattern observed at 9.70° , 22.20° , 26.72° and 29.71° which are ascribed to (0 2 0), (4 0 0), (3 1 2) and (1 5 1) plane reflections (Mortazavi et al. 2021; Hosseinzadeh, Ghasemian, and Zinatloo-Ajabshir 2022). They were appeared after the immobilization of ZIF8 onto the CLN, corresponded to the CLN that is appropriate to the literature (Abdollahi et al. 2021; Ökte et al. 2017).

Ag-ZIF8 and Ag-ZIF8@CLN composites comprise characteristic diffraction peaks of ZIF-8, CLN and Ag. They include distinct peaks of Ag at 27.72° , 32.15° , 46.27° and 54.57° , which were ascribed to the (1 1 1), (2 0 0), (2 2 0) and (3 1 1) planes of AgCl, respectively (G. Fan, Zheng, et al. 2018). Furthermore, it is shown that the

intensity of the some diffraction peaks of ZIF-8 decreased after doping Ag nanoparticles. This confirms that Ag was successfully attached on the surface and in the porous ZIF-8 structure (Abdi 2020). All characteristic peaks of ZIF-8, CLN and Ag were observed in Ag-ZIF8@CLN, showing the successful combination of them.

The XRD analysis was performed to examine average minimum particle size with Scherrer equation (Eq. 4.1).

$$D = \frac{K\lambda}{\beta \cos\theta} \quad (4.1)$$

where, D is particle diameter (nm), λ is X-ray wavelength (0.15406 Å), β is line broadening (0.00263 radian for Ag-ZIF8@CLN) by using the full width at half maximum (FWHM), and θ is Bragg angle (0.283456 radian for Ag-ZIF8@CLN). The shape factor K is 0.94 with the assumption of spherical shape of particles (Tsai and Langner 2016).

By using XRD Scherrer equation, it was seen that the particle size of ZIF-8 was increased from 33.17 nm to 38.27 nm after immobilization on the CLN surface (Table 4.1). Ag doping also affected the particle size. The particle size of Ag-ZIF8 and Ag-ZIF8@CLN was 51.67 and 57.46 nm, respectively.

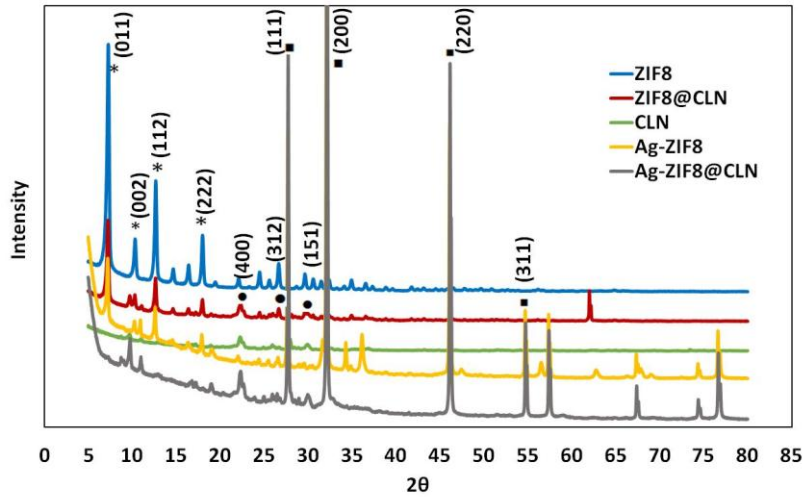


Figure 4.1. XRD spectra of synthesized catalysts.

4.1.2. Surface Analysis

The surface area of the photocatalysts was determined by nitrogen adsorption-desorption method. The results were given in Table 4.1. The surface area of CLN was only $24.47 \text{ m}^2 \text{ g}^{-1}$. However, ZIF8@CLN composite was much superior in surface area, ($1120.07 \text{ m}^2 \text{ g}^{-1}$), which was still lower than ZIF-8. After Ag doping, the surface area of ZIF8 and ZIF8@CLN decreased to 383.91 and $23.49 \text{ m}^2 \text{ g}^{-1}$, respectively. The external surface area values were also diminished after Ag doping. This demonstrated that Ag ions were incorporated on the ZIF-8 surface and in the porous ZIF-8 structure.

Various adsorption isotherms have been reported for vapors on many solids. Brunauer (1945) divided the isotherms into the five main classes from type I to V (Chiou 2003). As shown in Figure 4.2, BET adsorption-desorption isotherms of all ZIF-8-based photocatalysts were fitted to the type I, which is characteristic of the microporous adsorbents. The pores can not be more than a few diameters in width. The interaction between the adsorbate and adsorbent can be increased owing to the overlapping potential fields with neighbouring walls. In this way, the pore filling was achieved at the relatively low pressure and the adsorption was high at the lower relative pressure of isotherm (Palantavida and Warriar, n.d.). Afterthat, the adsorption reached a plateau and no hysteresis was observed at the isotherms of ZIF-8, ZIF8@CLN, CLN and Ag-ZIF8. The plateau indicated to the complete filling of pores. The BET isotherm of Ag-ZIF8@CLN included the small hysteresis loop, which can be attributed to the existence of mesopores due to the packing of the ZIF-8 particles and there can be also capillary condensation in the ZIF-8 nanopores (Luanwuthi et al. 2015).

Table 4.1. Textural properties of the synthesized photocatalysts.

Adsorbent	S_{Lang} ($\text{m}^2 \text{ g}^{-1}$)	External Surface Area ($\text{m}^2 \text{ g}^{-1}$)*	Crystal size (nm)**
ZIF8	1912.46	137.33	33.17
CLN	24.47	14.28	21.09
ZIF-8@CLN	1120.07	80.14	38.27
Ag-ZIF8	383.91	14.54	51.67
Ag-ZIF8@CLN	23.49	5.29	57.46

* External area was calculated from t-plot.

** Crystal size was calculated from XRD Scherrer equation.

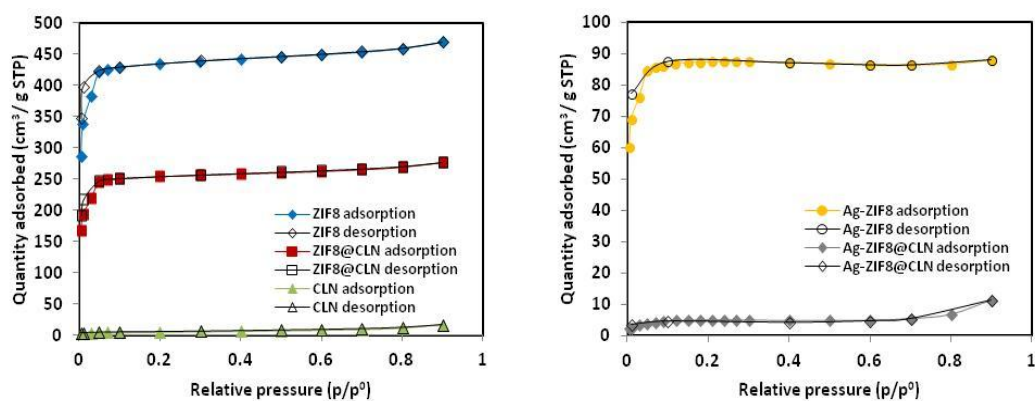


Figure 4.2. BET adsorption-desorption isotherms of synthesized photocatalysts.

4.1.3. Structural Properties

Figure 4.3 presents the ATR-IR spectra of synthesized ZIF-8, ZIF8@CLN, Ag-ZIF8 and Ag-ZIF8@CLN photocatalysts. The characteristic peaks of the imidazole ring at 1577 cm^{-1} (C=N stretching vibrations), $1080\text{--}1450\text{ cm}^{-1}$ region (C-N stretching vibrations), 755 cm^{-1} and 685 cm^{-1} (entire imidazole ring stretching) were observed in ZIF-8 and also in ATR-IR spectra of synthesized composites (Chakraborty, Islam, and Acharya 2019; Jia et al. 2020). Comparing the ATR-IR spectra of pure ZIF-8 and CLN-based composites, the new bands appeared at the spectrum of composites. The presence of peaks at 1042 cm^{-1} , 590 cm^{-1} and 790 cm^{-1} indicated the bending vibrations of O-Si(Al)-O group and also showed the tetrahedral atoms of the zeolite structure (Ullah et al. 2020). A considerable shifts in the spectrum of Ag nanocomposites (at $1080\text{--}1450\text{ cm}^{-1}$ region, 770 cm^{-1} and 692 cm^{-1}) can be attributed to the some interactions of Ag and N of the imidazole ring.

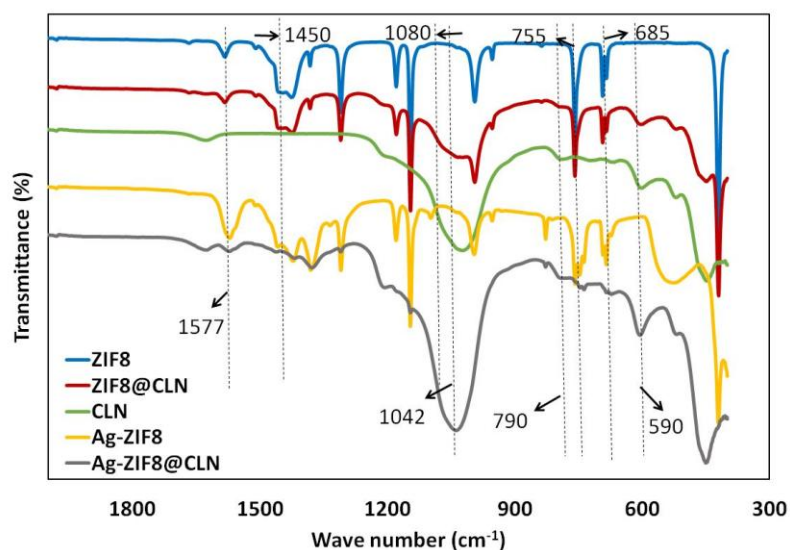


Figure 4.3. ATR-IR spectra of synthesized photocatalysts.

4.1.4. Morphology Analysis

Figure 4.4 demonstrated the SEM images of ZIF-8, ZIF8@CLN, Ag-ZIF8 and Ag-ZIF8@CLN samples. The SEM image of pure ZIF-8 indicated the aggregation of uniform cubic particles (Figure 4.4.a). After immobilization on the CLN, the uniform particle structure of ZIF-8 was well maintained and coated the CLN surface (Figure 4.4.b), which can be explained by the formation of ZIF-8 on the CLN surface.

After Ag doping, the morphology of the uniform ZIF-8 particles changed (Figure 4.4.(c-d)). A rough surface with small particles was shown for Ag-ZIF8@CLN (Figure 4.4.d). As seen in Figure 4.4.(e-f), a homogeneous Zn and Ag distribution was observed for Ag-ZIF8 and Ag-ZIF8@CLN, suggesting that Ag nanoparticles were uniformly doped on the ZIF8. The Ag-ZIF8 was composed of many needle-like structures.

Table 4.2 shows the results of the SEM-EDX analysis for the photocatalysts. The ZIF-8 contains 40.0 wt % Zn, after immobilization and metal doping, Zn percentage of ZIF-8 decreased. Ag-ZIF8 involves 33.3 wt % Zn and 14.8 wt % Ag, whereas, Ag-ZIF8@CLN consists of 8.8 wt% Zn and 25.1 wt % Ag as major component. The existence of all other elements, including C, N, O, Na, Al and Si, over

the surface of the photocatalysts were denoted as others in Table 4.2 and also the nonexistence of any impurity was verified by EDX analysis.

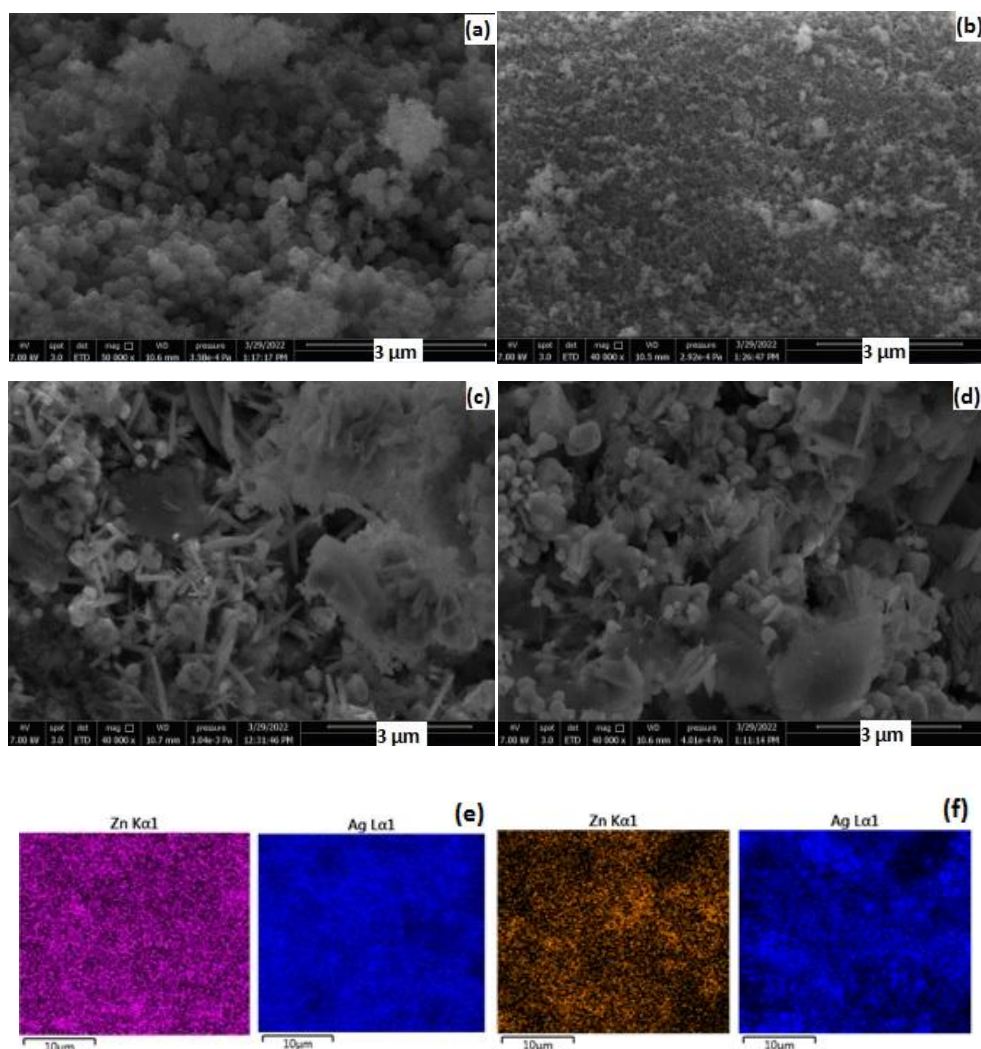


Figure 4.4. SEM images of (a) ZIF8, (b) ZIF8@CLN, (c) Ag-ZIF8 and (d) Ag-ZIF8@CLN. The mapping analysis of (e) Ag-ZIF8 and (f) Ag-ZIF8@CLN.

Table 4.2. SEM-EDX Results.

Photocatalyst	Zn (wt%)	Ag (wt%)	Others (wt%)
ZIF8	40.0	0.0	60.0
ZIF8@CLN	27.5	0.0	72.5
Ag-ZIF8	33.3	14.8	51.9
Ag-ZIF8@CLN	8.8	25.1	66.1

4.1.5. Thermal Analysis

The thermal stability of photocatalysts was determined by thermal gravimetric analysis. The ZIF-8, raw CLN and ZIF8@CLN were highly stable up to 455 °C (Figure 4.5.a). Beyond this temperature, the framework began to decompose and the flat valley was observed after 628 °C. The incorporation of ZIF-8 on CLN surface made the catalyst more stable compared to pure ZIF-8. This situation was also obtained as silver was doped at ZIF-8 and ZIF-8@CLN. The Ag-ZIF8 and Ag-ZIF8@CLN were highly stable up to 609 °C (Figure 4.5.b). Until 800 °C, the photocatalysts were decomposed slowly. The decomposition reactions caused the loss of 34.91 % and 24.75 % total mass of Ag-ZIF8 and Ag-ZIF8@CLN at 800 °C, respectively.

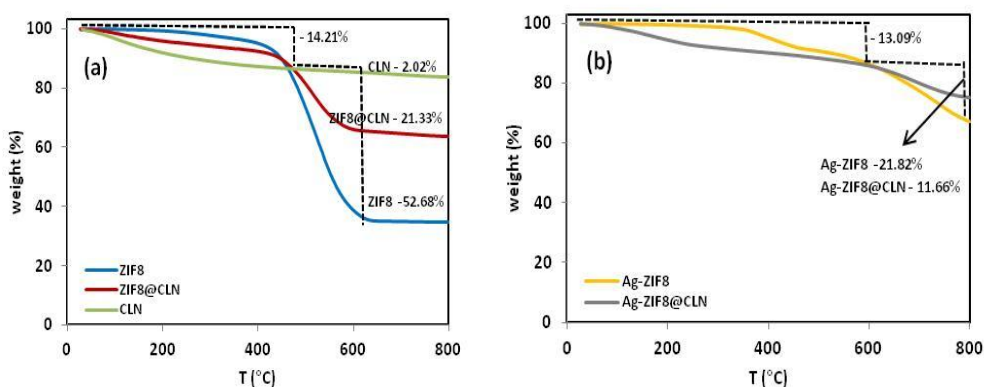


Figure 4.5. TGA spectra of (a) ZIF-8, raw CLN, ZIF8@CLN and (b) Ag-ZIF8, Ag-ZIF8@CLN.

From the TGA analysis, there were different temperature regions showed the weight losses of ZIF-8. The initial small weight loss at <100 °C can be ascribed to the loss of the solvent and adsorbed water existing in the sample. The other weight loss at 100-455 °C was due to the oxidative decomposition of imidazole ring. The weight loss beginning from 455 °C can be attributed to the degradation of the organic linkers of ZIF-8.

4.1.6. Optical Properties

The photophysical properties of all the synthesized photocatalysts were studied by using the diffuse reflectance spectra (UV-DRS) to confirm the presence of Ag on the ZIF-8 structure. From Figure 4.6.(a-b), all the photocatalysts showed the absorbance below 240 nm in the ultraviolet spectra. There were slight variations at the absorbance spectra of ZIF-8 and its composites. Moreover, the Tauc plot indicated the measured band gap energies of ZIF-8 and ZIF8@CLN as 5.18 and 5.16 eV, respectively (Figure 4.6.c). As seen in Figure 4.6.d, the band gap energies of the Ag-ZIF8 and Ag-ZIF8@CLN were measured as 5.12 and 5.10 eV respectively, which were slightly less than the photocatalysts before Ag doping. The lowest band gap of Ag-ZIF8@CLN indicated its higher photocatalytic performance compared to the other synthesized photocatalysts.

To further investigation of the photophysical properties, photoluminescence (PL) spectra of the photocatalysts were recorded to understand the lifetimes of e^-/h^+ pair (Figure 4.6.e). PL spectra also ensures the understand the separation efficiency of generated e^-/h^+ pairs (Varangane et al. 2022). The combination of ZIF-8, CLN and Ag was remarkably reduced PL intensity, which showed that the recombination of h^+ pairs carried to the ZIF-8 surface is hindered. Because, the doping of Ag on ZIF-8 and immobilization on the CLN surface decreased the recombination rate of the charge carriers with the extention of their lifetime. The peak intensity of Ag-ZIF8@CLN is lower than other photocatalysts, which confirmed that immobilization and doping diminished recombination by interacting with ZIF-8, CLN and Ag.

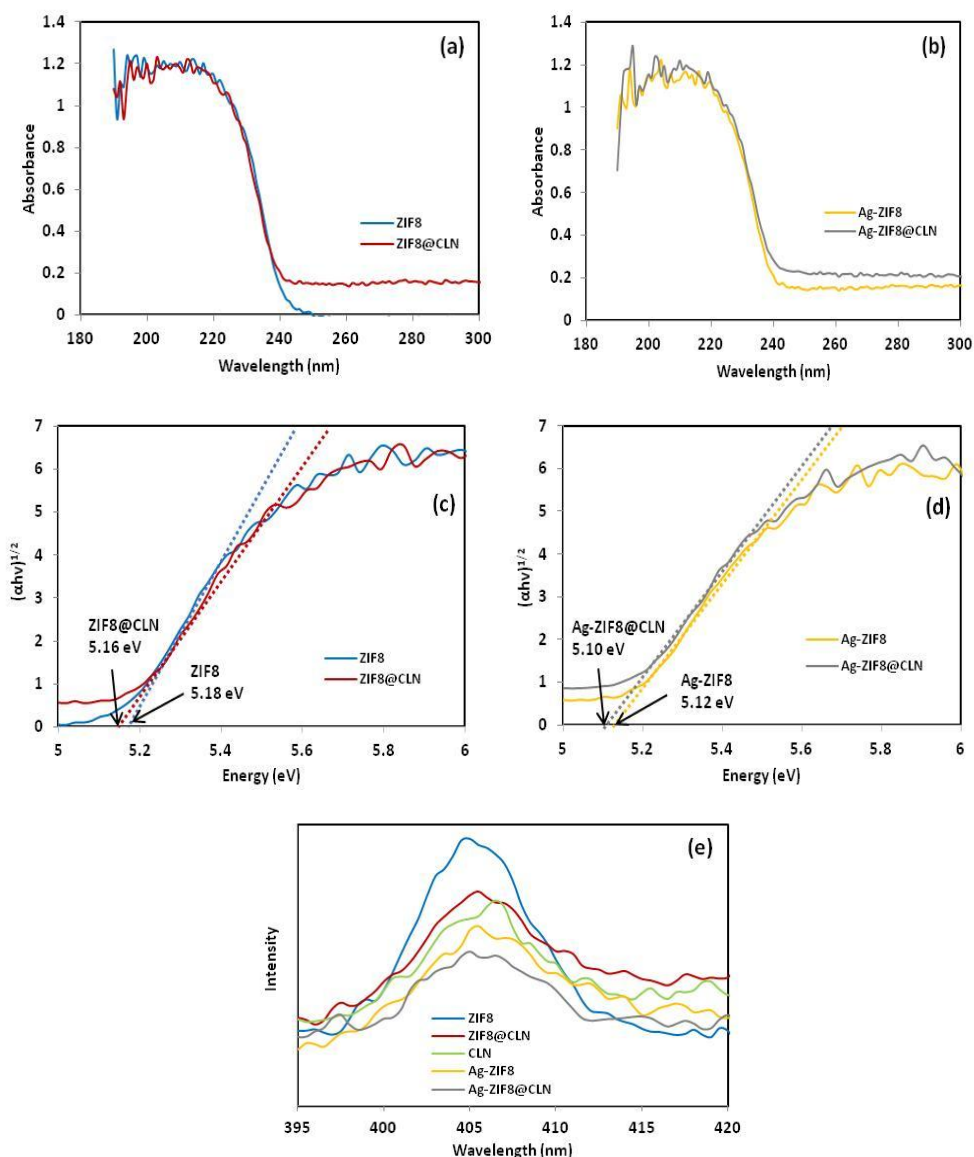


Figure 4.6. Optical properties, (a) and (b) the UV-DRS spectra of photocatalysts, (c) and (d) Bandgap of photocatalysts, (e) PL spectra.

4.1.7. XPS Analysis

The structure of photocatalysts was also investigated by XPS analysis. Figure 4.7 demonstrated the survey spectrum of the photocatalysts. In the C1s, N1s, and O1s region of ZIF-8, three signals around 285.29 eV for C1s, 399.14 eV for N1s, and 532.19 eV for O1s were observed respectively, which were belong to C and N exist in the

ligand (Chirra et al. 2021). In the zinc region, the peak shown at 1022.02 eV (Zn2p), expressed the presence of Zn^{4+} . Ag-ZIF-8@CLN composite showed the signals around 285.73 eV for C1s, 399.81 eV for N1s, and 531.81 eV for O1s, 1021.94 eV for Zn2p. The positions of the Zn 2p, C1s, O1s and N 1s peaks in ZIF-8 were shifted a little after immobilization and doping, indicating that the ZIF-8, CLN and Ag were interacting with each other. In the Si2p and Al2p region of CLN, the signals around 102.29 eV for Si2p and for 74.06 eV for Al2p were observed in Ag-ZIF8@CLN spectrum. Due to Ag doping, the two more signal around 367.81eV for Ag3d and 198.38 eV for Cl2p were also observed in the spectra of Ag-ZIF8@CLN. These assignments of the elements confirmed the presence of ZIF-8, CLN and the Ag particles on the synthesized photocatalysts.

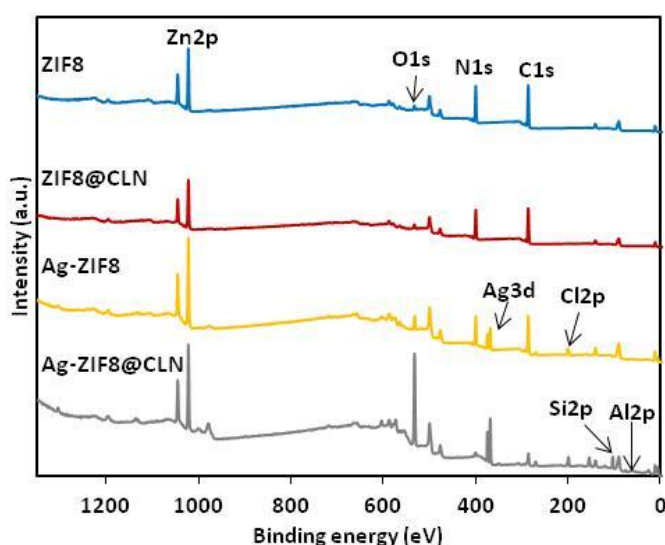


Figure 4.7. XPS survey of the synthesized photocatalysts.

As seen in Figure 4.8.a, the XPS peaks of Zn $2p_{1/2}$ and Zn $2p_{3/2}$ were observed at 1044.65 and 1021.65 eV, respectively, indicating Zn cations of ZIF-8. Zn $2p_{3/2}$ was attributed to the attachment of hydroxyl groups with the Zn ions on the surface. Meanwhile, Zn $2p_{1/2}$ indicated to the Zn atoms bonding to oxygen atoms (Makhetha, Ray, and Moutloali 2020). The slight increase in the binding energies of zinc ions at the Ag-ZIF8 and Ag-ZIF8@CLN spectra was caused by the bonding of the Zn cation with the Ag (Abd El Khalk et al. 2021). It shows that there could be ion exchange between

Zn²⁺ in the ZIF-8 structure and Ag⁺ in the solution. At the Zn2p states, there were positive shifts in binding energies, which indicated to the oxidation of Zn ions. Due to the metal doping, Zn species can deliver partial electrons to the Ag species, thus, these electrons transfer between Zn and Ag. Therefore, the Zn2p spectra of Ag-ZIF8 and Ag-ZIF8@CLN approved the formation of the new chemical bonds between ZIF-8 and Ag. This is compatible with the previous reports (Xin Guo et al. 2022).

The C1s spectra of the photocatalysts were deconvolved in three subpeaks (Figure 4.8.b). The C1s spectra of ZIF-8 included the peak at 284.77 eV that indicated to the C-H bond and the sp²-hybridized carbon (C-C). The peak at 285.83 eV assigned the presence of C-N bond on the methyl imidazole and the hydroxyl carbon (C-O) (Jia Liu et al. 2012; W. Q. Chen et al. 2019). The other peak at 291.76 eV showed the C=N bond (Abd El Khalk et al. 2021). When the C1s spectra of Ag-ZIF8@CLN and pure ZIF-8 were compared, the results demonstrated that the spectra of Ag-ZIF8@CLN shifted to the higher binding energies. An increase in binding energies can be displayed the loss of electron density, which could form more active vacancies, thereby increased the photocatalytic performance (W. Q. Chen et al. 2019).

As shown in Figure 4.8.c, the N1s spectra of ZIF-8 was deconvolved in three subpeaks. However, the spectra of ZIF8@CLN and Ag-ZIF8 composite catalysts were deconvolved in the two subpeaks and Ag-ZIF8@CLN had only one subpeak. The N1s band peaks of ZIF-8 was observed at 398.73 and 399.58, which were corresponding to the pyridinic N and pyrrolic N, respectively, originated from 2-methyl imidazole. Moreover, the peak at 406.68 eV was associated with the N1s of oxynitride (O-Zn-N) (Jia Liu et al. 2012). The peak areas at around 399.58 eV were decreased at the ZIF8@CLN and Ag-ZIF8 spectra, and disappeared in the Ag-ZIF8@CLN spectra. It means that the pyrrolic N of the imidazole ring of ZIF-8 was diminished after modification. The peak at 406.68 eV corresponding to the existence of O-Zn-N bond was not observed in the spectra of composites.

Figure 4.8.d indicated that the O1s spectra of all catalysts contained the peak around 531.06 eV indicating the C=O bond (Abd El Khalk et al. 2021). However, the peak at 531.68 eV, corresponding to the Zn-OH, observed only in Ag-ZIF8 and Ag-ZIF8@CLN spectrum (Zhu et al. 2017). The presence of Zn-OH denoted that the generation of the H₃O⁺ protons can be the charge compensating species, therefore, the surface conductivity could be protonic in nature (Muñoz-Gil and Figueiredo 2019). These spectra revealed that the Ag-ZIF8@CLN catalyst involved more O1S species

with the larger peak areas. XPS also suggested the interaction between the Zn from ZIF-8 with the oxygen-containing groups in CLN. In Ag-ZIF8 spectrum, there was one more deconvoluted peak at 530.36 eV associated with the O-C carbonate (Muñoz-Gil and Figueiredo 2019).

Two peaks at 367.50 and 373.51 eV with 6.01 eV splitting were defined as Ag 3d_{5/2} and Ag 3d_{3/2}, respectively (Figure 4.8.e), which were corresponding to the formation of metallic Ag. The slightly lower binding energies of Ag in composite than bulk Ag (368.3 eV of Ag 3d_{5/2} and 374.3 eV of Ag 3d_{3/2}) showed the strong interactions between Ag and ZIF-8/ZIF8@CLN and also the electron transfer from the Ag to the ZIF-8. In addition, the narrow width of the peaks indicated that only the single-element silver existed in the system, and proved the encapsulation of zero valence Ag by ZIF-8 (Tran, Kadam, and Lee 2020).

Figure 4.8.f showed the XPS Cl2p spectra of Ag-ZIF8 and Ag-ZIF8@CLN. The peak of Cl 2p_{3/2} and Cl 2p_{1/2} associated with Cl⁻ anion was observed at around 198.18 and 197.68 eV. The Cl2p peaks at 198.18 eV was also assigned to C-Cl bond (Takehira et al. 2018; Zheng et al. 2012).

XPS results comply with the XRD and ATR-IR spectra, suggesting the successful synthesis of Ag-ZIF8 and Ag-ZIF8@CLN. The results showed that the synthesized composite photocatalysts had more active sites and more considerable photocatalytic effects than pure ZIF-8.

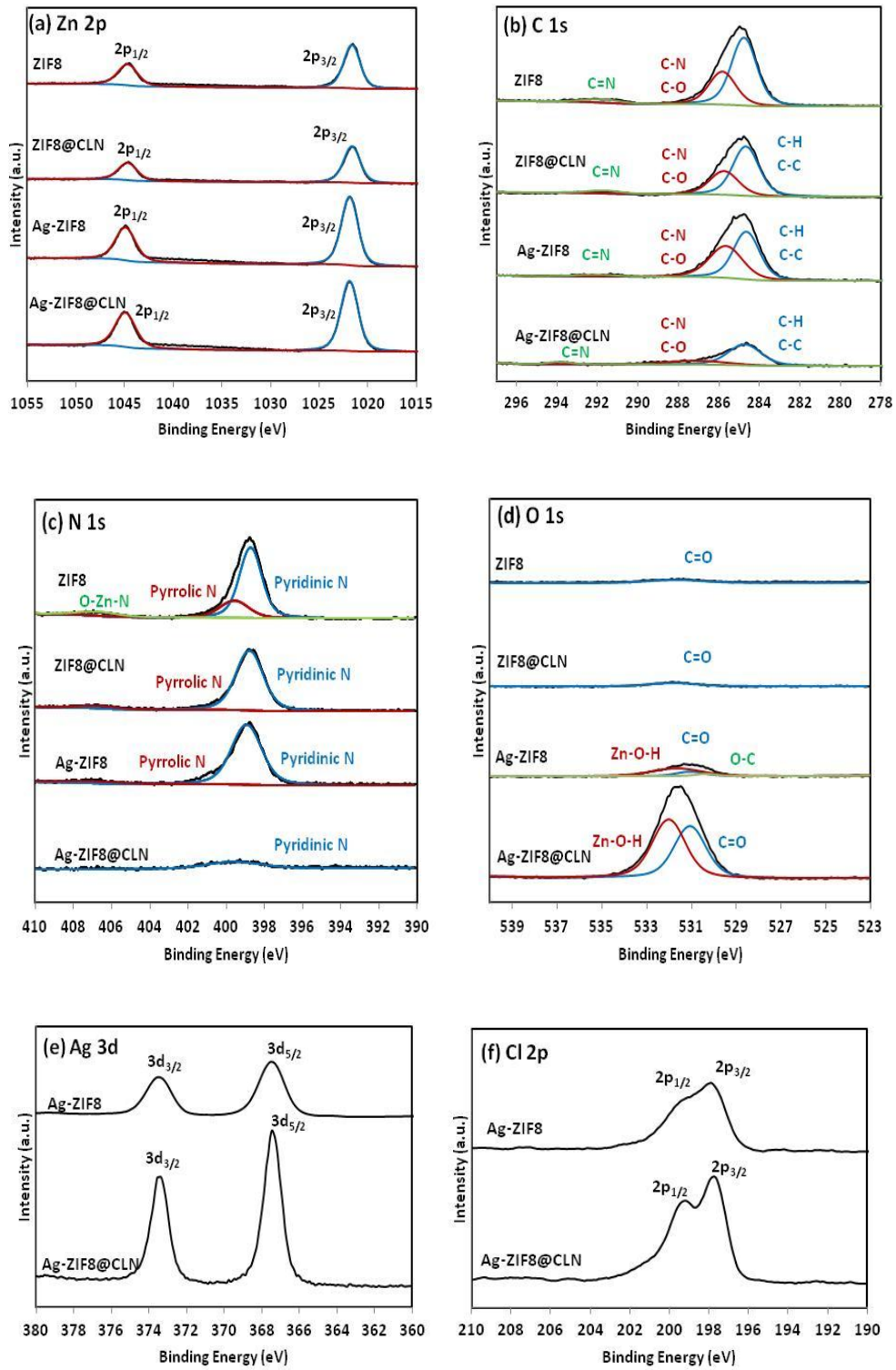


Figure 4.8. XPS spectra of the synthesized photocatalysts (a) Zn2p, (b) C1s, (c) N1s, (d) O1s, (e) Ag3d and (f) Cl2p.

4.2. Adsorption

The synthesized ZIF-8 and ZIF-8@CLN were used for the removal of the dyes (Methylene blue, Methyl orange, Congo red and Rhodamine B) and the antibiotic (Tetracycline) from aqueous solution.

4.2.1. Adsorption of Dyes

In this part, the adsorption of cationic MB, anionic MO and CR, and zwitterionic RhB dyes by using ZIF-8 and ZIF-8@CLN were considered detailed.

4.2.1.1. Dyes Adsorption Parameter

The pH was the main factor affecting the adsorption capacity of ZIF-8 and ZIF-8@CLN. Figure 4.9 demonstrated that the adsorption behavior of each dyes were different.

When the solution pH was increased from 2 to 10, the adsorption capacity of MB by ZIF-8 and ZIF8@CLN increased from 3.31 to 9.71 mg g⁻¹, and from 6.38 to 9.88 mg g⁻¹, respectively. Then the adsorption capacity remained almost constant until the pH 12.

The adsorption of MO by ZIF8 and ZIF-8@CLN slightly increased from pH 2 to pH 4, however, at the rising pH from 4 to 12, the adsorption capacities of MO were decreased.

A substantial decrease in adsorption capacity for the CR was obtained under basic conditions. As the pH was increased from 4 to 12, the adsorption capacities of ZIF-8 and ZIF-8@CLN reduced from 39.67 to 7.41 mg g⁻¹ and from 39.29 to 6.39 mg g⁻¹, respectively. There is no dramatic change on the adsorption capacities of ZIF-

8@CLN for RhB by increasing pH from 2 to 12. However, the adsorption capacities of ZIF-8 were decreased from 13.1 to 6.3 mg g⁻¹, during the pH was increased from 8 to 12.

Similar adsorption behavior with respect to pH has been reported in the literature (Yating Wang et al. 2019). The suitable pH for the removal of MB, MO, CR and RhB (by ZIF-8 and ZIF-8@CLN) were determined as pH 10, pH 4, pH 4, and pH 8, respectively.

The adsorption capacity is generally explained with the point of zero charge (PZC) of the adsorbent. The PZC for ZIF-8 is at pH 9.8 (C. S. Wu et al. 2015). As the pH is below 9.8, the surface charge of ZIF-8 is positive. When the pH is higher than 9.8, it turns from positive to negative.

Cationic MB molecules could attract with the negatively charged ZIF-8 (at pH >9.8), which improves the adsorption efficiency. At the pH below than 3.47 (pKa), the MO is protonated (Avila et al. 2021). When the solution pH increases even until the acidic pH of 4.4, the protonated ion predominates. At the lower pH values, MO has electrostatic interaction with the positively charged adsorbent surfaces. At the pH of MO is equal or greater than 3.2, MO has resonant structures such as double-charged zwitterion. This double charge consists of positive and negative charge of the MO. These resonant forms in the zwitterion provides to the additional electrostatic interaction that is effective for the adsorption of the azo dye (Avila et al. 2021).

At the acidic pH values, adsorption of the azo dye CR was also substantially enhanced. The protonation of the amino groups on CR increases the electrostatic attraction between CR and the adsorbents (Tang et al. 2020). At alkaline pH, the adsorption of the anionic dyes (MO and CR) decreases dramatically due to the hydroxyl ions which compete with the anionic dye for the active sites (Elmoubarki et al. 2015). There is an electrostatic repulsion between the negatively charged ZIF-8 and the anionic dye molecules.

RhB could be adsorbed even at low pH of 2. The reason for the adsorption at lower pH was the presence of cationic and zwitterionic forms of RhB (Khamparia and Jaspal 2016). When the pH was higher than 8.0, the adsorption of RhB decreased due to excessive OH⁻ ions compete with COO⁻ ions in binding with -N⁺.

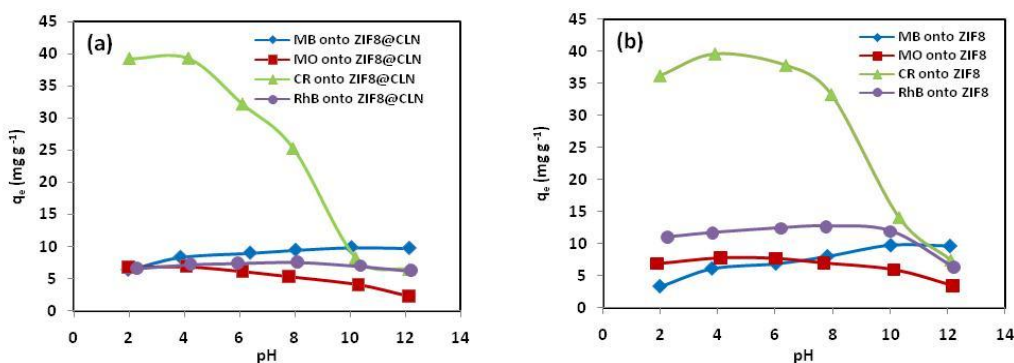


Figure 4.9. Effect of pH (a) ZIF-8@CLN and (b) ZIF-8. Experimental conditions: volume of dye solution=40 ml; pH range 2-12; MB ($C_0=10\text{ mg L}^{-1}$, $m_{\text{ads}}=1\text{ g L}^{-1}$); MO ($C_0=10\text{ mg L}^{-1}$, $m_{\text{ads}}=1\text{ g L}^{-1}$); CR ($C_0=20\text{ mg L}^{-1}$, $m_{\text{ads}}=1\text{ g L}^{-1}$); RhB ($C_0=10\text{ mg L}^{-1}$, $m_{\text{ads}}=1\text{ g L}^{-1}$).

The adsorbent amount plays an important role in the removal performance of the system. The effect of adsorbent amount was studied from 0.25 to 2 g L^{-1} at their optimum pHs and room temperature.

When the ZIF-8 amount varies from 0.25 to 1 g L^{-1} , the percentage removal of MB increases from 64.88% to 96.27% (Figure 4.10.a). Likewise, with the increase of the ZIF-8@CLN amount from 0.25 to 0.75 g L^{-1} , MB removal is increased from 85.69% to 96.85% . The removal efficiency of ZIF-8 for MO at 1.25 g L^{-1} adsorbent dose was observed to be 97.01% , and for CR at 0.5 g L^{-1} adsorbent dose, it was 99.29% , and for RhB at 0.75 g L^{-1} adsorbent, it was 98.24% (Figure 4.10.(b-d)). Almost complete removal of MO, CR and RhB was accomplished at the ZIF-8@CLN dosages of 1.5 , 0.5 and 1.25 g L^{-1} , respectively.

Therefore, in all the subsequent experiments, the amounts of ZIF-8 and ZIF-8@CLN were maintained at these dosages due to the achieving almost complete removal. With an increase in the adsorbent dosage, the density of active sites was increased and the rate of adsorption was also rised (Kirandeep et al. 2021).

When the adsorbent amounts were further increased, the percentage removal was not changed and the adsorption capacities decreased (Figure 4.10). The further increase in the adsorbent amount decreases the homogeneous distribution of adsorbent, which causes adsorption resistance. At higher dosages, there could be the agglomeration between ZIF-8 particles, the active sites would be decreased.

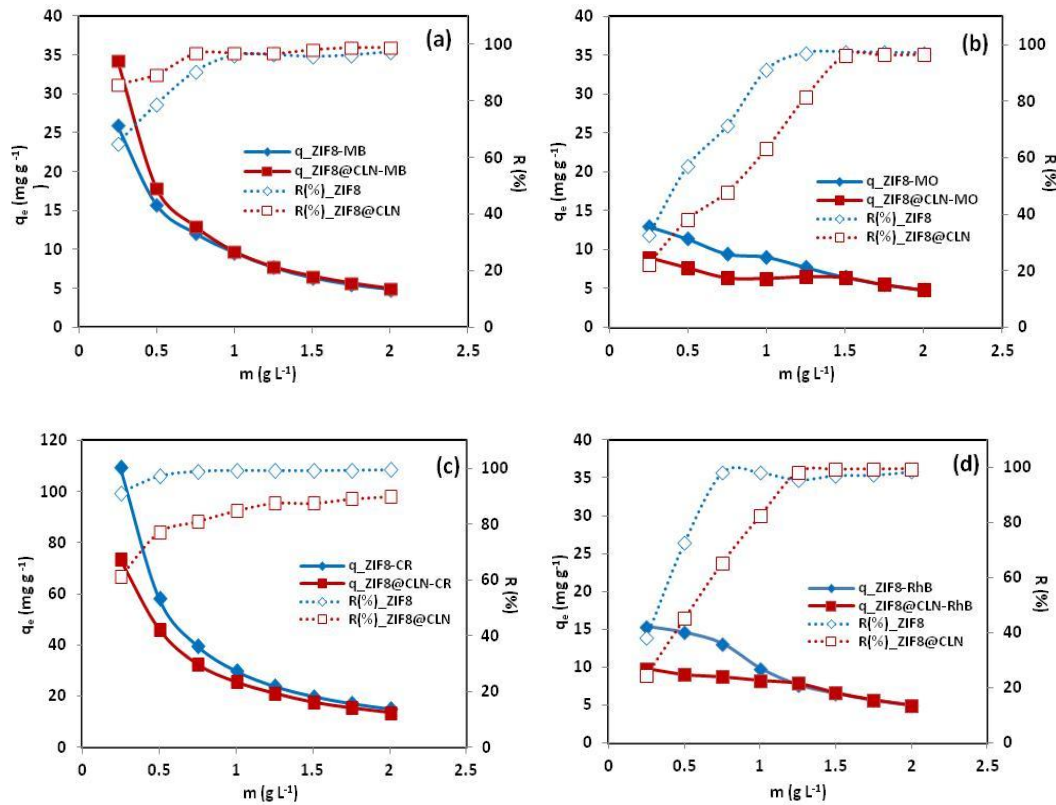


Figure 4.10. Effect of adsorbent amount (a) MB, (b) MO, (c) CR and (d) RhB. Experimental conditions: volume of dye solution=40 ml; adsorbent amount range 0.25 - 2 g L⁻¹; MB ($C_0=10$ mg L⁻¹, pH=10); MO ($C_0=10$ mg L⁻¹, pH=4); CR ($C_0=20$ mg L⁻¹, pH=4); RhB ($C_0=10$ mg L⁻¹, pH=8).

The effect of initial dye concentrations of MB, MO and RhB were studied for 1.25 to 17.5 mg L⁻¹; and CR was investigated for 5 to 40 mg L⁻¹ (Figure 4.11). Almost complete removal of MB, MO, CR and RhB dyes by using the ZIF-8 was accomplished at the initial concentrations of 10, 10, 30 and 10 mg L⁻¹; and by using the ZIF-8@CLN, the complete removal were obtained at 12.5, 10, 20 and 10 mg L⁻¹, respectively. Due to the high removal efficiencies, the dye concentrations were maintained at these values during the subsequent experiments. The removal efficiencies of ZIF-8@CLN for MB at 12.5 mg L⁻¹ was observed to be 96.64 %; and for MO at 10 mg L⁻¹, it was 97.77 %; and for CR at 20 mg L⁻¹, it was 98.60 %; and for RhB at 10 mg L⁻¹, it was 97.03 % (Figure 4.11).

When the dye concentration is increased, the accessibility of active sites is enhanced until the saturation level (Kirandeep et al. 2021). At higher dye

concentrations, the removal efficiencies were reduced. The adsorption process was slowed down due to the molecular competition for a few empty active sites (Al-Sadoon, Mohammed, and Al-Tameemi 2021). Due to the increasing driving force, the film thickness of the adsorbent and mass transfer resistance increase, thus, the adsorption rate decreases. Therefore, when the MB, MO, CR and RhB concentrations was increased from the above values, the efficiencies were decreased, however, the adsorption capacities were further increased, which is owing to the increase of the driving force (Figure 4.11).

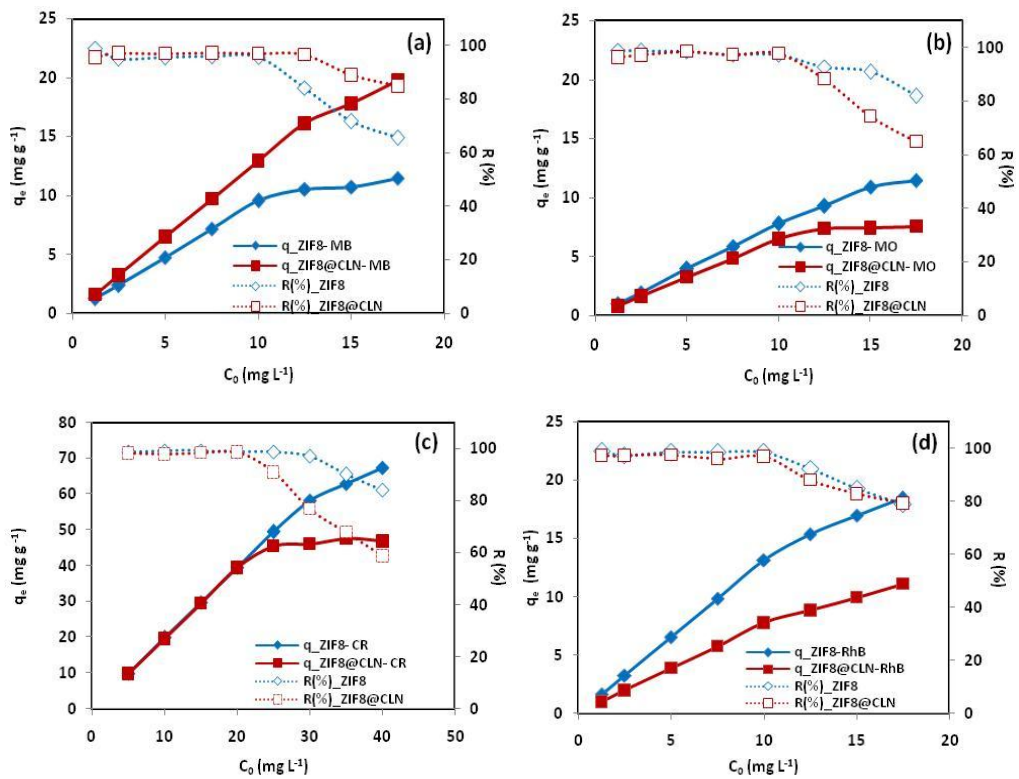


Figure 4.11. Effect of dye concentration (a) MB, (b) MO, (c) CR and (d) RhB. Experimental conditions: volume of dye solution=40 ml; MB ($C_0=1.25-17.5$ mg L⁻¹, pH=10, $m_{ZIF-8}=1$ g L⁻¹, $m_{ZIF-8@CLN}=0.75$ g L⁻¹); MO ($C_0=1.25-17.5$ mg L⁻¹, pH=4, $m_{ZIF-8}=1.25$ g L⁻¹, $m_{ZIF-8@CLN}=1.5$ g L⁻¹); CR ($C_0=5-40$ mg L⁻¹, pH=4, $m_{ZIF-8}=0.5$ g L⁻¹, $m_{ZIF-8@CLN}=0.5$ g L⁻¹); RhB ($C_0=1.25-17.5$ mg L⁻¹, pH=8, $m_{ZIF-8}=0.75$ g L⁻¹, $m_{ZIF-8@CLN}=1.25$ g L⁻¹).

Electrostatic interactions are the main forces for the adsorption of dyes, and therefore, the presence of coexisting ions causes to competition for the active sites. Dye

wastewater generally comprises some salts such as chloride, carbonate and sulfate (J. Pan et al. 2021). Figure 4.12 indicates the ionic effects on the adsorption of MB, MO, CR and RhB onto ZIF-8 and ZIF-8@CLN as a function of pH by using NaCl (0.05 M and 0.2 M). The presence of ion affected the adsorption of four dyes in varying degrees. With increasing the NaCl concentration, the adsorption capacities of both adsorbents for MB and MO were slightly decreased at the pH range 2 to 12 (Figure 4.12). The removal of CR was substantially reduced at the presence of salt, especially in the pH range from 2 to 10. At pH 4, in the existence of 0.2 M NaCl, the adsorption capacity of ZIF-8 for CR was decreased from 59.59 to 23.86 mg g⁻¹; and the adsorption capacity of ZIF-8@CLN was decreased from 45.53 to 14.43 mg g⁻¹. The RhB adsorption on the ZIF-8 also decreased with an increase in NaCl concentration.

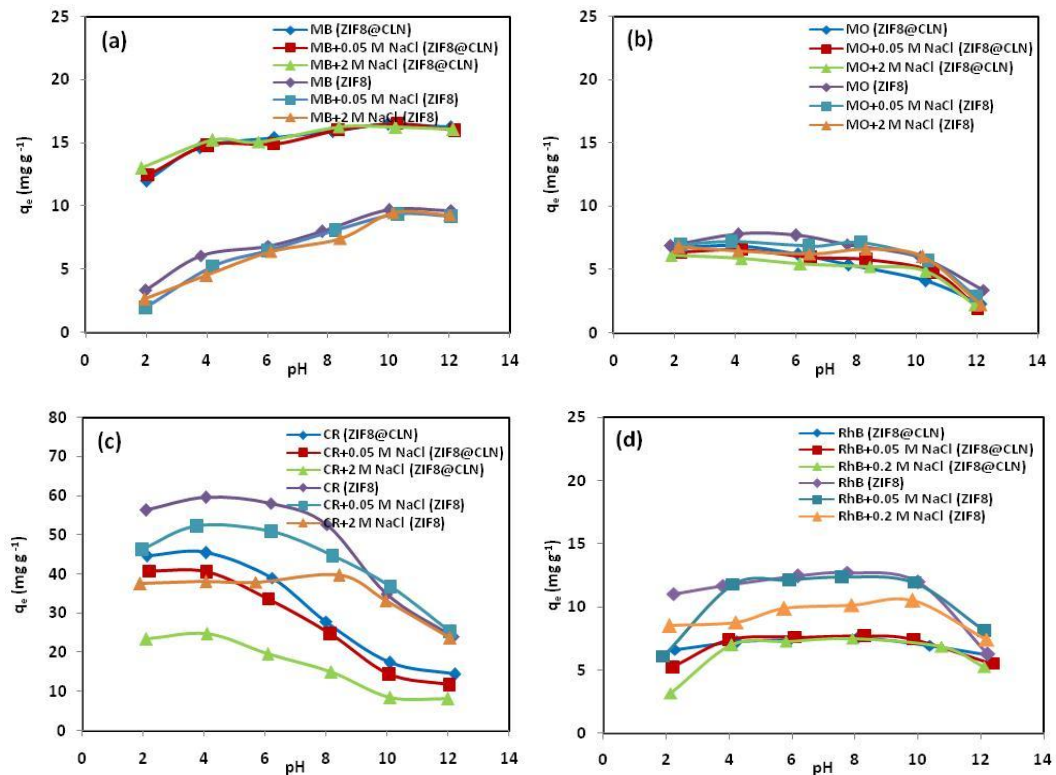


Figure 4.12. Effect of ionic strength (a) MB, (b) MO, (c) CR and (d) RhB. Experimental conditions: volume of dye solution=40 ml; pH range 2-12; MB ($C_0=10\text{ mg L}^{-1}$, $m_{\text{ZIF-8}}=1\text{ g L}^{-1}$); MB ($C_0=12.5\text{ mg L}^{-1}$, $m_{\text{ZIF-8@CLN}}=0.75\text{ g L}^{-1}$); MO ($C_0=10\text{ mg L}^{-1}$, $m_{\text{ZIF-8}}=1.25\text{ g L}^{-1}$); MO ($C_0=10\text{ mg L}^{-1}$, $m_{\text{ZIF-8@CLN}}=1.5\text{ g L}^{-1}$); CR ($C_0=30\text{ mg L}^{-1}$, $m_{\text{ZIF-8}}=0.5\text{ g L}^{-1}$); CR ($C_0=20\text{ mg L}^{-1}$, $m_{\text{ZIF-8@CLN}}=0.5\text{ g L}^{-1}$); RhB ($C_0=10\text{ mg L}^{-1}$, $m_{\text{ZIF-8}}=0.03\text{ g L}^{-1}$); RhB ($C_0=10\text{ mg L}^{-1}$, $m_{\text{ZIF-8@CLN}}=1.25\text{ g L}^{-1}$).

There could be the competition between dye molecules and coexisting ions for the effective adsorption sites. The activity coefficient of dyes may be also changed by the existence of salt, which inhibits the adsorption process (Fu et al. 2021). As the ionic strength increased, the electrical double layer of the adsorbents was compressed, and caused to decrease in dye adsorption.

4.2.1.2. Dyes Adsorption Isotherms

The knowledge on how the dyes adsorbed on the adsorbent surface is acquired by the isotherms (Nimbalkar and Bhat 2021). Isotherms give the information about adsorption states of adsorbent, surface structure and the adsorption mechanism. As shown in Figure 4.13, as the initial concentration of dyes increased, the equilibrium capacity increased rapidly, then slowed down, and finally reached equilibrium. All experimental data were evaluated with Langmuir, Freundlich, Dubinin-Radushkevich, Radke Prausnitz, Redlich Peterson and Langmuir-Freundlich isothermal models, as defined by the equations in part 2.2.1.3.

The isotherm parameters were calculated by nonlinear fit of experimental data. The model parameters, corresponding deviation (Δq) and error functions were determined by using the Microsoft excel solver. For each isotherm model above, three error functions (R^2 , Δq and RMSE) were calculated by using the Eq. 3.3-3.4. The best fitting isotherm model was determined by R^2 near to unity, lower Δq and lower error function values (Nimbalkar and Bhat 2021; Almeida-Naranjo et al. 2021; Khamparia and Jaspal 2016).

The experimental data and fitting isotherm models were demonstrated in Figure 4.13 and calculated model parameters and error functions were given in Table 4.3. MB adsorption by ZIF-8 follows Redlich Petterson isotherm, and MO and CR adsorption by ZIF-8 follows Langmuir-Freundlich isotherm model. For MB, MO and CR adsorption by ZIF-8@CLN, the datas fitted better with Langmuir-Freundlich model. In other words, the adsorption between MB/MO/CR dyes and ZIF-8/ZIF-8@CLN adsorbents happened as an adsorption systems of hybrid Langmuir and Freundlich models. RhB adsorption follows the Langmuir model for both adsorbents with homogeneous

surfaces. According to the fitted models, the adsorption capacities of ZIF-8@CLN (MB: $19.22 \pm 2.1 \text{ mg g}^{-1}$; MO: $7.47 \pm 7.6 \text{ mg g}^{-1}$; CR: $46.79 \pm 1.2 \text{ mg g}^{-1}$ and RhB: $10.25 \pm 1.0 \text{ mg g}^{-1}$ at 293 K) and ZIF-8 (MB: $11.46 \pm 2.0 \text{ mg g}^{-1}$; MO: $12.45 \pm 0.21 \text{ mg g}^{-1}$; CR: $63.35 \pm 4.6 \text{ mg g}^{-1}$ and RhB: $19.23 \pm 2.1 \text{ mg g}^{-1}$ at 293 K) were calculated.

Table 4.3. Isotherm parameters and error functions calculated for MB, MO, CR and RhB adsorption onto ZIF-8 and ZIF-8@CLN.

Model	Parameter	Dyes/Adsorbents							
		MB		MO		CR		RhB	
		ZIF-8	ZIF-8 @CLN	ZIF-8	ZIF-8 @CLN	ZIF-8	ZIF-8 @CLN	ZIF-8	ZIF-8 @CLN
Langmuir	$q_m(\text{mg g}^{-1})$	10.27	19.78	11.44	7.57	67.36	46.88	19.23	10.25
	$K_L(\text{L mg}^{-1})$	3.88	4.59	6.49	8.13	6.15	5.94	5.05	4.07
	R_L	0.025	0.017	0.015	0.012	0.005	0.008	0.019	0.024
	R^2	0.88	0.92	0.98	0.88	0.94	0.91	0.99	0.99
	Δq	0.133	0.238	0.027	0.236	0.109	0.082	0.021	0.010
	RMSE	1.311	1.70	0.55	0.88	4.50	4.33	0.782	0.408
Freundlich	$K_F(\text{L g}^{-1})$	7.99	15.22	9.03	5.70	48.05	33.27	14.54	6.80
	$1/n$	0.24	0.35	0.30	0.22	0.21	0.16	0.42	0.42
	R^2	0.81	0.81	0.92	0.70	0.75	0.73	0.78	0.89
	Δq	0.234	0.390	0.226	0.391	0.209	0.151	0.54	0.16
	RMSE	1.65	2.78	1.14	1.41	9.54	7.28	4.20	2.01
Dubinin-Radushkevich	$q_m(\text{mg g}^{-1})$	11.47	19.61	11.47	7.57	64.36	46.54	18.48	8.75
	K_{DR}	2.20x	2.38x	4.60x	2.23x	5.0x	1.36x	2.8x	2.7x
	$(\text{mol}^2 \text{kJ}^{-2})$	10^{-8}	10^{-8}	10^{-8}	10^{-8}	10^{-8}	10^{-8}	10^{-8}	10^{-8}
	R^2	0.78	0.83	0.88	0.90	0.68	0.53	0.95	0.96
	Δq	0.252	0.581	0.367	0.243	0.291	0.394	0.029	0.018
	RMSE	1.76	2.66	1.37	0.80	10.92	9.65	1.55	0.82
Radke-Prausnitz	$q_m(\text{mg g}^{-1})$	11.47	19.78	11.07	7.57	64.36	46.88	18.49	9.72
	$K_{RP}(\text{L mg}^{-1})$	4.38	4.33	6.17	7.94	6.61	5.84	7.11	4.29
	m_{RP}	0.99	0.96	0.98	0.99	0.99	0.99	0.99	0.94
	R^2	0.92	0.94	0.98	0.89	0.94	0.91	0.98	0.98
	Δq	0.008	0.240	0.057	0.242	0.109	0.091	0.138	0.059
	RMSE	1.04	1.62	0.50	0.86	4.64	4.23	1.33	0.76
Redlich-Peterson	$K_R(\text{L g}^{-1})$	35.12	57.07	84.61	43.64	328.54	50.02	118.72	41.84
	$\alpha_R(\text{L mg}^{-1})$	2.31	1.94	7.43	4.57	4.30	0.50	6.09	4.23
	B	1.16	1.34	0.99	1.14	1.09	1.28	1.06	0.87
	R^2	0.95	0.97	0.98	0.92	0.96	0.35	0.98	0.98
	Δq	0.020	0.149	0.023	0.198	0.084	0.277	0.126	0.011
	RMSE	0.91	1.14	0.51	0.73	3.88	11.32	1.31	0.85
Langmuir-Freundlich	$q_m(\text{mg g}^{-1})$	11.01	19.22	12.45	7.47	63.35	46.79	17.13	9.71
	$K_{LF}(\text{L mg}^{-1})$	5.31	4.99	5.44	8.82	7.10	5.30	9.06	4.51
	m_{LF}	2.46	1.87	0.95	1.93	1.55	2.27	1.91	1.08
	R^2	0.93	0.99	0.99	0.96	0.98	0.96	0.98	0.98
	Δq	0.022	0.021	0.002	0.076	0.046	0.012	0.033	0.028
	RMSE	0.96	0.46	0.31	0.56	3.08	3.00	0.93	0.42

In addition, R_L , a dimensional separation factor indicated the affinity between dyes and adsorbents, was determined by the Langmuir isotherm. As shown in Table 4.3, all R_L values were smaller than 1, indicating that there were favorable adsorption processes. By using Freundlich model, the value of $1/n$ predicts the surface heterogeneity and adsorption intensity. The $0.1 < 1/n < 1$ indicates that the adsorption process is preferential and easy to perform (Duan, Hu, and Sun 2020).

Langmuir-Freundlich isotherm model can be interpreted with the exponent of the model (m_{LF}). Due to the fact that the m_{LF} value approaches to unity, there was homogeneous distribution of adsorption sites. Langmuir-Freundlich model approaches Langmuir model for MO and CR adsorption on both adsorbents. The fitted Redlich Petterson isotherm model of the MB adsorption by ZIF-8 approaches also the Langmuir model due to operating at low concentration. RhB adsorption also followed the Langmuir model. Therefore it can be said that the adsorption processes consist of a monolayer adsorption. The thickness of the adsorption layer is only single molecule. There is identical localized sites with no lateral interactions and steric barrier between the hold molecules (Vijayaraghavan et al. 2006). These adsorption processes can be evaluated as a homogenous adsorption. The constant enthalpies and homogenous activation energies of each molecule provides the same affinity to the adsorbate on the active sites (Kundu and Gupta 2006).

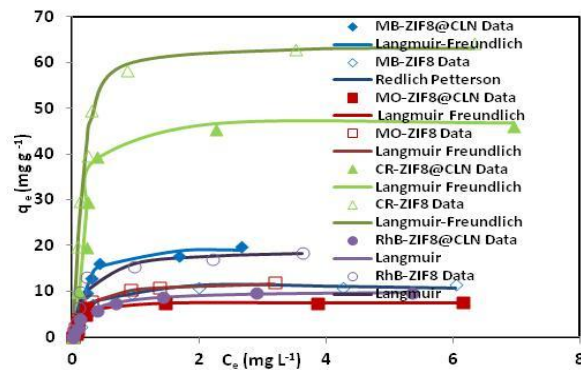


Figure 4.13. Adsorption isotherms of dyes. Experimental conditions: volume of dye solution=40 ml; Temperature 293 K; MB ($C_0 = 1.25-17.5 \text{ mg L}^{-1}$, $\text{pH}=10$, $m_{\text{ZIF-8}}=1 \text{ g L}^{-1}$, $m_{\text{ZIF-8@CLN}}=0.75 \text{ g L}^{-1}$); MO ($C_0 = 1.25-17.5 \text{ mg L}^{-1}$, $\text{pH}=4$, $m_{\text{ZIF-8}}=1.25 \text{ g L}^{-1}$, $m_{\text{ZIF-8@CLN}}=1.5 \text{ g L}^{-1}$); CR ($C_0 = 5-40 \text{ mg L}^{-1}$, $\text{pH}=4$, $m_{\text{ZIF-8}}=0.5 \text{ g L}^{-1}$, $m_{\text{ZIF-8@CLN}}=0.5 \text{ g L}^{-1}$); RhB ($C_0 = 1.25-17.5 \text{ mg L}^{-1}$, $\text{pH}=8$, $m_{\text{ZIF-8}}=0.75 \text{ g L}^{-1}$, $m_{\text{ZIF-8@CLN}}=1.25 \text{ g L}^{-1}$); Points: experimental data, Lines: suitable models.

4.2.1.3. Dyes Adsorption Kinetics

The adsorption capacity of MB, MO, CR and RhB dyes on ZIF-8 and ZIF-8@CLN were studied as a function of contact time. The MB, MO, CR and RhB adsorption of these adsorbents reached equilibrium within 100 min. The removal percentages of dyes were higher than 96 % at equilibrium time. As shown in Figure 4.14, the adsorption of dyes was rapid at the beginning, and decreased gradually approaching to equilibrium time, and then remained almost constant. The common kinetic models such as Pseudo-first-order, Pseudo-second-order, Weber-Morris intraparticle diffusion and Boyd models (Eq. 2.8-2.12) were applied to the adsorption kinetics data.

As clearly observed in Figure 4.14.(a-b), the experimental kinetic data were fitted well to the pseudo-second-order model. The kinetic parameters and error functions were listed in Table 4.4. The R^2 values for the pseudo-second-order model were highest and the error functions were lowest compared to other models. In literature, several authors have mentioned that the adsorption of MB, MO, CR and RhB by ZIF-8-based adsorbents comply with pseudo-second-order kinetic model (Ba Mohammed et al. 2021; Cao et al. 2021; Santoso et al. 2021).

According to the intraparticle diffusion model in Figure 4.14.(c-d), there are multi-linearity stages for each dyes. MB, MO and RhB have two adsorption steps, and CR has three stages. At the first stage, the removal rate was high due to the external surface adsorption or diffusion of dyes on the boundary layer. At other stages, the adsorption is slower and finally reaches equilibrium. Each portion has linearity but not to pass through the origin. It shows that the intraparticle diffusion was not the only rate controlling step, there could be other rate controlling mechanisms like ion-exchange and complexation mechanism (Vimonses et al. 2009).

The value of B_i , shown in Table 4.4, was about the internal diffusion phase and it defines the thickness of the diffusion boundary layer. The non-zero value of B_i shows that there was intraparticle diffusion during dye adsorption. However, this step was not the only rate-controlling step. The higher B_i value was attributed to the higher boundary layer thickness (Duan, Hu, and Sun 2020). As seen in Table 4.4, the B_i value reduced and the thickness of the boundary layer became shorter with the immobilization of ZIF-

8 on the CLN surface for MO, CR and RhB dyes adsorption. The inner surface adsorption became less sensitive than the outer surface adsorption after immobilization.

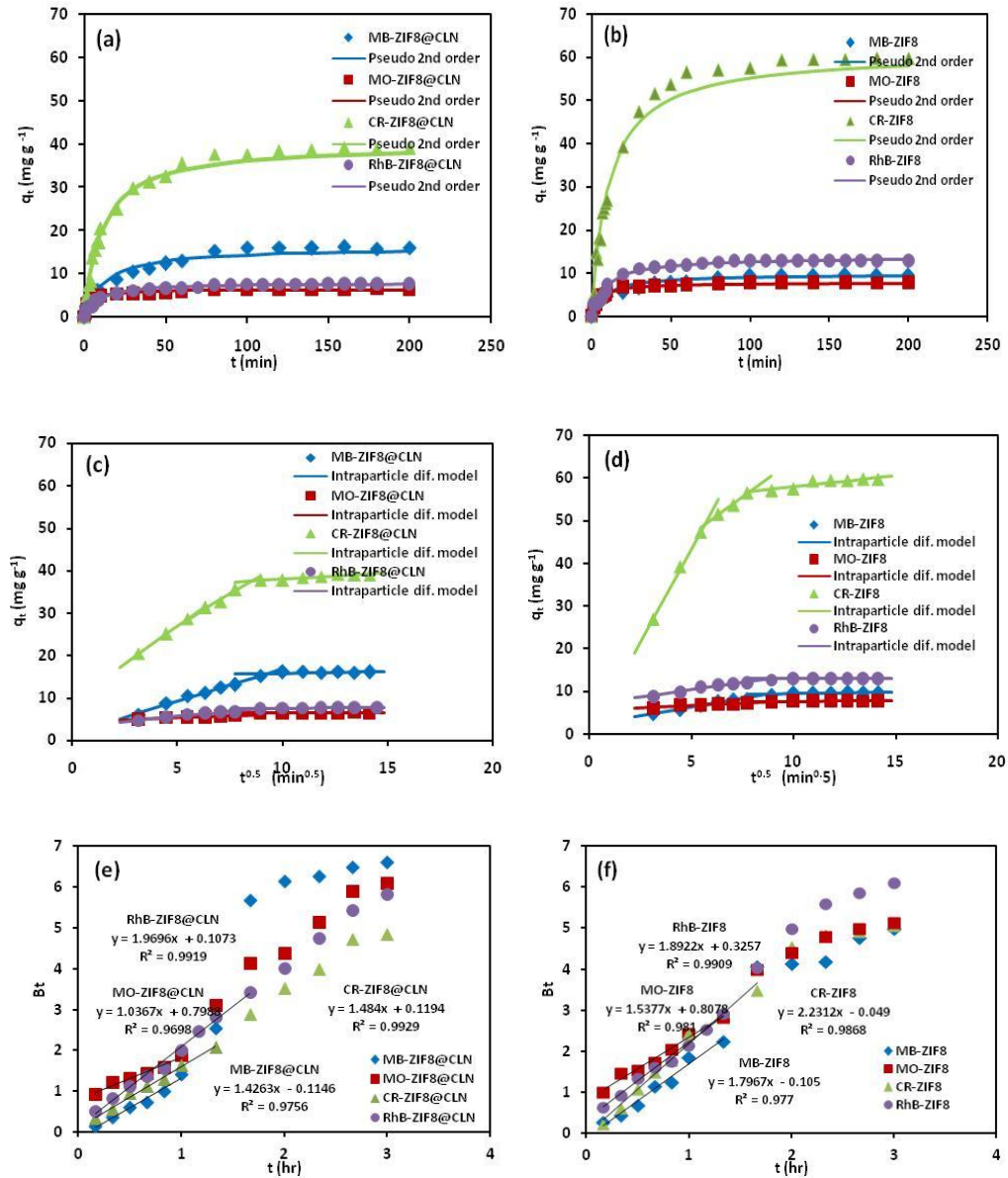


Figure 4.14. Pseudo-second-order kinetics for (a) ZIF-8@CLN, (b) ZIF-8. Intraparticle diffusion model for (c) ZIF-8@CLN, (d) ZIF-8. Boyd model for (e) ZIF-8@CLN, (f) ZIF-8. Experimental conditions: volume of dye solution=40 ml; MB ($C_0=10 \text{ mg L}^{-1}$, $m_{\text{ZIF-8}}=1 \text{ g L}^{-1}$, $\text{pH}=10$); MB ($C_0=12.5 \text{ mg L}^{-1}$, $m_{\text{ZIF-8@CLN}}=0.75 \text{ g L}^{-1}$, $\text{pH}=10$); MO ($C_0=10 \text{ mg L}^{-1}$, $m_{\text{ZIF-8}}=1.25 \text{ g L}^{-1}$, $\text{pH}=4$); MO ($C_0=10 \text{ mg L}^{-1}$, $m_{\text{ZIF-8@CLN}}=1.5 \text{ g L}^{-1}$, $\text{pH}=4$); CR ($C_0=30 \text{ mg L}^{-1}$, $m_{\text{ZIF-8}}=0.5 \text{ g L}^{-1}$, $\text{pH}=4$); CR ($C_0=20 \text{ mg L}^{-1}$, $m_{\text{ZIF-8@CLN}}=0.5 \text{ g L}^{-1}$, $\text{pH}=4$); RhB ($C_0=10 \text{ mg L}^{-1}$, $m_{\text{ZIF-8}}=0.75 \text{ g L}^{-1}$, $\text{pH}=8$); RhB ($C_0=10 \text{ mg L}^{-1}$, $m_{\text{ZIF-8@CLN}}=1.25 \text{ g L}^{-1}$, $\text{pH}=8$). Points: experimental data; lines: Pseudo-second-order kinetic model.

The Boyd plots (Bt vs t) were given in Figure 4.14.(e-f). The Boyd plots contains straight lines, however they were not passing through the origin. It indicates that the adsorption process is controlled by both the intraparticle and film diffusions or only film diffusion (Yao and Chen 2017). The slopes of lines in Figure 4.14.e gives the B values of 1.4263, 1.0367, 1.484 and 1.9696 for MB, MO, CR and RhB adsorption on ZIF8@CLN, respectively. In Figure 4.14.f, the B values of MB, MO, CR and RhB adsorption on ZIF8 were also determined as 1.7967, 1.5377, 2.2312 and 1.8922, respectively. The effective intraparticle diffusion coefficient (B) values of ZIF-8 were higher than ZIF-8@CLN for target dyes except RhB.

Table 4.4. Kinetic parameters and error functions calculated for MB, MO, CR and RhB adsorption onto ZIF-8 and ZIF8@CLN

Model	Parameter	Dyes/Adsorbents							
		MB		MO		CR		RhB	
		ZIF-8	ZIF-8@CLN	ZIF-8	ZIF-8@CLN	ZIF-8	ZIF-8@CLN	ZIF-8	ZIF-8@CLN
Pseudo-first-order	$q_{e1,cal}(\text{mg g}^{-1})$	8.94	15.29	7.91	6.53	58.11	37.22	8.70	5.75
	$k_1(\text{min}^{-1})$	0.088	0.052	0.134	0.179	0.076	0.063	0.021	0.025
	R^2	0.90	0.93	0.94	0.83	0.98	0.97	0.72	0.92
	Δq	0.049	0.112	0.015	0.042	0.061	0.050	0.557	0.481
	RMSE	0.85	1.32	0.50	0.59	2.69	2.04	4.99	2.43
Pseudo-second-order	$q_{e2,cal}(\text{mg g}^{-1})$	9.66	16.17	7.83	6.42	61.02	40.02	13.59	7.94
	$k_2(\text{g mg}^{-1}\text{min}^{-1})$	0.012	0.005	0.029	0.051	0.002	0.002	0.008	0.016
	R^2	0.97	0.97	0.98	0.96	0.99	0.99	1	1
	Δq	0.018	0.047	0.013	0.037	0.048	0.049	0.107	0.065
	RMSE	0.54	0.99	0.29	0.32	2.69	1.31	0.738	0.290
Weber-Morris intra particle diffusion	$k_{id}(\text{m g g}^{-1}\text{min}^{-1/2})$	0.608	1.135	0.397	0.713	4.269	2.715	0.713	0.381
	B_i	2.62	2.83	3.39	0.24	11.64	8.11	4.08	2.81
	R^2	0.89	0.93	0.71	0.83	0.84	0.85	0.76	0.80
	Δq	0.096	0.048	0.122	0.140	0.237	0.269	0.264	0.198
	RMSE	0.92	1.33	1.08	2.04	7.98	4.81	2.06	0.98

4.2.1.4. Dyes Adsorption Thermodynamics

The effect of temperature on MB, MO, CR and RhB adsorption by ZIF-8 and ZIF-8@CLN was studied in the range of 20-50 °C. The thermodynamic parameters

such as Gibb's free energy (ΔG°), enthalpy (ΔH°) and entropy (ΔS°) were determined by using the Eq. 2.13 - 2.16 (H. N. Tran et al. 2017).

The Van't Hoff plots were drawn (Figure 4.15) to calculate ΔH° and ΔS° values given in Table 4.5.

As shown in Table 4.5, all the ΔG° values of adsorption were negative, indicated that the adsorption processes were spontaneous and possible in this temperature range (Nguyen et al. 2022).

The positive enthalpy values for the MB adsorption on the ZIF-8 and ZIF-8@CLN (+ 3.85 and + 11.65 kJ mol⁻¹, respectively) showed that the adsorption was an endothermic process. Rising temperature may possibly cause to form of new active sites or enhance penetration of MB inside the micropores (Al-Degs et al. 2008). The negative enthalpy values for the MO adsorption on the ZIF-8 and ZIF-8@CLN (- 6.45 and - 22.90 kJ mol⁻¹, respectively) and CR adsorption on these adsorbents (- 21.45 and - 21.75 kJ mol⁻¹, respectively) and RhB adsorption (- 20.71 and - 35.60 kJ mol⁻¹, respectively) indicated that the adsorption processes were exothermic. There can be heat released during the bond creation between dyes and adsorbents (Al-Degs et al. 2008).

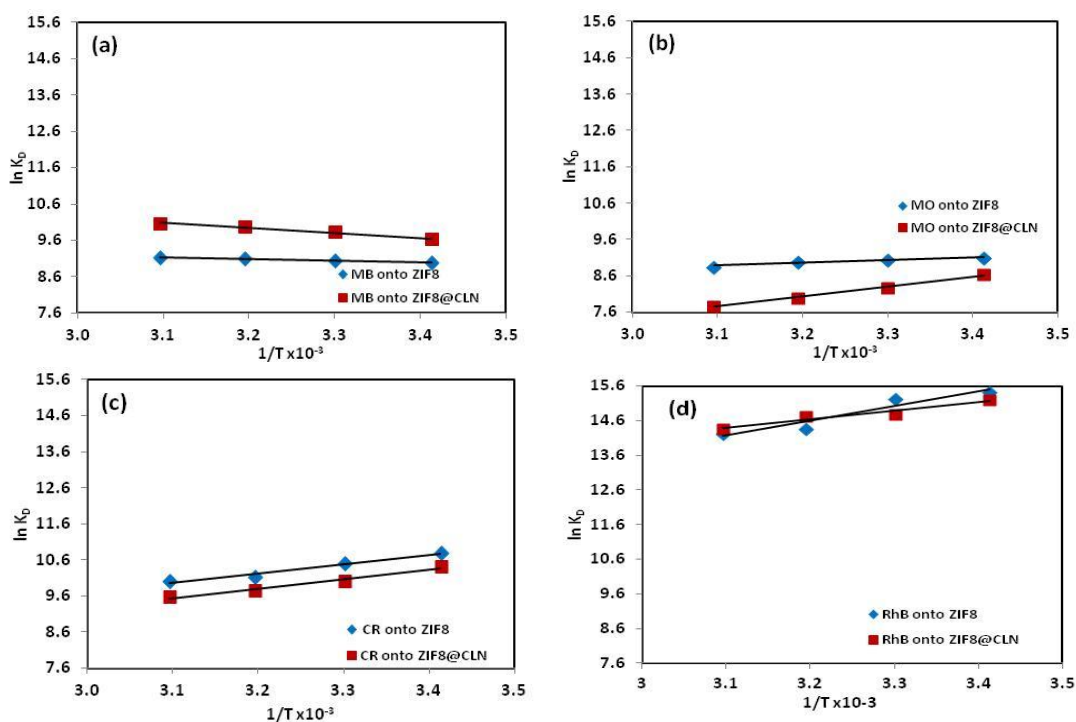


Figure 4.15. Van't Hoff plots for ΔH° and ΔS° calculations (a) MB, (b) MO, (c) CR and (d) RhB.

The endothermic MB adsorption and exothermic MO, CR and RhB adsorption processes can be observed in Figure 4.16. Additionally, the adsorption isotherms (6 different models above) of each dyes at different temperatures were studied and suitable models were presented in Figure 4.16. Besides, physical and chemical adsorption processes can be defined by the value of the enthalpy change. The calculated ΔH° values ($\Delta H^\circ < 84 \text{ kJ mol}^{-1}$) proved that the processes were physical (Yaneva, Georgieva, and Yaneva 2012). At higher temperatures, physical interactions between MO, CR or RhB and adsorbents could be weakened due to the weakening of van der Waals forces and hydrogen bonds, which causes the decreasing removal efficiency (Litefti et al. 2019).

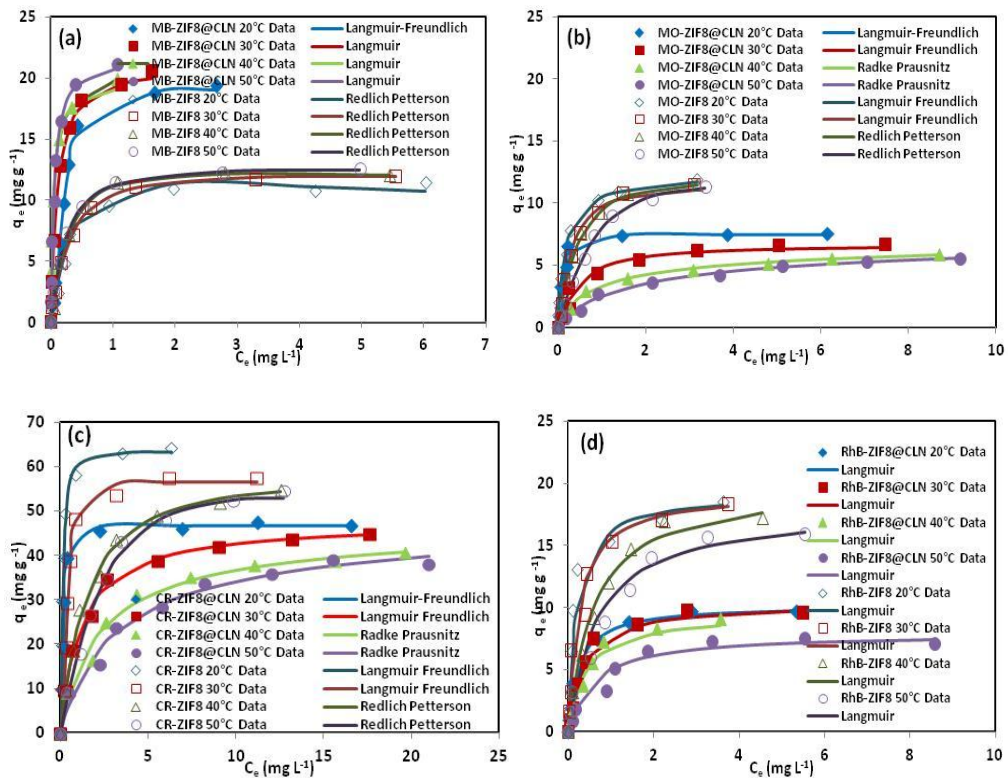


Figure 4.16. Adsorption isotherms of dyes at various temperatures (a) MB, (b) MO, (c) CR and (d) RhB. Experimental conditions: volume of dye solution=40 ml; Temperature range 20-50 °C; MB ($C_0= 1.25-17.5 \text{ mg L}^{-1}$, pH=10, $m_{\text{ZIF-8}}=1 \text{ g L}^{-1}$, $m_{\text{ZIF-8@CLN}}=0.75 \text{ g L}^{-1}$); MO ($C_0= 1.25-17.5 \text{ mg L}^{-1}$, pH=4, $m_{\text{ZIF-8}}=1.25 \text{ g L}^{-1}$, $m_{\text{ZIF-8@CLN}}=1.5 \text{ g L}^{-1}$); CR ($C_0= 5-40 \text{ mg L}^{-1}$, pH=4, $m_{\text{ZIF-8}}=0.5 \text{ g L}^{-1}$, $m_{\text{ZIF-8@CLN}}=0.5 \text{ g L}^{-1}$); RhB ($C_0= 1.25-17.5 \text{ mg L}^{-1}$, pH=8, $m_{\text{ZIF-8}}=0.03 \text{ g L}^{-1}$, $m_{\text{ZIF-8@CLN}}=1.25 \text{ g L}^{-1}$); Points: experimental data, Lines: suitable models.

In table 4.5, the positive value of ΔS° indicated that the randomness and entropy of the adsorption system was increased. There could be co-existed adsorption and desorption processes. During the adsorption of dyes, randomness was decreased. However, desorption of water would be more than adsorption of dyes, this provided positive entropy (Hussain et al. 2021; C. Chen et al. 2012). The negative value of ΔS° demonstrated that randomness and entropy was decreased during the MO adsorption by ZIF-8@CLN.

Table 4.5. Thermodynamic parameters calculated for MB, MO, CR and RhB adsorption onto ZIF-8 and ZIF-8@CLN at various temperatures.

Dyes	Adsorbents	T (K)	lnK _D	ΔG^0 (kJ mol ⁻¹)	ΔH^0 (kJ mol ⁻¹)	ΔS^0 (Jmol ⁻¹ K ⁻¹)
MB	ZIF-8	293	8.99	-21.89	3.85	87.89
		303	9.05	-22.80		
		313	9.09	-23.66		
		323	9.14	-24.53		
	ZIF-8@CLN	293	9.63	-23.46	11.65	119.98
		303	9.83	-24.76		
		313	9.98	-25.97		
		323	10.07	-27.04		
MO	ZIF-8	293	9.11	-22.19	-6.45	53.84
		303	9.03	-22.76		
		313	9.00	-23.42		
		323	8.84	-23.75		
	ZIF-8@CLN	293	8.65	-21.07	-22.90	-6.51
		303	8.27	-20.84		
		313	7.99	-20.80		
		323	7.78	-20.88		
CR	ZIF-8	293	10.78	-26.26	-21.45	16.30
		303	10.50	-26.44		
		313	10.12	-26.35		
		323	10.00	-26.85		
	ZIF-8@CLN	293	10.41	-25.36	-21.75	11.88
		303	10.00	-25.20		
		313	9.74	-25.36		
		323	9.58	-25.73		
RhB	ZIF-8	293	15.43	-37.60	-20.71	55.51
		303	15.25	-38.41		
		313	14.36	-37.37		
		323	14.22	-38.19		
	ZIF-8@CLN	293	15.22	-37.07	-35.60	7.45
		303	14.79	-37.27		
		313	14.73	-38.32		
		323	14.36	-38.57		

4.2.1.5. Reusability

An adsorbent can be cost effective when it is used repeatedly after elution. The removal of MB, MO, CR and RhB dyes by using the ZIF-8 and ZIF-8@CLN adsorbents was investigated after elution with ethanol. There was a slight change in the removal percentages of the dyes after four consecutive adsorption cycles. The removal efficiencies of the ZIF-8 after fourth cycle for MB, MO, CR and RhB were found to be 94.0%, 90.2%, 85.1% and 81.52% respectively (Figure 4.17). Meanwhile, after fourth cycle, the removal efficiencies of ZIF-8@CLN for MB, MO, CR and RhB were 75.2%, 82.0%, 82.7% and 66.74%, respectively. These decreases in removal efficiencies can be based on the blockage of active sites of the adsorbents (El-Sewify et al. 2022). The adsorption capacity versus time curves of MB, MO, CR and RhB adsorptions for four consecutive cycles were presented in Figure A.1 and Figure A.2. Additionally, the characteristic ATR-IR peaks of adsorbents maintained well after dye adsorption (Figure 4.18- 4.22), it indicated that the stability of the adsorbents were appropriate to reuse.

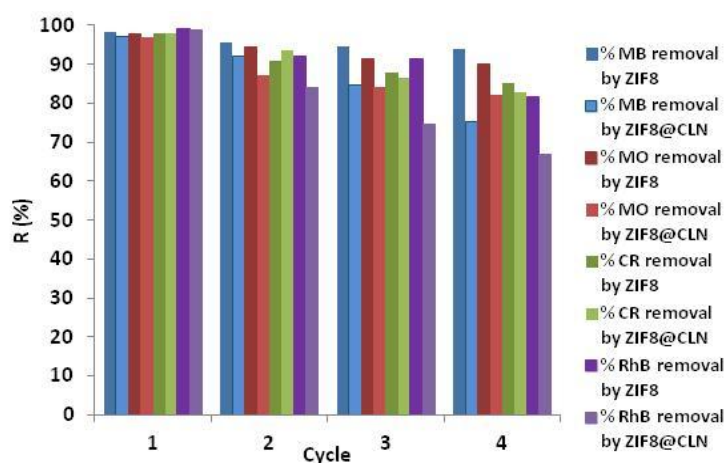


Figure 4.17. The removal efficiencies of MB, MO, CR and RhB for four consecutive cycles. Experimental conditions: volume of dye solution=40 ml; MB ($C_0=10 \text{ mg L}^{-1}$, $m_{\text{ZIF-8}}=1 \text{ g L}^{-1}$, $\text{pH}=10$); MB ($C_0=12.5 \text{ mg L}^{-1}$, $m_{\text{ZIF-8@CLN}}=0.75 \text{ g L}^{-1}$, $\text{pH}=10$); MO ($C_0=10 \text{ mg L}^{-1}$, $m_{\text{ZIF-8}}=1.25 \text{ g L}^{-1}$, $\text{pH}=4$); MO ($C_0=10 \text{ mg L}^{-1}$, $m_{\text{ZIF-8@CLN}}=1.5 \text{ g L}^{-1}$, $\text{pH}=4$); CR ($C_0=30 \text{ mg L}^{-1}$, $m_{\text{ZIF-8}}=0.5 \text{ g L}^{-1}$, $\text{pH}=4$); CR ($C_0=20 \text{ mg L}^{-1}$, $m_{\text{ZIF-8@CLN}}=0.5 \text{ g L}^{-1}$, $\text{pH}=4$); RhB ($C_0=10 \text{ mg L}^{-1}$, $m_{\text{ZIF-8}}=0.75 \text{ g L}^{-1}$, $\text{pH}=8$); RhB ($C_0=10 \text{ mg L}^{-1}$, $m_{\text{ZIF-8@CLN}}=1.25 \text{ g L}^{-1}$, $\text{pH}=8$).

4.2.1.6. Dyes Adsorption Mechanism

The adsorption mechanism of target dyes (MB, MO, CR and RhB) on the ZIF-8 and ZIF-8@CLN surface can be controlled by various ways, such as electrostatic interactions, π - π stacking interactions, hydrogen bonding, metal coordination and ion exchange (Ba Mohammed et al. 2021; Santoso et al. 2021). The possible adsorption mechanisms for each dye and the ATR-IR spectra of ZIF-8 and ZIF8@CLN before and after dye adsorption were shown in Figure 4.18 - 4.22. These figures indicated some changes of the ATR-IR bands after adsorption of the dyes.

The order of adsorption capacities of ZIF-8@CLN for the dyes is CR>MB>RhB>MO. The order of adsorption capacities for ZIF-8 is also as CR>RhB>MO>MB due to the various interactions between the dyes and the adsorbents. The adsorption performance of ZIF-8@CLN is higher than ZIF-8 for MB dye. Because, CLN has cations in its interconnected cages. The ion exchange can be significant mechanism between the cations in CLN and the cationic MB dyes. However, the adsorption performance of ZIF-8@CLN is lower for the MO, CR and RhB dyes. Although the adsorption capacities of the other dyes decreased some amount, ZIF-8@CLN has some important advantages compared to pure ZIF-8 such as easy separation from water phase, lower treatment cost, inexpensiveness, inhibition of ZIF-8 particle agglomeration. The ZIF-8@CLN is much more practicable and cheap compared to pristine ZIF-8.

After adsorption of MB, MO and CR, there were bands at around 3670 cm^{-1} , which attributed to O-H and N-H vibrational bands based on the formed hydrogen bridges or hydrogen bonds between the dyes and adsorbents (Xia et al. 2019). In each adsorption process, there is π - π stacking interaction between the 2-methyl imidazole ring and the aromatic compounds of these dyes (Figure 4.19 - 4.22).

In Figure 4.19, the increase intensity of the absorption bands at 1584 cm^{-1} and 1145 cm^{-1} that were attributed to the vibrational bands of N-H, and shifting at 1300 cm^{-1} band, indicated the aromatic peaks of MB (Ainane et al. 2014). The adsorption band at 953 cm^{-1} attributed to the S-N interaction between MB and ZIF-8 (Santoso et al. 2021). There could be donor-acceptor electrostatic interactions between MB and ZIF-8 due to the attraction between the lone pair of nitrogen in ZIF-8 and the electron deficient sulfur

and nitrogen in MB, shown in Figure 4.19 (Santoso et al. 2021; Ainane et al. 2014). In these MB adsorption process, Zn^{2+} behaves as the metal *coordination* centre. There could be also the ion exchange between the positively charged MB and Na^+ or Ca^{2+} in CLN channels.

After MO adsorption (Figure 4.20), the rising intensity at 1586 cm^{-1} demonstrated the C=N stretching vibration on imidazole ring of ZIF-8 (Chakraborty, Islam, and Acharya 2019). The electrostatic interaction occurred between the negatively charged sulfonic acid group of MO and the positively charged groups (Zn^{2+} , Na^+ , Ca^{2+}) of ZIF-8@CLN, shown in Figure 4.20. The metal coordination is observed due to the Zn^{2+} . The peak at 829 cm^{-1} showed the π - π interactions between the MO and the adsorbents. The intensity of the peak at 757 cm^{-1} decreased and shifted, which assigned to the aromatic C-H bending (Jia et al. 2020).

Meanwhile, shown in Figure 4.21, after CR adsorption, there was a band at 1094.0 cm^{-1} , which is corresponded to S=O stretching vibration based on CR adsorption (Cao et al. 2021). At solution pH of 4, the negatively charged sulfonic acid group of CR caused the electrostatic interaction with the positively charged groups of ZIF-8@CLN (amino, Zn^{2+} , Na^+ , Ca^{2+}). The Zn^{2+} of ZIF-8@CLN provided the metal *coordination* mechanism. The characteristic peak at 1590 cm^{-1} was attributed to C=C stretching vibration. CR adsorption strengthened the C-C peaks at 1381 cm^{-1} . The peak at 513 cm^{-1} was corresponded to Zn-O bond (Cao et al. 2021). After CR adsorption, the intensity of Zn-N peak at 429 cm^{-1} weakened, showed that the ZIF-8 hydrolyzed partially and Zn-N cracked. The imidazole ring was protonated and hydroxyl group coordinated the Zn (Cao et al. 2021; Zhang et al. 2019).

As seen in Figure 4.22, the peak at 1578 cm^{-1} that shows the C=N stretching vibrations of imidazole in ZIF-8 shifted to 1583 cm^{-1} after adsorption of RhB, which attributed that there could be hydrogen bonding interaction between the RhB dye and ZIF-8. The negatively charged carboxylic acid of RhB attracted the positively charged groups of ZIF-8@CLN through electrostatic interaction, shown in Figure 4.22. The ion exchange can be carried out between the positively charged RhB and the Na^+ or Ca^{2+} in CLN channels. There is also the metal coordination mechanism around the Zn^{2+} . There are shifts for the peaks in ATR-IR spectra representing C-N stretching from 1450 to 1466 cm^{-1} and 1140 to 1149 cm^{-1} , after adsorption (Chakraborty, Islam, and Acharya 2019). The peak at 831 cm^{-1} indicates the aromatic ring stretching of RhB (Anh Tran et al. 2021), which proves the π - π interaction between the π -electrons of RhB and ZIF-8.

The intensity of the peaks at 755 cm^{-1} (the aromatic C-H bending (Jia et al. 2020)) decreased and shifted to 763 cm^{-1} , and the peak at 685 cm^{-1} shifted to 680 cm^{-1} after adsorption, which indicates the attachment of RhB on ZIF-8.

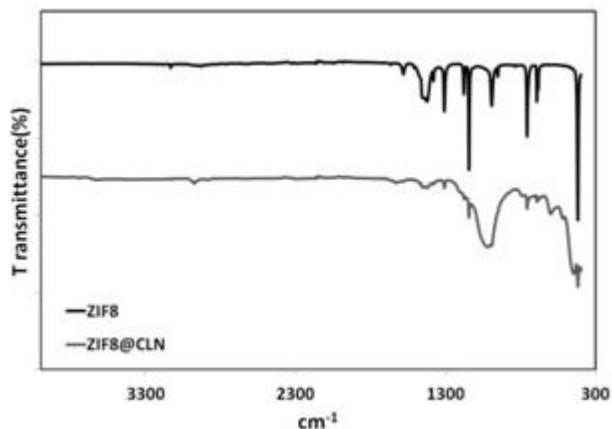


Figure 4.18. ATR-IR spectra of ZIF-8 and ZIF-8@CLN before adsorption.

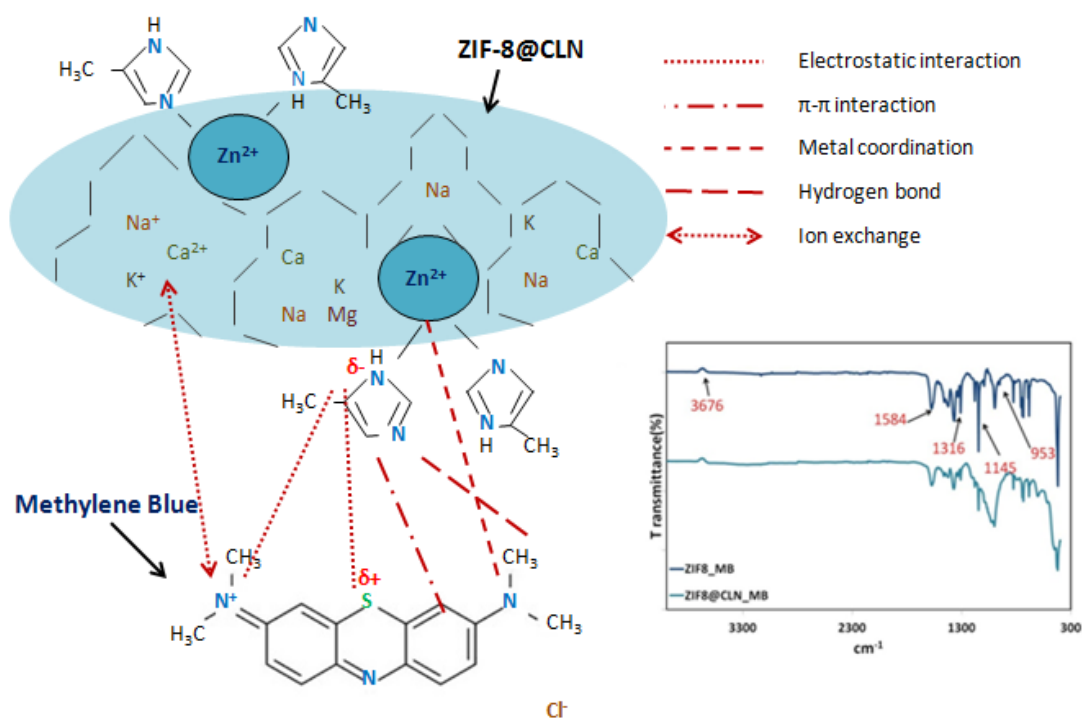


Figure 4.19. Possible mechanism for MB adsorption on ZIF-8@CLN and ATR-IR spectra of ZIF-8 and ZIF-8@CLN after MB adsorption.

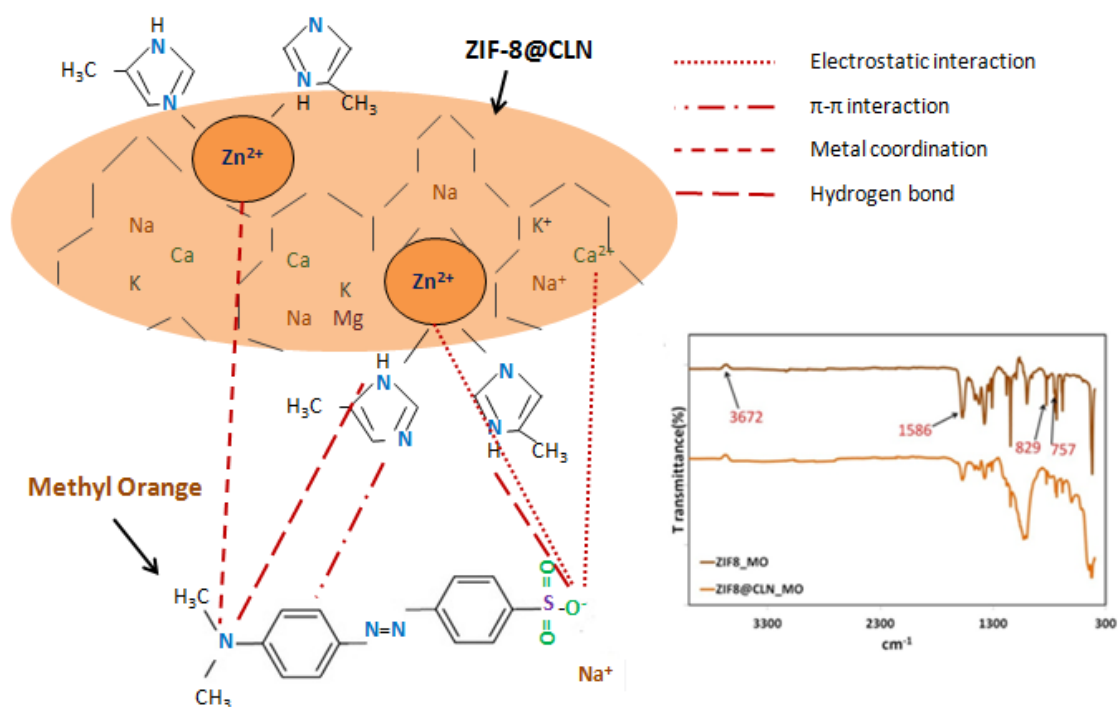


Figure 4.20. Possible mechanism for MO adsorption on ZIF8@CLN and ATR-IR spectra of ZIF-8 and ZIF-8@CLN after MO adsorption.

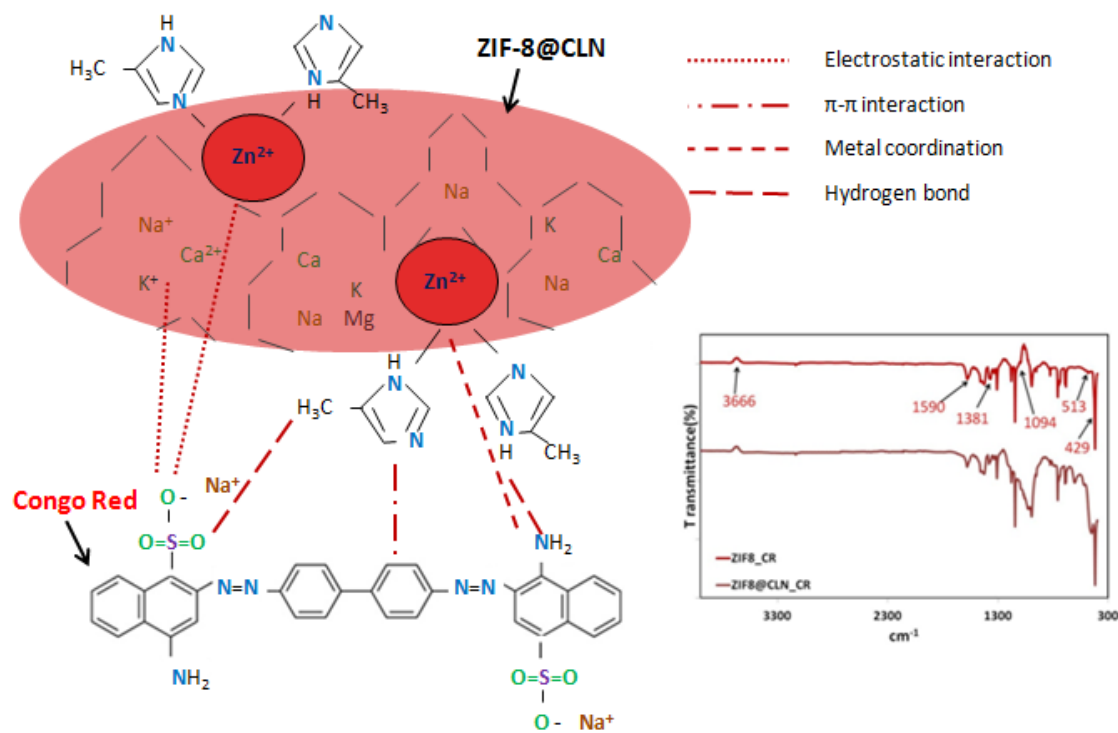


Figure 4.21. Possible mechanism for CR adsorption on ZIF8@CLN and ATR-IR spectra of ZIF-8 and ZIF-8@CLN after CR adsorption.

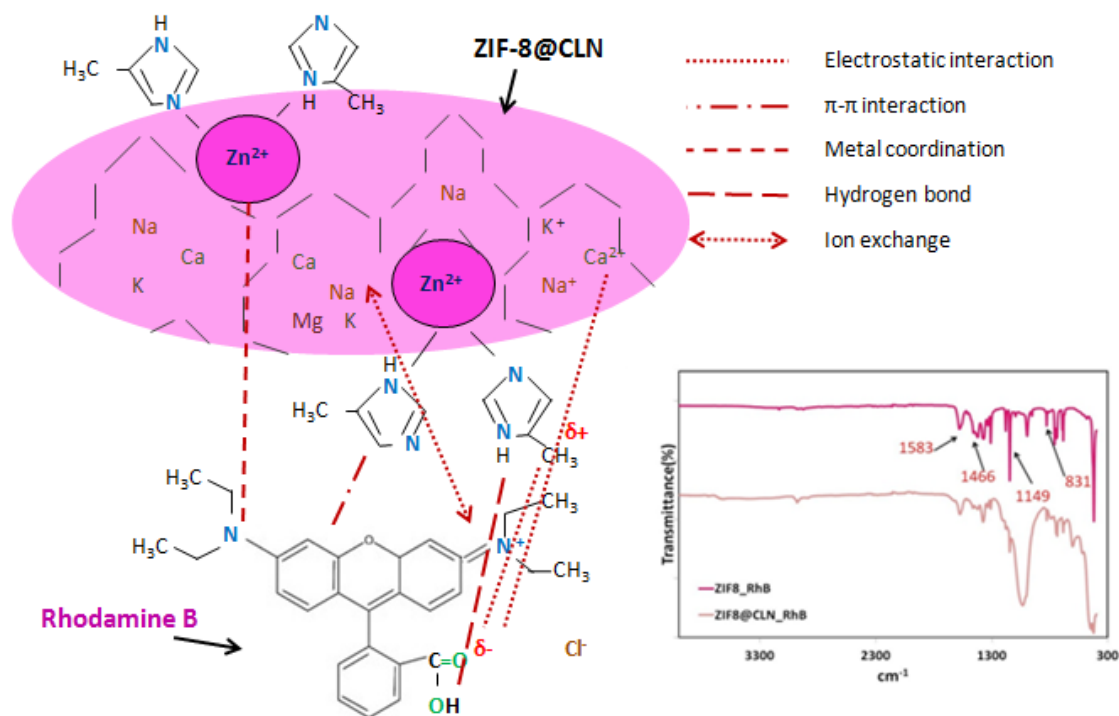


Figure 4.22. Possible mechanism for RhB adsorption on ZIF8@CLN and ATR-IR spectra of ZIF-8 and ZIF-8@CLN after RhB adsorption.

4.2.2. Adsorption of Tetracycline

The adsorption properties of ZIF-8 and ZIF8@CLN were also investigated for tetracycline removal from aqueous solution.

4.2.2.1. TC Adsorption Parameter

In Figure 4.23, the effect of initial pH on adsorption of TC was investigated and a series of experiments were performed with pH values varying from 2 to 12. The pH shows the significant role that affects the adsorption performance by changing the ionizing degree of the adsorbate and altering the surface charge of the adsorbents.

Tetracycline is an amphiphilic molecule, which has multiple ionizable functional groups (Yang et al. 2021). TC can present in cationic, zwitterionic, and anionic form due to the possessing of three different pK_a values (acid dissociation constants) of 3.3, 7.7 and 9.7 (Gao et al. 2012). In other words, different ionic species of TC exist at different pH values. When the pH of solution is below 3.3, TC presents as a cation (TCH_3^+), attributed to existence of dimethyl-ammonium (C4) group. When solution pH is between 3.3 and 7.7, TC presents as a zwitterion (TCH_2°), corresponding to the proton loss from the phenolic diketone moiety (C10-C12) (Li et al. 2010). Additionally, when solution pH is greater than 7.7, TC presents as an anion (TCH^- or TC^{2-}), corresponding to deprotonation of the tricarbonyl system (C1-C3) (Mirsoleimani-Azizi et al. 2018).

ZIF-8 has the PZC of 9.8 (Wu et al. 2015). The TC adsorption on the ZIF-8 and ZIF8@CLN was dependent on the pH. As shown in Figure 4.23, the adsorption capacity of the ZIF-8 and ZIF8@CLN grown up first and afterthat fell down with the increasing pH. When $2 < pH < 3.3$, there was the deprotonation of TC and a lot of positive charges aggregated on the adsorbent surface. This caused the electrostatic repulsion between the cationic TC molecule and the positively charged adsorbents, resulted in lower adsorption of TC (Yang et al. 2021). In this range, the removal can be attributed to the intermolecular π - π interactions between TC and ZIF-8 (Mirsoleimani-Azizi et al. 2018).

When $3.3 < pH < 7.53$ with rising of the pH, the surface of ZIF-8 and ZIF8@CLN was still positively charged. The zeta potential of the adsorbents gradually reduced, meanwhile, the TC molecules were deprotonated. Therefore, the electrostatic repulsion was weakened, provided to the increasing adsorption capacity. When the $7.53 < pH < 9.8$, the adsorption capacity was also high. The highest adsorption capacities were obtained 93.81% and 97.08% at $pH = 8$ for ZIF-8 and ZIF8@CLN, respectively. Therefore, the subsequent experiments were conducted at $pH = 8$. The ZIF-8 and ZIF8@CLN indicated very high adsorption capacities for TC in the large range of 4.0-10.0, which can be corresponding to the electrostatic interaction between positively charged ZIF-8 and ZIF8@CLN and zwitterionic TC. However, when the $9.8 < pH < 12$, the surface of ZIF-8 and ZIF8@CLN were negatively charged. At $pH=12$, the alkalinity increased and the adsorption capacities reduced sharply. There could be the degradation of ZIF-8 skeleton at $pH=12$ due to extreme alkalinity conditions (Yang et al. 2021). In short, electrostatic interactions gain significant role in adsorption mechanism.

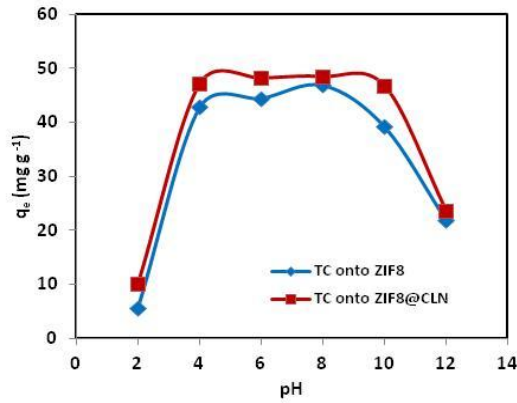


Figure 4.23. Effect of pH on TC adsorption. Experimental conditions: volume of TC solution=40 ml; pH range 2-12; $C_0=50\text{ mg L}^{-1}$, $m_{\text{ads}}=1\text{ g L}^{-1}$.

The effect of the adsorbent amount on TC removal indicated in Figure 4.24. The removal efficiencies rised with increasing in the ZIF-8 and ZIF8@CLN amount up to a certain limit of 1 g L^{-1} . The reason is that the presence of more active sites exposed to the TC molecules. On the other hand, further rising in the adsorbent amount caused to the decrease of the removal efficiency. The reduce of the adsorption efficiency after 1 g L^{-1} could be attributed to the aggregation of the adsorbent particles that led to diminish of the total active sites (Mirsoleimani-Azizi et al. 2018). Additionally, the higher adsorbent amount reduces the homogeneous distribution of the adsorbent. It causes the adsorption resistance.

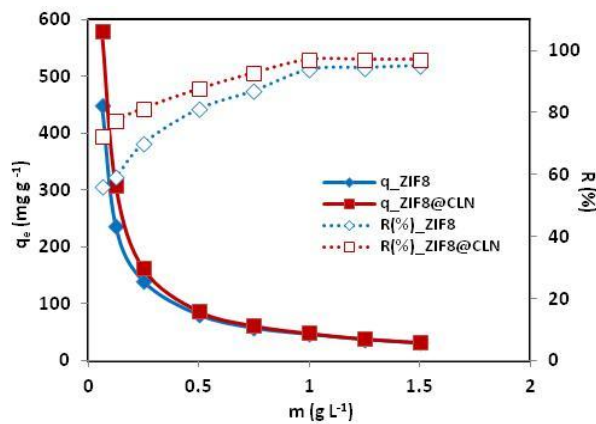


Figure 4.24. Effect of adsorbent amount on TC adsorption. Experimental conditions: volume of TC solution=40 ml; adsorbent amount range $0.0625\text{-}1.5\text{ g L}^{-1}$; $C_0=50\text{ mg L}^{-1}$; pH=8.

The initial TC concentration is the driving force that overcomes the mass transfer resistance resulted from the all molecules between the TC and the adsorbents. Thus, the effect of initial TC concentration on the adsorption capacities of ZIF-8 and ZIF8@CLN were examined. As shown in Figure 4.25, the adsorption capacities of the adsorbents considerably enhanced by increasing of initial TC concentration. In the concentrated solution, there was a higher adsorption driving force. However, in a lower initial TC concentration, removal efficiencies were higher. Because, there were favorable active sites on the sorbent surface for lower amounts of the TC species (Mirsoleimani-Azizi et al. 2018). Therefore, TC adsorption efficiencies were decreasing after 60 ppm, as the adsorption capacities were still increasing.

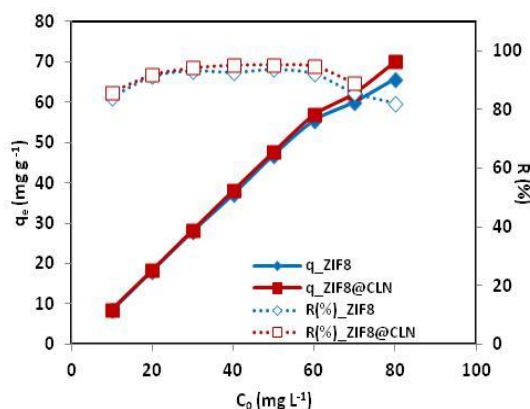


Figure 4.25. Effect of TC concentration. Experimental conditions: volume of TC solution=40 ml; $C_0= 10-80 \text{ mg L}^{-1}$, pH=8, $m_{\text{adsorbent}}=1 \text{ g L}^{-1}$.

The effect of ionic strength (NaCl) on TC adsorption was investigated with initial pH between 2-12 (Figure 4.26). The adsorption capacity of TC by ZIF-8 and ZIF8@CLN slightly reduced with increasing NaCl concentration from 0.05 M to 0.2 M. When the NaCl concentration was 0.2 M, the adsorption capacities reduced slightly from 46.90 mg g^{-1} to 41.86 mg g^{-1} for ZIF-8 and from 48.54 mg g^{-1} to 42.52 mg g^{-1} for ZIF-8@CLN.

The hydrophobic interactions and the electrostatic force between TC molecules and ZIF-8 or ZIF8@CLN could be changed due to the ionic strength. Some active sites could be neutralized with adding NaCl, and there can be reduction in the electrostatic interaction between the adsorption sites and TC. Additionally, the hydrophobic action

was generally increased. The thickness of ZIF-8 or ZIF8@CLN surface electric double layer was compressed with higher NaCl concentration. The decrease in electrostatic force between TC and the adsorbents was the main reason to reduce the TC adsorption capacity. Meanwhile, there was an adsorption competition between TC and NaCl. The NaCl molecule covered many adsorption sites on ZIF-8 and ZIF8@CLN, which decreased the adsorption efficiency (Duan, Hu, and Sun 2020).

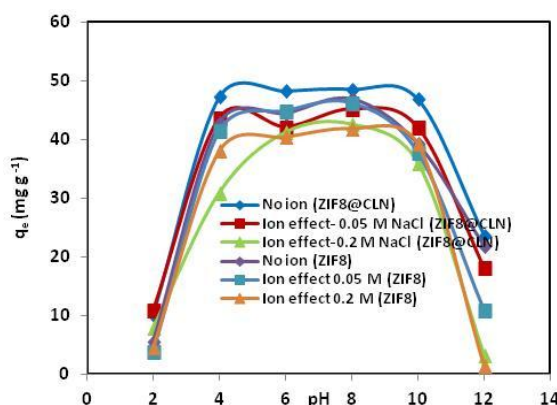


Figure 4.26. Effect of ionic strength on TC adsorption. Experimental conditions: volume of TC solution=40 ml; pH range 2-12; $C_0=50 \text{ mg L}^{-1}$, $m_{\text{adsorbent}}=1 \text{ g L}^{-1}$.

4.2.2.2. TC Adsorption Isotherms

The Langmuir, Freundlich, Dubinin-Radushkevich, Radke-Prausnitz, Redlich-Peterson and Langmuir-Freundlich isotherm models (Eq. 2.1 – 2.7) were applied to explain the adsorption process of TC by ZIF-8 and ZIF8@CLN. The best fitting model and the isotherm parameters were indicated in Figure 4.27 and Table 4.6.

Among these models, the Langmuir-Freundlich isotherm model showed the largest R^2 (0.97 and 0.97), the smallest Δq (0.06 and 0.05) and the smallest RMSE (3.31 and 3.46), for ZIF8 and ZIF8@CLN respectively, revealing that the adsorption process includes both Langmuir and Freundlich behaviour with heterogeneous system. According to the fitted model, the TC adsorption capacities of ZIF-8@CLN and ZIF-8 were 64.57 ± 5.0 and $63.0 \pm 6.1 \text{ mg g}^{-1}$, respectively. As shown in Table 4.6, both R_L values were lower than 1, showing that the adsorption processes were favorable. The

range of $0.1 < 1/n < 1$ generally shows that the adsorption process is preferential and the adsorption process of TC on ZIF-8 and ZIF8@CLN was easy to perform.

Table 4.6. Isotherm parameters and error functions for TC adsorption on ZIF-8 and ZIF-8@CLN.

Model	Parameter	ZIF-8	ZIF8@CLN
Langmuir	q_m (mg g ⁻¹)	65.72	75.41
	K_L (L mg ⁻¹)	0.39	0.43
	R_L	0.17	0.19
	R^2	0.73	0.71
	Δq	0.21	0.30
	RMSE	8.99	11.05
Freundlich	K_F (L g ⁻¹)	20.62	22.97
	$1/n$	0.47	0.51
	R^2	0.75	0.71
	Δq	0.25	0.28
	RMSE	9.56	10.90
Dubinin-Radushkevich	q_m (mg g ⁻¹)	65.61	70.10
	K_{DR} (mol ² kJ ⁻²)	9.62×10^{-7}	7.21×10^{-7}
	R^2	0.95	0.90
	Δq	0.09	0.15
	RMSE	3.86	6.58
Radke Prausnitz	q_m (mg g ⁻¹)	65.78	70.11
	K_{RP} (L mg ⁻¹)	0.33	0.38
	m_{RP}	0.96	0.84
	R^2	0.75	0.76
	Δq	0.14	0.27
	RMSE	9.73	9.94
Redlich Peterson	K_R (L g ⁻¹)	13.99	17.87
	α_R (L mg ⁻¹)	0.013	0.011
	β	1.923	2.185
	R^2	0.89	0.82
	Δq	0.19	0.25
	RMSE	6.42	8.68
Langmuir-Freundlich	q_m (mg g ⁻¹)	63.0	64.57
	K_{LF} (L mg ⁻¹)	0.42	0.54
	m_{LF}	3.20	5.37
	R^2	0.97	0.97
	Δq	0.06	0.05
	RMSE	3.31	3.46

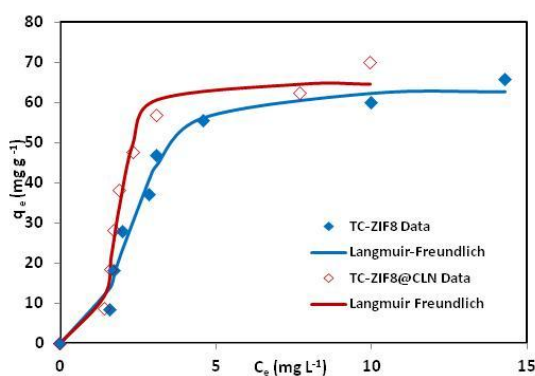


Figure 4.27. Suitable adsorption isotherm models of TC on ZIF-8 and ZIF-8@CLN. Experimental conditions: volume of TC solution=40 ml, $C_0=10-80$ mg L⁻¹, pH=8, $m_{\text{adsorbent}}=1$ g L⁻¹.

4.2.2.3. TC Adsorption Kinetics

The kinetic study of TC removal by ZIF-8 and ZIF8@CLN were illustrated in Figure 4.28. The kinetic parameters were given in Tables 4.7 and a comparison of Pseudo first-order, Pseudo second-order and intraparticle diffusion models demonstrated that the R^2 of the Pseudo second-order kinetics model (>0.98) was higher than the others with the lower Δq and less RMSE value. It was seen in Figure 4.28.a that Pseudo second-order kinetics fitted well for the adsorption of TC on ZIF-8 and ZIF8@CLN.

The curve of Weber-Morris intra-particle diffusion model was given in Figure 4.28.b. It showed that the adsorption process contained three distinct stages. The curve (q_t and $t_{1/2}$) was not pass via the origin, showing that the intraparticle diffusion could not be the only rate control step (Moral-Rodríguez et al. 2016). The largest slope of the first stage was corresponding to the outer surface adsorption. The reduced slope was attributed to the reduced diffusion rate and the adsorption on the inner surface. The third stage demonstrated the adsorption equilibrium, where the inner surface active sites of the adsorbents achieved the equilibrium. The concentration gradient of TC was poor at the solution and the rate limiting step was not longer internal diffusion rate (Duan, Hu, and Sun 2020).

As seen in Table 4.7, the value of B_i was not zero, which indicated that there was intraparticle diffusion during process, however, this step was not the only rate-controlling one. The B_i was about the internal diffusion phase and it indicated the thickness of the diffusion boundary layer. The higher B_i value was based on the higher boundary layer thickness (Duan, Hu, and Sun 2020). As seen in Table 4.7, the B_i value rised and the thickness of the boundary layer became larger with the immobilization of ZIF-8 on the CLN surface. It can be explained that the inner surface adsorption became more sensitive than the adsorption of outer surface after immobilization process.

The Boyd plots (Bt vs t) were illustrated in Figure 4.28.c. The Boyd plots included straight lines which were not pass through the origin. There can be only film diffusion or existing both intraparticle and film diffusions (Yao and Chen 2017). The B values of 1.0426 and 1.3563 for TC adsorption on ZIF-8 and ZIF8@CLN, respectively, determined by the slopes of lines in Figure 4.28.c. The effective intraparticle diffusion coefficient (B) value of ZIF-8@CLN was higher than ZIF-8 for TC.

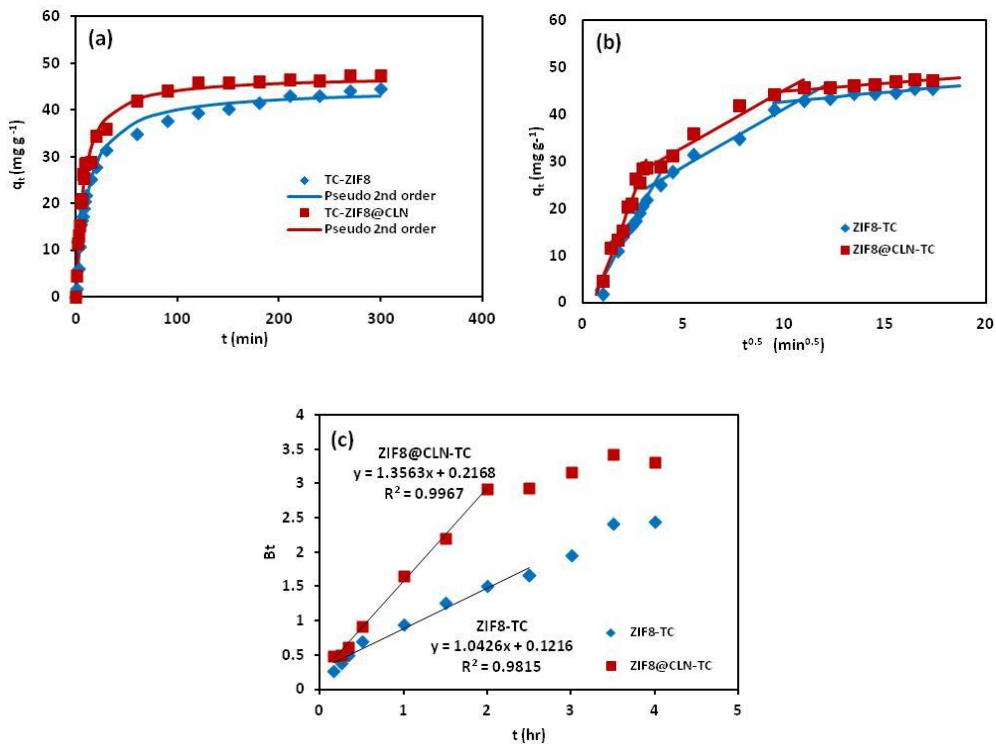


Figure 4.28. Kinetics model, (a) Pseudo-second-order kinetics, (b) Intraparticle diffusion model, (c) Boyd model. Experimental conditions: volume of TC solution=40 ml, $C_0= 50 \text{ mg L}^{-1}$, $m_{\text{adsorbent}}=1 \text{ g L}^{-1}$, pH= 8. Points: experimental data; lines: kinetic model.

Table 4.7. Kinetic parameters and error functions for TC adsorption on ZIF-8 and ZIF-8@CLN.

Model	Parameter	ZIF-8	ZIF8@CLN
Pseudo-first-order	$q_{e1,cal}$ (mg g^{-1})	40.64	44.57
	k_1 (min^{-1})	0.072	0.100
	R^2	0.95	0.95
	Δq	0.07	0.03
	RMSE	2.84	3.05
Pseudo-second-order	$q_{e2,cal}$ (mg g^{-1})	44.57	47.34
	k_2 ($\text{g mg}^{-1} \text{min}^{-1}$)	0.002	0.003
	R^2	0.98	0.99
	Δq	0.05	0.01
	RMSE	1.75	1.39
Weber-Morris intraparticle diffusion	k_i ($\text{mg g}^{-1} \text{min}^{-1/2}$)	2.255	2.169
	B_i	11.21	16.72
	R^2	0.86	0.83
	Δq	0.37	0.16
	RMSE	4.96	5.92

4.2.2.4. Reusability

Figure 4.29 indicated that the synthesized adsorbents still showed high adsorption capacities after four cycles, showing the novel adsorbent (ZIF8@CLN) performed excellent reusability and stability. The adsorption capacities of ZIF-8 and ZIF8@CLN after four cycles were 85.12 % and 86.69 %, respectively. The adsorption capacities of the synthesized adsorbents slightly diminished after four cycles, which could be depend on the loss of some adsorption sites with the recovery process.

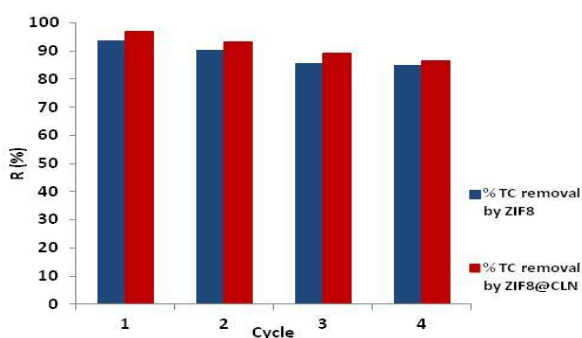


Figure 4.29. The adsorption efficiencies of TC for four consecutive cycles. Experimental conditions: volume of TC solution=40 ml; $C_0=50 \text{ mg L}^{-1}$, $m_{\text{adsorbent}}=1 \text{ g L}^{-1}$, pH= 8.

Moreover, the characteristic ATR-IR peaks of adsorbents maintained well after TC adsorption (Figure 4.30), it showed that the stability of the adsorbents were appropriate to reuse. This study indicated that ZIF-8 and the novel composite ZIF8@CLN are promising for TC adsorption.

4.2.2.5. TC Adsorption Mechanism

The possible adsorption mechanism of TC on ZIF-8 and ZIF8@CLN and the ATR-IR spectrum of the adsorbents after TC adsorption were illustrated in Figure 4.30. In order to compare of before and after adsorption, the ATR-IR spectra of ZIF-8 and ZIF-8@CLN before adsorption of TC was given in Figure 4.18. It was seen that the peak in the range of 3100-3700 cm^{-1} was very weak, indicating the hydrogen bonds were not dominant effect. However, some of the N-sites of the ZIF-8 could interact with the carbonyl and hydroxyl of the TC due to the hydrogen bond (Yang et al. 2021).

The peak at 1592 cm^{-1} increased and moved to 1585 cm^{-1} after TC adsorption, which was corresponding to the π - π stacking interaction, showed in Figure 4.30 (Sheng et al. 2022). In other words, the band at 1585 cm^{-1} indicated that the adsorbents contain characteristic peak of C=C aromatic carbon, which was grown after adsorption, showing that the π - π interaction between TC and ZIF-8@CLN was a significant adsorption mechanism (D. Liu et al. 2023). The conjugated benzene ring of the TC structure and the imidazole ring of ZIF-8 and ZIF8@CLN can interact with each other via π - π interactions (Yang et al. 2021).

Furthermore, compared with the ZIF8@CLN before adsorption, the peaks located at 2929 and 1450 cm^{-1} were observed in the ZIF8@CLN after adsorption, which demonstrated the anti-symmetric stretching vibration of -CH₃ groups and the skeleton vibration of the benzene ring of TC, respectively. These proofs showed that the TC molecules were adsorbed on ZIF8@CLN surface successfully. There can be also the surface complexation between the electron-defect sites of the ZIF-8 and ZIF8@CLN and the amide, hydroxy and carbonyl groups (the electron-rich O-including groups) in the TC molecule (Figure 4.30) (Yang et al. 2021).

From the pH effect analysis, adsorption capacities of the adsorbents were the best at the pH of 8, which indicated the electrostatic interaction between TC and synthesized adsorbents. The electrostatic interaction between the functional groups of TC and ZIF-8@CLN were illustrated in Figure 4.30. The three different pK_a values of TC affect the form of TC molecules as explained before. At pH 8, the negatively charged of the electron-rich-O-including groups of TC attracted to the positively charged groups of ZIF-8@CLN (Zn^{2+} , Na^+ , Ca^{2+}), showed in Figure 4.30.

Additionally, the coordination between TC and ZIF8@CLN can highly enhance adsorption performance owing to the presence of ZIF-8. The adsorption capacity of ZIF8@CLN was high due to the great specific surface area and distinctive pore structure of ZIF-8, demonstrating the ZIF-8 had crucial effect during the process (Sheng et al. 2022). Considering physical adsorption, although the Langmuir surface area of ZIF-8 was reduced from 1912.46 to 1120.07 $m^2 g^{-1}$ after immobilization on the CLN surface, ZIF8@CLN still has many adsorption sites and high adsorption areas made it remove TC molecules easier to the adsorbent surface.

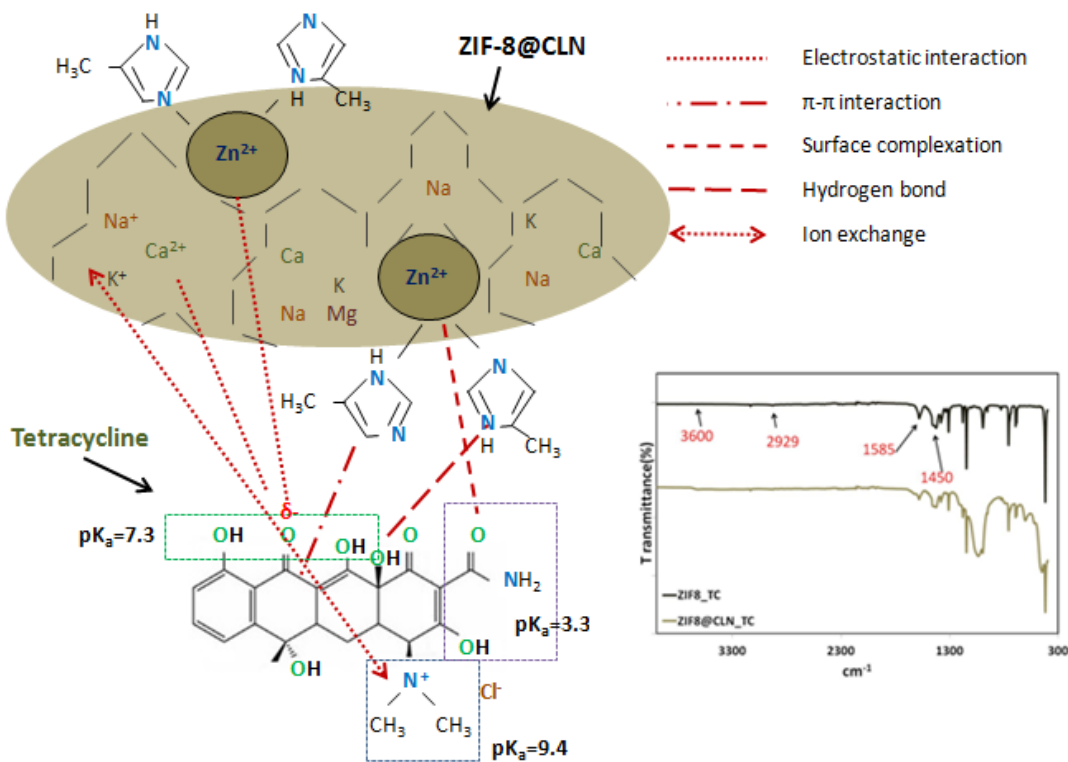


Figure 4.30. Possible mechanism for TC adsorption on ZIF8@CLN and ATR-IR spectra of ZIF-8 and ZIF-8@CLN after TC adsorption.

According to the above results, as illustrated in the Figure 4.30, the mechanism of TC adsorption on ZIF8@CLN included the electrostatic interaction, the π - π interaction, the hydrogen bond, surface complexation and coordination, and ion exchange which were synergistically provide the high adsorption capacity.

4.3. Photocatalytic Degradation

After detailed adsorption studies, the photocatalytic degradation activity of ZIF-8, ZIF8@CLN, Ag-ZIF8 and Ag-ZIF8@CLN were investigated for the dyes such as MB, MO, CR and RhB.

4.3.1. Photodegradation Parameter

4.3.1.1. Effect of pH

Effect of initial solution pH (4, 8 and 11) on photocatalytic degradation of MB, MO, CR and RhB by using the synthesized photocatalysts was investigated. The results were given in Table 4.8 and the concentration (C/C_0) versus time plots were shown in Figure 4.31 for Ag-ZIF8 and Ag-ZIF8@CLN. The degradation of these dyes by using pure ZIF-8 and ZIF8@CLN were also given in Table A.1.

The results showed that the Ag-ZIF8 and Ag-ZIF8@CLN composites were photocatalytically active, however, the photodegradation activity of ZIF-8 and ZIF8@CLN was not effective for all selected dyes. Because the adsorption phenomenon played a major role for them at the removal of the dyes, thus, the ZIF-8 and ZIF8@CLN can be used as excellent adsorbents for the wastewater treatment.

The pH of the dye solution is a significant parameter that affects the amount of adsorbed dye. It can alter the surface charge properties of the catalyst and also change

the photocatalytic degradation reactions. The formation of the number of hydroxyl radicals and size of aggregates are also influenced by pH.

The results demonstrated that increasing the pH of MB (pH=11) and RhB (pH=8) solutions caused to higher adsorption capacity and increasing photodegradation efficiency for all the photocatalysts. In alkaline medium, the generation of more OH[•] increased the removal activity. The solubilization of unprotonated form of MB owing to quite low pK_a value (<1) was the main reason for the removal of MB dye (Chandra and Nath 2017). The high adsorption efficiencies of Ag-ZIF8 (50.2 %) and Ag-ZIF8@CLN (54.4 %) for MB can be caused by the electrostatic attraction between the negatively charged catalyst surface and the positively charged cationic MB dye (Jing et al. 2014).

The pH of the MB dye solution (pH 11) was higher than PZC of ZIF-8 (9.52) and very greater than pK_a. Additionally, the increased OH⁻ concentration enhanced the photodegradation activity as the OH⁻ neutralized the H⁺ generated by Ag-ZIF8 (75.6 %) and Ag-ZIF8@CLN (97.1 %) (Chandra and Nath 2017). At higher pH values such as 11, OH⁻ can also react with h⁺ (holes) to generate OH[•] and the electrostatic interaction was increased between Ag-ZIF8 and the positive charges of MB (Fan, Luo, et al. 2018). The adsorption capacity of the catalysts influenced the photodegradation system remarkably.

For RhB, the higher adsorption efficiencies of Ag-ZIF8 (64.1 %) and Ag-ZIF8@CLN (51.4 %) and high photodegradation efficiencies of Ag-ZIF8 (91.5 %) and Ag-ZIF8@CLN (97.2 %) was obtained at pH 8.

As seen in Table 4.8, the MO and CR degradation over Ag-ZIF8 (98.8 % and 85.4 %) and Ag-ZIF8@CLN (98.7 % and 94.4 %) were higher at the initial solution pH of 4 compared to other solution pH values. MO and CR were anionic dyes and the photocatalysts surface was positive at pH=4, therefore, they considerably attracted each other. In alkaline pH, the surface of photocatalysts was negative, so they repel the MO and CR molecules, which caused a reduced dye adsorption capacity, and less photocatalytic activity.

The results indicated that pH 11, pH 4, pH 4 and pH 8 were selected as optimum pH for photodegradation of MB, MO, CR and RhB dyes, respectively. Ag-ZIF8@CLN composite was better photocatalyst than Ag-ZIF8 and pristine ZIF-8 for the degradation of MB, MO, CR and RhB dyes.

Table 4.8. Effect of pH. (Experimental conditions: pH range=4-11, $m_{\text{catalyst}}=0.04$ g, $C_0=25$ mg L⁻¹)

	pH	Ag-ZIF8		Ag-ZIF8@CLN	
		Dark Adsorption (%)	Total Removal (Ads+Photodeg) (%)	Dark Adsorption (%)	Total Removal (Ads+Photodeg) (%)
MB	4	42.8	59.8	39.2	77.4
	8	45.3	65.1	48.3	88.1
	11	50.2	75.6	54.4	97.1
MO	4	40.0	98.8	39.0	98.7
	8	35.5	89.9	27.5	83.9
	11	25.6	76.0	16.4	69.6
CR	4	46.3	85.4	52.3	94.4
	8	29.9	57.4	28.3	68.5
	11	11.0	36.3	18.9	50.4
RhB	4	56.5	83.5	51.1	94.7
	8	64.1	91.5	51.4	97.2
	11	39.5	66.0	41.3	80.4

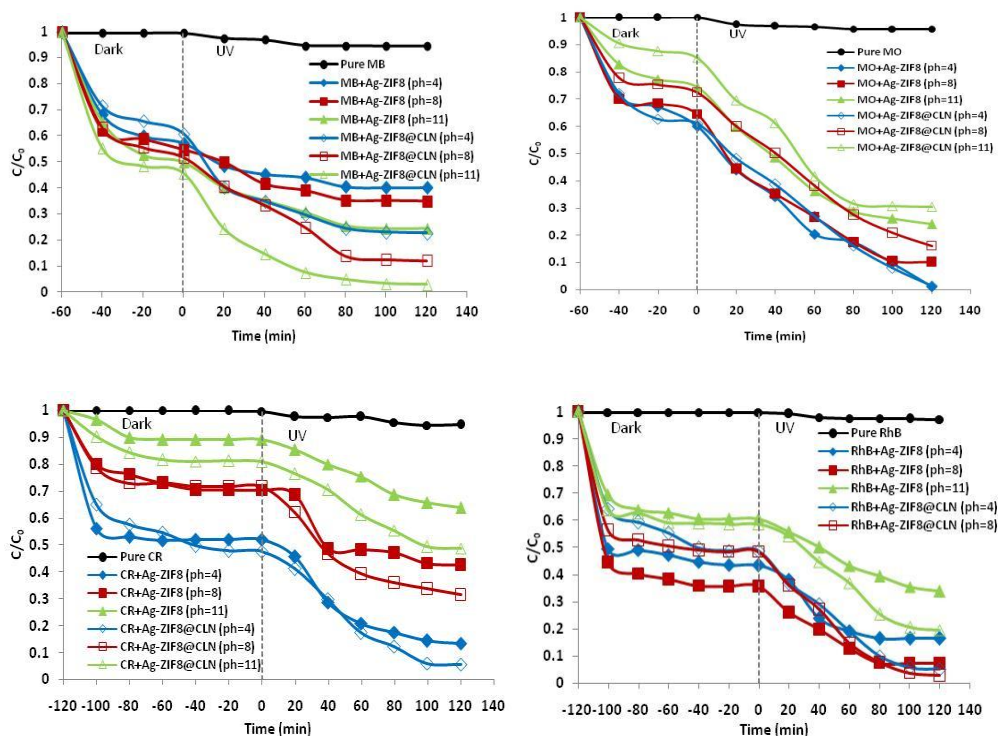


Figure 4.31. The effect of pH for photodegradation of MB, MO, CR and RhB by using Ag-ZIF8 and Ag-ZIF8@CLN. (Experimental conditions: pH range=4-11, $m_{\text{catalyst}}=0.04$ g, $C_0=25$ mg L⁻¹)

4.3.1.2. Effect of Photocatalyst Amount

Figure 4.32 shows the change of MB, MO, CR and RhB dye concentration (C/C_0) with reaction time in presence of Ag-ZIF8 and Ag-ZIF8@CLN varying catalyst amount (0.01 g, 0.04 g and 0.08 g). The results demonstrated that the degradation of all target dyes were increased by rising the amount of photocatalysts from 0.01 to 0.08 g at the reactor condition (Table 4.9). The effect of photocatalyst amount on degradation of the dyes by using pure ZIF-8 and ZIF8@CLN were also given in Table A.2.

In Table 4.9, by using 0.08 g of catalyst, the high adsorption capacity of MB, MO, CR and RhB on the Ag-ZIF8 (63.0%, 40.2%, 49.2%, 73.7%) and Ag-ZIF8@CLN (55.7%, 38.2%, 51.8%, 55.4%) was achieved at their optimum pHs, respectively. The high MB, MO, CR and RhB degradation efficiency over Ag-ZIF8 (93.2%, 99.9%, 87.9%, 97.3%) and Ag-ZIF8@CLN (99.6%, 99.5%, 95.0%, 99.9%) were also achieved, respectively.

In general, the reaction rate enhances with increasing photocatalyst amount up to a certain dosage. Because the number of active sites and available sites are increased with the rising of the photocatalyst amount, which enhances the photocatalytic activity.

Table 4.9. Effect of photocatalyst amount (m). (Experimental conditions: catalyst amount range= 0.01-0.08 g, $C_0 = 25 \text{ mg L}^{-1}$, pH (MB)=11, pH (MO)=4; pH (CR)=4, pH (RhB)=8)

	m (g)	Ag-ZIF8		Ag-ZIF8@CLN	
		Dark Adsorption (%)	Total Removal (Ads+Photodeg) (%)	Dark Adsorption (%)	Total Removal (Ads+Photodeg) (%)
MB	0.01	34.1	57.1	38.8	72.9
	0.04	50.2	75.6	54.4	97.1
	0.08	63.0	93.2	55.7	99.6
MO	0.01	25.3	79.2	14.3	71.7
	0.04	40.0	98.8	39.0	99.0
	0.08	40.2	99.9	38.2	99.5
CR	0.01	22.3	55.8	25.9	63.0
	0.04	48.3	85.2	49.2	91.8
	0.08	49.2	87.9	51.8	95.1
RhB	0.01	35.3	53.3	29.7	68.6
	0.04	63.8	92.7	51.5	96.3
	0.08	73.7	97.3	55.4	99.9

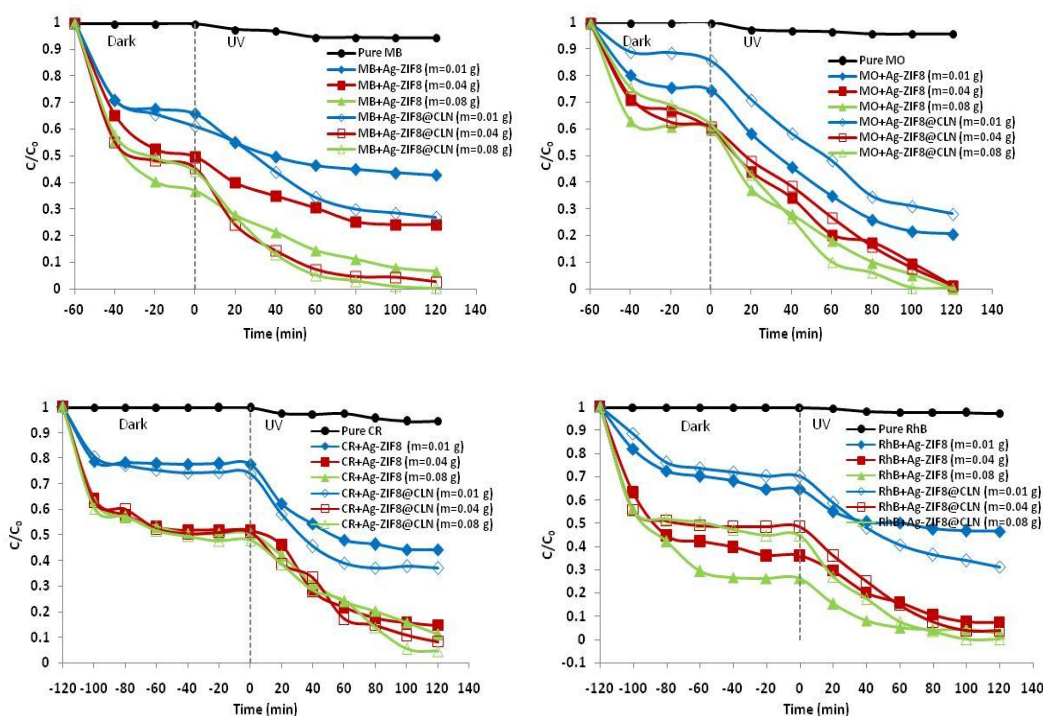


Figure 4.32. The effect of catalyst amount for photodegradation of MB, MO, CR and RhB by using Ag-ZIF8 and Ag-ZIF8@CLN. (Experimental conditions: catalyst amount range= 0.01-0.08 g, $C_0 = 25 \text{ mg L}^{-1}$, pH (MB)=11, pH (MO)=4; pH (CR)=4, pH (RhB)=8)

4.3.1.3. Effect of Initial Dye Concentration

The effects of the initial concentration of dyes for photocatalytic degradation of MB, MO, CR and RhB were illustrated in Table 4.10 and the concentration (C/C_0) versus time plots were given in Figure 4.33 for Ag-ZIF8 and Ag-ZIF8@CLN. The effect of initial dye concentration on degradation of these dyes by using pure ZIF-8 and ZIF8@CLN were also given in Table A.3.

Table 4.10 showed that both the adsorption (%) and photodegradation (%) over Ag-ZIF8 and Ag-ZIF8@CLN depend on initial dye concentration. The results indicated that increasing the initial MB, MO, CR and RhB concentration from 5 to 35 mg L^{-1} caused to the decrease in the degradation efficiency of Ag-ZIF8@CLN from 99.3% to 83.8%; 99.6% to 81.8%; 90.3% to 84.2%; and 99.7% to 94.0%, respectively. Same trends in the photodegradation of all these dyes were observed for Ag-ZIF8 composite.

The adsorption efficiencies of ZIF-8 and ZIF8@CLN also decreased with rising initial dye concentration.

The photocatalytic activity reduced with increasing the dye concentration. Because the number of available active sites were higher than the dye molecules at the low dye concentration. However, at the high dye concentration, the dye molecules around the active sites inhibited the light penetration to the photocatalyst surface. Even if irradiation time and light intensity were constant, the formation of OH^\bullet and $\text{O}_2^{\bullet -}$ on the photocatalyst surface were reduced. The dyes degraded by reactive oxygen species. However, increasing initial dye concentration reduced the reactive oxygen species and utilization of light. The reactive oxygen species were not enough to degrade all dye molecules, which decreased photodegradation efficiency.

Table 4.10. Effect of initial dye concentration (C_0). (Experimental conditions: dye conc. range $C_0= 5\text{-}35 \text{ mg L}^{-1}$, $m_{\text{catalyst}}=0.04 \text{ g}$, pH (MB)=11, pH (MO)=4; pH (CR)=4, pH (RhB)=8)

	C_0 (mg L^{-1})	Ag-ZIF8		Ag-ZIF8@CLN	
		Dark Adsorption (%)	Total Removal (Ads+Photodeg) (%)	Dark Adsorption (%)	Total Removal (Ads+Photodeg) (%)
MB	5	66.7	99.7	53.5	99.3
	15	51.6	78.8	54.2	98.7
	25	50.2	75.6	54.4	97.1
	35	42.1	65.6	45.7	83.9
MO	5	41.3	99.9	39.7	99.5
	15	40.6	99.3	39.3	99.7
	25	40.0	98.8	39.0	98.7
	35	31.3	84.3	24.3	81.8
CR	5	57.7	90.4	55.1	90.3
	15	48.3	85.2	51.8	94.7
	25	48.3	85.2	49.2	91.8
	35	47.3	75.0	49.1	84.2
RhB	5	66.9	99.6	48.6	99.7
	15	67.4	97.8	48.8	97.5
	25	64.0	92.6	47.9	97.3
	35	49.6	73.5	44.9	94.0

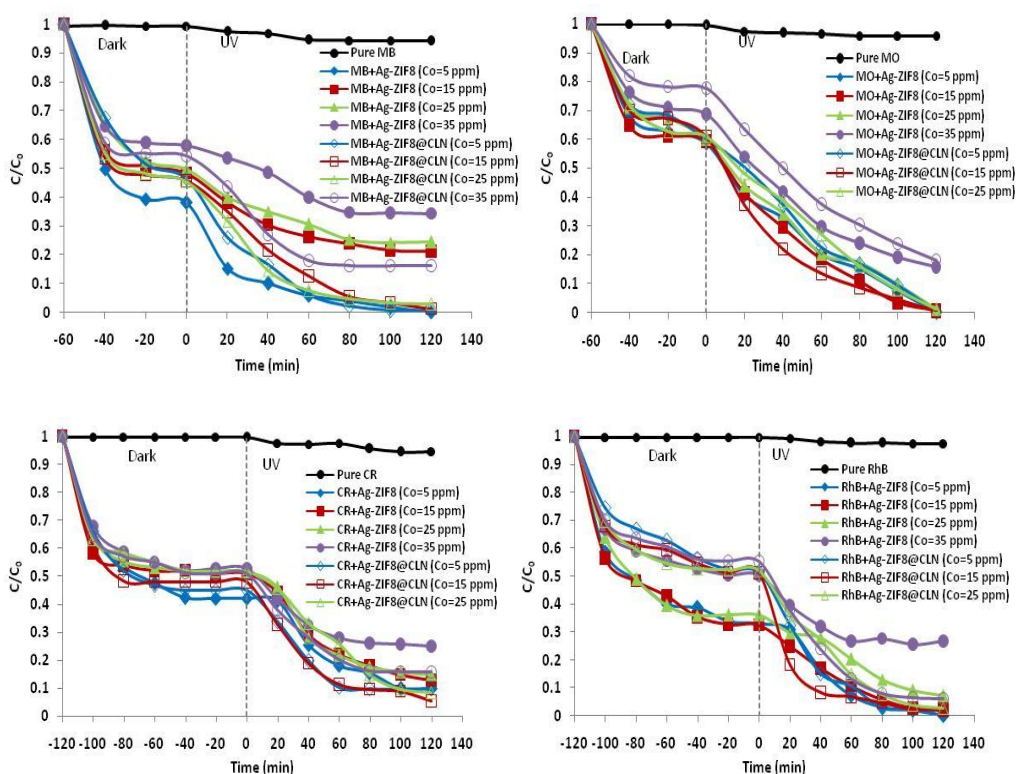


Figure 4.33. The effect of initial dye concentration for photodegradation of MB, MO, CR and RhB by using Ag-ZIF8 and Ag-ZIF8@CLN. (Experimental conditions: dye conc. range $C_0 = 5\text{--}35 \text{ mg L}^{-1}$, $m_{\text{catalyst}} = 0.04 \text{ g}$, pH (MB)=11, pH (MO)=4; pH (CR)=4, pH (RhB)=8)

4.3.2. Photodegradation Kinetics

The photocatalytic degradation rate of MB, MO, CR and RhB over Ag-ZIF8@CLN was illustrated in Figure 4.34. The degradation rates of these dyes over ZIF-8, ZIF8@CLN and Ag-ZIF8 were also given in appendix (Figure A.3-A.6).

The initial rate method was used to explain reaction kinetics. The method is explained in part: "2.2.2.3 Photocatalytic Degradation Kinetics". Figure 4.34 represented the plots of C_t versus t . The r_0 values was determined for each initial concentration (C_0) and listed in Table 4.11.

The graph of the $\ln r_0$ vs $\ln C_0$ gave a straight line, where the slope gave n value and the intercept on the ordinate showed $\ln k_i$ (inset of Figure 4.34). The determined values of n and k were given in Table 4.12. Linear regression ensured a compatibility

with high R^2 . The reaction orders of photocatalytic degradation were close to unity for some cases such as MB degradation by ZIF8 ($n=0.923$), ZIF8@CLN ($n=0.984$) and Ag-ZIF8@CLN ($n=0.935$). The value of n varying from 0.548 to 0.984 can be explained by the contribution of both adsorption process and photocatalytic degradation. The rate constant values (k) for Ag-ZIF8@CLN is higher than the other catalysts for all dyes.

Langmuir-Hinshelwood model is the other used model to understand kinetics of heterogeneous catalytic process and represented with the Eq. 2.27. Figure 4.35 indicated the Langmuir-Hinshelwood plot for the photocatalytic degradation of MB, MO, CR and RhB over Ag-ZIF8@CLN. The plot of $1/r_0$ vs $1/C_0$ gave the Langmuir-Hinshelwood model parameters (kr and K) (Tang and Huren An 1995). Figure A.7 also demonstrated the photodegradation of these dyes over Ag-ZIF8. The calculated model parameters were presented at Table 4.13. The rate constant (k_r) values of ZIF-8 and ZIF8@CLN were lower than Ag-ZIF8@CLN and Ag-ZIF8@CLN. However the adsorption constants (K) of ZIF-8 and ZIF8@CLN were high. The photocatalytic degradation is limited for ZIF-8 and ZIF8@CLN. The degradation efficiency was enhanced by Ag-doping.

The high R^2 in the range of 0.960 to 0.999 showed that the Langmuir-Hinshelwood kinetic model was compatible with the data of MB, MO, CR and RhB degradation by all the catalysts.

The results can be explained that the dye molecules initially adsorbed on the active sites of ZIF8-based catalysts and the intermediates ($\text{Dye}_{(\text{ads})}$) were generated. The rate determining step was decomposition of $\text{Dye}_{(\text{ads})}$ (Thanh et al. 2018).

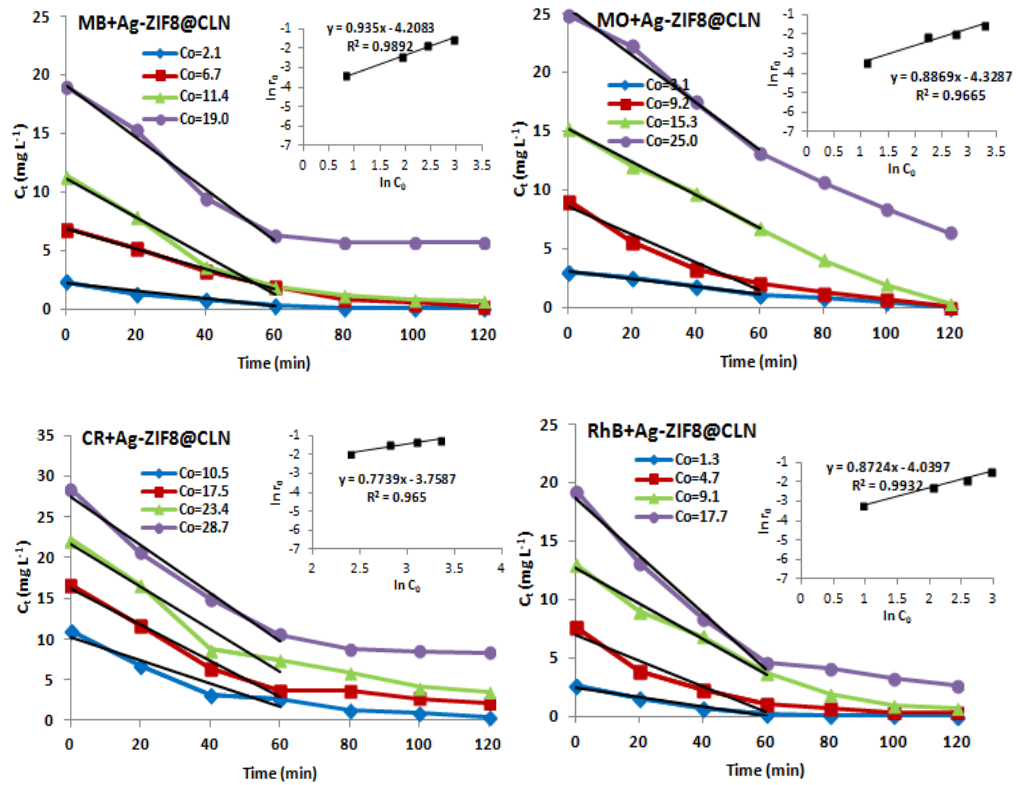


Figure 4.34. The initial rate of a reaction method for the photodegradation of MB, MO, CR and RhB over Ag-ZIF8@CLN. (Experimental conditions: $m_{\text{Ag-ZIF8@CLN}}=0.04$ g, pH (MB)=11, pH (MO)=4; pH (CR)=4, pH (RhB)=8)

Table 4.11. Initial rates (r_0) at different concentrations (C_0).

	ZIF8		ZIF8@CLN		Ag-ZIF8		Ag-ZIF8@CLN	
	C_0 (mg L^{-1})	r_0	C_0 (mg L^{-1})	r_0	C_0 (mg L^{-1})	r_0	C_0 (mg L^{-1})	r_0
MB	1.1	0.002	1.0	0.006	1.7	0.022	2.3	0.033
	4.9	0.008	2.5	0.015	7.3	0.055	6.9	0.085
	10.1	0.016	4.9	0.034	12.5	0.078	11.4	0.164
	16.9	0.030	8.2	0.046	20.3	0.103	19.0	0.220
MO	1.0	0.006	1.1	0.006	2.9	0.030	3.0	0.032
	2.5	0.012	7.0	0.009	8.9	0.101	9.1	0.118
	5.0	0.014	13.8	0.013	15.0	0.161	15.3	0.140
	10.3	0.039	21.2	0.012	24.0	0.226	26.5	0.225
CR	2.1	0.017	2.9	0.016	10.5	0.111	11.0	0.142
	3.6	0.022	11.3	0.032	17.5	0.176	16.7	0.223
	8.4	0.044	19.1	0.040	23.4	0.241	22.2	0.261
	12.0	0.040	31.5	0.061	28.7	0.270	28.5	0.297
RhB	1.1	0.004	1.1	0.001	1.6	0.020	2.6	0.041
	2.2	0.011	3.6	0.009	4.7	0.048	7.7	0.109
	6.8	0.022	6.9	0.022	9.0	0.061	13.0	0.151
	12.1	0.032	12.0	0.029	17.7	0.107	19.3	0.245

Table 4.12. The rate constants (k_i) and the reaction orders (n).

Dye	Catalyst	k_i	n	R^2
MB	ZIF8	0.002	0.923	0.990
	ZIF8@CLN	0.006	0.984	0.992
	Ag-ZIF8	0.016	0.632	0.999
	Ag-ZIF8@CLN	0.015	0.935	0.989
MO	ZIF8	0.005	0.769	0.941
	ZIF8@CLN	0.006	0.773	0.959
	Ag-ZIF8	0.012	0.957	0.994
	Ag-ZIF8@CLN	0.013	0.887	0.967
CR	ZIF8	0.011	0.564	0.943
	ZIF8@CLN	0.009	0.548	0.990
	Ag-ZIF8	0.013	0.913	0.994
	Ag-ZIF8@CLN	0.023	0.774	0.965
RhB	ZIF8	0.004	0.853	0.952
	ZIF8@CLN	0.001	0.944	0.973
	Ag-ZIF8	0.015	0.682	0.985
	Ag-ZIF8@CLN	0.018	0.872	0.993

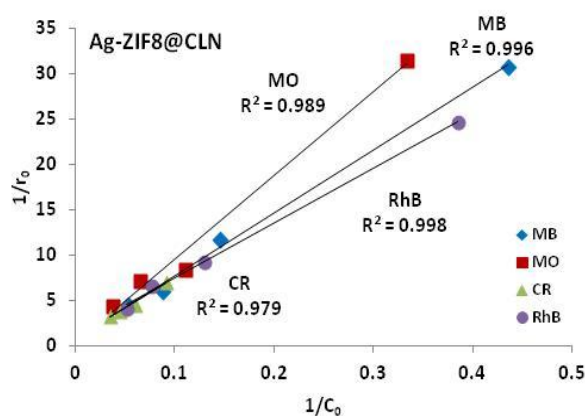


Figure 4.35. The Langmuir-Hinshelwood plot for the photodegradation of MB, MO, CR and RhB over Ag-ZIF8@CLN. (Experimental conditions: $m_{\text{Ag-ZIF8@CLN}}=0.04$ g, pH (MB)=11, pH (MO)=4; pH (CR)=4, pH (RhB)=8)

Table 4.13. Parameters of Langmuir-Hinshelwood model.

Dye	Catalyst	k_r (mg L ⁻¹ s ⁻¹)	K (L mg ⁻¹)	R^2
MB	ZIF8	0.051	0.043	0.995
	ZIF8@CLN	0.734	0.001	0.998
	Ag-ZIF8	0.131	0.116	0.996
	Ag-ZIF8@CLN	1.150	0.100	0.996
MO	ZIF8	0.040	0.163	0.960
	ZIF8@CLN	0.012	0.841	0.961
	Ag-ZIF8	8.726	0.001	0.999
	Ag-ZIF8@CLN	3.830	0.003	0.989
CR	ZIF8	0.067	0.156	0.972
	ZIF8@CLN	0.062	0.115	0.977
	Ag-ZIF8	2.180	0.005	0.997
	Ag-ZIF8@CLN	1.194	0.013	0.979
RhB	ZIF8	0.030	0.355	0.991
	ZIF8@CLN	0.073	0.045	0.999
	Ag-ZIF8	0.153	0.093	0.994
	Ag-ZIF8@CLN	0.712	0.023	0.998

4.3.3. Reusability

The reusability results were shown in Figure 4.36. Ag-ZIF8 and Ag-ZIF8@CLN catalysts maintained high adsorption and photocatalytic degradation capacities for all selected dyes after three run cycles. At the end of the third cycle, the MB, MO, CR and RhB removal amount was reduced only 8%, 13%, 22% and 10% by using Ag-ZIF8 and 7%, 13%, 18% and 11% by using Ag-ZIF8@CLN, respectively.

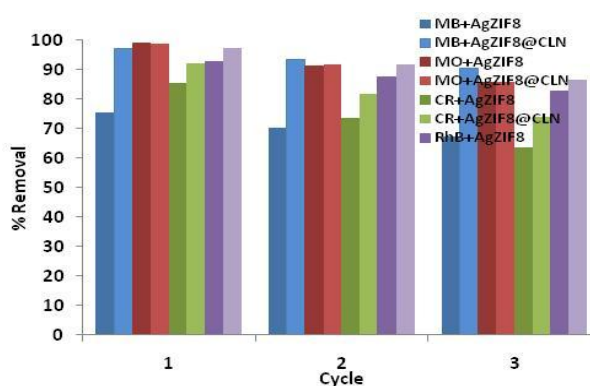


Figure 4.36. Reusability of Ag-ZIF8 and Ag-ZIF8@CLN. (Experimental conditions: $m_{\text{catalyst}} = 0.04$ g, $C_0 = 25$ mg L⁻¹, pH (MB)=11, pH (MO)=4; pH (CR)=4, pH (RhB)=8)

A slight decrease in photodegradation rate was due to the accumulation of the dye molecules on the photocatalyst surface, which directly influenced the adsorption of dyes and decreased the photocatalytic activity of photocatalysts. Therefore, Ag-ZIF8 and Ag-ZIF8@CLN are sustainable, economic and efficient photocatalysts for the dye removal.

4.3.4. Photodegradation Mechanism

The photodegradation of MB, MO, CR and RhB dyes on Ag-ZIF8 and Ag-ZIF8@CLN can be explained by two primary mechanisms:

- 1) adsorption-catalysis model that ZIF-8 and ZIF-8@CLN have the high adsorption capacity toward the dye molecules.
- 2) enhanced electron transfer owing to the tiny and well-dispersed Ag nanoparticles on ZIF-8.

Firstly, the dye molecules were adsorbed by the Ag-ZIF8 and Ag-ZIF8@CLN composite surfaces where the photocatalytic reaction occurs. The dyes were adsorbed by ZIF-8@CLN via three main mechanisms: (1) interaction between the functional groups on ZIF-8@CLN and the dyes; (2) binding of the dyes to the open metal sites over ZIF-8; (3) electrostatic interactions between the adsorbents and the dyes.

Moreover, the imidazole rings of 2-methyl imidazole have a major role on interactions between ZIF-8 and the dyes. Their double bonds and electron-rich nitrogen atoms could attract to the aromatic rings of the dye molecules through the π - π stacking interaction, additionally, hydrogen atoms could be provided to hydrogen bonding (Ba Mohammed et al. 2021). All of these interactions provided perspective how MB, MO, CR and RhB molecules can interact with Ag-ZIF8 and Ag-ZIF8@CLN.

Obviously, the Ag-ZIF8 and Ag-ZIF8@CLN composite catalysts were successfully synthesized through a simple doping and immobilization approach, which acquired better photocatalytic activity than pure ZIF-8 and ZIF8@CLN in MB, MO, CR and RhB degradation. Based on the previous characterizations, the higher photocatalytic performance of these photocatalysts could be associated with the higher BET surface areas, the better optical properties, the higher charge migration efficiency and well

separation of electron-hole pairs. With respect to the specific surface area, BET analysis results showed that the specific surface area of Ag-ZIF8 ($383.91 \text{ m}^2 \text{ g}^{-1}$) was considerably higher than Ag-ZIF8@CLN ($23.49 \text{ m}^2 \text{ g}^{-1}$), which expressed the Ag-ZIF8 had more adsorption sites for the photodegradation process. Conversely, the photocatalytic degradation activity of Ag-ZIF8@CLN was higher than Ag-ZIF8. It reveals that the BET surface area was not the dominant factor influencing the photocatalytic process.

The optical properties of Ag-ZIF8@CLN catalyst were better than that of Ag-ZIF8 composite and pure ZIF-8 and CLN. This photocatalyst with the better optical properties displayed the higher degradation rate. The enhanced photocatalytic performance can be explained by the better separation efficiency of electron-hole pairs with less carrier transport resistance. Although the ZIF-8 catalyst can be evaluated as an insulator due to the large band gap energies, the doping of Ag on ZIF-8 increased the charge separation efficiency (He et al. 2020).

According to XPS results, the higher binding energy at C1s spectra of Ag-ZIF8@CLN compare to the other composite and pure materials demonstrated a loss of electron density, which caused the formation of more active vacancies, thereby, increased the photocatalytic activity (W. Q. Chen et al. 2019). The O1s spectra of photocatalysts proved that the Ag-ZIF8@CLN photocatalyst involved more O1S species with the larger peak areas. The peak corresponding to Zn-OH observed only in Ag-ZIF8 and Ag-ZIF8@CLN spectrum. Slightly less binding energy of Ag in composite catalysts than the bulk Ag showed the strong interactions between Ag and ZIF-8/ZIF8@CLN and the electron transfer from the Ag to ZIF-8 (V. A. Tran, Kadam, and Lee 2020).

The band gap energies of 5.18 eV in ZIF-8 and 5.16 eV in ZIF8@CLN were corresponding to the intra-linker excitation from the highest occupied molecular orbital (HOMO) to the lowest unoccupied molecular orbital (LUMO) levels, defined as valence band and conduction band, respectively. However, the charge transfer transition of ZIF-8 is different from other semiconductors. After photo excitations, there is ligand to metal charge transfer transition. The organic linker provides an electron to the metal node (Chakraborty, Islam, and Acharya 2019; Yu et al. 2015). Under light irradiation, the electrons and holes are excited on organic ligands. Then, the electrons at excited state transfer to the zinc-nitrogen tetrahedron and convert O_2 to $\text{O}_2^{\cdot -}$ (Yu et al. 2015).

Such a transition is weak in ZIF-8 and cause to a rapid electron-hole recombination, which is not efficient for photocatalytic degradation. To develop the photocatalytic performance, Ag nanoparticles were anchored on ZIF-8. Although the band gap energy of ZIF-8 was narrowed by doping with Ag, it was still not sufficient for photodegradation under visible light region. The photocatalytic activity of the Ag-doped ZIF-8 composite depends on both the band gap energies and hybrid nature of conduction band edges (Chakraborty, Islam, and Acharya 2019; Yu et al. 2015). Under UV irradiation, the interaction between ZIF-8 and Ag remarkably enhanced the charge carrier transfer process.

The role of doping metal was to decrease the recombination rate, enhance the transition rate of electron hole pairs and separation efficiency, and improve the stability of the catalyst, which increase the photocatalytic efficiency (Fan, Zheng, et al. 2018). Furthermore, doping Ag in ZIF-8 also presented the other electronic levels at the ZIF-8 band by forming the other LUMO and HOMO which can be called as interband trap sites. Trapping of electrons by these interband trap sites also provided to reduce electron-hole recombination in the Ag-doped ZIF-8, which improved the photocatalytic activity (Thanh et al. 2018).

To determine the main oxidation species of Ag-ZIF8@CLN, the different scavengers were used in the photodegradation reaction of MB, MO, CR and RhB, to understand the relative roles of the reactive species and explain the mechanism. The synthesized Ag-ZIF8@CLN as the best photocatalyst was used in this analysis. The methanol, L-ascorbic acid and disodium ethylenediaminetetraacetate (EDTA) were used as scavengers and introduced into the reaction to trap the specific reactive species such as hydroxyl radicals (OH^\bullet), superoxide ions ($\text{O}_2^{\bullet -}$) and holes (h^+), respectively. The scavengers concentration were fixed at 1mM. The results in Figure 4.37 demonstrated that the degradation efficiencies of MB, MO, CR and RhB dyes were reduced with the presence of methanol and EDTA scavengers, while the addition of the L ascorbic acid had no significant effect on photodegradation. Thus, $\text{O}_2^{\bullet -}$ can be one of the active species but it was not dominant specie. It was concluded that, the h^+ and the OH^\bullet were the main active species at the photocatalytic degradation of the MO, CR and RhB over the Ag-ZIF8@CLN. The h^+ was the main specie at the photodegradation reaction of MB. The varying of the active species during the degradation process of different dyes can be explained by their different energy gaps for the electron transition (Kong et al.

2017). The proposed dye degradation mechanisms of Ag-ZIF8 and Ag-ZIF8@CLN were summarized below.

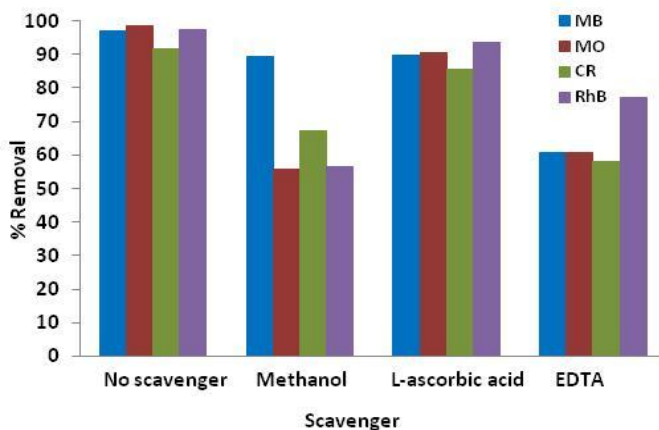


Figure 4.37. The active species trapping experiment.

Since the conduction band (CB) of ZIF-8 is highly negative (~ -1.0 V), the direct electron transfer from Ag/AgCl to CB of ZIF-8 could be thermodynamically prohibited. However, the ZIF-8 is not a perfect crystal generally and there are many defects on its surface. These defects can act as a shallow electron trapper to adopt the excited electrons from the Ag/AgCl, afterthat, deliver them for using in the photocatalytic reaction (He et al. 2020).

As for the Ag-ZIF8@CLN composite, ZIF-8 was immobilized on CLN surface through seeding method. The CLN structure can enhance the electron migration from AgCl to Ag, and then Ag to ZIF-8 via multiple transfers on support area. The recombination rate of electron-hole pairs could be highly reduced with the help of CLN support. The e^- and h^+ can be transferred further to the surfaces of AgCl and ZIF-8 and they would be used in the reaction continuously. Therefore, Ag-ZIF8@CLN showed better photodegradation activity than Ag-ZIF8. The possible reactions for the photodegradation of MB, MO, CR and RhB dyes were given via Eq. 4.2 - 4.13 and the schematic representation of the dyes degradation mechanism was displayed in Figure 4.38.

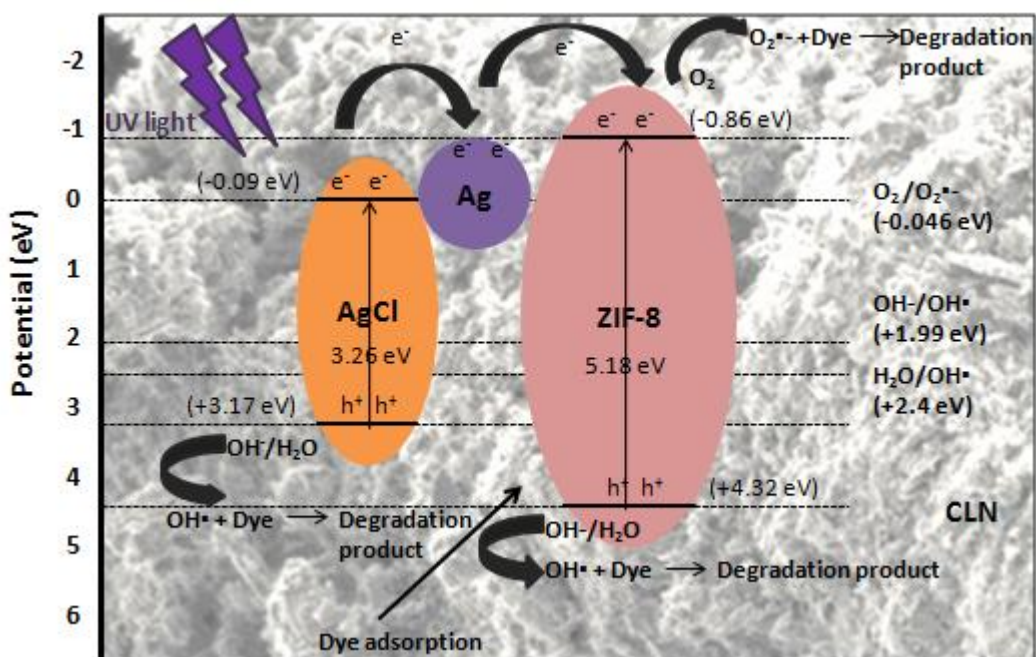
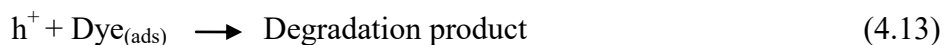
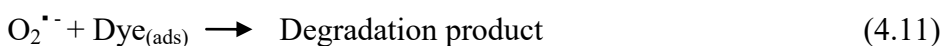
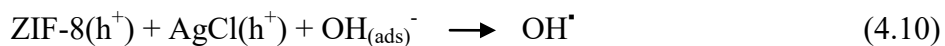
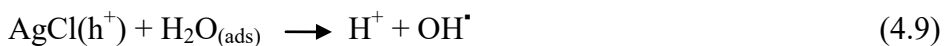
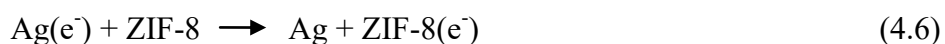
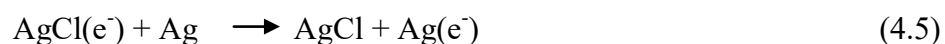
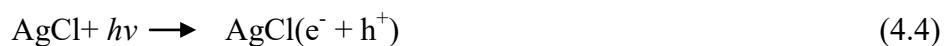


Figure 4.38. Proposed photodegradation mechanism of the dyes over Ag-ZIF8@CLN.



Firstly, the dyes (MB, MO, CR and RhB) were adsorbed on the Ag-ZIF8@CLN surface where the photocatalytic reactions occur (Eq. 4.2) as seen in Figure 4.38. Due to the fact that the energy of the photon was higher than the bandgap values of ZIF-8 and AgCl, electrons on the CB migrated to the VB forming h^+ and e^- , respectively (Eq. 4.3 and 4.4). AgCl was excited under UV light because of its narrow band gap of 3.26 eV (Fan, Luo, et al. 2018).

Ag nanoparticles are great electron acceptors and their Fermi level is lower than CB of AgCl crystals, which provided to transfer of photoelectron from AgCl crystal to the Ag nanoparticle under UV light (Eq. 4.5). Afterthat, photoelectrons swiftly moved from Ag nanoparticles to the ZIF-8 surface, owing to the well adsorption ability and high reducing power of ZIF-8 (Eq. 4.6) (Fan, Luo, et al. 2018; J. Liu, Li, Wang, et al. 2017). In other words, Ag nanoparticles at the surface of AgCl act as a bridge to transfer electron to ZIF-8 surface and hindering electron hole pairs recombination significantly (Fan, Zheng, et al. 2018). Therefore, this electron migration from Ag nanoparticles to ZIF-8 had a significant role on the photocatalytic performance of Ag-ZIF8 and Ag-ZIF8@CLN.

Afterthat, the electrons were taken by O_2 and the reactive oxygen species ($O_2^{\cdot-}$) were generated ($E_0(O_2/O_2^{\cdot-})$ (-0.046 eV)) (J. Liu, Li, Wang, et al. 2017). The $O_2^{\cdot-}$ was formed on the ZIF-8 surface because of the more negative CB of ZIF-8 (-0.86 eV) than AgCl (-0.09 eV). It can be said that ZIF-8 was an oxygen activator at this process (Fan, Luo, et al. 2018). Thereby, the oxidation of the dyes with $O_2^{\cdot-}$ mostly carried out on the ZIF-8 surface (Eq. 4.7) (J. Liu, Li, Wang, et al. 2017).

Moreover, the oxidized silver ions existing on the ZIF-8 surface were reduced to metallic form of silver under UV light (Abdi 2020), confirmed by the XPS analysis. The generated metallic silver would act different roles through the different location of the system. On the AgCl surface, metallic silver plays a role as the surface plasmon resonance (SPR) metal that affects the light-harvesting. However, metallic silver on the ZIF-8 surface behaves as electronic medium to improve the photoinduced electrons utilization and separation (J. Liu, Li, Hu, et al. 2017).

Simultaneously, h^+ remained on the AgCl crystal assisted the electron-hole separation and hindered the electron-hole recombination. Meanwhile, the h^+ at the VB of ZIF-8 and AgCl oxidized OH^- groups on surface and/or reacted with H_2O to form very reactive OH^{\cdot} radicals (Eq. 4.8 - 4.10). Because, the VB of ZIF-8 (+4.32 eV) and

AgCl (+3.17 eV) was more positive than the oxidation potentials of H₂O and OH⁻ (E₀(H₂O/OH[•])(+2.4 eV) and E₀(OH/OH[•])(+1.99 eV)) (Yalçın and Dükkancı 2022).

The O₂^{•-}, OH[•] and h⁺ exhibited high dye degradation capability (Eq. 4.11 - 4.13) (Fan, Luo, et al. 2018). Then, the dye molecules were subsequently degraded to CO₂ and H₂O by these reactive species.

As a result, the presence of Ag nanoparticles was significantly enhanced the photocatalytic degradation efficiency. Furthermore, due to the high activity of the reactive species, the diffusion of these reactive species into the bulk solution was hard. Thus, only the adsorbed dyes molecules on the photocatalyst could be oxidized (J. Liu, Li, Wang, et al. 2017). Therefore, owing to the strong adsorption capacities of Ag-ZIF8 and Ag-ZIF8@CLN for the dyes, these photocatalysts encouraged the utilization of the reactive species for the degradation reactions.

When the adsorbed dyes were degraded, the adsorption equilibrium was broken, and the new dye molecules transported quickly from the solution to the photocatalyst surface. There was an adsorption-desorption process between the dyes and catalysts. This efficient adsorption-desorption process enhanced the photodegradation performance (Fan, Zheng, et al. 2018).

Finally, the comparison of our study with the ZIF8-based adsorbents/photocatalysts in literature was summarized in Table 4.14. Under quite similar conditions, the synthesized Ag-ZIF8@CLN provided high adsorption and photocatalytic performances compared to the other ZIF8-based photocatalysts reported in literature.

Table 4.14. The comparison of ZIF8-based photocatalysts' removal performances for the target organic pollutants.

Dye	Photocatalyst	Dye Concentration (mg L ⁻¹)	Dye/Catalyst (mg/mg)	Results, Dark ads. % (time, min)	Result, Photocat. degradation % (time, min)	Reference
Methylene Blue	ZIF8	10	0.02	30% (120)	82% (120)	(Jing et al. 2014)
Methylene Blue	TiO ₂ @ZIF8	1.64	0.0033	22% (60)	89% (120)	(Chandra et al. 2017)
Methylene Blue	Ag-ZIF8 Ag-ZIF8@CLN	25	0.025	50.2% 54.4% (60)	75.6% 97.1% (120)	This Study
Methyl Orange	ZnO@ ZIF8 TiO ₂ @ ZIF8	3.27	0.0033	20% (100)	97% (100)	(Okte et al. 2017)
Methyl Orange	Ag-ZIF8 Ag-ZIF8@CLN	25	0.025	40.0% 39.0% (60)	98.7% 98.8% (120)	This Study
Congo Red	AgNPs@ZIF8	1.6	0.0032	4.5% (120)	97% (120)	(Chandra et al. 2020)
Congo Red	Ag-ZIF8 Ag-ZIF8@CLN	25	0.025	47.9% 51.8% (60)	86.6% 91.9% (120)	This Study
Rhodamine B	ZIF8/TiO ₂	10	0.02	50% (60)	90% (40)	(Zhong et al. 2020)
Rhodamine B	ZIF8@Zeolite A	10	0.01	16.6% (30)	95.5% (60)	(Du et al. 2017)
Rhodamine B	CuInS ₂ @ZIF-8	4.8	0.024	31% (30)	91% (60)	(Liu et al. 2019)
Rhodamine B	Ag-ZIF8 Ag-ZIF8@CLN	25	0.025	63.8% 51.4% (60)	92.7% 97.2% (120)	This Study
Tetracycline	Cu ₂ O/ZIF-8	50	0.125	38% (60)	84% (120)	(Zhou et al. 2022)
Tetracycline	Fe ₃ O ₄ @PDA-ZIF-8	20	0.16	93% (360)	-	(Sheng et al. 2022)
Tetracycline	ZIF8 ZIF8@CLN	50	0.05	93.8% 97.1% (360)	94.0% 97.4% (120)	This Study

CHAPTER 5

CONCLUSION

In summary, ZIF-8, ZIF-8@CLN, Ag-ZIF8 and Ag-ZIF8@CLN adsorbents/photocatalysts were successfully synthesized and their adsorption and photocatalytic degradation performance were investigated for the organic pollutants such as various dyes (Methylene blue, Methyl orange, Congo red and Rhodamine B) and antibiotics (Tetracycline). Various characterizations, including XRD, ATR-IR, SEM-EDX, BET, UV-DRS, TGA, PL and XPS were performed to determine their structure, composition, morphology, stability, textural properties and optical properties.

The adsorption capacities of MB, MO, CR and RhB were higher than 96 % by using ZIF-8 and ZIF-8@CLN at optimum conditions within 100 min. The ZIF-8 adsorption process was suitable to the Redlich Pettersen isotherm model for MB, Langmuir-Freundlich isotherm model for MO and CR, and Langmuir model for RhB. The ZIF-8@CLN adsorption data followed to the Langmuir-Freundlich model for the MB, MO and CR dyes and Langmuir model for RhB dye. Kinetics results fitted better with pseudo second order kinetics model. Thermodynamic analysis demonstrated that MB adsorption by these adsorbents was endothermic and MO, CR and RhB adsorption were exothermic, all adsorption processes were spontaneous. The regenerated ZIF-8 and ZIF-8@CLN adsorbents indicated more than 82% and 67% removal efficiencies respectively, after four consecutive cycles.

The synthesized ZIF-8 and ZIF-8@CLN were also used for the TC removal from aqueous solution. The Langmuir-Freundlich isotherm model was the best fitted to the TC adsorption data of ZIF-8 and ZIF-8@CLN with the maximum adsorption capacities of 63.0 ± 6.1 and 64.57 ± 5.0 mg g⁻¹. It is obvious that ZIF-8 and ZIF-8@CLN are efficient adsorbents to eliminate TC from aqueous solutions.

Compared to pure ZIF-8 and ZIF-8@CLN, the presence of Ag nanoparticle enhanced the photocatalytic performance significantly for degradation of the dyes. Thanks to the high surface area and strong adsorption ability of ZIF-8, the dyes

molecules easily diffused and interacted on ZIF-8-based catalyst surface. The Ag nanoparticles enhanced the optical properties, and improved the separation efficiency of electron hole pairs. The influence of some reaction parameters, such as pH, photocatalyst amount, and initial dye concentration, were investigated. The highest photocatalytic performance of the synthesized catalysts was achieved at the pHs of 11, 4, 4, 8, and by using 0.08 g of photocatalyst for MB, MO, CR and RhB, respectively. The initial rate of a reaction method and Langmuir-Hinshelwood model were used to explain reaction kinetics. The reaction order, n was varied between 0.564 and 0.984 considering four dyes and four catalysts. Langmuir-Hinshelwood kinetic model was also competent to the experimental kinetic data.

Due to the high adsorption potential, ZIF-8 and ZIF-8@CLN are one of the promising candidates for elimination of organic pollutants such as cationic and anionic dyes and antibiotics from wastewater. Additionally, the novel ZIF-8@CLN composite is efficient, more practicable and cheaper adsorbent compare to pure ZIF-8, thus, it is promising for the treatment of textile and pharmaceutical wastewater. The synergetic effect of each ZIF-8, CLN and Ag nanoparticle were observed in the photodegradation study. Therefore, the novel Ag-ZIF8@CLN photocatalyst can be potentially used in similar catalytic applications.

REFERENCES

- Abbasnia, Abbas, Ahmad Zarei, Mojtaba Yeganeh, Hamid Reza Sobhi, Mitra Gholami, and Ali Esrafil. 2022. "Removal of Tetracycline Antibiotics by Adsorption and Photocatalytic-Degradation Processes in Aqueous Solutions Using Metal Organic Frameworks (MOFs): A Systematic Review." *Inorganic Chemistry Communications*. Elsevier B.V. <https://doi.org/10.1016/j.inoche.2022.109959>.
- Abd El Khalk, Amira Ahmed, Mohamed Ahmed Betiha, Ahmed Sadek Mansour, Mohamed Gamal Abd El Wahed, and Ahmad Mohamad Al-Sabagh. 2021. "High Degradation of Methylene Blue Using a New Nanocomposite Based on Zeolitic Imidazolate Framework-8." *ACS Omega* 6 (40): 26210–20. <https://doi.org/10.1021/acsomega.1c03195>.
- Abdi, Jafar. 2020. "Synthesis of Ag-Doped ZIF-8 Photocatalyst with Excellent Performance for Dye Degradation and Antibacterial Activity." *Colloids and Surfaces A: Physicochemical and Engineering Aspects* 604 (November). <https://doi.org/10.1016/j.colsurfa.2020.125330>.
- Abdollahi, Bahman, Ahmad Najafidoust, Ebrahim Abbasi Asl, and Mika Sillanpaa. 2021. "Fabrication of ZIF-8 Metal Organic Framework (MOFs)-Based CuO-ZnO Photocatalyst with Enhanced Solar-Light-Driven Property for Degradation of Organic Dyes." *Arabian Journal of Chemistry* 14 (12). <https://doi.org/10.1016/j.arabjc.2021.103444>.
- Ackley, Mark W., R. F. Giese, and Ralph T. Yang. 1992. "Clinoptilolite: Untapped Potential for Kinetics Gas Separations." *Zeolites* 12 (7): 780–88. [https://doi.org/10.1016/0144-2449\(92\)90050-Y](https://doi.org/10.1016/0144-2449(92)90050-Y).
- Ahad, Jason M.E., Robie W. Macdonald, Joanne L. Parrott, Zeyu Yang, Yifeng Zhang, Tariq Siddique, Alsu Kuznetsova, et al. 2020. "Polycyclic Aromatic Compounds (PACs) in the Canadian Environment: A Review of Sampling Techniques, Strategies and Instrumentation." *Environmental Pollution*. Elsevier Ltd. <https://doi.org/10.1016/j.envpol.2020.114988>.
- Ahmad, Khalil, Habib ur Rehman Shah, Muhammad Shahzeb Khan, Amjad Iqbal, Erich Potrich, Larissa Souza Amaral, Sidra Rasheed, et al. 2022. "Lead In Drinking Water: Adsorption Method and Role of Zeolitic Imidazolate Frameworks for Its

- Remediation: A Review.” *Journal of Cleaner Production*. Elsevier Ltd.
<https://doi.org/10.1016/j.jclepro.2022.133010>.
- Ahmad, Nafees, Jerry Anae, Mohammad Zain Khan, Suhail Sabir, Xiao Jin Yang, Vijay Kumar Thakur, Pablo Campo, and Frederic Coulon. 2021. “Visible Light-Conducting Polymer Nanocomposites as Efficient Photocatalysts for the Treatment of Organic Pollutants in Wastewater.” *Journal of Environmental Management*. Academic Press. <https://doi.org/10.1016/j.jenvman.2021.113362>.
- Ahmadi, Babak, and Mohammad Shekarchi. 2010. “Use of Natural Zeolite as a Supplementary Cementitious Material.” *Cement and Concrete Composites* 32 (2): 134–41. <https://doi.org/10.1016/j.cemconcomp.2009.10.006>.
- Ahmed, Saber, M. G. Rasul, Wayde N. Martens, Richard Brown, and M. A. Hashib. 2011. “Advances in Heterogeneous Photocatalytic Degradation of Phenols and Dyes in Wastewater: A Review.” *Water, Air, and Soil Pollution* 215 (1–4): 3–29. <https://doi.org/10.1007/s11270-010-0456-3>.
- Ainane, Tarik, Fatima Khammour, Mohammed Talbi, and M’Hamed Elkouali. 2014. “A Novel Bio-Adsorbent of Mint Waste for Dyes Remediation in Aqueous Environments: Study and Modeling of Isotherms for Removal of Methylene Blue.” *Oriental Journal of Chemistry* 30 (3): 1183–89. <https://doi.org/10.13005/ojc/300332>.
- Akgül, Murat. 2014. “Enhancement of the Anionic Dye Adsorption Capacity of Clinoptilolite by Fe³⁺-Grafting.” *Journal of Hazardous Materials* 267 (February): 1–8. <https://doi.org/10.1016/j.jhazmat.2013.12.040>.
- Akpan, U. G., and B. H. Hameed. 2009. “Parameters Affecting the Photocatalytic Degradation of Dyes Using TiO₂-Based Photocatalysts: A Review.” *Journal of Hazardous Materials*. Elsevier. <https://doi.org/10.1016/j.jhazmat.2009.05.039>.
- Akpan, U. G., and B. H. Hameed. 2010. “The Advancements in Sol-Gel Method of Doped-TiO₂ Photocatalysts.” *Applied Catalysis A: General*. Elsevier. <https://doi.org/10.1016/j.apcata.2009.12.023>.
- Al-Degs, Yahya S., Musa I. El-Barghouthi, Amjad H. El-Sheikh, and Gavin M. Walker. 2008. “Effect of Solution PH, Ionic Strength, and Temperature on Adsorption Behavior of Reactive Dyes on Activated Carbon.” *Dyes and Pigments* 77 (1): 16–23. <https://doi.org/10.1016/j.dyepig.2007.03.001>.
- Alfonso Herrera, Luis Ángel, Paola Karen Camarillo Reyes, Ali M. Huerta Flores, Leticia Torres Martínez, and José María Rivera Villanueva. 2020. “BDC-Zn MOF

- Sensitization by MO/MB Adsorption for Photocatalytic Hydrogen Evolution under Solar Light.” *Materials Science in Semiconductor Processing* 109 (April): 104950. <https://doi.org/10.1016/j.mssp.2020.104950>.
- Al-Ghouti, Mohammad A., and Dana A. Da’ana. 2020. “Guidelines for the Use and Interpretation of Adsorption Isotherm Models: A Review.” *Journal of Hazardous Materials*. Elsevier B.V. <https://doi.org/10.1016/j.jhazmat.2020.122383>.
- Ali, Nisar, Amir Said, Farman Ali, Fazal Raziq, Zarshad Ali, Muhammad Bilal, Laurence Reinert, Tasleem Begum, and Hafiz M.N. Iqbal. 2020. “Photocatalytic Degradation of Congo Red Dye from Aqueous Environment Using Cobalt Ferrite Nanostructures: Development, Characterization, and Photocatalytic Performance.” *Water, Air, and Soil Pollution* 231 (2): 1–16. <https://doi.org/10.1007/s11270-020-4410-8>.
- Almeida-Naranjo, Cristina E., María Belén Aldás, Génesis Cabrera, and Victor H. Guerrero. 2021. “Caffeine Removal from Synthetic Wastewater Using Magnetic Fruit Peel Composites: Material Characterization, Isotherm and Kinetic Studies.” *Environmental Challenges* 5(December). <https://doi.org/10.1016/j.envc.2021.100343>.
- Al-Naddaf, Qasim, Harshul Thakkar, and Fateme Rezaei. 2018. “Novel Zeolite-5A@MOF-74 Composite Adsorbents with Core-Shell Structure for H₂ Purification.” *ACS Applied Materials and Interfaces* 10 (35): 29656–66. <https://doi.org/10.1021/acsami.8b10494>.
- Al-Sadoon, Ali A.T., Mustafa R. Mohammed, and Mohammed S.M. Al-Tameemi. 2021. “WITHDRAWN: Adsorption of Remove Methyl Green Dye from Wastewater by Using Fava Bean Peel Waste: Kinetic and Thermodynamic Studies.” *Materials Today: Proceedings*, November. <https://doi.org/10.1016/j.matpr.2021.09.552>.
- Al-Shaalan, Nora Hamad, Imran Ali, Zeid A. AlOthman, Lamya Hamad Al-Wahaibi, and Hadeel Alabdulmonem. 2019. “High Performance Removal and Simulation Studies of Diuron Pesticide in Water on MWCNTs.” *Journal of Molecular Liquids* 289 (September): 111039. <https://doi.org/10.1016/j.molliq.2019.111039>.
- Altın, Orhan, H O ˆ Nder O ˆ Zbelge, and Timur Dog. 1998. “Use of General Purpose Adsorption Isotherms for Heavy Metal-Clay Mineral Interactions.” *Journal of Colloid and Interface Science*. Vol. 198.

- Ambigadevi, J., P. Senthil Kumar, Dai Viet N. Vo, S. Hari Haran, and T. N. Srinivasa Raghavan. 2021. "Recent Developments in Photocatalytic Remediation of Textile Effluent Using Semiconductor Based Nanostructured Catalyst: A Review." *Journal of Environmental Chemical Engineering*. Elsevier Ltd. <https://doi.org/10.1016/j.jece.2020.104881>.
- An, Liangliang, Chuanling Si, Jin Ho Bae, Hanseob Jeong, and Yong Sik Kim. 2020. "One-Step Silanization and Amination of Lignin and Its Adsorption of Congo Red and Cu(II) Ions in Aqueous Solution." *International Journal of Biological Macromolecules* 159 (September): 222–30. <https://doi.org/10.1016/j.ijbiomac.2020.05.072>.
- Anh Tran, Vy, Khanh B. Vu, Thu Thao Thi Vo, Van Thuan Le, Ha Huu Do, Long Giang Bach, and Sang Wha Lee. 2021. "Experimental and Computational Investigation on Interaction Mechanism of Rhodamine B Adsorption and Photodegradation by Zeolite Imidazole Frameworks-8." *Applied Surface Science* 538 (February). <https://doi.org/10.1016/j.apsusc.2020.148065>.
- Anirudhan, T. S., and M. Ramachandran. 2007. "Surfactant-Modified Bentonite as Adsorbent for the Removal of Humic Acid from Wastewaters." *Applied Clay Science* 35 (3–4): 276–81. <https://doi.org/10.1016/j.clay.2006.09.009>.
- Antoniadou, Maria, Pinelopi P. Falara, and Vlassis Likodimos. 2021. "Photocatalytic Degradation of Pharmaceuticals and Organic Contaminants of Emerging Concern Using Nanotubular Structures." *Current Opinion in Green and Sustainable Chemistry*. Elsevier B.V. <https://doi.org/10.1016/j.cogsc.2021.100470>.
- Argun, Mehmet Emin, Sukru Dursun, Mustafa Karatas, and Metin Gürü. 2008. "Activation of Pine Cone Using Fenton Oxidation for Cd(II) and Pb(II) Removal." *Bioresource Technology* 99 (18): 8691–98. <https://doi.org/10.1016/j.biortech.2008.04.014>.
- Avila, Maria C., Ileana D. Lick, Nora A. Comelli, and Maria L. Ruiz. 2021. "Adsorption of an Anionic Dye from Aqueous Solution on a Treated Clay." *Groundwater for Sustainable Development* 15 (November). <https://doi.org/10.1016/j.gsd.2021.100688>.
- Ayawei, Nimibofa, Augustus Newton Ebelegi, and Donbebe Wankasi. 2017. "Modelling and Interpretation of Adsorption Isotherms." *Journal of Chemistry*. Hindawi Limited. <https://doi.org/10.1155/2017/3039817>.

- Ba Mohammed, Bouchra, Hassane Lgaz, Awad A. Alrashdi, Khalid Yamni, Najib Tijani, Younes Dehmani, Hicham el Hamdani, and Ill Min Chung. 2021. "Insights into Methyl Orange Adsorption Behavior on a Cadmium Zeolitic-Imidazolate Framework Cd-ZIF-8: A Joint Experimental and Theoretical Study." *Arabian Journal of Chemistry* 14 (1). <https://doi.org/10.1016/j.arabjc.2020.11.003>.
- Baynes, Ronald E., Keith Dedonder, Lindsey Kissell, Danielle Mzyk, Tara Marmulak, Geof Smith, Lisa Tell, Ronette Gehring, Jennifer Davis, and Jim E. Riviere. 2016. "Health Concerns and Management of Select Veterinary Drug Residues." *Food and Chemical Toxicology*. Elsevier Ltd. <https://doi.org/10.1016/j.fct.2015.12.020>.
- Baziar, Mansour, Hamid Reza Zakeri, Sahar Ghalehaskar, Zahra Derakhshan Nejad, Mahmoud Shams, Ioannis Anastopoulos, Dimitrios A. Giannakoudakis, and Eder C. Lima. 2021. "Metal-Organic and Zeolitic Imidazole Frameworks as Cationic Dye Adsorbents: Physicochemical Optimizations by Parametric Modeling and Kinetic Studies." *Journal of Molecular Liquids* 332 (June). <https://doi.org/10.1016/j.molliq.2021.115832>.
- Belkheiri, Daouia, Florence Fourcade, Florence Geneste, Didier Floner, Hamid Aït-Amar, and Abdeltif Amrane. 2015. "Combined Process for Removal of Tetracycline Antibiotic - Coupling Pre-Treatment with a Nickel-Modified Graphite Felt Electrode and a Biological Treatment." *International Biodeterioration and Biodegradation* 103 (November): 147–53. <https://doi.org/10.1016/j.ibiod.2015.02.032>.
- Blachnio, Magdalena, Anna Derylo-Marczewska, Barbara Charmas, Malgorzata Zienkiewicz-Strzalka, Viktor Bogatyrov, and Mariia Galaburda. 2020. "Activated Carbon from Agricultural Wastes for Adsorption of Organic Pollutants." *Molecules* 25 (21): 5105. <https://doi.org/10.3390/molecules25215105>.
- Brausch, John M., and Gary M. Rand. 2011. "A Review of Personal Care Products in the Aquatic Environment: Environmental Concentrations and Toxicity." *Chemosphere*. Elsevier Ltd. <https://doi.org/10.1016/j.chemosphere.2010.11.018>.
- Camacho, Lucy M., Arely Torres, Dipendu Saha, and Shuguang Deng. 2010. "Adsorption Equilibrium and Kinetics of Fluoride on Sol-Gel-Derived Activated Alumina Adsorbents." *Journal of Colloid and Interface Science* 349 (1): 307–13. <https://doi.org/10.1016/j.jcis.2010.05.066>.
- Cao, Xiao qiang, Xuan Wang, Ming Chen, Fei Xiao, Yi meng Huang, and Xian jun Lyu. 2021. "Synthesis of Nanoscale Zeolitic Imidazolate Framework-8 (ZIF-8)

- Using Reverse Micro-Emulsion for Congo Red Adsorption.” *Separation and Purification Technology* 260 (April). <https://doi.org/10.1016/j.seppur.2020.118062>.
- Carp, O., C. L. Huisman, and A. Reller. 2004. “Photoinduced Reactivity of Titanium Dioxide.” *Progress in Solid State Chemistry*. Elsevier Ltd. <https://doi.org/10.1016/j.progsolidstchem.2004.08.001>.
- Chakraborty, Anindita, Dewan Azharul Islam, and Himadri Acharya. 2019. “Facile Synthesis of CuO Nanoparticles Deposited Zeolitic Imidazolate Frameworks (ZIF-8) for Efficient Photocatalytic Dye Degradation.” *Journal of Solid State Chemistry* 269 (January): 566–74. <https://doi.org/10.1016/j.jssc.2018.10.036>.
- Chandra, Ramesh, and Mala Nath. 2017. “Multi-Core–Shell TiO₂NPs@ZIF-8 Composite for Enhanced Photocatalytic Degradation and Adsorption of Methylene Blue and Rhodamine-B.” *ChemistrySelect* 2 (25): 7711–22. <https://doi.org/10.1002/slct.201701195>.
- Chandra, Ramesh, and Mala Nath. 2020. “Controlled Synthesis of AgNPs@ZIF-8 Composite: Efficient Heterogeneous Photocatalyst for Degradation of Methylene Blue and Congo Red.” *Journal of Water Process Engineering* 36 (August): 101266. <https://doi.org/10.1016/j.jwpe.2020.101266>.
- Chang, Chun, Huanchun Yang, Li Kan, Weina Mu, Qiong Wang, Shih Yuan Lu, and Baole Deng. 2021. “Mechanism and Impacts of Inorganic Ion Addition on Photocatalytic Degradation of Triclosan Catalyzed by Heterostructured Bi₇O₉I₃/Bi.” *Journal of the Taiwan Institute of Chemical Engineers* 125 (August): 176–85. <https://doi.org/10.1016/j.jtice.2021.06.014>.
- Chen, Bing, Yanhui Li, Meixiu Li, Mingfei Cui, Wenshuo Xu, Liubo Li, Yaohui Sun, Mingzhen Wang, Yang Zhang, and Kewei Chen. 2021. “Rapid Adsorption of Tetracycline in Aqueous Solution by Using MOF-525/Graphene Oxide Composite.” *Microporous and Mesoporous Materials* 328 (December): 111457. <https://doi.org/10.1016/j.micromeso.2021.111457>.
- Chen, Chen, Meng Zhang, Qingxin Guan, and Wei Li. 2012. “Kinetic and Thermodynamic Studies on the Adsorption of Xylenol Orange onto MIL-101(Cr).” *Chemical Engineering Journal* 183 (February): 60–67. <https://doi.org/10.1016/j.cej.2011.12.021>.
- Chen, Wen Qian, Lin Yue Li, Lin Li, Wen Hui Qiu, Liang Tang, Ling Xu, Ke Jun Xu, and Ming Hong Wu. 2019. “MoS₂/ZIF-8 Hybrid Materials for Environmental

- Catalysis: Solar-Driven Antibiotic-Degradation Engineering.” *Engineering* 5 (4): 755–67. <https://doi.org/10.1016/j.eng.2019.02.003>.
- Chen, Xin, Xingfeng Lei, Hong Zheng, Xue Jiang, Baoliang Zhang, Hepeng Zhang, Chuan Lu, and Qiuyu Zhang. 2021. “Facile One-Step Synthesis of Magnetic Zeolitic Imidazolate Framework for Ultra Fast Removal of Congo Red from Water.” *Microporous and Mesoporous Materials* 311 (February). <https://doi.org/10.1016/j.micromeso.2020.110712>.
- Chen, Xunjun. 2015. “Modeling of Experimental Adsorption Isotherm Data.” *Information (Switzerland)* 6 (1): 14–22. <https://doi.org/10.3390/info6010014>.
- Chiou, Cary T. 2003. “Fundamentals of the Adsorption Theory.” In *Partition and Adsorption of Organic Contaminants in Environmental Systems*, 39–52. John Wiley & Sons, Inc. <https://doi.org/10.1002/0471264326.ch4>.
- Chirra, Suman, Li Fang Wang, Himanshu Aggarwal, Ming Fong Tsai, Siva Sankari Soorian, Suresh Siliveri, Srinath Goskula, Sripal Reddy Gujjula, and Venkatathri Narayanan. 2021. “Rapid Synthesis of a Novel Nano-Crystalline Mesoporous Faujasite Type Metal-Organic Framework, ZIF-8 Catalyst, Its Detailed Characterization, and NaBH₄ Assisted, Enhanced Catalytic Rhodamine B Degradation.” *Materials Today Communications* 26 (March). <https://doi.org/10.1016/j.mtcomm.2020.101993>.
- Costanzo, Joseph A., Courtney A. Ober, Richard Black, Giorgio Carta, and Erik J. Fernandez. 2010. “Evaluation of Polymer Matrices for an Adsorptive Approach to Plasma Detoxification.” *Biomaterials* 31 (10): 2857–65. <https://doi.org/10.1016/j.biomaterials.2009.12.036>.
- Couvreur, P., R. Gref, K. Andrieux, and C. Malvy. 2006. “Nanotechnologies for Drug Delivery: Application to Cancer and Autoimmune Diseases.” *Progress in Solid State Chemistry* 34 (2–4): 231–35. <https://doi.org/10.1016/j.progsolidstchem.2005.11.009>.
- Cui, Yuanjing, Banglin Chen, and Guodong Qian. 2014. “Lanthanide Metal-Organic Frameworks for Luminescent Sensing and Light-Emitting Applications.” *Coordination Chemistry Reviews*. Elsevier. <https://doi.org/10.1016/j.ccr.2013.10.023>.
- Çalik, Fatma Defne, Bilgesu Erdoğan, Esra Yılmaz, Gizem Saygi, and Fehime Çakıcıoğlu-Özkan. 2022. “Photocatalytic Degradation of Aquatic Organic Pollutants with Zn- and Zr-Based Metalorganic Frameworks: ZIF-8 and UiO-66.”

- Turkish Journal of Chemistry*. TUBITAK. <https://doi.org/10.55730/1300-0527.3444>.
- Da, A. 2001. "Adsorption from Theory to Practice."
- Daghrir, R., and P. Drogui. 2013. "Tetracycline Antibiotics in the Environment: A Review." *Environmental Chemistry Letters*. Springer. <https://doi.org/10.1007/s10311-013-0404-8>.
- Deng, Fang, Hui Shi, Yicheng Guo, Xubiao Luo, and Jian Zhou. 2021. "Engineering Paths of Sustainable and Green Photocatalytic Degradation Technology for Pharmaceuticals and Organic Contaminants of Emerging Concern." *Current Opinion in Green and Sustainable Chemistry*. Elsevier B.V. <https://doi.org/10.1016/j.cogsc.2021.100465>.
- Dong, Shuying, Lingfang Cui, Wei Zhang, Longji Xia, Shaojun Zhou, Christopher K. Russell, Maohong Fan, Jinglan Feng, and Jianhui Sun. 2020. "Double-Shelled ZnSnO₃ Hollow Cubes for Efficient Photocatalytic Degradation of Antibiotic Wastewater." *Chemical Engineering Journal* 384 (March): 123279. <https://doi.org/10.1016/j.cej.2019.123279>.
- Du, Guiqing, Pingjing Feng, Xian Cheng, Jintang Li, and Xuetao Luo. 2017. "Immobilizing of ZIF-8 Derived ZnO with Controllable Morphologies on Zeolite A for Efficient Photocatalysis." *Journal of Solid State Chemistry* 255 (November): 215–18. <https://doi.org/10.1016/j.jssc.2017.07.035>.
- Duan, Hanxiao, Xiang Hu, and Zhirong Sun. 2020. "Magnetic Zeolite Imidazole Framework Material-8 as an Effective and Recyclable Adsorbent for Removal of Ceftazidime from Aqueous Solution." *Journal of Hazardous Materials* 384 (February). <https://doi.org/10.1016/j.jhazmat.2019.121406>.
- Dubinin, M. M. 1960. "The Potential Theory of Adsorption of Gases and Vapors for Adsorbents with Energetically Nonuniform Surfaces." *Chemical Reviews* 60 (2): 235–41. https://doi.org/10.1021/CR60204A006/ASSET/CR60204A006.FP.PNG_V03.
- Duirk, Stephen E, and Timothy W Collette. n.d. "Organophosphate Pesticide Degradation Under Drinking Water Treatment Conditions: Modeling Perspectives."
- Elmoubarki, R., F. Z. Mahjoubi, H. Tounsadi, J. Moustadraf, M. Abdennouri, A. Zouhri, A. el Albani, and N. Barka. 2015. "Adsorption of Textile Dyes on Raw and Decanted Moroccan Clays: Kinetics, Equilibrium and Thermodynamics." *Water*

- Resources and Industry* 9 (March): 16–29.
<https://doi.org/10.1016/j.wri.2014.11.001>.
- El-Sewify, Islam M., Ahmed Radwan, Ahmed Shahat, M. F. El-Shahat, and Mostafa M.H. Khalil. 2022. “Superior Adsorption and Removal of Aquaculture and Bio-Staining Dye from Industrial Wastewater Using Microporous Nanocubic Zn-MOFs.” *Microporous and Mesoporous Materials* 329 (January).
<https://doi.org/10.1016/j.micromeso.2021.111506>.
- Enesca, Alexandru. 2021. “The Influence of Photocatalytic Reactors Design and Operating Parameters on the Wastewater Organic Pollutants Removal— a Mini-review.” *Catalysts*. MDPI. <https://doi.org/10.3390/catal11050556>.
- Eren, Zeynep, and Filiz Nuran Acar. 2006. “Adsorption of Reactive Black 5 from an Aqueous Solution: Equilibrium and Kinetic Studies.” *Desalination* 194 (1–3): 1–10. <https://doi.org/10.1016/j.desal.2005.10.022>.
- Estrada-Cabrera, E., L. R. Torres-Ferrer, G. Luna-Barcenas, and R. Ramirez-Bon. 2021. “Cellulose Dialysis Membrane Containing Raw Clinoptilolite Enhances the Removal of Rhodamine 6G from Aqueous Solutions.” *Microporous and Mesoporous Materials* 321 (July).
<https://doi.org/10.1016/j.micromeso.2021.111113>.
- Fan, Gongduan, Jing Luo, Liang Guo, Rujing Lin, Xiaomei Zheng, and Shane A. Snyder. 2018. “Doping Ag/AgCl in Zeolitic Imidazolate Framework-8 (ZIF-8) to Enhance the Performance of Photodegradation of Methylene Blue.” *Chemosphere* 209 (October): 44–52. <https://doi.org/10.1016/j.chemosphere.2018.06.036>.
- Fan, Gongduan, Xiaomei Zheng, Jing Luo, Huiping Peng, Hui Lin, Minchen Bao, Liang Hong, and Jinjin Zhou. 2018. “Rapid Synthesis of Ag/AgCl@ZIF-8 as a Highly Efficient Photocatalyst for Degradation of Acetaminophen under Visible Light.” *Chemical Engineering Journal* 351 (November): 782–90.
<https://doi.org/10.1016/j.cej.2018.06.119>.
- Fan, Kun, Song Song Bao, Wei Xuan Nie, Chwen Haw Liao, and Li Min Zheng. 2018. “Iridium(III)-Based Metal-Organic Frameworks as Multiresponsive Luminescent Sensors for Fe³⁺, CrO₄²⁻, and ATP²⁻ in Aqueous Media.” *Inorganic Chemistry* 57 (3): 1079–89. <https://doi.org/10.1021/acs.inorgchem.7b02513>.
- Feng, Yi, Yu Li, Minying Xu, Shichang Liu, and Jianfeng Yao. 2016. “Fast Adsorption of Methyl Blue on Zeolitic Imidazolate Framework-8 and Its Adsorption

- Mechanism.” *RSC Advances* 6 (111): 109608–12.
<https://doi.org/10.1039/c6ra23870j>.
- Foo, K. Y., and B. H. Hameed. 2010. “Insights into the Modeling of Adsorption Isotherm Systems.” *Chemical Engineering Journal*.
<https://doi.org/10.1016/j.cej.2009.09.013>.
- Fu, Qiuping, Jie Lou, Rongbin Zhang, Lei Peng, Shaoqi Zhou, Wei Yan, Changli Mo, and Jun Luo. 2021. “Highly Effective and Fast Removal of Congo Red from Wastewater with Metal-Organic Framework Fe-MIL-88NH₂.” *Journal of Solid State Chemistry* 294 (February). <https://doi.org/10.1016/j.jssc.2020.121836>.
- Gao, Bo, Hairong Yu, Jingya Wen, Hongju Zeng, Ting Liang, Fang Zuo, and Changjing Cheng. 2021. “Super-Adsorbent Poly(Acrylic Acid)/Laponite Hydrogel with Ultrahigh Mechanical Property for Adsorption of Methylene Blue.” *Journal of Environmental Chemical Engineering* 9 (6).
<https://doi.org/10.1016/j.jece.2021.106346>.
- Gao, Yuan, Yan Li, Liang Zhang, Hui Huang, Junjie Hu, Syed Mazhar Shah, and Xingguang Su. 2012. “Adsorption and Removal of Tetracycline Antibiotics from Aqueous Solution by Graphene Oxide.” *Journal of Colloid and Interface Science* 368 (1): 540–46. <https://doi.org/10.1016/j.jcis.2011.11.015>.
- Gong, Han, Wei Chu, Yumei Huang, Lijie Xu, Meijuan Chen, and Muting Yan. 2021. “Solar Photocatalytic Degradation of Ibuprofen with a Magnetic Catalyst: Effects of Parameters, Efficiency in Effluent, Mechanism and Toxicity Evolution.” *Environmental Pollution* 276 (May): 116691.
<https://doi.org/10.1016/j.envpol.2021.116691>.
- Guo, Xin, Siyuan He, Zhe Meng, Yinghui Wang, and Yuan Peng. 2022. “Ag@ZIF-8/g-C₃N₄ Z-Scheme Photocatalyst for the Enhanced Removal of Multiple Classes of Antibiotics by Integrated Adsorption and Photocatalytic Degradation under Visible Light Irradiation.” *RSC Advances* 12 (28): 17919–31.
<https://doi.org/10.1039/d2ra02194c>.
- Guo, Xuan, and Jianlong Wang. 2019. “A General Kinetic Model for Adsorption: Theoretical Analysis and Modeling.” *Journal of Molecular Liquids* 288 (August).
<https://doi.org/10.1016/j.molliq.2019.111100>.
- Guo, Xuan, and Jianlong Wang. 2019. “Comparison of Linearization Methods for Modeling the Langmuir Adsorption Isotherm.” *Journal of Molecular Liquids* 296 (December). <https://doi.org/10.1016/j.molliq.2019.111850>.

- Gupta, Susmita Sen, and Krishna G. Bhattacharyya. 2011. "Kinetics of Adsorption of Metal Ions on Inorganic Materials: A Review." *Advances in Colloid and Interface Science*. <https://doi.org/10.1016/j.cis.2010.12.004>.
- Gupta, Vinod Kumar, Rajeev Kumar, Arunima Nayak, Tawfik A. Saleh, and M. A. Barakat. 2013. "Adsorptive Removal of Dyes from Aqueous Solution onto Carbon Nanotubes: A Review." *Advances in Colloid and Interface Science* 193–194 (June): 24–34. <https://doi.org/10.1016/J.CIS.2013.03.003>.
- Haider, Junaid, Anum Shahzadi, Muhammad Usama Akbar, Izan Hafeez, Iram Shahzadi, Ayesha Khalid, Atif Ashfaq, et al. 2022. "A Review of Synthesis, Fabrication, and Emerging Biomedical Applications of Metal-Organic Frameworks." *Biomaterials Advances*. Elsevier Ltd. <https://doi.org/10.1016/j.bioadv.2022.213049>.
- Hamdaoui, Oualid, and Emmanuel Naffrechoux. 2007. "Modeling of Adsorption Isotherms of Phenol and Chlorophenols onto Granular Activated Carbon. Part I. Two-Parameter Models and Equations Allowing Determination of Thermodynamic Parameters." *Journal of Hazardous Materials* 147 (1–2): 381–94. <https://doi.org/10.1016/j.jhazmat.2007.01.021>.
- He, Yiming, Lin Zeng, Zhe Feng, Qingle Zhang, Xinyue Zhao, Shifeng Ge, Xin Hu, and Hongjun Lin. 2020. "Preparation, Characterization, and Photocatalytic Activity of Novel AgBr/ZIF-8 Composites for Water Purification." *Advanced Powder Technology* 31 (1): 439–47. <https://doi.org/10.1016/j.apt.2019.11.002>.
- Heydari Moghaddam, Masoumeh, Ramin Nabizadeh, Mohammad Hadi Dehghani, Bahman Akbarpour, Ali Azari, and Mahmood Yousefi. 2019. "Performance Investigation of Zeolitic Imidazolate Framework – 8 (ZIF-8) in the Removal of Trichloroethylene from Aqueous Solutions." *Microchemical Journal* 150 (November): 104185. <https://doi.org/10.1016/j.microc.2019.104185>.
- Ho, Y. S., and G. McKay. 1998. "A Comparison of Chemisorption Kinetic Models Applied to Pollutant Removal on Various Sorbents." *Process Safety and Environmental Protection* 76 (4): 332–40. <https://doi.org/10.1205/095758298529696>.
- Hosseinzadeh, Ghader, Naser Ghasemian, and Sahar Zinatloo-Ajabshir. 2022. "TiO₂/Graphene Nanocomposite Supported on Clinoptilolite Nanoplate and Its Enhanced Visible Light Photocatalytic Activity." *Inorganic Chemistry Communications* 136 (February). <https://doi.org/10.1016/j.inoche.2021.109144>.

- Hu, Jian Qiang, Shi Zhao Yang, Li Guo, Xin Xu, Ting Yao, and Feng Xie. 2017. "Microscopic Investigation on the Adsorption of Lubrication Oil on Microplastics." *Journal of Molecular Liquids* 227 (February): 351–55. <https://doi.org/10.1016/j.molliq.2016.12.043>.
- Hu, Xinjiang, Yunlin Zhao, Hui Wang, Xiaofei Tan, Yuanxiu Yang, and Yunguo Liu. 2017. "Efficient Removal of Tetracycline from Aqueous Media with a Fe₃O₄ Nanoparticles@graphene Oxide Nanosheets Assembly." *International Journal of Environmental Research and Public Health* 14 (12). <https://doi.org/10.3390/ijerph14121495>.
- Huang, Miaoliang, Chunfang Xu, Zibao Wu, Yunfang Huang, Jianming Lin, and Jihuai Wu. 2008. "Photocatalytic Discolorization of Methyl Orange Solution by Pt Modified TiO₂ Loaded on Natural Zeolite." *Dyes and Pigments* 77 (2): 327–34. <https://doi.org/10.1016/j.dyepig.2007.01.026>.
- Hussain, Shah, Muhammad Kamran, Shahid Ali Khan, Kausar Shaheen, Zarbad Shah, Hongli Suo, Qadeer Khan, et al. 2021. "Adsorption, Kinetics and Thermodynamics Studies of Methyl Orange Dye Sequestration through Chitosan Composites Films." *International Journal of Biological Macromolecules* 168 (January): 383–94. <https://doi.org/10.1016/j.ijbiomac.2020.12.054>.
- Hyun Chung, Tae, Mohamed N.A. Meshref, and Bipro Ranjan Dhar. 2021. "A Review and Roadmap for Developing Microbial Electrochemical Cell-Based Biosensors for Recalcitrant Environmental Contaminants, Emphasis on Aromatic Compounds." *Chemical Engineering Journal*. Elsevier B.V. <https://doi.org/10.1016/j.cej.2021.130245>.
- Israel, U, and U M Eduok. n.d. "Biosorption of Zinc from Aqueous Solution Using Coconut (Cocos Nucifera L) Coir Dust." *Scholars Research Library Archives of Applied Science Research*. Vol. 2012. www.scholarsresearchlibrary.com.
- Jia, Mingmin, Xiong Fei Zhang, Yi Feng, Yichen Zhou, and Jianfeng Yao. 2020. "In-Situ Growing ZIF-8 on Cellulose Nanofibers to Form Gas Separation Membrane for CO₂ Separation." *Journal of Membrane Science* 595 (February). <https://doi.org/10.1016/j.memsci.2019.117579>.
- Jin, Xiaowei, Yeyao Wang, Wei Jin, Kaifeng Rao, John P. Giesy, Henner Hollert, Kristine L. Richardson, and Zijian Wang. 2014. "Ecological Risk of Nonylphenol in China Surface Waters Based on Reproductive Fitness." *Environmental Science and Technology* 48 (2): 1256–62. <https://doi.org/10.1021/es403781z>.

- Jin, Ya Feng, Chuang Ye Ge, Xiao Bo Li, Miao Zhang, Guang Ri Xu, and Dong Hao Li. 2018. "A Sensitive Electrochemical Sensor Based on ZIF-8-Acetylene Black-Chitosan Nanocomposites for Rutin Detection." *RSC Advances* 8 (57): 32740–46. <https://doi.org/10.1039/c8ra06452k>.
- Jing, Huan Ping, Chong Chen Wang, Yi Wen Zhang, Peng Wang, and Ran Li. 2014. "Photocatalytic Degradation of Methylene Blue in ZIF-8." *RSC Advances* 4 (97): 54454–62. <https://doi.org/10.1039/c4ra08820d>.
- Kadhom, Mohammed, Noor Albayati, Hayder Alalwan, and Mustafa Al-Furaiji. 2020. "Removal of Dyes by Agricultural Waste." *Sustainable Chemistry and Pharmacy*. Elsevier B.V. <https://doi.org/10.1016/j.scp.2020.100259>.
- Karami, Kazem, Somayeh Mahmodi Beram, Parvaneh Bayat, Firouzeh Siadatnasab, and Azar Ramezanzpour. 2022. "A Novel Nanohybrid Based on Metal–Organic Framework MIL101–Cr/PANI/Ag for the Adsorption of Cationic Methylene Blue Dye from Aqueous Solution." *Journal of Molecular Structure* 1247 (January). <https://doi.org/10.1016/j.molstruc.2021.131352>.
- Kashmery, Heba A., and Soliman I. El-Hout. 2022. "Bi₂S₃/Bi₂O₃ Nanocomposites as Effective Photocatalysts for Photocatalytic Degradation of Tetracycline under Visible-Light Exposure." *Optical Materials*. <https://doi.org/10.1016/j.optmat.2022.113231>.
- Kennedy, D. A., and F. H. Tezel. 2018. "Cation Exchange Modification of Clinoptilolite – Screening Analysis for Potential Equilibrium and Kinetic Adsorption Separations Involving Methane, Nitrogen, and Carbon Dioxide." *Microporous and Mesoporous Materials* 262 (May): 235–50. <https://doi.org/10.1016/j.micromeso.2017.11.054>.
- Keser Demir, Nilay, Berna Topuz, Levent Yilmaz, and Halil Kalipcilar. 2014. "Synthesis of ZIF-8 from Recycled Mother Liquors." *Microporous and Mesoporous Materials* 198 (November): 291–300. <https://doi.org/10.1016/j.micromeso.2014.07.052>.
- Khamparia, Shraddha, and Dipika Jaspal. 2016. "Investigation of Adsorption of Rhodamine B onto a Natural Adsorbent Argemone Mexicana." *Journal of Environmental Management* 183 (December): 786–93. <https://doi.org/10.1016/j.jenvman.2016.09.036>.
- Khan, Samreen Heena, and Bhawana Pathak. 2020. "Zinc Oxide Based Photocatalytic Degradation of Persistent Pesticides: A Comprehensive Review." *Environmental*

- Nanotechnology, Monitoring and Management*. Elsevier B.V.
<https://doi.org/10.1016/j.enmm.2020.100290>.
- Khavar, Amir Hossein Cheshme, Gholamreza Moussavi, Ali Reza Mahjoub, Mohammad Satari, and Parviz Abdolmaleki. 2018. "Synthesis and Visible-Light Photocatalytic Activity of In,S-TiO₂@rGO Nanocomposite for Degradation and Detoxification of Pesticide Atrazine in Water." *Chemical Engineering Journal* 345 (August): 300–311. <https://doi.org/10.1016/j.cej.2018.03.095>.
- Kirandeep, Sushila, Aashima Sharma, Subhash Chandra Sahoo, Girijesh Kumar, Surinder Kumar Mehta, and Ramesh Kataria. 2021. "Synthesis and Characterization of 1D-Co/Zn MOFs Having Potential for Efficient Dye Adsorption from Wastewater." *Journal of Molecular Structure* 1226 (February). <https://doi.org/10.1016/j.molstruc.2020.129327>.
- Kitazono, Yumika, Ikko Ihara, Gen Yoshida, Kiyohiko Toyoda, and Kazutaka Umetsu. 2012. "Selective Degradation of Tetracycline Antibiotics Present in Raw Milk by Electrochemical Method." *Journal of Hazardous Materials* 243 (December): 112–16. <https://doi.org/10.1016/j.jhazmat.2012.10.009>.
- Kong, Rong Mei, Yan Zhao, Yiqun Zheng, and Fengli Qu. 2017. "Facile Synthesis of ZnO/CdS@ZIF-8 Core-Shell Nanocomposites and Their Applications in Photocatalytic Degradation of Organic Dyes." *RSC Advances* 7 (50): 31365–71. <https://doi.org/10.1039/c7ra03918b>.
- Konstantinou, Ioannis K., and Triantafyllos A. Albanis. 2004. "TiO₂-Assisted Photocatalytic Degradation of Azo Dyes in Aqueous Solution: Kinetic and Mechanistic Investigations: A Review." *Applied Catalysis B: Environmental*. Elsevier. <https://doi.org/10.1016/j.apcatb.2003.11.010>.
- Król, Magdalena. 2020. "Natural vs. Synthetic Zeolites." *Crystals* 10 (7): 622. <https://doi.org/10.3390/cryst10070622>.
- Kukkar, Preeti, Ki Hyun Kim, Deepak Kukkar, and Pritpal Singh. 2021. "Recent Advances in the Synthesis Techniques for Zeolitic Imidazolate Frameworks and Their Sensing Applications." *Coordination Chemistry Reviews*. Elsevier B.V. <https://doi.org/10.1016/j.ccr.2021.214109>.
- Kumar, Azad. 2017. "A Review on the Factors Affecting the Photocatalytic Degradation of Hazardous Materials." *Material Science & Engineering International Journal* 1 (3). <https://doi.org/10.15406/mseij.2017.01.00018>.

- Kumar, Naresh, and Rajesh Kumar. 2022. "Efficient Adsorption of Methylene Blue on Hybrid Structural Phase of MoO₃ Nanostructures." *Materials Chemistry and Physics* 275 (January). <https://doi.org/10.1016/j.matchemphys.2021.125211>.
- Kundu, Sanghamitra, and A. K. Gupta. 2006. "Arsenic Adsorption onto Iron Oxide-Coated Cement (IOCC): Regression Analysis of Equilibrium Data with Several Isotherm Models and Their Optimization." *Chemical Engineering Journal* 122 (1–2): 93–106. <https://doi.org/10.1016/j.cej.2006.06.002>.
- Lan, Dawei, Huiwen Zhu, Jianwen Zhang, Shuai Li, Quhan Chen, Chenxi Wang, Tao Wu, and Mengxia Xu. 2022. "Adsorptive Removal of Organic Dyes via Porous Materials for Wastewater Treatment in Recent Decades: A Review on Species, Mechanisms and Perspectives." *Chemosphere*. Elsevier Ltd. <https://doi.org/10.1016/j.chemosphere.2021.133464>.
- Langmuir, Irving. 1918. "The Adsorption of Gases on Plane Surfaces of Glass, Mica and Platinum." *Journal of the American Chemical Society* 40 (9): 1361–1403. https://doi.org/10.1021/JA02242A004/ASSET/JA02242A004.FP.PNG_V03.
- Lee, Yu Ri, Min Seok Jang, Hye Young Cho, Hee Jin Kwon, Sangho Kim, and Wha Seung Ahn. 2015. "ZIF-8: A Comparison of Synthesis Methods." *Chemical Engineering Journal* 271 (July): 276–80. <https://doi.org/10.1016/j.cej.2015.02.094>.
- Li, Feng, Yong Chen, Haimei Huang, Wei Cao, and Taohai Li. 2015. "Removal of Rhodamine B and Cr(VI) from Aqueous Solutions by a Polyoxometalate Adsorbent." *Chemical Engineering Research and Design* 100 (August): 192–202. <https://doi.org/10.1016/j.cherd.2015.05.030>.
- Li, Shimei, Longfei Tan, and Xianwei Meng. 2020. "Nanoscale Metal-Organic Frameworks: Synthesis, Biocompatibility, Imaging Applications, and Thermal and Dynamic Therapy of Tumors." *Advanced Functional Materials* 30 (13): 1908924. <https://doi.org/10.1002/adfm.201908924>.
- Li, Zhaohui, Laura Schulz, Caren Ackley, and Nancy Fenske. 2010. "Adsorption of Tetracycline on Kaolinite with PH-Dependent Surface Charges." *Journal of Colloid and Interface Science* 351 (1): 254–60. <https://doi.org/10.1016/j.jcis.2010.07.034>.
- Litefti, Khaoula, M. Sonia Freire, Mostafa Stitou, and Julia González-Álvarez. 2019. "Adsorption of an Anionic Dye (Congo Red) from Aqueous Solutions by Pine Bark." *Scientific Reports* 9 (1). <https://doi.org/10.1038/s41598-019-53046-z>.

- Liu, Aiping, Chao Yu, Jing Lin, Guanghui Sun, Guohai Xu, Yang Huang, Zhenya Liu, and Chengchun Tang. 2019. "Construction of CuInS₂@ZIF-8 Nanocomposites with Enhanced Photocatalytic Activity and Durability." *Materials Research Bulletin* 112 (April): 147–53. <https://doi.org/10.1016/j.materresbull.2018.12.020>
- Liu, Da, Wenyi Gu, Liang Zhou, Juying Lei, Lingzhi Wang, Jinlong Zhang, and Yongdi Liu. 2023. "From Biochar to Functions: Lignin Induced Formation of Fe₃C in Carbon/Fe Composites for Efficient Adsorption of Tetracycline from Wastewater." *Separation and Purification Technology* 304 (January). <https://doi.org/10.1016/j.seppur.2022.122217>.
- Liu, Jia, Zhi Wang, Yang Zhao, Huhu Cheng, Chuangang Hu, Lan Jiang, and Liangti Qu. 2012. "Three-Dimensional Graphene-Polypyrrole Hybrid Electrochemical Actuator." *Nanoscale* 4 (23): 7563–68. <https://doi.org/10.1039/c2nr32699j>.
- Liu, Jianxin, Rui Li, Yingyuan Hu, Tan Li, Zehui Jia, Yunfang Wang, Yawen Wang, Xiaochao Zhang, and Caimei Fan. 2017. "Harnessing Ag Nanofilm as an Electrons Transfer Mediator for Enhanced Visible Light Photocatalytic Performance of Ag@AgCl/Ag Nanofilm/ZIF-8 Photocatalyst." *Applied Catalysis B: Environmental* 202 (March): 64–71. <https://doi.org/10.1016/j.apcatb.2016.09.015>.
- Liu, Jianxin, Rui Li, Yunfang Wang, Yawen Wang, Xiaochao Zhang, and Caimei Fan. 2017. "The Active Roles of ZIF-8 on the Enhanced Visible Photocatalytic Activity of Ag/AgCl: Generation of Superoxide Radical and Adsorption." *Journal of Alloys and Compounds* 693: 543–49. <https://doi.org/10.1016/j.jallcom.2016.09.201>.
- Liu, Jianxin, Rui Li, Yunfang Wang, Yawen Wang, Xiaochao Zhang, and Caimei Fan. 2017. "The Active Roles of ZIF-8 on the Enhanced Visible Photocatalytic Activity of Ag/AgCl: Generation of Superoxide Radical and Adsorption." *Journal of Alloys and Compounds* 693: 543–49. <https://doi.org/10.1016/j.jallcom.2016.09.201>.
- Liu, Jiaqiang, Liu Pei, Zhiguo Xia, and Yan Xu. 2019. "Hierarchical Accordion-like Lanthanide-Based Metal-Organic Frameworks: Solvent-Free Syntheses and Ratiometric Luminescence Temperature-Sensing Properties." *Crystal Growth and Design* 19 (11): 6586–91. <https://doi.org/10.1021/acs.cgd.9b01014>.
- Lou, Lihua, Odia Osemwegie, and Seshadri S. Ramkumar. 2020. "Functional Nanofibers and Their Applications." *Industrial and Engineering Chemistry Research* 59 (13): 5439–55. <https://doi.org/10.1021/acs.iecr.9b07066>.
- Luanwuthi, Santamon, Atiweena Krittayavathananon, Pattarachai Srimuk, and Montree Sawangphruk. 2015. "In Situ Synthesis of Permselective Zeolitic Imidazolate

- Framework-8/Graphene Oxide Composites: Rotating Disk Electrode and Langmuir Adsorption Isotherm.” *RSC Advances* 5 (58): 46617–23.
<https://doi.org/10.1039/c5ra05950j>.
- Luna, Manuel, José M. Gatica, Hilario Vidal, and Maria J. Mosquera. 2019. “One-Pot Synthesis of Au/N-TiO₂ Photocatalysts for Environmental Applications: Enhancement of Dyes and NO_x Photodegradation.” *Powder Technology* 355 (October): 793–807. <https://doi.org/10.1016/j.powtec.2019.07.102>.
- Ma, Zhijun, Weibo Chen, Zhongliang Hu, Xuanzhao Pan, Mingying Peng, Guoping Dong, Shifeng Zhou, Qinyuan Zhang, Zhongmin Yang, and Jianrong Qiu. 2013. “Luffa-Sponge-like Glass-TiO₂ Composite Fibers as Efficient Photocatalysts for Environmental Remediation.” *ACS Applied Materials and Interfaces* 5 (15): 7527–36. <https://doi.org/10.1021/am401827k>.
- Mahvi, A. H., M. Ghanbarian, S. Nasser, and A. Khairi. 2009. “Mineralization and Discoloration of Textile Wastewater by TiO₂ Nanoparticles.” *Desalination* 239 (1–3): 309–16. <https://doi.org/10.1016/j.desal.2008.04.002>.
- Makhetha, Thollwana Andretta, Sekhar Chandra Ray, and Richard Motlhaletsi Moutloali. 2020. “Zeolitic Imidazolate Framework-8-Encapsulated Nanoparticle of Ag/Cu Composites Supported on Graphene Oxide: Synthesis and Antibacterial Activity.” *ACS Omega* 5 (17): 9626–40.
<https://doi.org/10.1021/acsomega.9b03215>.
- Malik, Ankur, and Mala Nath. 2019. “Multicore-Shell Nanocomposite Formed by Encapsulation of WO₃ in Zeolitic Imidazolate Framework (ZIF-8): As an Efficient Photocatalyst.” *Journal of Environmental Chemical Engineering* 7 (5).
<https://doi.org/10.1016/j.jece.2019.103401>.
- Malik, Ritu, Vandna Chaudhary, Vijay K. Tomer, Pawan S. Rana, S. P. Nehra, and Surender Duhan. 2016. “Visible Light-Driven Mesoporous Au-TiO₂/SiO₂ Photocatalysts for Advanced Oxidation Process.” *Ceramics International* 42 (9): 10892–901. <https://doi.org/10.1016/j.ceramint.2016.03.222>.
- Mamaghani, Alireza Haghghat, Fariborz Haghghat, and Chang Seo Lee. 2017. “Photocatalytic Oxidation Technology for Indoor Environment Air Purification: The State-of-the-Art.” *Applied Catalysis B: Environmental*. Elsevier B.V.
<https://doi.org/10.1016/j.apcatb.2016.10.037>.
- Meng, Xin, Chao Duan, Yanling Zhang, Wanli Lu, Wenliang Wang, and Yonghao Ni. 2020. “Corn-cob-Supported Ag NPs@ ZIF-8 Nanohybrids as Multifunction

- Biosorbents for Wastewater Remediation: Robust Adsorption, Catalysis and Antibacterial Activity.” *Composites Science and Technology* 200 (November). <https://doi.org/10.1016/j.compscitech.2020.108384>.
- Meng, Yang, Xu Chen, Dan Ai, Taiqing Wei, Zhiping Fan, and Bo Wang. 2022. “Sulfur-Doped Zero-Valent Iron Supported on Biochar for Tetracycline Adsorption and Removal.” *Journal of Cleaner Production* 379 (December). <https://doi.org/10.1016/j.jclepro.2022.134769>.
- Mesbah, Mohammad, Soudabeh Hamedshahraki, Shahin Ahmadi, Mostafa Sharifi, and Chinenye Adaobi Igwegbe. 2020. “Hydrothermal Synthesis of LaFeO₃ Nanoparticles Adsorbent: Characterization and Application of Error Functions for Adsorption of Fluoride.” *MethodsX* 7 (January): 100786. <https://doi.org/10.1016/j.mex.2020.100786>.
- Miao, Miao, Lan Mu, Shaomei Cao, Yuhuan Yang, and Xin Feng. 2022. “Dual-Functional CDs@ZIF-8/Chitosan Luminescent Film Sensors for Simultaneous Detection and Adsorption of Tetracycline.” *Carbohydrate Polymers* 291 (September). <https://doi.org/10.1016/j.carbpol.2022.119587>.
- Mirsoleimani-Azizi, Seyed Mohammad, Payam Setoodeh, Sedigheh Zeinali, and Mohammad Reza Rahimpour. 2018. “Tetracycline Antibiotic Removal from Aqueous Solutions by MOF-5: Adsorption Isotherm, Kinetic and Thermodynamic Studies.” *Journal of Environmental Chemical Engineering* 6 (5): 6118–30. <https://doi.org/10.1016/j.jece.2018.09.017>.
- Molla Mahmoudi, Mohammad, Azam Nadali, Hamid Reza Soheil Arezoomand, and Amir Hossein Mahvi. 2019. “Adsorption of Cationic Dye Textile Wastewater Using Clinoptilolite: Isotherm and Kinetic Study.” *Journal of the Textile Institute* 110 (1): 74–80. <https://doi.org/10.1080/00405000.2018.1465329>.
- Moral-Rodríguez, A. I., R. Leyva-Ramos, R. Ocampo-Pérez, J. Mendoza-Barron, I. N. Serratos-Alvarez, and J. J. Salazar-Rabago. 2016. “Removal of Ronidazole and Sulfamethoxazole from Water Solutions by Adsorption on Granular Activated Carbon: Equilibrium and Intraparticle Diffusion Mechanisms.” *Adsorption* 22 (1): 89–103. <https://doi.org/10.1007/s10450-016-9758-0>.
- Mortazavi, Nooshin, Mehrnaz Bahadori, Afsaneh Marandi, Shahram Tangestaninejad, Majid Moghadam, Valiollah Mirkhani, and Iraj Mohammadpoor-Baltork. 2021. “Enhancement of CO₂ Adsorption on Natural Zeolite, Modified Clinoptilolite with

- Cations, Amines and Ionic Liquids.” *Sustainable Chemistry and Pharmacy* 22 (September). <https://doi.org/10.1016/j.scp.2021.100495>.
- Mozaffari Majd, Mahdieh, Vahid Kordzadeh-Kermani, Vahab Ghalandari, Anis Askari, and Mika Sillanpää. 2022. “Adsorption Isotherm Models: A Comprehensive and Systematic Review (2010–2020).” *Science of the Total Environment*. Elsevier B.V. <https://doi.org/10.1016/j.scitotenv.2021.151334>.
- Mozia, Sylwia. 2010. “Photocatalytic Membrane Reactors (PMRs) in Water and Wastewater Treatment. A Review.” *Separation and Purification Technology*. Elsevier. <https://doi.org/10.1016/j.seppur.2010.03.021>.
- Mudunkotuwa, Imali A., and Vicki H. Grassian. 2010. “Citric Acid Adsorption on TiO₂ Nanoparticles in Aqueous Suspensions at Acidic and Circumneutral PH: Surface Coverage, Surface Speciation, and Its Impact on Nanoparticle-Nanoparticle Interactions.” *Journal of the American Chemical Society* 132 (42): 14986–94. <https://doi.org/10.1021/ja106091q>.
- Muhamad, Sulaiman Gafar. 2010. “Kinetic Studies of Catalytic Photodegradation of Chlorpyrifos Insecticide in Various Natural Waters.” *Arabian Journal of Chemistry* 3 (2): 127–33. <https://doi.org/10.1016/j.arabjc.2010.02.009>.
- Muñoz-Gil, Daniel, and Filipe M.L. Figueiredo. 2019. “High Surface Proton Conduction in Nanostructured ZIF-8.” *Nanomaterials* 9 (10). <https://doi.org/10.3390/nano9101369>.
- Naikwade, Altafhusen G., Megha B. Jagadale, Dolly P. Kale, Anna D. Gophane, Kalyanrao M. Garadkar, and Gajanan S. Rashinkar. 2020. “Photocatalytic Degradation of Methyl Orange by Magnetically Retrievable Supported Ionic Liquid Phase Photocatalyst.” *ACS Omega* 5 (1): 131–44. <https://doi.org/10.1021/acsomega.9b02040>.
- Nazir, Muhammad Altaf, Muhammad Sohail Bashir, Muhammad Jamshaid, Aqsa Anum, Tayyaba Najam, Khurram Shahzad, Muhammad Imran, Syed Shoaib Ahmad Shah, and Aziz ur Rehman. 2021. “Synthesis of Porous Secondary Metal-Doped MOFs for Removal of Rhodamine B from Water: Role of Secondary Metal on Efficiency and Kinetics.” *Surfaces and Interfaces* 25 (August). <https://doi.org/10.1016/j.surfin.2021.101261>.
- Ng, J. C.Y., W. H. Cheung, and G. McKay. 2002. “Equilibrium Studies of the Sorption of Cu(II) Ions onto Chitosan.” *Journal of Colloid and Interface Science* 255 (1): 64–74. <https://doi.org/10.1006/jcis.2002.8664>.

- Nguyen, Linh Ho Thuy, Hue Thi Thu Nguyen, Bao Quang Gia Le, Minh Huy Dinh Dang, Trang Thi Thu Nguyen, Ngoc Xuan Dat Mai, and Tan Le Hoang Doan. 2022. "Microwave-Assisted Solvothermal Synthesis of Defective Zirconium-Organic Framework as a Recyclable Nano-Adsorbent with Superior Adsorption Capacity for Efficient Removal of Toxic Organic Dyes." *Colloids and Interface Science Communications* 46 (January).
<https://doi.org/10.1016/j.colcom.2021.100511>.
- Nimbalkar, Madhu N., and Badekai Ramachandra Bhat. 2021. "Simultaneous Adsorption of Methylene Blue and Heavy Metals from Water Using Zr-MOF Having Free Carboxylic Group." *Journal of Environmental Chemical Engineering* 9 (5). <https://doi.org/10.1016/j.jece.2021.106216>.
- Noviello, Mirella, Concetta Eliana Gattullo, Michele Faccia, Vito Michele Paradiso, and Giuseppe Gambacorta. 2021. "Application of Natural and Synthetic Zeolites in the Oenological Field." *Food Research International*. Elsevier Ltd.
<https://doi.org/10.1016/j.foodres.2021.110737>.
- Ökte, A. N., D. Karamanis, E. Chalkia, and D. Tuncel. 2017. "The Effect of ZnO or TiO₂ Loaded Nanoparticles on the Adsorption and Photocatalytic Performance of Cu-BTC and ZIF-8 MOFs." *Materials Chemistry and Physics* 187 (February): 5–10. <https://doi.org/10.1016/j.matchemphys.2016.11.059>.
- Osagie, Christian, Amina Othmani, Soumya Ghosh, Alhadji Malloum, Zahra Kashitarash Esfahani, and Shahin Ahmadi. 2021. "Dyes Adsorption from Aqueous Media through the Nanotechnology: A Review." *Journal of Materials Research and Technology*. Elsevier Editora Ltda. <https://doi.org/10.1016/j.jmrt.2021.07.085>.
- Palantavida, Shajesh, and Krishna Gopakumar Warriar. n.d. "Organically Modified Sol-Gel Derived Siloxane Networks: Mesoporous, Hybrid Aerogels Through Ambient Pressure Drying Hybrid Aerogels by Ambient Pressure Drying View Project Bright Fluorescent Multiplexing Particles View Project Chapter 1." <https://www.researchgate.net/publication/48410783>.
- Pálfí, Tamás, László Wojnárovits, and Erzsébet Takács. 2011. "Mechanism of Azo Dye Degradation in Advanced Oxidation Processes: Degradation of Sulfanilic Acid Azochromotrop and Its Parent Compounds in Aqueous Solution by Ionizing Radiation." *Radiation Physics and Chemistry* 80 (3): 462–70.
<https://doi.org/10.1016/j.radphyschem.2010.11.009>.

- Pan, Junyin, Lijia Zhou, Haihua Chen, Xiaohan Liu, Chenlu Hong, Du Chen, and Bingjun Pan. 2021. "Mechanistically Understanding Adsorption of Methyl Orange, Indigo Carmine, and Methylene Blue onto Ionic/Nonionic Polystyrene Adsorbents." *Journal of Hazardous Materials* 418 (September). <https://doi.org/10.1016/j.jhazmat.2021.126300>.
- Pan, Yichang, Tao Li, Gabriella Lestari, and Zhiping Lai. 2012. "Effective Separation of Propylene/Propane Binary Mixtures by ZIF-8 Membranes." *Journal of Membrane Science* 390–391 (February): 93–98. <https://doi.org/10.1016/j.memsci.2011.11.024>.
- Pan, Yichang, Yunyang Liu, Gaofeng Zeng, Lan Zhao, and Zhiping Lai. 2011. "Rapid Synthesis of Zeolitic Imidazolate Framework-8 (ZIF-8) Nanocrystals in an Aqueous System." *Chemical Communications* 47 (7): 2071–73. <https://doi.org/10.1039/c0cc05002d>.
- Park, Kyo Sung, Zheng Ni, Adrien P. Côté, Jae Yong Choi, Rudan Huang, Fernando J. Uribe-Romo, Hee K. Chae, Michael O’Keeffe, and Omar M. Yaghi. 2006. "Exceptional Chemical and Thermal Stability of Zeolitic Imidazolate Frameworks." *Proceedings of the National Academy of Sciences of the United States of America* 103 (27): 10186–91. <https://doi.org/10.1073/pnas.0602439103>.
- Priyadharshini, S. Shwetha, Jayachamarajapura Pranesh Shubha, Jaydev Shivalingappa, Syed Farooq Adil, Mufsir Kuniyil, Mohammad Rafe Hatshan, Baji Shaik, and Kiran Kavalli. 2021. "Photocatalytic Degradation of Methylene Blue and Metanil Yellow Dyes Using Green Synthesized Zinc Oxide (ZnO) Nanocrystals." *Crystals* 12 (1): 22. <https://doi.org/10.3390/cryst12010022>.
- Radke, C. J., J. M. Prausnitz, and C. J. Radke. 1972. "Adsorption of Organic Solutes from Dilute Aqueous Solution on Activated Carbon." *Industrial and Engineering Chemistry Fundamentals* 11 (4): 445–51. https://doi.org/10.1021/I160044A003/ASSET/I160044A003.FP.PNG_V03.
- Rafiq, Asma, Muhammad Ikram, S. Ali, Faiza Niaz, Maaz Khan, Qasim Khan, and Muhammad Maqbool. 2021. "Photocatalytic Degradation of Dyes Using Semiconductor Photocatalysts to Clean Industrial Water Pollution." *Journal of Industrial and Engineering Chemistry*. Korean Society of Industrial Engineering Chemistry. <https://doi.org/10.1016/j.jiec.2021.02.017>.

- Raja, Bupesh, Raj, Krishna, Sairam, Deepak, Kasyap, Anipeddi, Kumar, Ganesh, Padmapriya, Baalamurugan and Sonawane. 2021. "Geopolymer green technology." *Materials Today: Proceedings* 46 (February): 1003–1007.
- Rasheed, Haroon Ur, Xiaomeng Lv, Wei Wei, Daniel Kobina Sam, Nabi Ullah, Jimin Xie, and Weihua Zhu. 2019. "Highly Efficient Photocatalytic Degradation of the Tetracycline Hydrochloride on the α -Fe₂O₃@CN Composite under the Visible Light." *Journal of Environmental Chemical Engineering* 7 (5): 103322. <https://doi.org/10.1016/j.jece.2019.103322>.
- Razmi, Fatin Amirah, Norzita Ngadi, Syieluing Wong, Ibrahim Mohammed Inuwa, and Lawal Anako Opotu. 2019. "Kinetics, Thermodynamics, Isotherm and Regeneration Analysis of Chitosan Modified Pandan Adsorbent." *Journal of Cleaner Production* 231 (September): 98–109. <https://doi.org/10.1016/j.jclepro.2019.05.228>.
- Redlich, O., and D. L. Peterson. 1959. "A Useful Adsorption Isotherm." *Journal of Physical Chemistry* 63 (6): 1024. https://doi.org/10.1021/J150576A611/ASSET/J150576A611.FP.PNG_V03.
- Reza, Khan Mamun, ASW Kurny, and Fahmida Gulshan. 2017. "Parameters Affecting the Photocatalytic Degradation of Dyes Using TiO₂: A Review." *Applied Water Science* 7 (4): 1569–78. <https://doi.org/10.1007/s13201-015-0367-y>.
- Riaz, Shahina, and Soo Jin Park. 2020. "An Overview of TiO₂-Based Photocatalytic Membrane Reactors for Water and Wastewater Treatments." *Journal of Industrial and Engineering Chemistry*. Korean Society of Industrial Engineering Chemistry. <https://doi.org/10.1016/j.jiec.2019.12.021>.
- Rodríguez-González, Vicente, Rodolfo Zanella, Gloria del Angel, and Ricardo Gómez. 2008. "MTBE Visible-Light Photocatalytic Decomposition over Au/TiO₂ and Au/TiO₂-Al₂O₃ Sol-Gel Prepared Catalysts." *Journal of Molecular Catalysis A: Chemical* 281 (1–2): 93–98. <https://doi.org/10.1016/j.molcata.2007.07.009>.
- Romero-Anaya, A. J., M. A. Lillo-Ródenas, and A. Linares-Solano. 2010. "Spherical Activated Carbons for Low Concentration Toluene Adsorption." *Carbon* 48 (9): 2625–33. <https://doi.org/10.1016/j.carbon.2010.03.067>.
- Rönfeldt, Pia, Helge Reinsch, Mirjam Patricia Margarete Poschmann, Huayna Terraschke, and Norbert Stock. 2020. "Scandium Metal-Organic Frameworks Containing Tetracarboxylate Linker Molecules: Synthesis, Structural

- Relationships, and Properties.” *Crystal Growth and Design* 20 (7): 4686–94.
<https://doi.org/10.1021/acs.cgd.0c00478>.
- Saeed, Tooba, Abdul Naeem, Israf Ud Din, Mshari A. Alotaibi, Abdulrah I. Alharthi, Ihtisham Wali Khan, Nazish Huma Khan, and Tabassum Malik. 2020. “Structure, Nomenclature and Viable Synthesis of Micro/Nanoscale Metal Organic Frameworks and Their Remarkable Applications in Adsorption of Organic Pollutants.” *Microchemical Journal*. Elsevier Inc.
<https://doi.org/10.1016/j.microc.2020.105579>.
- Saien, J., and S. Khezrianjoo. 2008. “Degradation of the Fungicide Carbendazim in Aqueous Solutions with UV/TiO₂ Process: Optimization, Kinetics and Toxicity Studies.” *Journal of Hazardous Materials* 157 (2–3): 269–76.
<https://doi.org/10.1016/j.jhazmat.2007.12.094>.
- Santoso, Eko, Ratna Edianti, Zahrotul Istiqomah, Dety Oktavia Sulistiono, Reva Edra Nugraha, Yuly Kusumawati, Hasliza Bahruji, and Didik Prasetyoko. 2021. “Facile Synthesis of ZIF-8 Nanoparticles Using Polar Acetic Acid Solvent for Enhanced Adsorption of Methylene Blue.” *Microporous and Mesoporous Materials* 310 (January). <https://doi.org/10.1016/j.micromeso.2020.110620>.
- Sarkodie, Bismark, Jeremiah Amesimeku, Charles Frimpong, Ebenezer Kofi Howard, Quan Feng, and Zhenzhen Xu. 2023. “Photocatalytic Degradation of Dyes by Novel Electrospun Nanofibers: A Review.” *Chemosphere*. Elsevier Ltd.
<https://doi.org/10.1016/j.chemosphere.2022.137654>.
- Saygı, Gizem, Özlem Kap, Fehime Çakıcıoğlu Özkan, and Canan Varlikli. 2023. “Photocatalytic Reactors Design and Operating Parameters on the Wastewater Organic Pollutants Removal.” In , 103–51. Springer, Cham.
https://doi.org/10.1007/978-3-031-27707-8_5.
- Serrà, Albert, Laetitia Philippe, François Perreault, and Sergi Garcia-Segura. 2021. “Photocatalytic Treatment of Natural Waters. Reality or Hype? The Case of Cyanotoxins Remediation.” *Water Research*. Elsevier Ltd.
<https://doi.org/10.1016/j.watres.2020.116543>.
- Shahriyari Far, Hossein, Mahdi Hasanzadeh, Mina Najafi, and Rahmatollah Rahimi. 2022. “In-Situ Self-Assembly of Mono- and Bi-Metal Organic Frameworks onto Clay Mineral for Highly Efficient Adsorption of Pollutants from Wastewater.” *Chemical Physics Letters* 799 (July): 139626.
<https://doi.org/10.1016/j.cplett.2022.139626>.

- Shen, Aoyun, Xinrong Liao, and Yongqiang Li. 2021. "Polyamine Functionalized Cotton Fibers Selectively Capture Negatively Charged Dye Pollutants." *Colloids and Surfaces A: Physicochemical and Engineering Aspects* 623 (August).
<https://doi.org/10.1016/j.colsurfa.2021.126666>.
- Sheng, Daohu, Xintong Ying, Rui Li, Siyao Cheng, Cheng Zhang, Wei Dong, and Xihao Pan. 2022. "Polydopamine-Mediated Modification of ZIF-8 onto Magnetic Nanoparticles for Enhanced Tetracycline Adsorption from Wastewater." *Chemosphere* 308 (December).
<https://doi.org/10.1016/j.chemosphere.2022.136249>.
- Silva Bruckmann, Franciele da, Cristian Mafra Ledur, Ivana Zanella da Silva, Guilherme Luiz Dotto, and Cristiano Rodrigo Bohn Rhoden. 2022. "A DFT Theoretical and Experimental Study about Tetracycline Adsorption onto Magnetic Graphene Oxide." *Journal of Molecular Liquids* 353 (May).
<https://doi.org/10.1016/j.molliq.2022.118837>.
- Singh, O., A. Agrawal, B. M. Abraham, R. Goyal, C. Pendem, and B. Sarkar. 2022. "Integration of Zeolite@metal–Organic Framework: A Composite Catalyst for Isopropyl Alcohol Conversion to Aromatics." *Materials Today Chemistry* 24 (June): 100796. <https://doi.org/10.1016/j.mtchem.2022.100796>.
- Singh, Ram Lakhan, Pradeep Kumar Singh, and Rajat Pratap Singh. 2015. "Enzymatic Decolorization and Degradation of Azo Dyes - A Review." *International Biodeterioration and Biodegradation*. Elsevier Ltd.
<https://doi.org/10.1016/j.ibiod.2015.04.027>.
- Sonawane, G. H., and V. S. Shrivastava. 2009. "Kinetics of Decolourization of Malachite Green from Aqueous Medium by Maize Cob (Zea Maize): An Agricultural Solid Waste." *Desalination* 247 (1–3): 430–41.
<https://doi.org/10.1016/j.desal.2009.01.006>.
- Souza, Vanessa Castro de, Jhonny Villarroel-Rocha, Maria José Gomes de Araújo, Karim Sapag, and Sibebe B.C. Pergher. 2018. "Basic Treatment in Natural Clinoptilolite for Improvement of Physicochemical Properties." *Minerals* 8 (12).
<https://doi.org/10.3390/min8120595>.
- Streit, Angélica F.M., Letícia N. Côrtes, Susanne P. Druzian, Marcelo Godinho, Gabriela C. Collazzo, Daniele Perondi, and Guilherme L. Dotto. 2019. "Development of High Quality Activated Carbon from Biological Sludge and Its

- Application for Dyes Removal from Aqueous Solutions.” *Science of the Total Environment* 660 (April): 277–87. <https://doi.org/10.1016/j.scitotenv.2019.01.027>.
- Swenson, Hans, and Nicholas P. Stadie. 2019. “Langmuir’s Theory of Adsorption: A Centennial Review.” *Langmuir*. <https://doi.org/10.1021/acs.langmuir.9b00154>.
- Szczeńśniak, Barbara, Jerzy Choma, and Mietek Jaroniec. 2019. “Ultrahigh Benzene Adsorption Capacity of Graphene-MOF Composite Fabricated via MOF Crystallization in 3D Mesoporous Graphene.” *Microporous and Mesoporous Materials* 279 (May): 387–94. <https://doi.org/10.1016/j.micromeso.2019.01.022>.
- Takehira, Hiroshi, Mohammad Razaul Karim, Yuta Shudo, Masahiro Fukuda, Tsutomu Mashimo, and Shinya Hayami. 2018. “Modulating the Work Function of Graphene by Pulsed Plasma Aided Controlled Chlorination.” *Scientific Reports* 8 (1). <https://doi.org/10.1038/s41598-018-35668-x>.
- Tang, Jian, Yue Fei Zhang, Yun Liu, Yan Li, and Hui Hu. 2020. “Efficient Ion-Enhanced Adsorption of Congo Red on Polyacrolein from Aqueous Solution: Experiments, Characterization and Mechanism Studies.” *Separation and Purification Technology* 252 (December). <https://doi.org/10.1016/j.seppur.2020.117445>.
- Tang, Walter Z., and Huren An. 1995. “Photocatalytic Degradation Kinetics and Mechanism of Acid Blue 40 by TiO₂/UV in Aqueous Solution.” *Chemosphere* 31 (9): 4171–83. [https://doi.org/10.1016/0045-6535\(95\)80016-E](https://doi.org/10.1016/0045-6535(95)80016-E).
- Tate, Kirby L., Shiguang Li, Miao Yu, and Moises A. Carreon. 2017. “Zeolite Adsorbent-MOF Layered Nanovalves for CH₄ Storage.” *Adsorption* 23 (1): 19–24. <https://doi.org/10.1007/s10450-016-9813-x>.
- Thanh, Mai Thi, Tran Vinh Thien, Pham Dinh Du, Nguyen Phi Hung, and Dinh Quang Khieu. 2018. “Iron Doped Zeolitic Imidazolate Framework (Fe-ZIF-8): Synthesis and Photocatalytic Degradation of RDB Dye in Fe-ZIF-8.” *Journal of Porous Materials* 25 (3): 857–69. <https://doi.org/10.1007/s10934-017-0498-7>.
- Thi Thanh, Mai, Tran Vinh Thien, Vo Thi Thanh Chau, Pham Dinh Du, Nguyen Phi Hung, and Dinh Quang Khieu. 2017. “Synthesis of Iron Doped Zeolite Imidazolate Framework-8 and Its Remazol Deep Black RGB Dye Adsorption Ability.” *Journal of Chemistry* 2017. <https://doi.org/10.1155/2017/5045973>.
- Thinley, Tenzin, Sneha Yadav, Jijoe Samuel Prabagar, Anusha Hosakote, K.M. Anil Kumar, and Harikaranahalli Puttaiah Shivaraju. 2022. “Facile Synthesis of MnTiO₃/Ag/GC₃N₄ Nanocomposite for Photocatalytic Degradation of

- Tetracycline Antibiotic and Synthesis of Ammonia.” *Materials Today: Proceedings*, November. <https://doi.org/10.1016/j.matpr.2022.10.232>.
- Tian, Ruiyuan, Haiqiang Liu, Yi Jiang, Jiankun Chen, Xinghua Tan, Guangyao Liu, Lina Zhang, et al. 2015. “Drastically Enhanced High-Rate Performance of Carbon-Coated LiFePO₄ Nanorods Using a Green Chemical Vapor Deposition (CVD) Method for Lithium Ion Battery: A Selective Carbon Coating Process.” *ACS Applied Materials and Interfaces* 7 (21): 11377–86. <https://doi.org/10.1021/acsami.5b01891>.
- Tong, Yanbin, Shengxin Zhao, Jing Kang, Jimin Shen, Zhonglin Chen, Binyuan Wang, Lanbo Bi, and Jinjun Deng. 2021. “Preparation of Small-Sized BiVO₄ Particles with Improved Photocatalytic Performance and Its Photocatalytic Degradation of Doxycycline in Water.” *Colloids and Surfaces A: Physicochemical and Engineering Aspects* 620 (July): 126412. <https://doi.org/10.1016/j.colsurfa.2021.126412>.
- Tran, Hai Nguyen, Eder C. Lima, Ruey Shin Juang, Jean Claude Bollinger, and Huan Ping Chao. 2021. “Thermodynamic Parameters of Liquid–Phase Adsorption Process Calculated from Different Equilibrium Constants Related to Adsorption Isotherms: A Comparison Study.” *Journal of Environmental Chemical Engineering* 9 (6). <https://doi.org/10.1016/j.jece.2021.106674>.
- Tran, Hai Nguyen, Sheng Jie You, Ahmad Hosseini-Bandegharai, and Huan Ping Chao. 2017. “Mistakes and Inconsistencies Regarding Adsorption of Contaminants from Aqueous Solutions: A Critical Review.” *Water Research* 120 (September): 88–116. <https://doi.org/10.1016/J.WATRES.2017.04.014>.
- Tran, Hai Nguyen, Sheng Jie You, and Huan Ping Chao. 2016. “Thermodynamic Parameters of Cadmium Adsorption onto Orange Peel Calculated from Various Methods: A Comparison Study.” *Journal of Environmental Chemical Engineering* 4 (3): 2671–82. <https://doi.org/10.1016/j.jece.2016.05.009>.
- Tran, Vy Anh, Abhijit N. Kadam, and Sang Wha Lee. 2020. “Adsorption-Assisted Photocatalytic Degradation of Methyl Orange Dye by Zeolite-Imidazole-Framework-Derived Nanoparticles.” *Journal of Alloys and Compounds* 835 (September). <https://doi.org/10.1016/j.jallcom.2020.155414>.
- Tsai, Chih Wei, and Ernie H.G. Langner. 2016. “The Effect of Synthesis Temperature on the Particle Size of Nano-ZIF-8.” *Microporous and Mesoporous Materials* 221 (February): 8–13. <https://doi.org/10.1016/j.micromeso.2015.08.041>.

- Tümsek, Fatma, and Özlem Avci. 2013. "Investigation of Kinetics and Isotherm Models for the Acid Orange 95 Adsorption from Aqueous Solution onto Natural Minerals." *Journal of Chemical and Engineering Data* 58 (3): 551–59. <https://doi.org/10.1021/je301215s>.
- Tzvetkova, P., P. Vassileva, and R. Nickolov. 2010. "Modified Silica Gel with 5-Amino-1,3,4-Thiadiazole-2-Thiol for Heavy Metal Ions Removal." *Journal of Porous Materials* 17 (4): 459–63. <https://doi.org/10.1007/s10934-009-9308-1>.
- Ullah, Raza, Chang Liu, Hamida Panezai, Anadil Gul, Jihong Sun, and Xia Wu. 2020. "Controlled Crystal Phase and Particle Size of Loaded-TiO₂ Using Clinoptilolite as Support via Hydrothermal Method for Degradation of Crystal Violet Dye in Aqueous Solution." *Arabian Journal of Chemistry* 13 (2): 4092–4101. <https://doi.org/10.1016/j.arabjc.2019.06.011>.
- Uzunkavak, Onur, María Silvina Patterer, Franco Medici, and Günseli Özdemir. 2019. "Modeling of Single and Binary Adsorption of Lead and Cadmium Ions onto Modified Olive Pomace." *Desalination and Water Treatment* 162 (September): 278–89. <https://doi.org/10.5004/dwt.2019.24340>.
- Varangane, Sagar, Chandra Shobha Vennapoosa, Amritanjali Tiwari, Sanna Kotrappanavar Nataraj, Taraka Prabhu Yendrapati, and Ujjwal Pal. 2022. "In Situ Synthesis of Cu-Doped ZIF-8 for Efficient Photocatalytic Water Splitting." *Applied Organometallic Chemistry* 36 (9). <https://doi.org/10.1002/aoc.6815>.
- Vareda, João P. 2023. "On Validity, Physical Meaning, Mechanism Insights and Regression of Adsorption Kinetic Models." *Journal of Molecular Liquids*. Elsevier B.V. <https://doi.org/10.1016/j.molliq.2023.121416>.
- Variar, Akhil G., M. S. Ramyashree, Veekshit Udayakumar Ail, Shanmuga Priya S., K. Sudhakar, and Muhammad Tahir. 2021. "Influence of Various Operational Parameters in Enhancing Photocatalytic Reduction Efficiency of Carbon Dioxide in a Photoreactor: A Review." *Journal of Industrial and Engineering Chemistry*. Korean Society of Industrial Engineering Chemistry. <https://doi.org/10.1016/j.jiec.2021.04.017>.
- Vaya, Dipti, and Praveen K. Surolia. 2020. "Semiconductor Based Photocatalytic Degradation of Pesticides: An Overview." *Environmental Technology and Innovation*. Elsevier B.V. <https://doi.org/10.1016/j.eti.2020.101128>.
- Vecchiato, Marco, Tiziano Bonato, Carlo Barbante, Andrea Gambaro, and Rossano Piazza. 2021. "Organic Pollutants in Protected Plain Areas: The Occurrence of

- PAHs, Musks, UV-Filters, Flame Retardants and Hydrocarbons in Woodland Soils.” *Science of the Total Environment* 796 (November): 149003.
<https://doi.org/10.1016/j.scitotenv.2021.149003>.
- Velempini, T., E. Prabakaran, and K. Pillay. 2021. “Recent Developments in the Use of Metal Oxides for Photocatalytic Degradation of Pharmaceutical Pollutants in Water—a Review.” *Materials Today Chemistry*. Elsevier Ltd.
<https://doi.org/10.1016/j.mtchem.2020.100380>.
- Vijayaraghavan, K., T. V.N. Padmesh, K. Palanivelu, and M. Velan. 2006. “Biosorption of Nickel(II) Ions onto Sargassum Wightii: Application of Two-Parameter and Three-Parameter Isotherm Models.” *Journal of Hazardous Materials* 133 (1–3): 304–8. <https://doi.org/10.1016/j.jhazmat.2005.10.016>.
- Vimonses, Vipasiri, Shaomin Lei, Bo Jin, Chris W.K. Chow, and Chris Saint. 2009. “Kinetic Study and Equilibrium Isotherm Analysis of Congo Red Adsorption by Clay Materials.” *Chemical Engineering Journal* 148 (2–3): 354–64.
<https://doi.org/10.1016/j.cej.2008.09.009>.
- Wallace, S. J., S. R. de Solla, J. A. Head, P. v. Hodson, J. L. Parrott, P. J. Thomas, A. Berthiaume, and V. S. Langlois. 2020. “Polycyclic Aromatic Compounds (PACs) in the Canadian Environment: Exposure and Effects on Wildlife.” *Environmental Pollution*. Elsevier Ltd. <https://doi.org/10.1016/j.envpol.2020.114863>.
- Wang, Jianlong, and Xuan Guo. 2020. “Adsorption Isotherm Models: Classification, Physical Meaning, Application and Solving Method.” *Chemosphere*. Elsevier Ltd.
<https://doi.org/10.1016/j.chemosphere.2020.127279>.
- Wang, Jie, Qian Zhang, Fang Deng, Xubiao Luo, and Dionysios D. Dionysiou. 2020. “Rapid Toxicity Elimination of Organic Pollutants by the Photocatalysis of Environment-Friendly and Magnetically Recoverable Step-Scheme SnFe₂O₄/ZnFe₂O₄ Nano-Heterojunctions.” *Chemical Engineering Journal* 379 (January): 122264. <https://doi.org/10.1016/j.cej.2019.122264>.
- Wang, Jing, Yuelin Wang, Ye Liang, Jicheng Zhou, Licheng Liu, Shirong Huang, and Jinjun Cai. 2021. “Nitrogen-Doped Carbons from in-Situ Glucose-Coated ZIF-8 as Efficient Adsorbents for Rhodamine B Removal from Wastewater.” *Microporous and Mesoporous Materials* 310 (January).
<https://doi.org/10.1016/j.micromeso.2020.110662>.
- Wang, Wanjun, Taicheng An, Guiying Li, Yecheng Li, Jimmy C. Yu, and Po Keung Wong. 2018. “Free-Standing Red Phosphorous/Silver Sponge Monolith as an

- Efficient and Easily Recyclable Macroscale Photocatalyst for Organic Pollutant Degradation under Visible Light Irradiation.” *Journal of Colloid and Interface Science* 518 (May): 130–39. <https://doi.org/10.1016/j.jcis.2018.02.008>.
- Wang, Yanzhi, Yidi Sun, Hongyang Chen, Qi Wu, and Daocai Chi. 2021. “Assessing the Performance of Clinoptilolite for Controlling and Releasing Ammonium in Agricultural Applications.” *Energy Reports* 7 (November): 887–95. <https://doi.org/10.1016/j.egy.2021.09.184>.
- Wang, Yating, Xiu Dai, Yixing Zhan, Xiaoqing Ding, Ming Wang, and Xinlong Wang. 2019. “In Situ Growth of ZIF-8 Nanoparticles on Chitosan to Form the Hybrid Nanocomposites for High-Efficiency Removal of Congo Red.” *International Journal of Biological Macromolecules* 137 (September): 77–86. <https://doi.org/10.1016/j.ijbiomac.2019.06.195>.
- Wang, Yiren, and Ralph T. Yang. 2019. “Chemical Liquid Deposition Modified 4A Zeolite as a Size-Selective Adsorbent for Methane Upgrading, CO₂ Capture and Air Separation.” *ACS Sustainable Chemistry and Engineering* 7 (3): 3301–8. <https://doi.org/10.1021/acssuschemeng.8b05339>.
- Weber Jr., Walter J., and J. Carrell Morris. 1963. “Kinetics of Adsorption on Carbon from Solution.” *Journal of the Sanitary Engineering Division* 89 (2): 31–59. <https://doi.org/10.1061/JSEDAI.0000430>.
- Weber, Thomas W., and Ranjit K. Chakravorti. 1974. “Pore and Solid Diffusion Models for Fixed-bed Adsorbers.” *AIChE Journal* 20 (2): 228–38. <https://doi.org/10.1002/aic.690200204>.
- Weber, Walter J., and Jr. Edward H. Smith. 1987. “Simulation and Design Models for Adsorption Processes.” *ES&T Critical Review*.
- Wu, Chun Sheng, Zhen Hu Xiong, Chen Li, and Jin Miao Zhang. 2015. “Zeolitic Imidazolate Metal Organic Framework ZIF-8 with Ultra-High Adsorption Capacity Bound Tetracycline in Aqueous Solution.” *RSC Advances* 5 (100): 82127–37. <https://doi.org/10.1039/c5ra15497a>.
- Wu, Jiafei, Yingzhi Zhu, Kunpeng Xue, Yan Lu, Jiahao Hu, and Wei Dai. 2021. “Efficient Elimination of Organic Contaminants with Novel and Stable Zeolite@MOF Layer Adsorbents.” *Particuology* 58 (October): 74–84. <https://doi.org/10.1016/j.partic.2021.01.014>.
- Xia, Yunxue, Qin Yao, Wei Zhang, Yunsong Zhang, and Maojun Zhao. 2019. “Comparative Adsorption of Methylene Blue by Magnetic Baker’s Yeast and

- EDTAD-Modified Magnetic Baker's Yeast: Equilibrium and Kinetic Study." *Arabian Journal of Chemistry* 12 (8): 2448–56.
<https://doi.org/10.1016/j.arabjc.2015.03.010>.
- Xiong, Zikang, Huaili Zheng, Yadan Hu, Xuebin Hu, Wei Ding, Jiangya Ma, and Yisen Li. 2021. "Selective Adsorption of Congo Red and Cu(II) from Complex Wastewater by Core-Shell Structured Magnetic Carbon@zeolitic Imidazolate Frameworks-8 Nanocomposites." *Separation and Purification Technology* 277 (December). <https://doi.org/10.1016/j.seppur.2021.119053>.
- Yang, Huaiyu, Fan Zhang, and Han Wu. 2018. "Review on Life Cycle of Parabens: Synthesis, Degradation, Characterization and Safety Analysis." *Current Organic Chemistry* 22 (8): 769–79. <https://doi.org/10.2174/1385272822666180123150323>.
- Yao, Pengzhao, Hongli Liu, Dongtao Wang, Jiangyao Chen, Guiying Li, and Taicheng An. 2018. "Enhanced Visible-Light Photocatalytic Activity to Volatile Organic Compounds Degradation and Deactivation Resistance Mechanism of Titania Confined inside a Metal-Organic Framework." *Journal of Colloid and Interface Science* 522 (July): 174–82. <https://doi.org/10.1016/j.jcis.2018.03.075>.
- Yalçın, Ecem, and Meral Dükkancı. 2022. "Ternary CuS@Ag/BiVO₄ Composite for Enhanced Photo-Catalytic and Sono-Photocatalytic Performance under Visible Light." *Journal of Solid State Chemistry* 313 (September).
<https://doi.org/10.1016/j.jssc.2022.123319>.
- Yaneva, Zvezdelina, Nedyalka v Georgieva, and Zvezdelina L Yaneva. 2012. "Insights into Congo Red Adsorption on Agro-Industrial Materials-Spectral, Equilibrium, Kinetic, Thermodynamic, Dynamic and Desorption Studies. A Review." *International Review of Chemical Engineering (I.RE.C.H.E.)* 4 (2).
<https://www.researchgate.net/publication/231520472>.
- Yang, Huan, Shuai Hu, Hui Zhao, Xiaofei Luo, Yi Liu, Chengfei Deng, Yulan Yu, et al. 2021. "High-Performance Fe-Doped ZIF-8 Adsorbent for Capturing Tetracycline from Aqueous Solution." *Journal of Hazardous Materials* 416 (August).
<https://doi.org/10.1016/j.jhazmat.2021.126046>.
- Yang, Junhao, Lin Han, Wanyong Yang, Qing Liu, Zhaoyang Fei, Xian Chen, Zhuxiu Zhang, Jihai Tang, Mifen Cui, and Xu Qiao. 2022. "In Situ Synthetic Hierarchical Porous MIL-53(Cr) as an Efficient Adsorbent for Mesopores-Controlled Adsorption of Tetracycline." *Microporous and Mesoporous Materials* 332 (February). <https://doi.org/10.1016/j.micromeso.2021.111667>.

- Yao, Chuncai, and Tianjiao Chen. 2017. "A Film-Diffusion-Based Adsorption Kinetic Equation and Its Application." *Chemical Engineering Research and Design* 119 (March): 87–92. <https://doi.org/10.1016/j.cherd.2017.01.004>.
- Ye, Shangshi, Yingxu Chen, Xiaoling Yao, and Jingdong Zhang. 2021. "Simultaneous Removal of Organic Pollutants and Heavy Metals in Wastewater by Photoelectrocatalysis: A Review." *Chemosphere*. Elsevier Ltd. <https://doi.org/10.1016/j.chemosphere.2020.128503>.
- You, Junhua, Yaozu Guo, Rui Guo, and Xuanwen Liu. 2019. "A Review of Visible Light-Active Photocatalysts for Water Disinfection: Features and Prospects." *Chemical Engineering Journal*. Elsevier B.V. <https://doi.org/10.1016/j.cej.2019.05.071>.
- Yousefi, Azam, Ali Allahverdi, and Parisa Hejazi. 2013. "Effective Dispersion of Nano-TiO₂ Powder for Enhancement of Photocatalytic Properties in Cement Mixes." *Construction and Building Materials* 41 (April): 224–30. <https://doi.org/10.1016/j.conbuildmat.2012.11.057>.
- Yu, Bo, Feifei Wang, Weibing Dong, Jie Hou, Pingchao Lu, and Junbo Gong. 2015. "Self-Template Synthesis of Core-Shell ZnO@ZIF-8 Nanospheres and the Photocatalysis under UV Irradiation." *Materials Letters* 156 (May): 50–53. <https://doi.org/10.1016/j.matlet.2015.04.142>.
- Yu, Ruobing, and Zhicong Wu. 2020. "High Adsorption for Ofloxacin and Reusability by the Use of ZIF-8 for Wastewater Treatment." *Microporous and Mesoporous Materials* 308 (December). <https://doi.org/10.1016/J.MICROMESO.2020.110494>.
- Zare, Ehsan Nazarzadeh, Sidra Iftexhar, Yuri Park, Jessy Joseph, Varsha Srivastava, Moonis Ali Khan, Pooyan Makvandi, Mika Sillanpaa, and Rajender S. Varma. 2021. "An Overview on Non-Spherical Semiconductors for Heterogeneous Photocatalytic Degradation of Organic Water Contaminants." *Chemosphere*. Elsevier Ltd. <https://doi.org/10.1016/j.chemosphere.2021.130907>.
- Zhang, Chen, Donghui He, Shanshan Fu, Guangming Zeng, Qinghua Liang, Yang Yang, Danlian Huang, Wenjun Wang, and Yin Zhou. 2021. "Silver Iodide Decorated ZnSn(OH)₆ Hollow Cube: Room-Temperature Preparation and Application for Highly Efficient Photocatalytic Oxytetracycline Degradation." *Chemical Engineering Journal* 421 (October): 129810. <https://doi.org/10.1016/j.cej.2021.129810>.

- Zhang, Gaosheng, Jiuhui Qu, Huijuan Liu, Adrienne T. Cooper, and Rongcheng Wu. 2007. "CuFe₂O₄/Activated Carbon Composite: A Novel Magnetic Adsorbent for the Removal of Acid Orange II and Catalytic Regeneration." *Chemosphere* 68 (6): 1058–66. <https://doi.org/10.1016/j.chemosphere.2007.01.081>.
- Zhang, Huifeng, Man Zhao, Yang Yang, and Y. S. Lin. 2019. "Hydrolysis and Condensation of ZIF-8 in Water." *Microporous and Mesoporous Materials* 288 (November). <https://doi.org/10.1016/j.micromeso.2019.109568>.
- Zhang, Qingchun, Lei Jiang, Jun Wang, Yongfa Zhu, Yujuan Pu, and Weidong Dai. 2020. "Photocatalytic Degradation of Tetracycline Antibiotics Using Three-Dimensional Network Structure Perylene Diimide Supramolecular Organic Photocatalyst under Visible-Light Irradiation." *Applied Catalysis B: Environmental* 277 (November): 119122. <https://doi.org/10.1016/j.apcatb.2020.119122>.
- Zhang, Quan, Qinghong Zhang, Hongzhi Wang, and Yaogang Li. 2013. "A High Efficiency Microreactor with Pt/ZnO Nanorod Arrays on the Inner Wall for Photodegradation of Phenol." *Journal of Hazardous Materials* 254–255 (1): 318–24. <https://doi.org/10.1016/j.jhazmat.2013.04.012>.
- Zhang, Ruiyang, Minzhi Ma, Qian Zhang, Fan Dong, and Ying Zhou. 2018. "Multifunctional G-C₃N₄/Graphene Oxide Wrapped Sponge Monoliths as Highly Efficient Adsorbent and Photocatalyst." *Applied Catalysis B: Environmental* 235 (November): 17–25. <https://doi.org/10.1016/j.apcatb.2018.04.061>.
- Zhang, Wenhai, Zhaoyong Bian, Yiyin Peng, Hanyu Tang, and Hui Wang. 2023. "Dual-Function Oxygen Vacancy of BiOBr Intensifies Pollutant Adsorption and Molecular Oxygen Activation to Remove Tetracycline Hydrochloride." *Chemical Engineering Journal* 451 (January). <https://doi.org/10.1016/j.cej.2022.138731>.
- Zhang, Yizhe, Bin Wang, Giovanni Cagnetta, Lei Duan, Jian Yang, Shubo Deng, Jun Huang, Yujue Wang, and Gang Yu. 2018. "Typical Pharmaceuticals in Major WWTPs in Beijing, China: Occurrence, Load Pattern and Calculation Reliability." *Water Research* 140 (September): 291–300. <https://doi.org/10.1016/j.watres.2018.04.056>.
- Zhao, Xue, Yi Zheng, Shiyao Hu, Wenhui Qiu, Jiping Jiang, Chuanzi Gao, Jianzhi Xiong, Haiyan Lu, and Feng Quan. 2021. "Improving Urban Drainage Systems to Mitigate PPCPs Pollution in Surface Water: A Watershed Perspective." *Journal of*

- Hazardous Materials* 411 (June): 125047.
<https://doi.org/10.1016/j.jhazmat.2021.125047>.
- Zhao, Xuesong, Guan Zhang, and Zhenghua Zhang. 2020. "TiO₂-Based Catalysts for Photocatalytic Reduction of Aqueous Oxyanions: State-of-the-Art and Future Prospects." *Environment International*. Elsevier Ltd.
<https://doi.org/10.1016/j.envint.2019.105453>.
- Zheng, Jian, Hong Tao Liu, Bin Wu, Chong An Di, Yun Long Guo, Ti Wu, Gui Yu, Yun Qi Liu, and Dao ben Zhu. 2012. "Production of Graphite Chloride and Bromide Using Microwave Sparks." *Scientific Reports* 2.
<https://doi.org/10.1038/srep00662>.
- Zhong, Wan Ling, Chao Li, Xiao Ming Liu, Xiu Kui Bai, Gang Sheng Zhang, and Cai Xia Lei. 2020. "Liquid Phase Deposition of Flower-like TiO₂ Microspheres Decorated by ZIF-8 Nanoparticles with Enhanced Photocatalytic Activity." *Microporous and Mesoporous Materials* 306 (October): 110401.
<https://doi.org/10.1016/j.micromeso.2020.110401>
- Zhou, Long, Na Li, Gary Owens, and Zuliang Chen. 2019. "Simultaneous Removal of Mixed Contaminants, Copper and Norfloxacin, from Aqueous Solution by ZIF-8." *Chemical Engineering Journal* 362 (April): 628–37.
<https://doi.org/10.1016/j.cej.2019.01.068>.
- Zhu, Kairuo, Changlun Chen, Huan Xu, Yang Gao, Xiaoli Tan, Ahmed Alsaedi, and Tasawar Hayat. 2017. "Cr(VI) Reduction and Immobilization by Core-Double-Shell Structured Magnetic Polydopamine@Zeolitic Imidazolate Frameworks-8 Microspheres." *ACS Sustainable Chemistry and Engineering* 5 (8): 6795–6802.
<https://doi.org/10.1021/acssuschemeng.7b01036>.
- Zhou, Yun, Sheng Feng, Xuemei Duan, Wei Wu, Zhiwei Ye, Xiaojun Dai, Yang Wang, and Xun Cao. 2022. "Stable Self-Assembly Cu₂O/ZIF-8 Heterojunction as Efficient Visible Light Responsive Photocatalyst for Tetracycline Degradation and Mechanism Insight." *Journal of Solid State Chemistry* 305 (January): 122628.
<https://doi.org/10.1016/j.jssc.2021.122628>.

APPENDIX A

SUPPLEMENTARY INFORMATION FOR CHAPTER-4

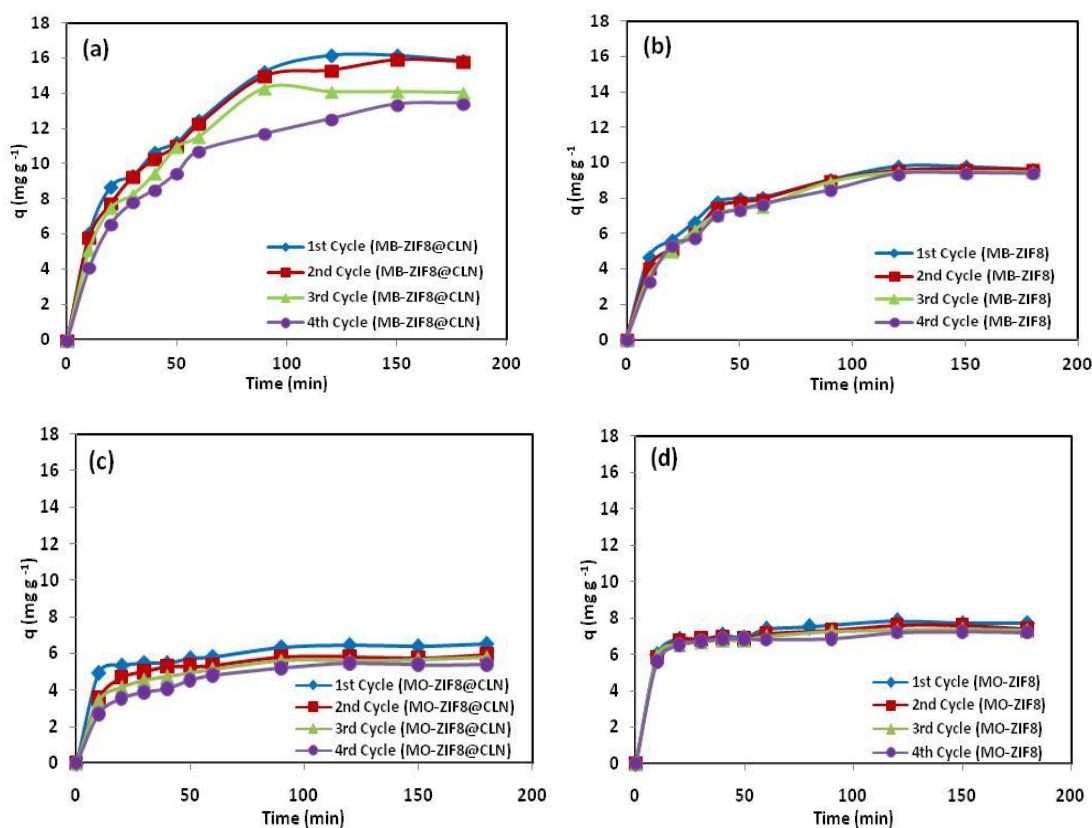


Figure A.1. (a) MB adsorption by ZIF-8@CLN, (b) MB adsorption by ZIF-8, (c) MO adsorption by ZIF-8@CLN, (d) MO adsorption by ZIF-8 for four consecutive cycles. Experimental conditions: volume of dye solution=40 ml; MB ($C_0=10 \text{ mg L}^{-1}$, $m_{\text{ZIF-8}}=1 \text{ g L}^{-1}$, pH= 10); MB ($C_0=12.5 \text{ mg L}^{-1}$, $m_{\text{ZIF-8@CLN}}=0.75 \text{ g L}^{-1}$, pH= 10); MO ($C_0=10 \text{ mg L}^{-1}$, $m_{\text{ZIF-8}}=1.25 \text{ g L}^{-1}$, pH= 4); MO ($C_0=10 \text{ mg L}^{-1}$, $m_{\text{ZIF-8@CLN}}=1.5 \text{ g L}^{-1}$, pH= 4).

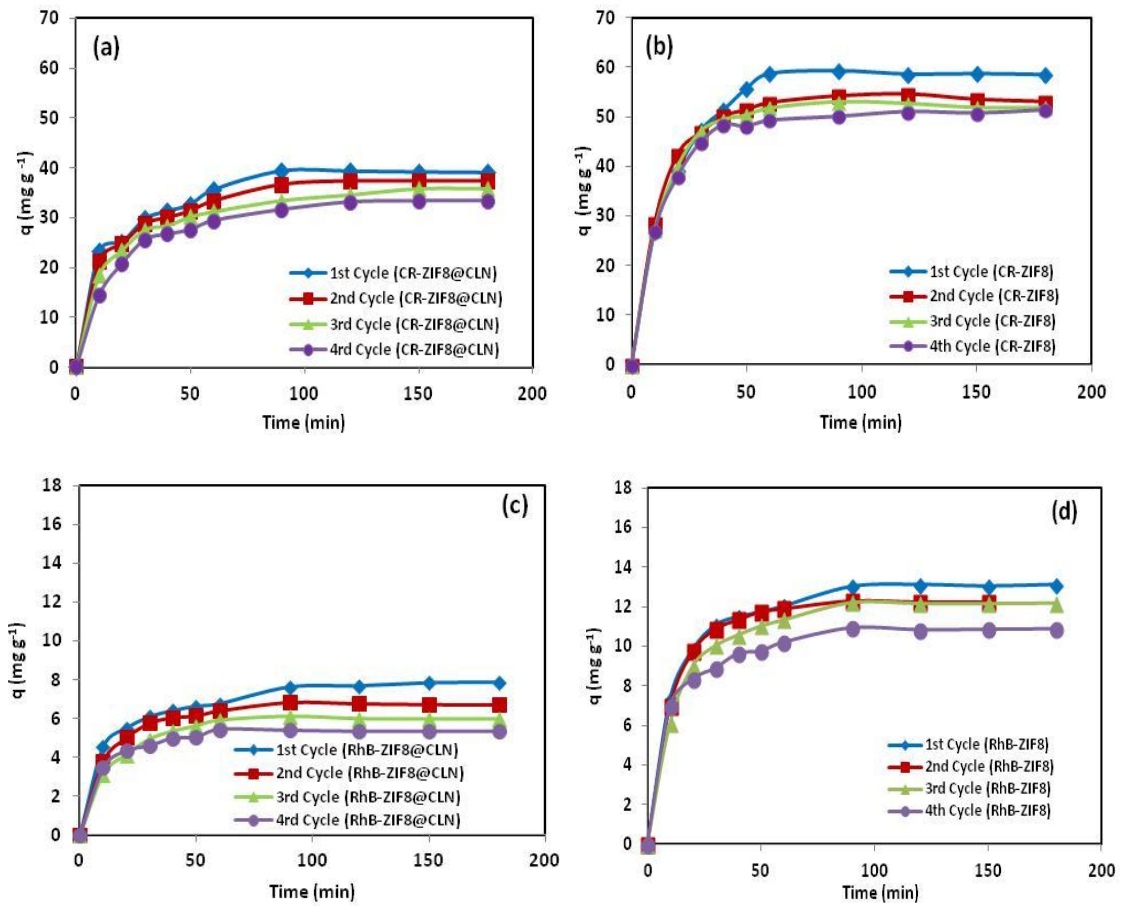


Figure A.2. (a) CR adsorption by ZIF-8@CLN, (b) CR adsorption by ZIF-8, (c) RhB adsorption by ZIF-8@CLN, (g) RhB adsorption by ZIF-8. Experimental conditions: volume of dye solution=40 ml; CR ($C_0=30 \text{ mg L}^{-1}$, $m_{\text{ZIF-8}}=0.5 \text{ g L}^{-1}$, $\text{pH}=4$); CR ($C_0=20 \text{ mg L}^{-1}$, $m_{\text{ZIF-8@CLN}}=0.5 \text{ g L}^{-1}$, $\text{pH}=4$); RhB ($C_0=10 \text{ mg L}^{-1}$, $m_{\text{ZIF-8}}=0.75 \text{ g L}^{-1}$, $\text{pH}=8$); RhB ($C_0=10 \text{ mg L}^{-1}$, $m_{\text{ZIF-8@CLN}}=1.25 \text{ g L}^{-1}$, $\text{pH}=8$).

Table A.1. Effect of pH for ZIF-8 and ZIF8@CLN. (Experimental conditions: pH range=4-11, $m_{\text{catalyst}}=0.04$ g, $C_0=25$ mg L⁻¹)

		ZIF-8		ZIF8@CLN	
	pH	Dark Adsorption (%)	Total Removal (Ads+Photodeg) (%)	Dark Adsorption (%)	Total Removal (Ads+Photodeg) (%)
MB	4	45.7	53.8	51.2	65.6
	8	53.9	60.7	60.0	74.7
	11	59.7	67.9	80.4	95.5
MO	4	74.2	81.8	44.8	53.0
	8	66.5	71.6	30.7	37.0
	11	51.5	57.3	24.7	29.2
CR	4	98.6	98.7	97.7	98.3
	8	95.0	97.5	83.1	87.0
	11	53.2	57.6	41.0	45.2
RhB	4	65.1	71.6	64.8	70.7
	8	73.0	81.2	72.4	80.3
	11	65.8	73.1	64.3	70.8

Table A.2. Effect of photocatalyst amount for ZIF-8 and ZIF8@CLN. (Experimental conditions: catalyst amount range $m=0.01-0.08$ g, $C_0=25$ mg L⁻¹, pH (MB)=11, pH (MO)=4; pH (CR)=4, pH (RhB)=8)

		ZIF-8		ZIF8@CLN	
	m (g)	Dark Adsorption (%)	Total Removal (Ads+Photodeg) (%)	Dark Adsorption (%)	Total Removal (Ads+Photodeg) (%)
MB	0.01	41.3	51.1	54.8	64.8
	0.04	59.7	70.8	80.4	90.5
	0.08	68.0	81.0	86.9	97.9
MO	0.01	32.0	37.2	22.5	25.2
	0.04	74.2	79.5	44.8	49.8
	0.08	86.6	92.1	75.9	81.2
CR	0.01	91.7	92.1	90.2	91.6
	0.04	98.6	98.7	97.7	98.9
	0.08	97.4	98.3	95.2	97.7
RhB	0.01	56.4	62.5	53.1	58.5
	0.04	73.0	79.6	72.4	78.8
	0.08	85.4	93.5	83.2	90.2

Table A.3. Effect of initial dye concentration for ZIF-8 and ZIF8@CLN. (Experimental conditions: dye conc. range $C_0 = 5\text{-}35 \text{ mg L}^{-1}$, $m_{\text{catalyst}} = 0.04 \text{ g}$, pH (MB)=11, pH (MO)=4; pH (CR)=4, pH (RhB)=8)

	ZIF-8			ZIF8@CLN		
	C_0 (mg L^{-1})	Dark Adsorption (%)	Total Removal (Ads+Photodeg) (%)	Dark Adsorption (%)	Total Removal (Ads+Photodeg) (%)	
MB	5	88.7	92.4	90.6	99.2	
	15	67.1	72.9	83.7	93.7	
	25	59.7	64.5	80.4	90.5	
	35	51.6	58.0	76.6	88.1	
MO	5	87.4	95.4	77.8	84.7	
	15	83.7	90.7	53.2	60.0	
	25	77.9	79.5	44.8	49.8	
	35	70.6	77.3	39.3	44.9	
CR	5	97.6	98.0	97.3	97.8	
	15	97.8	98.2	97.8	98.3	
	25	98.6	98.7	97.7	98.3	
	35	88.7	91.1	67.5	69.3	
RhB	5	93.2	99.0	92.2	97.0	
	15	85.5	90.4	76.1	80.1	
	25	73.0	79.6	72.4	78.8	
	35	65.4	71.6	65.6	72.0	

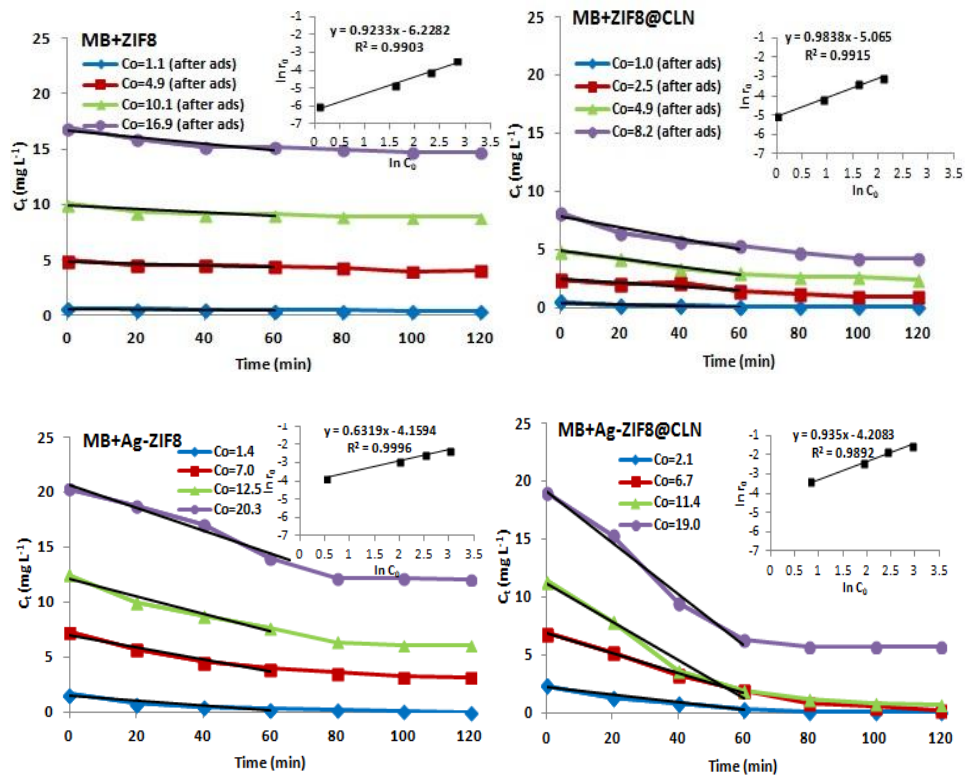


Figure A.3. Photocatalytic degradation reaction of MB with different initial concentrations. (Experimental conditions: $m_{\text{catalyst}}=0.04$ g, $\text{pH}=11$)

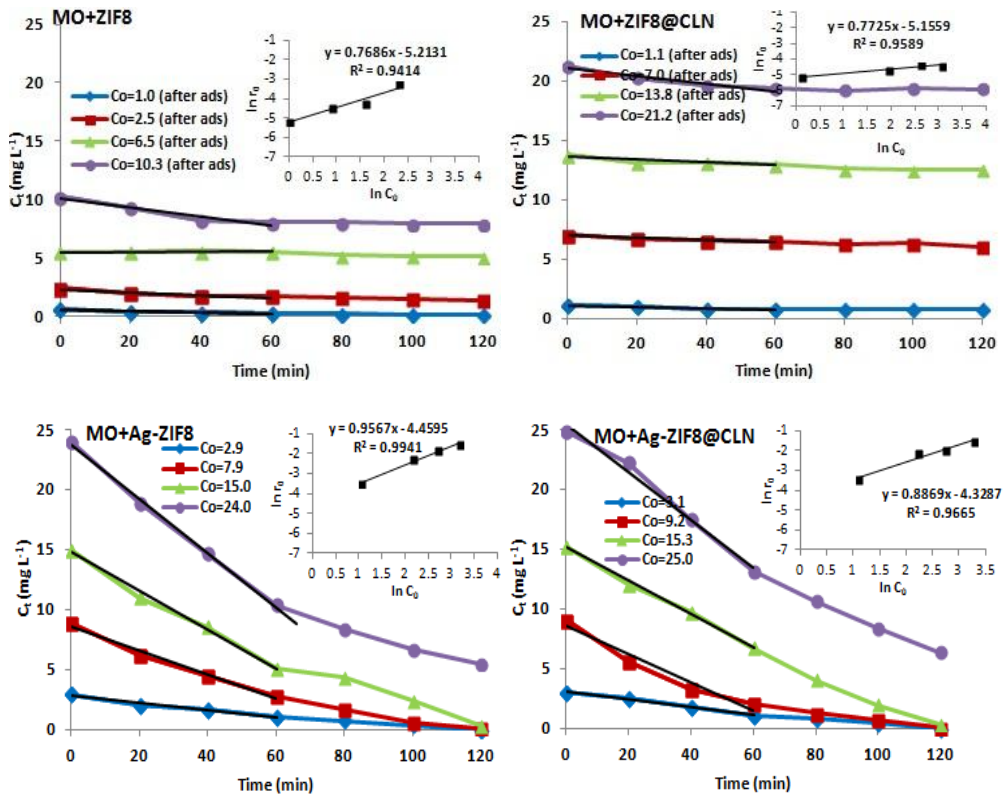


Figure A.4. Photocatalytic degradation reaction of MO with different initial concentrations. (Experimental conditions: $m_{\text{catalyst}}=0.04$ g, $\text{pH}=4$)

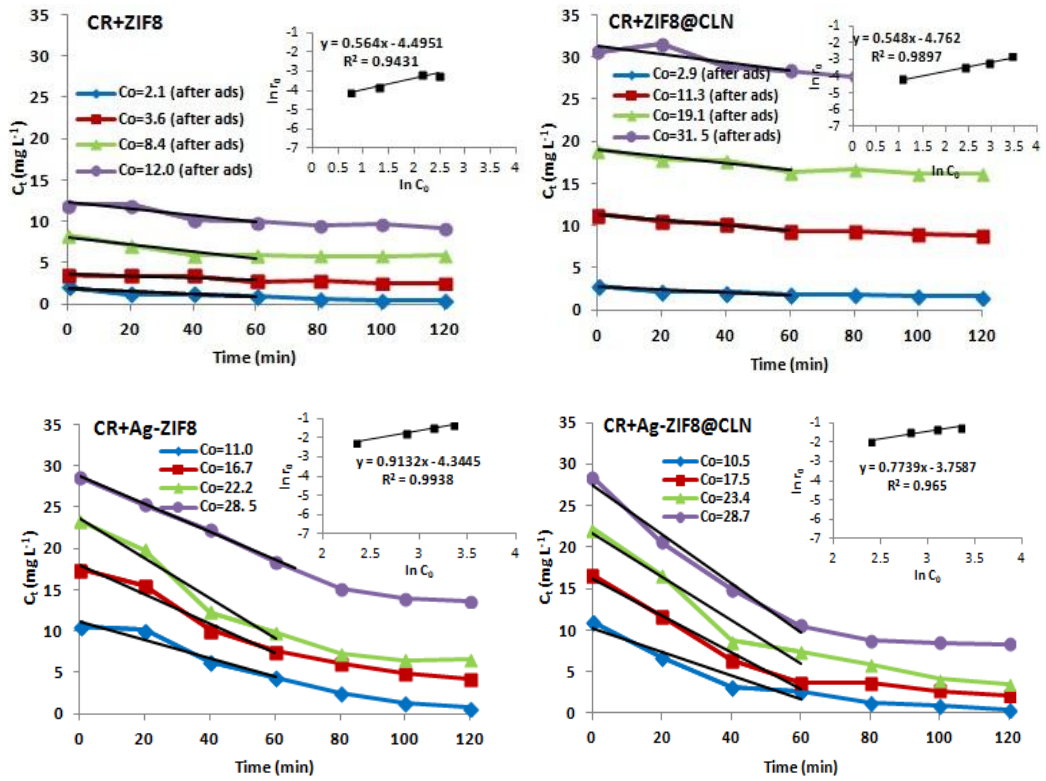


Figure A.5. Photocatalytic degradation reaction of CR with different initial concentrations. (Experimental conditions: $m_{\text{catalyst}}=0.04$ g, $\text{pH}=4$)

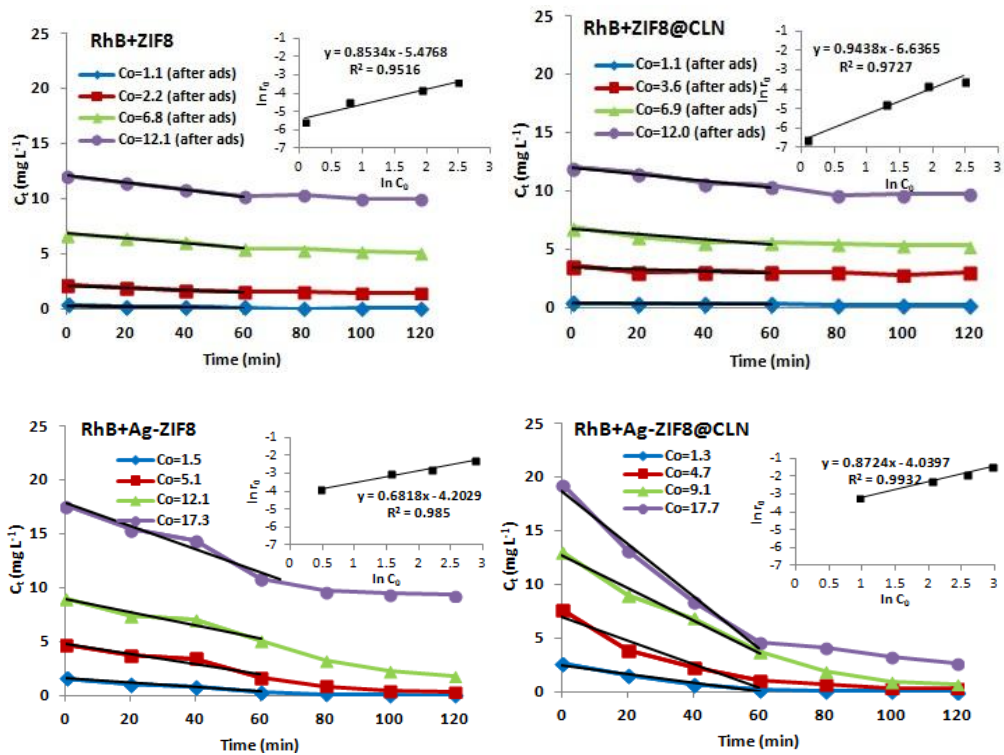


Figure A.6. Photocatalytic degradation reaction of RhB with different initial concentrations. (Experimental conditions: $m_{\text{catalyst}}=0.04$ g, $\text{pH}=8$)

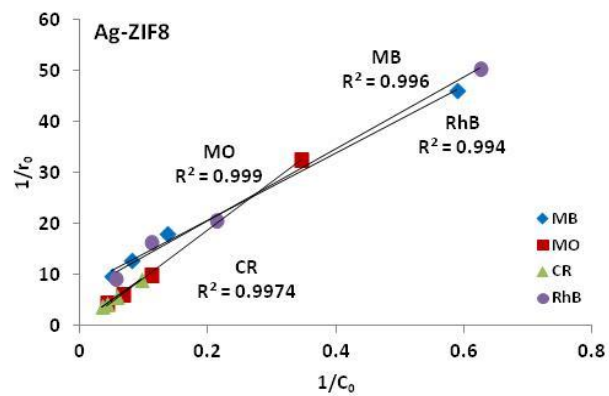


Figure A.7. The Langmuir–Hinshelwood plot for the photodegradation of MB, MO, CR and RhB over Ag-ZIF8. (Experimental conditions: $m_{\text{Ag-ZIF8}}=0.04$ g, pH (MB)=11, pH (MO)=4; pH (CR)=4, pH (RhB)=8)

APPENDIX B

PERMISSIONS FOR REPRODUCING PUBLISHED ARTICLE

The permission have been taken to reproduce the text in Chapter 2 from Springer Nature. The documentation of the approval is given in the following.

Thank you for your order!

Dear Miss. Gizem Saygi,

Thank you for placing your order through Copyright Clearance Center's RightsLink® service.

Order Summary

Licensee: İzmir Institute of Technology
Order Date: Jun 2, 2023
Order Number: 5560801296585
Publication: eBook
Title: Photocatalytic Reactors Design and Operating Parameters on the Wastewater Organic Pollutants Removal
Type of Use: Thesis/Dissertation
Order Total: 0.00 USD

(Original Order Number: 501817482)

VITA

Education

- Chemical Engineering, Izmir Institute of Technology, İzmir, Turkey
- Ph.D.* Thesis: “Removal of dyes and antibiotics by adsorption and photocatalytic degradation using Zn-based composites” 2023
Advisor: Prof. Dr. Fehime ÇAKICIOĞLU ÖZKAN
- Chemical Engineering, Ege University, İzmir, Turkey
- M.Sc.* Thesis: “The interaction among the cationic and anionic surfactants on the acid activated clay surface” 2016
Advisor: Prof. Dr. Saadet YAPAR
- Environmental Science, Ege University, İzmir, Turkey
- M.Sc.* Thesis: “Removal of copper (II), nickel (II) and zinc (II) ions from aqueous solutions by chemically modified iron tree cone” 2015
Advisor: Prof. Dr. Günseli ÖZDEMİR
- B.S.* Business Administration, Anadolu University, Eskişehir, Turkey 2014
- Chemical Engineering, Gazi University, Ankara, Turkey
- B.S.* Senior thesis: “The adsorption of Reactive yellow 176 by using bio adsorbents” 2012
Advisor: Assoc. Prof. Dr. Ayşe TOSUN

Academic Experience

<i>Research Assistant</i>	Chemical Engineering, Izmir Institute of Technology, Izmir, Turkey	2016-
<i>Project Supervisor</i>	TUBITAK 2209/A Project: The photocatalytic degradation of Rhodamine B by Zeolitic imidazolate framework (ZIF-8).	2022-2023
<i>Project Assistant</i>	Ege University Centre for Environmental Studies Project: Removal of heavy metal ions from aqueous solutions by biomaterials	2013-2014

Honors

High Honors Certificates

Gazi University

2008-2012

Academic Projects and Publications

- "Photocatalytic Reactors Design and Operating Parameters on the Wastewater Organic Pollutants Removal" Published Book Chapter (Springer, In book: Photocatalysis for Environmental Remediation and Energy Production) 2023
- "Photocatalytic Degradation of Aquatic Organic Pollutants with Zn and Zr based Metal-Organic Frameworks: ZIF-8 and UIO-66" Published Article (Turkish Journal of Chemistry, 46, 1358-1375) 2022
- Catalysis Symposium, A Key to Sustainability, Izmir/Turkey "Silver Doped Catalyst from ZIF-8-Coated-Clinoptilolite (Ag-ZIF8@CLN) for the Photocatalytic Degradation of Rhodamine B in Water, Poster Presentation. 2022
- International Fiber and Polymer Research Symposium-6, Bursa/Turkey "Immobilization of Cu-BTC on the Cotton Fibers for Sensor Applications" Oral Presentation and Publication. 2020
- Euroasiacongress-5, Adana/Turkey "Development of ZIF-8 and ZIF-8/Cu-BTC Photocatalysts and Immobilization onto the Supports" Oral Presentation and Publication. 2019
- Euroasiacongress-5, Adana/Turkey "Sensor Application of Cu-BTC Deposited Pulp Fibers" Oral Presentation and Publication. 2019
- International Porous and Powder Materials Symposium-4, Mugla/Turkey "Synthesis of Zn-Based Organic Frameworks as Photocatalyst" Oral Presentation and Publication. 2019